

**DECOMPOSED VIBRO-ACOUSTIC FREQUENCY
RESPONSE FUNCTIONS FOR THE PREDICTION OF
RADIATED SOUND**

Acoustics Research Centre, University of Salford

Salford, UK

Author: Lucy Barton

Supervisor: Dr Andrew Elliott

Submitted in partial fulfilment of the requirements of the degree of Doctor of Philosophy

May 2023

ABSTRACT

There are several methods employed to conduct analysis of vibrations in structures. These methods can be applied to various problems caused by vibrations, such as external noise, and also to monitor the behavior of the source or structure which is either producing or transmitting these vibrations. This project aims to work towards the development of a method which can conduct real-time prediction of radiated vehicle noise whilst also performing structural health monitoring in the presence of unmeasured background noise sources.

In order to predict receiver response from a vibro-acoustic sound source, several techniques can be employed to mathematically predict the acoustic emissions from a vibrating structure. In this case, the source- receiver assembly will be analysed using in-situ transfer path analysis to determine the frequency response functions and blocked forces of the structure to predict exterior noise. A novel volume velocity source will be used in conjunction with established blocked forces method of radiated noise prediction for calculating the noise produced by a plate in an anechoic chamber when excited by multiple vibration sources.

Further to this, a Singular Value Decomposition (SVD) approach is used to determine a description of predicted modes, with a view to implement the foundations of a method for condition monitoring and exterior noise emission prediction of complex structures due to vibro-acoustic excitation. A method including elements of the blocked force calculation, in combination with a modal analysis technique based on Singular Value Decomposition and the Blocked Force technique is investigated. This is conducted using an experiment based on the radiation of a plate with multiple vibration sources, with the aim to use decomposed transfer functions to predict the contribution to the radiated noise from a particular mode or group of modes.

CONTENTS

DECOMPOSED VIBRO-ACOUSTIC FREQUENCY RESPONSE FUNCTIONS FOR THE PREDICTION OF RADIATED SOUND	0
CONTENTS.....	2
LIST OF ACRONYMS	6
LIST OF SYMBOLS	6
LIST OF FIGURES	8
Acknowledgements.....	23
1 INTRODUCTION	24
1.1 Motivation and Context.....	25
1.2 Literature Review.....	27
1.2.1 Source Characterisation and TPA.....	28
1.2.2 Condition Monitoring and Modal Analysis	32
1.2.3 Volume Velocity Sources	40
1.3 Objectives.....	42
1.4 Thesis Outline	42
2 THEORY	44
2.1 Transfer Functions.....	44
2.2 In-Situ Blocked Forces: Matrix Inversion Method	46
2.2.1 Volume Velocity Source.....	49
2.3 Reciprocity	50

2.4	Singular Value Decomposition	51
2.5	Singular Value Extraction Method for Construction of a Transfer Function Containing a Single Mode: LvF Method	53
2.6	Modes in Beams	55
2.7	Modes in Plates	56
3	Methodology	59
3.1	Volume Velocity Source	60
3.1.1	Design	61
3.1.2	Comparison Between <i>H_{pf}</i> and <i>H_{vq}</i> at Accelerometer Positions on the Plate and Microphone Positions.....	65
3.1.3	For microphone position at 0°	68
3.1.4	For microphone position at 30°	70
3.1.5	For microphone position at 60°	72
3.1.6	For microphone position at 90°	74
3.2	Experimental Equipment.....	81
3.2.1	Scanning Laser Vibrometer (SLV)	81
3.2.2	Measurement Microphones.....	82
3.2.3	Impact Hammer	82
3.2.4	Accelerometers and Force Transducers	86
3.2.5	Shakers.....	88
3.2.6	Data Acquisition and Analysis.....	89
3.3	Experimental Methodology.....	90

3.3.1	Beam Model Experiment	90
3.3.2	Measured Beam Experiment.....	91
3.3.3	Scanning Laser Vibrometer Experiment.....	93
3.3.4	Anechoic Chamber Experiment.....	96
4	MODAL DECOMPOSITION METHOD USING SINGULAR VALUE DECOMPOSITION ON A BEAM MODEL	103
4.1	67 Response Position Model	105
4.1.1	SVD matrices of 67 response position model.....	105
4.1.2	67 response position Ξ transfer functions	110
4.2	17 response Position Model	115
4.2.1	SVD matrices of 17 response position model.....	115
4.2.2	17 Response Position Ξ Transfer Functions	119
4.3	Discussion	123
5	MODAL DECOMPOSITION METHOD USING SINGULAR VALUE DECOMPOSITION ON A MEASURED BEAM.....	126
5.1	SVD matrices of 17 Response Position Model	126
5.2	Single Mode Contribution Transfer Functions Ξ for Measured Beam	129
5.3	Discussion	132
6	MODAL DECOMPOSITION OF A PLATE MEASURED USING A SCANNING LASER VIBROMETER.....	134
6.1	Mode Shapes from Peak Picking Method	137
6.2	Decomposed Transfer Functions Ξ	143

6.2.1	Influence of reduction in grid resolution	153
6.3	Discussion	164
7	PREDICTION OF RADIATED SOUND USING THE BLOCKED FORCES METHOD AND VOLUME VELOCITY SOURCE	166
7.1	Introduction	166
7.2	Blocked Forces Method for the Prediction of Radiated Sound.....	167
7.3	Discussion	172
8	PREDICTION OF RADIATED NOISE USING AN SVD APPROACH TO THE BLOCKED FORCES METHOD	175
8.1	Introduction	175
8.2	Decomposed Transfer Functions \mathbf{E}	175
8.3	Blocked Force Predictions Using \mathbf{E}	179
8.4	Discussion	181
9	CONCLUSIONS.....	182
9.1	Further Work.....	184
	BIBLIOGRAPHY	186

LIST OF ACRONYMS

A list of frequently used acronyms. Those used infrequently are defined in the text.

Acronym	Definition
<i>FRF</i>	Frequency Response Function
<i>SVD</i>	Singular Value Decomposition
<i>L_vF</i>	SVD in terms of location versus frequency
<i>PP</i>	Peak Picking SVD method in terms of frequency by frequency
<i>SLV</i>	Scanning Laser Vibrometer
<i>PSD</i>	Power Spectral Density
<i>CPSD</i>	Cross Power Spectral Density

LIST OF SYMBOLS

Symbols used throughout the thesis. A definition of symbols used rarely, or in only one instance, is provided in the text. Where there are upper and lowercase symbols, the uppercase denotes a matrix and the lowercase a vector or scalar.

Symbol	Meaning	Units
<i>c</i>	Speed of Sound	m/s
<i>v</i>	Velocity	m/s
<i>A, a</i>	Accelerance/ Acceleration	m/s ²
<i>Y, y</i>	Mobility	m/s
<i>F, f</i>	Force/ Frequency	N, Hz
<i>P, p</i>	Pressure	Pa
<i>H</i>	Transfer Function	Pa/N, m/s ² /N, m/s/N
ω	Angular Frequency	Radians ⁻¹
<i>Q, q</i>	Volume Velocity	m ³ /s
<i>G</i>	Cross-power spectral matrix	Watts/Hertz
$\dot{\bar{F}}_{A,c}$	Blocked Force	N
<i>H_{vq}</i>	Volume velocity source transfer function	m/s
<i>H_{pf}</i>	Airborne transfer function of pressure due to force	Pa/N
<i>U</i>	SVD output: matrix of eigenvectors with elements <i>u</i>	No units
Ψ	SVD output: matrix of eigenvectors with elements φ	No units

Symbol	Meaning	Units
S	SVD output: diagonal matrix of non-negative square roots of eigenvalues /singular values with elements s	No units
Σ	SVD output: diagonal matrix of non-negative square roots of eigenvalues /singular values with elements σ	No units
V	SVD output: matrix of eigenvectors with elements v	No units
Φ	SVD output: matrix of eigenvectors with elements φ	No units
ξ	Matrix containing single singular value	No units
\bar{E}	Transfer function containing single singular value	Pa/N, m/s ² /N, m/s/N
G_{AA}	Autospectra of input	W/Hz
G_{BB}	Autospectra of output	W/Hz
G_{AB}	Crossspectra of input and output	W/Hz
k	Wavelength	m
θ	Poisson's ratio	No units
L	Length	m
h	Height	m
ρ	Density	Kg/m ³
D	Flexural rigidity	Nm ²
E	Young's modulus of elasticity	Pa
ζ	Damping ratio	No units
η	Loss factor	No units
$\check{\Phi}_{x,y}$	Eigenfunction	m

LIST OF FIGURES

Figure 2.1: Schematic of source receiver structure, consisting of vibration source ‘A’, which is coupled to a receiver structure ‘B’. When operational, the source creates multiple forces at ‘(a)’, which are then transmitted through the interface ‘(c)’ to the receiver structure ‘B’. The receiver ‘(d)’ is the point at which a combination of the radiated sound from the receiver ‘B’ and airborne radiated sound from the source ‘A’ are measured as sound pressures. ‘C’ denotes the assembly as a coupled structure, and ‘(b)’ the vibration velocities on the plate, which are the quantities use in this method.47

Figure 2.2: 4- pole representation in an acoustical system. Volume velocity Q and sound pressure p at positions 1 & 2, positive directions of these quantities denoted by arrows, figure based on [127].....50

Figure 3.1: Schematic diagram of volume velocity source. At the left, the nozzle from which the burst of air produced; the pressure transducer is inside, which is connected to the analyser. On the right is the canister of pressurised air, which is coupled to the body. The slide is used to arm the volume velocity source, and the trigger is used to release the air from the body after the slide has been cocked.....61

Figure 3.2: PCB piezoelectronics 113B21 pressure transducer.....62

Figure 3.3: diagram showing transfer functions used in calculation for volume velocity transfer function. The transfer function a_{qn} is that between the pressure sensor in the nozzle of the volume velocity source and the accelerometer array on the plate, and the transfer function a_{P2} is that between the accelerometers on the plate and the reference microphone.63

Figure 3.4: Comparison between H1 and H2 for the volume velocity source, measured at a single accelerometer mounted to a plate. Shown in blue is the H2 transfer function, and shown in red is the H1 transfer function.63

Figure 3.5: In the upper frame, the measured dB SPL at a microphone due to volume velocity source excitation is shown in blue, with the ambient background noise SPL of the anechoic chamber shown in red. The lower frame shows the signal to noise ratio between the volume velocity source signal and the ambient anechoic chamber. The x axes are between 10 Hz and 10 kHz.....64

Figure 3.6: diagram showing the angles of the response at the microphone positions, which are also the volume velocity excitation positions (black circles). The numbered accelerometer positions on the plate are excitation positions for the hammer transfer functions, and response positions for the volume velocity excitations.65

Figure 3.7: Visual representation of transfer function for plate radiation measured reciprocally, using the volume velocity source, for which measurements were taken at each microphone position to garner responses at each accelerometer position66

Figure 3.8: Visual representation of transfer function for plate radiation measured directly, using impact hammer, for which measurements were taken at each accelerometer position to garner responses at each microphone position.....67

Figure 3.9: Comparison between H_{pf} , pressure due to force in blue, and H_{vq} , velocity due to volume velocity, shown in red, for response microphone at 0° . In the left hand side frames, the y-axis is dBs, and the x-axis is frequency in Hertz, ranging between 10 Hz and 6 kHz. From top to bottom on the left, the responses at accelerometer positions 2, 10, 14, and 22 respectively. The right hand frames show the difference error in dB between the two transfer functions for the accelerometer positions on the left: from top to bottom, positions 2, 10, 14, and 22.....68

Figure 3.10: Comparison between H_{pf} , pressure due to force in blue, and H_{vq} , velocity due to volume velocity, shown in red, for response microphone at 30° . In the left hand side frames, the y-axis is dBs, and the x-axis is frequency in Hertz, ranging between 10 Hz and 6

kHz. From top to bottom on the left, the responses at accelerometer positions 2, 10, 14, and 22 respectively. The right hand frames show the difference error in dB between the two transfer functions for the accelerometer positions on the left: from top to bottom, positions 2, 10, 14, and 22.....70

Figure 3.11: Comparison between H_{pf} , pressure due to force in blue, and H_{vq} , velocity due to volume velocity, shown in red, for response microphone at 60° . In the left hand side frames, the y-axis dBs,, and the x-axis is frequency in Hertz, ranging between 10 Hz and 6 kHz. From top to bottom on the left, the responses at accelerometer positions 2, 10, 14, and 22 respectively. The right hand frames show the difference error in dB between the two transfer functions for the accelerometer positions on the left: from top to bottom, positions 2, 10, 14, and 22.....72

Figure 3.12: Comparison between H_{pf} , pressure due to force in blue, and H_{vq} , velocity due to volume velocity, shown in red, for response microphone at 90° . In the left hand side frames, the y-axis is dBs, and the x-axis is frequency in Hertz, ranging between 10 Hz and 6 kHz. From top to bottom on the left, the responses at accelerometer positions 2, 10, 14, and 22 respectively. The right hand frames show the difference error in dB between the two transfer functions for the accelerometer positions on the left: from top to bottom, positions 2, 10, 14, and 22.....74

Figure 3.13: Radiation pattern of the volume velocity source in dB with reference to a microphone at 0° . At the top of the plot is 90° , with $0^\circ/360^\circ$ to the right of the plot. Shown in blue is radiation for 10 Hz, shown in red is 50 Hz, in yellow 100 Hz, in purple 200 Hz, and in green 300 Hz. The radial axis is between zero and 120 dB.76

Figure 3.14: Radiation pattern of the volume velocity source in dB with reference to a microphone at 0° . At the top of the plot is 90° , with $0^\circ/360^\circ$ to the right of the plot. Shown in dark blue is radiation for 400 Hz, shown in red is 500 Hz, in yellow 1000 Hz, in purple 2000

Hz, in green 2500 Hz, and in light blue 3000 Hz. The radial axis is between zero and 120 dB.	77
Figure 3.15: Radiation pattern of the volume velocity source in dB with reference to a microphone at 0°. At the top of the plot is 90°, with 0°/360° to the right of the plot. Shown in dark blue is radiation for 3500 Hz, shown in red is 4000 Hz, in yellow 4500 Hz, in purple 5000 Hz, in green 5500 Hz, and in light blue 6000 Hz. The radial axis is between zero and 130 dB.....	78
Figure 3.16: Radiation pattern of the volume velocity source in dB with reference to a microphone at 0°. At the top of the plot is 90°, with 0°/360° to the right of the plot. Shown in dark blue is radiation for 7000 Hz, shown in red is 7500 Hz, in yellow 8000 Hz, in purple 8500 Hz, in green 9000 Hz, and in light blue 10000 Hz. The radial axis is between zero and 130 dB.....	79
Figure 3.17: PSV 400 scanning laser vibrometer in-situ for plate experiment detailed in Chapter 6.....	81
Figure 3.18: Bruel and Kjaer ½“ prepolarised free-field microphone Type 4966. Figure taken from product datasheet [153]......	82
Figure 3.19: Impact Hammer by Bruel & Kjaer, type 8206-001. Figure taken from the product datasheet [155]......	83
Figure 3.20: Shown left are the impulse shapes, pulse decay, and peak value for the three types of hammer tip as a function of time, shown right are the force spectra for the three hammer tips for an impact on an aluminium plate. Figure from product datasheet [155].	84
Figure 3.21: Impact hammer in case with tips shown in upper left of photograph. The left tip is the metal tip, the middle shows the side which is screwed into the hammer of another metal tip, and the left tip is the plastic tip. The bottom right element is a weight or extender which can be added to the hammer.....	85

Figure 3.22: Bruel & kjaer Type 4507 accelerometer	86
Figure 3.23: Sinocera CL-YD-303 2kN Compression only force transducer	87
Figure 3.24: Bruel & Kjaer LDS V101 permanent magnet shaker.....	88
Figure 3.25: Unbranded 4Ω, 25W shakers used in anechoic chamber experiment, detailed in chapters 7 and 8.	89
Figure 3.26: Dewesoft SIRIUS Data Acquisition System Interface.....	90
Figure 3.27: Experimental steel beam. 17 accelerometers are mounted on the bottom side of the beam at interval of 3.2cm. The beam was excited using an instrumented force hammer at each of the same positions on the upper face of the beam.....	92
Figure 3.28: Beam in testing position. The beam has been suspended using elastic bungee cords in order to approximate free-free boundary conditions.....	92
Figure 3.29: Plate mounted in-situ. The surface of the plate has been coated with a non-metallic matte white paint in order to reduce reflections, allowing the laser to take clearer measurements.....	94
Figure 3.30: Shaker in-situ for measurement of plate.....	95
Figure 3.31: Baffled plate installed in an anechoic chamber. An array of response microphones are arranged on an arc- shaped frame, allowing for the collection of frequency response functions and measured transfer functions at multiple degrees of radiation from the plate.....	96
Figure 3.32: Schematic diagrams of the plate in the anechoic chamber: on the left, a view from the side, and on the right; a view from above.	97
Figure 3.33: Interior of plate baffle showing acoustic foam.....	98
Figure 3.34: Rear side of plate showing damping application.....	99
Figure 3.35: Schematic diagram of the plate, shown from the rear, where the number grid denotes accelerometer positions. Two shakers are mounted on the plate, and a reference	

accelerometer is mounted on the other side of the plate where each shaker is attached as a further reference quantity..... 100

Figure 3.36: Schematic diagram of shaker. The shaker is rated as 4Ω , 25W, and is powered by a signal generator running through an amplifier. The shaker has been slightly modified, with the original coupling plate removed for a force transducer to be attached instead. A small grub screw is used to attach the shaker to a force transducer, which has an output to the analyser system. The face of the force transducer is superglued to the plate. 101

Figure 4.1: Diagonal of singular value matrix Σ . Each circle on the graph corresponds to a singular value ' σ ' for 67 response position model..... 105

Figure 4.2: Columns of Φ , representing temporal behaviour or frequency response, of modes 1 to 9, with respect to frequency from 10 Hz to 20 kHz in frame 1 to show the rigid body mode, and 100 Hz to 20 kHz for the other frames, for 67 response position model. 106

Figure 4.3: Singular value from PP method, showing mode frequencies at peaks for 67 response position model..... 107

Figure 4.4: Mode shapes ψ 2-9 from the columns of Ψ are shown in red, compared to the modes peak picked from the diagonal of S, shown in blue. The x-axis is the length of the beam from 0m to 0.555m, and the two y-axes are velocity. 108

Figure 4.5: Mode shapes ψ 10-17 from the columns of Ψ are shown in red, compared to the modes peak picked from the diagonal of S, shown in blue. The x-axis is the length of the beam from 0m to 0.555m, and the two y-axes are velocity. 109

Figure 4.6: Single singular value transfer function Ξ_1 plotted against full FRF for 67 response position, 20 kHz range beam model. Shown in red is the original FRF and shown in blue is the isolated singular value transfer function. The x- axis is between 1Hz and 20 kHz, as the rigid body mode is below 100 Hz..... 110

Figure 4.7 Reading from left to right, single singular value transfer functions Ξ_2 to Ξ_9 plotted against full FRF for 67 response position, 20 kHz range beam model. Shown in red is the original FRF and shown in blue is the isolated singular value model. The x- axis is between 100 Hz and 20 kHz. 111

Figure 4.8: Reading from left to right, single singular value transfer functions Ξ_{10} to Ξ_{18} plotted against full FRF for 67 response position, 20 kHz range beam model. Shown in red is the original FRF and shown in blue is the isolated singular value model. The x- axis is between 100 Hz and 20 kHz. 112

Figure 4.9: Reading from left to right, single singular value transfer functions Ξ_{18} to Ξ_{25} plotted against full FRF for 67 response position, 20 kHz range beam model. Shown in red is the original FRF and shown in blue is the isolated singular value model. The x- axis is between 100 Hz and 20 kHz. 113

Figure 4.10: Reconstructed FRF built by adding Ξ_{1-17} versus the complete model FRF for 67 response positions and a frequency range of 20 kHz. Shown in the solid line is the original model FRF and shown in the dashed red line is the reconstructed Ξ FRF. 114

Figure 4.11: Diagonal of singular value matrix Σ . Each circle on the graph corresponds to a singular value ' σ ' for 17 response position model..... 115

Figure 4.12: Singular value from PP method, showing mode frequencies at peaks for 17 response position model..... 116

Figure 4.13: First column of Ψ , showing rigid body mode of beam in terms of velocity with respect to length 116

Figure 4.14: Mode shapes ψ_{2-9} from the columns of Ψ are shown in red, compared to the modes peak picked from the diagonal of S, shown in blue. The x-axis is the length of the beam from 0m to 0.555m, and the two y-axes are velocity. 117

Figure 4.15: Mode shapes ψ 10-17 from the columns of Ψ are shown in red, compared to the modes peak picked from the diagonal of S , shown in blue. The x-axis is the length of the beam from 0m to 0.555m, and the two y-axes are velocity. 118

Figure 4.16: Single singular value transfer function Ξ_1 plotted against full FRF for 17 response position, 20 kHz range beam model. Shown in red is the original FRF and shown in blue is the isolated singular value transfer function. The x- axis is between 1Hz and 20 kHz, as the rigid body mode is below 100 Hz. 119

Figure 4.17: Reading from left to right, single singular value models Ξ_{2-9} plotted against full FRF for 17 response position, 20 kHz range beam model. Shown in red is the original FRF and shown in blue is the isolated singular value transfer function. 120

Figure 4.18: Reading from left to right, single singular value models Ξ_{10-17} plotted against full FRF for 17 response position, 20 kHz range beam model. Shown in red is the original FRF and shown in blue is the isolated singular value transfer function. 121

Figure 4.19: Reconstructed FRF using the all 17 singular value Ξ_i models versus the complete model FRF for 17 response positions and a frequency range of 20 kHz. Shown in the solid line is the original model FRF and shown in the dashed red line is the reconstructed FRF.. 122

Figure 5.1 Diagonal of singular value matrix Σ for measured beam. Each circle on the graph corresponds to a singular value ‘ σ ’ for the 17 response position measured beam. 126

Figure 5.2: Singular values from the ‘ S ’ matrix obtained from the Peak Picking SVD method, with a single force input at the first position along the beam. The SVD has been conducted on the velocity due force transfer functions, which have been converted to velocity from the measured quantity of acceleration by dividing by $j\omega$. The x-axis goes from 1 Hz to 6 kHz... 127

Figure 5.3: Mode shapes picked from the matrix of velocities at the frequency peaks shown in in the S plot, shown in black; and the mode shapes taken from the columns of Ψ , shown in grey. Shown here are Ψ 1- Ψ 18, showing picked modes up to 6 kHz. 128

Figure 5.4: Transfer functions Ξ_1 to Ξ_9 constructed using single singular values picked from the diagonal of Σ , compared to the mobility of the beam. The assembled transfer functions containing a single mode are shown in blue, and the unchanged mobility of the beam is shown in red. These are plotted as velocity, on the y-axis, against frequency on the x-axis, between 10 Hz and 6 kHz. 130

Figure 5.5: Transfer functions Ξ_{10} to Ξ_{17} constructed using single singular values picked from the diagonal of Σ , compared to the mobility of the beam. The assembled transfer functions containing a single mode are shown in blue, and the unchanged mobility FRF of the beam is shown in red. These are plotted as velocity, on the y-axis, against frequency from 10 Hz to 6 kHz on the x-axis. 131

Figure 5.6: Reconstructed FRF using the all 17 singular value Ξ_i models versus the complete model FRF for 17 response positions and a frequency range of 10 Hz to 6 kHz. Shown in the solid line is the original model FRF and shown in the dashed red line is the reconstructed FRF. 132

Figure 6.1: Diagonal of S matrix from SVD conducted on the velocity due to voltage transfer function matrix in a frequency- by-frequency loop for the PP method. The x-axis is frequency between 10 and 6400 Hz and the y-axis is velocity from 1 to 100 m/s. From this plot, the peaks are manually picked in order to determine the modes of the plate. 137

Figure 6.2: First nine mode shapes extracted using the Peak Picking Method. Seen in the first frame is the first mode of the plate, at 15 Hz. Reading left to right, the mode shapes increase in frequency. These are plotted by the dimensions of the plate in the x and y axes. 138

Figure 6.3: mode shapes 10 to 18 extracted using the Peak Picking Method. Seen in the first frame is the 10th mode of the plate, at 197 Hz. Reading left to right, the mode shapes increase in frequency. These are plotted by the dimensions of the plate in the x and y axes. 140

Figure 6.4: mode shapes 19 to 27 extracted using the Peak Picking Method. Seen in the first frame is the 19th mode of the plate, at 659 Hz. Reading left to right, the mode shapes increase in frequency. These are plotted by the dimensions of the plate in the x and y axes..... 142

Figure 6.5: Singular values on the diagonal of Σ 143

Figure 6.6: Singular transfer function Ξ_1 and Ψ_1 . The left hand plot shows Ξ_1 plotted against Y, with Ξ in blue and Y in black. The x-axis is velocity in metres per second and the y-axis is frequency in Hertz. The right hand plot shows the associated mode with the Ξ transfer function, Ψ_1 , plotted by the plate dimensions..... 144

Figure 6.7: reconstruction of SVD mode by adding the two peak frequencies in the Ξ transfer function 145

Figure 6.8: Singular transfer function Ξ_2 and Ψ_2 . The left hand plot shows Ξ_2 plotted against Y, with Ξ in blue and Y in black. The x-axis is velocity in metres per second and the y-axis is frequency in Hertz. The right hand plot shows the associated mode with the Ξ transfer function, Ψ_2 , plotted by the plate dimensions..... 146

Figure 6.9: Singular transfer function Ξ_3 and Ψ_3 . The left hand plot shows Ξ_3 plotted against Y, with Ξ in blue and Y in black. The x-axis is velocity in metres per second and the y-axis is frequency in Hertz. The right hand plot shows the associated mode with the Ξ transfer function, Ψ_3 , plotted by the plate dimensions..... 147

Figure 6.10: Singular transfer function Ξ_4 and Ψ_4 . The left hand plot shows Ξ_4 plotted against Y, with Ξ in blue and Y in black. The x-axis is velocity in metres per second and the y-axis is frequency in Hertz. The right hand plot shows the associated mode with the Ξ transfer function, Ψ_4 , plotted by the plate dimensions..... 148

Figure 6.11: Singular transfer function Ξ_5 and Ψ_5 . The left hand plot shows Ξ_5 plotted against Y, with Ξ in blue and Y in black. The x-axis is velocity in metres per second and the y-axis is

frequency in Hertz. The right hand plot shows the associated mode with the Ξ transfer function, Ψ_5 , plotted by the plate dimensions.	149
Figure 6.12: Singular transfer functions Ξ_{10} , Ξ_{20} , Ξ_{30} , Ξ_{40} , Ξ_{50} , and Ξ_{60} compared to Y . The constructed singular value transfer functions Ξ are shown in blue, and the original unaltered mobility of the plate is shown in black. The x-axes are frequency in Hertz and the y-axes are velocity in metres per second.	150
Figure 6.13: Singular transfer function Ξ_{20} and Ψ_{20} . The left hand plot shows Ξ_{20} plotted against Y , with Ξ in blue and Y in black. The x-axis is velocity in metres per second and the y-axis is frequency in Hertz. The right hand plot shows the associated mode with the Ξ transfer function, Ψ_{20} , plotted by the plate dimensions.	151
Figure 6.14: Ψ_1 to Ψ_9 mode shapes, plotted in terms of plate dimensions. There are modal shapes present in the first 5 frames	152
Figure 6.15: Diagonal of Σ , showing singular values for full dataset of 247 response positions, and with 6 remaining rows, giving 114 response positions, in red.	154
Figure 6.16: Singular transfer function Ξ_1 and Ψ_1 for reduced Y with 6 remaining rows of responses. The left hand plot shows Ξ_1 plotted against Y , with Ξ for 114 responses in red, Ξ for 247 responses in blue, and Y in black. The x-axis is velocity in metres per second and the y-axis is frequency in Hertz. The right hand plot shows the associated mode with the Ξ transfer function, Ψ_1 , plotted by the plate dimensions.	155
Figure 6.17: Singular transfer function Ξ_4 and Ψ_4 for reduced Y with 6 remaining rows of responses. The left hand plot shows Ξ_4 plotted against Y , with Ξ for 114 responses in red, Ξ for 247 responses in blue, and Y in black. The x-axis is velocity in metres per second and the y-axis is frequency in Hertz. The right hand plot shows the associated mode with the Ξ transfer function, Ψ_4 , plotted by the plate dimensions.	156

Figure 6.18: Singular transfer functions $\Xi_{10}, \Xi_{20}, \Xi_{30}, \Xi_{40}, \Xi_{50},$ and Ξ_{60} compared to Y for a reduction to 6 rows remaining in Y , with Ξ for 114 responses in red, Ξ for 247 responses in blue, and Y in black. The x-axes are frequency in Hertz and the y-axes are velocity in metres per second. 157

Figure 6.19: Singular transfer functions $\Xi_{70}, \Xi_{80}, \Xi_{90}, \Xi_{100}, \Xi_{110},$ and Ξ_{114} compared to Y for a reduction to 6 rows remaining in Y , with Ξ for 114 responses in red, Ξ for 247 responses in blue, and Y in black. The x-axes are frequency in Hertz and the y-axes are velocity in metres per second. 158

Figure 6.20 Ψ_1 to Ψ_9 mode shapes, plotted in terms of plate dimensions for 114 response positions 159

Figure 6.21: Diagonal of Σ , showing singular values for full dataset of 247 response positions, with 6 remaining rows, giving 114 response positions, in red, and with 3 remaining rows giving 57 positions, in yellow. 160

Figure 6.22: Singular transfer function Ξ_1 and Ψ_1 for reduced Y with 3 remaining rows of responses. The left hand plot shows Ξ_1 plotted against Y , with Ξ for 57 responses in red, Ξ for 247 responses in blue, and Y in black. The x-axis is velocity in metres per second and the y-axis is frequency in Hertz. The right hand plot shows the associated mode with the Ξ transfer function, Ψ_1 , plotted by the plate dimensions..... 161

Figure 6.23: Singular transfer function Ξ_5 and Ψ_5 for reduced Y with 3 remaining rows of responses. The left hand plot shows Ξ_5 plotted against Y , with Ξ for 57 responses in red, Ξ for 247 responses in blue, and Y in black. The x-axis is velocity in metres per second and the y-axis is frequency in Hertz. The right hand plot shows the associated mode with the Ξ transfer function, Ψ_5 , plotted by the plate dimensions..... 162

Figure 6.24: Ψ_1 to Ψ_9 mode shapes, plotted in terms of plate dimensions for 57 response positions 163

Figure 7.1: Predicted radiated pressure for Hpf and Hvq , plotted against measured pressure for Shaker 1 at microphone positioned at 30°. The x-axis shows frequency in Hertz between 10 Hz and 6 kHz, and the y-axis shows pressure in dB. The upper plots show the measured shaker response in black and the predicted pressure calculated using Hpf in red, with the error in second frame. The lower plots show the measured shaker response in black and the pressure calculated using Hvq in blue, with the error in the final plot 168

Figure 7.2: Predicted radiated pressure for Hpf and Hvq , plotted against measured pressure for Shaker 1 at microphone positioned at 30°. The x-axis shows frequency in Hertz between 100 Hz and 1.5 kHz, and the y-axis shows pressure in dB. The upper plots show the measured shaker response in black and the predicted pressure calculated using Hpf in red, with the error in second frame. The lower plots show the measured shaker response in black and the pressure calculated using Hvq in blue, with the error in the final plot. 169

Figure 7.3: Predicted radiated pressure for Hpf and Hvq , plotted against measured pressure for Shaker 1 at microphone positioned at 0°. The x-axis shows frequency in Hertz between 100 Hz and 1.5 kHz, and the y-axis shows pressure in dB. The upper plots show the measured shaker response in black and the predicted pressure calculated using Hpf in red, with the error in second frame. The lower plots show the measured shaker response in black and the pressure calculated using Hvq in blue, with the error in the final plot. 170

Figure 7.4: Predicted radiated pressure for Hpf and Hvq , plotted against measured pressure for Shaker 1 at microphone positioned at 60°. The x-axis shows frequency in Hertz between 100 Hz and 1.5 kHz, and the y-axis shows pressure in dB. The upper plots show the measured shaker response in black and the predicted pressure calculated using Hpf in red, with the error in second frame. The lower plots show the measured shaker response in black and the pressure calculated using Hvq in blue, with the error in the final plot. 171

Figure 7.5: Predicted radiated pressure for Hpf and Hvq , plotted against measured pressure for Shaker 1 at microphone positioned at 90°. The x-axis shows frequency in Hertz between 100 Hz and 1.5 kHz, and the y-axis shows pressure in dB. The upper plots show the measured shaker response in black and the predicted pressure calculated using Hpf in red, with the error in second frame. The lower plots show the measured shaker response in black and the pressure calculated using Hvq in blue, with the error in the final plot. 172

Figure 8.1: Plot of the singular values σ on the diagonal of singular value matrix Σ . The y-axis is magnitude and the x-axis is σ 175

Figure 8.2: First 9 Columns of Ψ which should contain the mode shapes of the plate, plotted in terms of plate dimensions. Shown are the shapes of Ψ for the volume velocity source at an angle of 60°. Due to under-sampling, the shapes are disturbed. 176

Figure 8.3: The left hand frames depict the single singular value transfer functions Ξ_1 to Ξ_4 , plotted against the original, unchanged Hvq transfer function. The x axis is frequency in Hertz and the y axis is velocity in metres per second. The right hand frames show the difference error in dB for the corresponding Ξ with respect to Hvq. 177

Figure 8.4: The left hand frames depict the single singular value transfer functions Ξ_{21} to Ξ_{24} , plotted against the original, unchanged Hvq transfer function. The x axis is frequency in Hertz and the y axis is velocity in metres per second. The right hand frames show the difference error in dB for the corresponding Ξ with respect to Hvq. 178

Figure 8.5: Predictions of radiated pressure contributions from singular value transfer functions Ξ_1 to Ξ_4 , for the microphone response and volume velocity excitation at the 60° position to the plate. The left hand frames show in blue is the original measured transfer function of pressure due to force for the operational shaker response., and plotted in red is the blocked force prediction using the constructed singular value transfer function Ξ_i . The x-axis

is frequency in Hertz and the y axis is pressure in dBs. The right hand frames show the error in dB between the prediction and the measured response in black..... 179

Figure 8.6: Predictions of radiated pressure contributions from singular value transfer functions Ξ_{21} to Ξ_{24} , for the microphone response and volume velocity excitation at the 60° position to the plate. The left hand frames show in blue is the original measured transfer function of pressure due to force for the operational shaker response., and plotted in red is the blocked force prediction using the constructed singular value transfer function Ξ_i . The x-axis is frequency in Hertz and the y axis is pressure in dBs. The right hand frames show the error in dB between the prediction and the measured response in black..... 180

Acknowledgements

Firstly, I must thank my supervisors Dr Andrew Elliott, Prof John Smith, and Prof Andy Moorhouse, for their ideas which have formed the basis of this work. In the initial stages of the project, Professor Moorhouse provided me with some invaluable insight and advice which I found massively helpful as the project progressed. I feel very fortunate to have had Professor Smith from DSTL as my industrial supervisor; he has been incredibly patient talking through ideas and has contributed a huge amount with his knowledgeable explanations and insight of complex concepts.

Dr Elliott has given me unwavering support throughout the project, and I have learnt so much under his guidance. I am immeasurably grateful to have had him as my supervisor. Thankyou to Mitch and everyone at QQ for making me so welcome on my placement.

Thanks to Dr Josh Meggitt and Dr Kevin Weinen for helping me to get started. Huge gratitude goes to Mike Clegg for building testing rigs from terrible schematic drawings. Also to Mike Jones, Henric, and Danny for their support with experiments, and thankyou to my fellow PhD students and the staff at the Acoustic Research Centre. I've made some wonderful friends for life during my PhD.

Many thanks to my all of my family and friends, for their cheerleading and belief in me when I have needed it, and finally, cheers to Ric for being there for me.

1 INTRODUCTION

This thesis details the development of a method for the external noise prediction of a structure when there is no external monitoring possible. It is necessary for the method to separate out the radiated noise into modal contributions, so that the operational conditions of the structure can be adjusted to regulate the external noise, and the noise profile can be estimated in terms of frequency. In addition to this, a volume velocity source has been developed.

By characterising the blocked forces of the structure and measuring a vibro-acoustic transfer function using a volume velocity source prior to installation, the continual monitoring of the structure will be achieved by instrumenting the structure with accelerometers and using the measured blocked forces and transfer functions for the external noise measurement.

Noise emissions from machinery and other vibrating sound sources are generally transmitted either via the structure connected to the source (structure-borne noise) or into the surrounding air (airborne noise) emission. There are exceptions to this, being emission into liquids, such as in pipes, or gases other than air surrounding the machine, such as gas inside an exhaust system [1]. Over the years, many ISO and BS standards have been developed to categorize these effects.

Structure-borne sound characterisation methods generally require two measurement stages: active- concerning free velocity and blocked forces, which are utilized when the machine is running; and passive – frequency response functions, such as mobility, when the machine is not operational [2]. The applications for effective analysis and prediction of noise are myriad, from domestic product quality assurance, to safety implications in vehicles or buildings.

Therefore, constant developments and innovations are apparent in the literature surrounding the topic.

In traditional Experimental Modal Analysis (EMA) methods, excitations (inputs) and responses (outputs) can be used in various algorithmic configurations, such as: Single-Input/Single-Output (SISO); Single-Input/ Multiple-Output (SIMO); and Multiple-Input/ Multiple-Output (MIMO), in order to estimate parameters of modal behaviour. These resulting parameters consist of damping ratios, modal frequencies, mode shapes, and modal participation factors [3]. Operational Modal Analysis (OMA) differs from EMA in the fact that it monitors only the output; rendering it a stochastic rather than deterministic method [4]. OMA is commonly used in industrial and structural condition monitoring applications. This thesis details a method combining a traditional Transfer Path Analysis (TPA) source characterisation with an OMA-style SVD for separating out modal contributions to radiated noise.

1.1 Motivation and Context

This project has a view to build upon an existing method of transfer path analysis, in order to implement a system of transmission path analysis, condition monitoring, and exterior noise emission level prediction based on the modal behaviour of a radiating structure. The aim of the method is for application in scenarios in which the blocked forces of the system are already known, and to modify the existing radiated noise prediction process for the prediction of specific contributions to the overall radiated noise from particular frequency elements. Instead of measuring the interface between a source and receiver within a complete structure, as in the traditional blocked forces approach, the entire structure is treated as the source, with the air between the structure and the remote measurement position treated as the receiver. Traditionally, sound power is used as the measure for this transfer function, whereas here an implementation of the blocked forces method is used. This is due to a lack of measurement external to structure in the intended application. The prediction of the radiated noise is measured using only the characterised blocked forces and the transfer functions measured

previous to installation. The blocked forces of the structure now translate to blocked pressures on the structure surface.

A volume velocity source for the reciprocal measurement of vibro-acoustic transfer functions is described and compared to a method using an impact hammer for direct airborne transfer function measurement. A method which combines a Singular Value Decomposition (SVD) approach with the blocked forces method is evaluated. This method uses a location vs frequency SVD on all frequencies of the vibro-acoustic transfer function simultaneously to produce a diagonal matrix of singular values. These singular values are then individually extracted and built into a new transfer function, \bar{E} , which, when inserted into the blocked force equation for the prediction of radiated sound, should provide the contribution of the mode or modes described by a single singular value.

This is motivated by a lack of methods using sparsely instrumented accelerometer arrays, and a lack of real-time prediction methods for this scenario. Applications for this research are varied, however the theory is predicted to be most useful in the monitoring and prediction of vehicle and machinery noise and vibration. For example, the method could be used to install a real time radiated noise prediction system of a machine which is situated in a factory but difficult to reach directly, for which the characterisation of the source individually is required for reasons of source separation and individual component monitoring. The machine would be characterised in terms of its blocked forces in situ, and remain instrumented with accelerometers throughout its use. The real time noise prediction system would allow for the modal behaviour of the machine to be monitored, and changes in the resonances of the machine could indicate that machine has changed in some way, or it could indicate a particular running speed of the machine which contributes excessive noise. This is important as factories must abide by strict noise level adherence for safety purposes. By knowing how the machine resonates at certain running speeds or other conditions, the noise level in the

factory can be optimised, as can reduction in wear and tear to the machinery. In this scenario, an ambient microphone measurement may be unsuitable due to noise contamination from other machinery, and the individual characteristics of the machine and its components can be monitored directly. There are multiple methods in use for similar applications, but there has not yet been a method combining EMA in terms of blocked forces with an OMA style SVD, the benefits of which will be investigated in terms of how characterising the structure using the blocked forces method could improve on existing OMA methods. Further to this, a volume velocity source has been developed, which is considered to be a low cost, simple to use alternative to those already commercially available. Therefore, the contributions to knowledge described in this thesis consist of an otherwise undescribed method for the separation and prediction of modal contributions to radiated noise from a vibrating structure which applies theory usually used in OMA to a blocked force characterisation, and a volume velocity source which is significantly simpler to use and lower cost than those already commercially available.

1.2 Literature Review

The work in this thesis combines a blocked forces in-situ Transfer Path Analysis (TPA) approach with an SVD method for modal analysis of a noise source, using an original volume velocity source. The blocked forces method is commonly used in source characterisation and TPA, which are methods for the identification of a source's vibro-acoustic properties and a procedure for identifying the route of vibration transmission through a system respectively. This is combined with an analysis method used to find the modal contributions of the structure to the radiated noise at a remote receiver position. Following is an overview methods in the literature for source characterisation, TPA, condition monitoring, modal analysis, and a description and review of volume velocity sources.

1.2.1 Source Characterisation and TPA

The basic concept behind methods of vibration analysis is a comparison between inputs and outputs, from which initial systems theory based on electrical circuit relationships gives equivalent quantities now commonly used in TPA [5]. The theory behind the impedance and mobility concepts for the analysis of mechanical systems originates in the use of analogous electrical circuit theory to determine the cause of problems in the system [6], [7]. The analogies which can be drawn from this method are force analogous to current, giving a mechanical-mobility analogue [8], and force analogous to voltage, giving a mechanical-impedance analogue. The impedance analogue was in use some time before the definition of the mobility analogue, initially for the description of electromagnetic fields by James Clerk Maxwell (1831-79), before it was extended to the mechanical domain in 1920 by Kennelly and Arthur Gordon Webster [9]. The advantage of the impedance method is that it preserves the analogy between the electrical and mechanical impedance; mechanical impedance is represented by electrical impedance and mechanical resistance is represented by electrical resistance. In the mobility method, mechanical impedance is represented by electrical admittance, and mechanical resistance is represented as electrical conductance; force is analogous to current rather than voltage [10]. However, the mobility method has an advantage over the impedance method in that the topology of the system is preserved, whereby elements of the system which are in series are also in series in the electrical equivalent circuit, and elements in parallel are in parallel in the electrical equivalent circuit. The opposite is true for the impedance method, which is the reason for the introduction of the mechanical admittance and mobility analogy [11], [12]. When dealing with acoustic and vibro-acoustic issues, the frequency domain is generally preferred over the time domain for making measurements and calculations [13].

Source characterisation is a procedure for the identification and characterisation of the sources of noise and vibrations in a structure or system. There are essentially two categories of methods for the characterisation of sources: direct, and indirect. Direct methods are used to measure the desired parameters in the first instance, for example such as an ambient noise measurement in a factory where a sound power level measurement is used to monitor the overall noise in the room. Indirect methods concern scenarios in which the direct quantity cannot be easily measured directly, such as when an individual noise contribution from a specific machine in the factory is required, for reasons of condition monitoring of the specific machine, or otherwise. Indirect methods are used to infer the desired parameters from other quantities which can be more easily or accurately measured, and these indirect methods often concern the use of inverse methods [14]. In terms of source characterisation, an acoustic source can generally be determined as a fluid-borne, including air-borne, source or a structure-borne source, which is dependent upon on the way in which the noise is generated [14]. Due to the weak coupling between the source and the surrounding air, air-borne source characterisation is considered relatively simple, with sound power methods for the measurement of radiated noise well established and standardised for use in industry[10], [15],[12]. However, when specific characteristics of individual sources or structural components are needed, the overall sound power is not a detailed enough descriptor to allow the separation of sources. In the case of a complex source-receiver system, the strong mechanical coupling between the elements of the system means the source may not be isolated individually and the system as individual elements must be characterised [14]. This has been a topic of great academic investment, with many methods developed over recent years for the characterisation of source-receiver structures. Various quantities can be used for description of sources and transfer paths within systems, including but not limited to methods

such as the operational force [17], the free velocity [18], the blocked force [19], and the characteristic power [20].

Indirect force determination [21], also referred to as operational force [17], is a standard method for source characterisation used in the automotive and aerospace industries [22],[17], and is essentially the basis method for Transfer Path Analysis [1],[10],[23],[24]. An inverse approach is used to evaluate the forces on a receiver structure the due to excitation by a source are measured as a mobility matrix and multiplied by the operational velocity vector when the source is active. As with other inverse methods, errors can be prominent due to ill-conditioning of the mobility matrix [14], though regularisation methods can be used to make improvements [25], [26]. Operational measurements can be made in-situ, though the source and receiver substructures must be decoupled, and the operational forces cannot be transferred between assemblies as they are not independent properties of the source [14]. An alternative approach to the operational force is the pseudo force method, conducted by emulating the operational forces on the surface using in-situ measurements [27]. Practical implementations of the pseudo force method include a comparison of sound source strengths and diagnostic testing for maritime applications [14], [28]–[30]. The pseudo force method is similar in theory to the equivalent force method [31], [32], though both methods suffer from difficulties with transferability due to dependence on measurement position and the lack of physical meaning of the parameters measured [14].

The free velocity, outlined in ISO 9611 [18], is used to describe the motion of a source's contact interface whilst freely suspended and uncoupled from the receiver structure, in contrast to the operational force method. This property is independent to the source, and so for the description of a system it must be combined with passive properties, such as the free mobility [33], [34]. Due to difficulties with achieving the freely suspended state of the source, the method is somewhat overlooked and is rarely used in practice [14]. However, the

issues involved with freely suspending the source, which arise from the physical difficulty in the procedure and also the source mounting conditions when the source is eventually mounted to the receiver structure, may be avoided by using the round trip [35] approach. In conjunction with the in-situ blocked forces [2] method, a procedure can be conducted to approximate the free velocity in-situ, allowing the source to be mounted to the receiver and not freely suspended [36].

The blocked forces method is a widely used method for the characterisation of sources and TPA, and is commonly used in industry with an ISO standard for the in-situ TPA method being introduced in 2019 [19], providing an alternative to the free velocity method and previous TPA methods using blocked forces [37]–[40]. The blocked force essentially refers to the force at which the velocity at a component interface is zero, allowing an independent characterisation of the vibratory source activity [41], [42]. The blocked forces approach, allowing in-situ characterisation of a source, was determined independently by Moorhouse [2] and De Klerk [43]. As the source is measured in-situ under realistic mounting conditions, the operational force and free velocity advantages are preserved [14]. In comparison to the forces determined using the pseudo forces method, the blocked forces are physical quantities at the source receiver interface, and can therefore be used for comparisons of different sources [14]. It is apparent however that pseudo forces determined at the contact interface between the source and receiver are identical [14]. Additionally, the blocked forces can be realised as a generalisation of the single point synthesised force proposed by Lai [44], and an equivalent field representation consequence shown in works by Bobrovnikskii [14], [45]. The most recent iteration of the blocked forces method, the in-situ blocked forces method [38], allows for the source to be measured whilst attached to a receiver in a representative mounting condition, allowing the assumption that the blocked forces will be similar for other similar mounting conditions [46]. The measurement is conducted in two stages: a

measurement of the mobility matrix which is a passive when the source is not active, and a measurement of the operational forces when the source is active. The mobility matrix is inverted and multiplied by the operational forces to give the blocked forces. This method may be susceptible to inversion faults, which are commonly addressed by employing Singular Value Rejection (SVR) for regularisation by rejection of smallest singular values. Multiple degree of freedom measurements are often improved by over-determination, which is measuring 6 degrees of freedom at a contact point with 7 accelerometers and discarding extraneous information.

1.2.2 Condition Monitoring and Modal Analysis

Condition monitoring, or structural health monitoring, is a process of measuring outputs of a device to determine the occurrence of faults or fatigue to machinery or other systems with vibrating parts, indicated by changes in the frequency response of the system [47]. A comparison is made between the normal operating conditions and those when a fault is present [48],[49]. When damage occurs, an extraneous change in the vibration of the structure may be observed, allowing for fault detection and localisation [50]. A blocked forces approach to condition monitoring was described in [51] for the measurement of rotating gears, in which the fault conditions were described by changes to the blocked forces measurements. As well as TPA methods, modal analysis methods are commonly applied in structural analysis for the fault detection and condition monitoring of structural health.

Modal analysis can be categorised into two types, Experimental Modal Analysis (EMA) and Operational Modal Analysis (OMA). OMA differs from traditional, or experimental, modal analysis (EMA) techniques in that the input excitation is unmeasured; only the response of the structure or device under test, due to environmental excitation or a surmised reference, is recorded. This input is assumed to be approximate to Gaussian white noise. EMA methods use measured input and output data to conduct modal analysis. The excitation can take many

different forms, for example: a vibrating pump or motor; wind and ground-borne vibration; or traffic over a bridge. OMA is most commonly used in structural and machinery condition monitoring processes, in which it can be used to ensure expected function, or detect faults and inconsistent behaviour [52]. The quantities analysed are the power spectral densities and correlation densities, to which frequency responses function (FRF) and Impulse Response Function (IRF) methods used in EMA can be adapted, with some modification. In OMA, a transfer function refers to the relationship between a response position and a reference response position, as opposed to that of the response over the input force used in EMA approaches. EMA is most commonly performed on measured data, rather than in a real-time condition monitoring scenario, which is the case for OMA.

OMA methods were first applied to civil engineering structures in the field of seismology, to evaluate the response of buildings due to earthquakes. The Shock Response Spectrum Method was introduced by MA Biot [53]–[55], upon which seismological analysis for buildings was established. Due to a lack of appropriate measurement equipment and insufficient technology for data analysis, the method was time consuming and often led to unreliable results. As digital computing became more viable in the late 1960's, and accelerographs were developed with higher sensitivities, the method was developed further with increased accuracy [56], [57]. From this point, Operational Modal Analysis was introduced into further vibration management applications beyond civil engineering and into mechanical processes.

A large set of roving accelerometers are used on the receiver structure, which are moved and used to collect multiple data sets at differing positions. A number of these accelerometers will be used as references and their position will remain the same throughout the data collection. Analysis is based on spectral density functions and correlation functions from the operational responses, due to the lack of input signal measurement. A fast and simple OMA method is

peak picking, whereby peaks in the power spectral densities, computed from time histories at measurement positions, can describe the natural frequencies of the structure, as modal response will be strongest at these frequencies [52].

Modern techniques use multiple input data. This is important as frequency domain decomposition shows relationships of the singular values of the spectral density matrix, and ‘by a stochastic subspace identification technique where a stabilisation diagram is being used’—these techniques are different but work much better with multiple input data, as with all further techniques [58]. Correlation function matrices and spectral density matrices make the multiple input data available, by just measuring the responses under ambient or operational conditions. It is imperative to ensure there are multiple input loads and to ensure the operating response data is of good quality; this can be done using SVD [59],[60],[61].

The initial frequency domain technique to be developed the Peak Picking (PP) or Basic Frequency Domain (BFD) Method is based on identifying natural frequencies by observation of the peaks in the power spectrum [62]. It is assumed that the damping of the system is low [63] and that modes are well separated, rendering the technique unsuitable for most real life, complex structures, where closely spaced modes are almost always inevitable [4], [62], [64]. This method lends itself to analysis of single degree of freedom structures with low damping and well separated modes, such as a simple beam structure. [65],[63], [66]. However, inadequate frequency resolution of measured data can invalidate results, as the estimated eigenfrequencies depends on the resolution of the spectra [63]. When there is low damping of the structure, the natural frequencies of the structure are depicted by the peaks of the normalised Power Spectral Density [67]. This method is most suited to being used as an initial data check for evaluating the dynamics of the system under test and resulting data quality [4], [68]. This method will be used in the thesis for comparison with the method under test.

The Frequency Domain Decomposition (FDD) technique was proposed as an alternative to the peak picking technique [69]. It is a development of the PP technique which uses singular value decomposition of the output response Power Spectral Density matrix to decompose the PSD matrix into sets of auto-spectra functions, allowing separation of modes for more accurate approximation [68], [70], [71]. SVD is used to describe the modes of the output PSD [52], [68],[62], [69], [72] . As damping ratios cannot be estimated, a further method known as Enhanced Frequency Domain Decomposition (EFDD) was introduced, extending capability to estimation of damping ratios as well as mode shape and natural frequency prediction [73]. The method involves transforming the PSD into the time domain using the Inverse Discrete Fourier Transform (IDFT) at resonant peaks, where the zero-crossing time determines the resonant frequencies. Damping is determined by the logarithmic decrement of the corresponding normalised auto-correlation function [62], [63]. Though with the EFDD method the mode and natural frequency prediction are improved upon from the FDD method, the accuracy of the damping estimation remains under discussion, with concerns over biased estimates present in the literature [74].

Time Domain Decomposition (TDD) is a single degree of freedom method, in which an SVD is used to extract un-damped mode shapes from the output correlation matrix with relation to sensor position. Peak Picking is then used to determine natural frequencies and damping ratios [62], [75]. As shown by Kim, et al [75], the basis of the output response vector contains the orthogonal mode shapes. It is assumed that in single degree of freedom methods, a single mode will dominate at resonances [76]. In practice, real systems are multiple degree of freedom, necessitating a method of extracting the mode isolated SDOF signals from the MDOF signal. A mode- isolated discrete-time response is created using filters for bandwidths containing identifiable modes.

The PP method is used to determine the natural frequency and damping ratio of the selected mode found in the first column of U [62], [75]. This method is efficient when using a large amount of sensors, and due to the filtering of mode shapes the attention required by an operator is reduced; this renders the method suitable for automated online analysis. However, as a SDOF approach, closely spaced modes will interfere with analysis and may reduce accuracy of modal parameters [62], [75].

The Natural Excitation Technique (NExT) is an early time domain method, based on auto-correlation and cross-correlation functions of the time history of the output responses [77], and as opposed to usual OMA methods being stochastic, NExT methods have a deterministic framework [63]. NExT was originally used as an EMA method, and is combined with a multi-input-multi-output time domain algorithm, such as: the polyreference complex exponential (PRCE) [60]; the eigensystem realisation algorithm (ERA) [61]; or the Extended Ibrahim Time Domain method (EITD) [78], to be used in OMA applications.

EITD is single input, multiple output (SIMO) method [59], and PRCE is a multiple input, multiple output (MIMO) method, an extension of the SIMO least square complex exponential (LSCE) method [79], [80]. These MIMO methods are used for identification of closely spaced modes [62]. The method involves acquisition of the correlation function from time histories for the structural response of the system due to ambient excitation at multiple points. Expressed as the sum of decaying sinusoids, correlation functions contain express the free vibration response, with structural mode natural frequency and damping ratio for each corresponding mode within the decaying sinusoids [77]. Further details of the theory used in NExT may be found in [77].

Auto Regressive Moving Average ARMA is an OMA modelling protocol for linear system analysis which predicts the instantaneous modal parameters of the system's time series using information from previous measurement values and a prediction error method (PEM), which

acts to minimise the estimation error [62], [81], [82]. For cases of multiple input excitations, vector ARMA, or ARMAV, is used [83], [84].

The ARMA model can be seen as having the auto-regressive (AR) aspect being the autoregressive coefficient matrix parameters, and the moving average (MA) aspect being the moving average matrix parameters. Eigenvalue decomposition is performed in order to determine the mode shapes and damping ratios[62]. Not necessarily preferred for OMA, this method has issues with non-convergence in all cases, and is computationally expensive [62], [63]. This is also an issue with the variant methods based on ARMA, such as linear multistage (LMS), instrumental variable (IV), and two stage least squares (2SLS), all of which the reader can find further information of in [85]. The high computational cost of ARMA methods has led to a decrease in its popularity, though it was in prominent usage for the analysis of civil engineering structures in the past [62], [86]. A more recently developed method known as time varying ARMA (TV-ARMA), designed specifically for identification of mode shapes, has been shown to work to some degree. However, inaccuracies in the mode shapes presented mean that the method is in need of further development [87].

There are two types of Stochastic Subspace Identification (SSI) methods: the Covariance-Driven Subspace Identification Method (COV-SSI), proposed by Ho and Kalman, which uses SVD to reduce noise in deterministic systems [88]; and the Data-Driven Stochastic Subspace Identification Method (DD-SSI), which was initially developed by Overschee and De Moor in 1991 [89]. COV-SSI is the faster method as it used an FFT, whereas DD-SSI uses the slower QR decomposition [63].

SSI methods use directly measured data to form a state space model of the measured dynamic system [90], and the main benefit of SSI methods compared to other such techniques is the considerable reduction in computational complexity [72].

The initial step in SSI methods is one of data reduction [91]. COV-SSI uses correlation data to form a block-Hankel matrix, which is weighted using a method such as Canonical Variant Analysis (CVA), Principal Component Analysis (PCA), and Unweighted Principal Component Analysis (UPCA), also known as Balanced Realisation (BR) [58], [92]. The accuracy of this weighting procedure using these methods is described as being similar to those identified in the system parameters [62], [63], [91], [93]. Following this weighting algorithm, SVD is used to decompose the matrix [62], [94].

The DD-SSI does not use covariances between inputs, and instead uses QR decomposition of the Hankel data matrix to project the row space of the future outputs into the rowspace of past outputs [58], [91], [95]. SVD is then performed on the projection matrix in order to identify the system parameters. Similarly to COV-SSI, weighting of the matrix can be added using PC, CVA, and UPC algorithms. Each has a preferred application status depending on the system: UPC is most effective when applied to system measurements with a good signal to noise ratio, and where the modes have equal dominance in in the time response; in systems with a poor signal to noise ratio and highly varying strengths of modes, the CVA method is preferred, which as a method is able to enhance under-excited modes; and when neither of these cases apply, the PC method can be used as a concession [62], [63], [96]. SSI has become a standard OMA method due to its high accuracy and computational efficiency, though it is more mathematically complex than other methods [62], [93], [97]–[99]. COV-SSI differentiates itself from DD-SSI in that it has a higher accuracy for at estimating damping ratios [62], [100], [101]. A recently developed SSI method, the Correlation Signal Subset-based SSI (CoS-SSI), has shown in an initial work that it has higher accuracy than COV-SSI when analysing data with a poor signal to noise ratio [62], [102]. Further details on SSI methods can be found in [89], [96], [103].

A recent EMA method by Palerm is perhaps the closest to the method described in this thesis, in which an SVD is performed on the acousto-elastic transmission matrix between an array of volumetric sources and the velocities on a free-free plate and a clamped plate, which have been measured using a scanning laser vibrometer [104][105]. This method aims to improve upon a method called the Complex Mode Indicator Function (CMIF) [106], which suffers from constraints related to making measurements in laboratory scenarios. Palerm's method allows for a contactless excitation and measurement, with volumetric sources and contactless SLV measurement. The principle behind both methods involves a MIMO system measurement, with an SVD performed on the resulting transmission matrix. The number of significant singular values estimates the number of combined modes in the plate [105]. Current results are encouraging, however the method may be susceptible to changes in ambient temperature and other environmental factors [105].

There are general drawbacks to OMA techniques. Due to the excitations being ambient, measurements can be disturbed by sudden or unexpected environmental conditions, such as wind or temperature, along with electrical noise associated with measurement equipment. In some cases all modes may not be excited, or may not be measured due to equipment sensitivity. Natural excitations, as opposed to forces applied in EMA, can result in very low levels of vibration, meaning OMA sensors generally should be much more sensitive- accelerographs are used for seismic measurements rather than the less- sensitive accelerometers used in other applications [57]. This demonstrates an advantage in EMA in the sense that the input quantity can be controlled and quantified accurately. Another difficulty faced can be the vast data sets needed to do a full characterisation; the analysis can become difficult to manage and analyse efficiently, as well as being computationally expensive. However, compared to time domain techniques, frequency domain techniques are, in general, less computationally expensive [107]. This leads to the approach proposed in this

thesis, which aims to combine the Blocked Forces method with an SVD in terms of spatial location versus frequency for an EMA approach, for which the input characteristics can be used as a reference for implementation in an OMA real-time condition monitoring system.

1.2.3 Volume Velocity Sources

A volume velocity source is an acoustic source which creates a sound wave, with a known volume velocity, which is defined as the volume of air displaced by the sound wave per unit time [108], [109]. Volume velocity sources can be used for the measurement of vibro-acoustic FRFs, and there are assumed criteria which should be met to assume that it will be satisfactory for use [110], [111]:

- Sufficient signal to noise ratio
- Adequate source strength for excitement of the device under test
- The behaviour of the volume velocity source should be that of a monopole for the analysed frequency range
- A measureable volume velocity output in interchangeable environmental situations

In general, most volume velocity sources used in research consist of an acoustic loudspeaker or compression driver, through which a sine sweep, or pink or white noise, is produced for exciting the device under test. The volume velocity of the source is usually calibrated using a measured voltage or a particle velocity sensor at the aperture of the source.

Loudspeakers, such as those used in audio applications, use an electrical signal to drive a diaphragm to generate a sound of a known volume velocity, emitted through a speaker cone. Adjustments are made to the volume velocity by altering the input amplitude and frequency [112]. With the input amplitude and frequency being adjustable, loudspeakers are adaptable to multiple scenarios in testing, though may suffer from nonlinearities and other types of distortion, leading to the need for additional calibration [113]. This renders them unsuitable for

scenarios which require high levels of precision. However, they are relatively easy to use and can be readily incorporated into setups including multiple pieces of equipment. They tend to be available separately for low and high frequency excitations [114], [115]. For example, Microflown manufacture two volume velocity sources with frequency ranges of 30- 500 Hz for a low frequency excitation [116], and one at 300 Hz – 12 kHz [117] for mid to high frequency excitation. Commercially available loudspeakers for volume velocity measurements and other noise source applications include the Bruel & Kjaer Omnipower type 4292-L [118], and the more recent Bruel & Kjaer Omnisource, which is of a significantly higher price than other loudspeaker type volume velocity sources [119]. Loudspeaker volume velocity sources can be enhanced by attaching a horn [109]. Adding a horn to a loudspeaker can greatly increase the sound pressure level achieved with a uniform sound field, however they can be physically inconvenient due to size and weight, and require careful calibration to ensure accuracy.

Another type of volume velocity source is the pistonphone [120]. They use an oscillating piston in a cylinder of gas or fluid to generate sound, and are commonly used for calibrating sound level meters and other types of measurement device, when high accuracy and stability are necessary. A calibrated electrical signal is used to power the piston and determine its displacement, allowing for alteration in the response of the signal [108]. Pistonphones are regarded as highly accurate, can have a wide frequency range, and have a low susceptibility to distortion, though are extremely delicate and can be an expensive alternative to a loudspeaker [113]. These tend to be most used for the calibration of sound level meters rather than ambient excitation of structures, with commercial examples such as the B&K type 4220 [121] and the G.R.A.S. 42AA [120] available.

1.3 Objectives

The objectives of the thesis are to:

- 1: Define a method using an Experimental Modal Analysis approach for transfer path analysis, based upon principle component analysis using Singular Value Decomposition elements and the in-situ blocked forces method. This method aims to extract the modal behaviour of the structure using an SVD, for the prediction of radiated noise contribution from individual modes or combinations of modes. The method is first investigated looking at structural modes, before it is applied to the radiation modes using a volume velocity source.
- 2: Design and validate an alternative volume velocity source to those which are already established, which achieves advantages in terms of financial cost, portability, and ease of use for the practitioner. Detail this volume velocity source and ascertain the efficiency of this method for the measurement of vibro-acoustic transfer functions reciprocally.
- 3: Predict radiated noise using blocked pressures at the discretised radiating surface of a structure, and the reciprocal vibro-acoustic transfer functions measured using the volume velocity source. These are compared to the same transfer functions measured directly using a force hammer.

1.4 Thesis Outline

This introduction includes a literature review of past and current methods which are related to the thesis, covering modal analysis and transfer path analysis methods. Chapter 2 details the background theory leading to the development of the methods used in the thesis, and gives an outline to the theory behind the volume velocity source. Chapter 3 will detail the methodology of the experiments conducted, along with description of the hardware and software utilised. Volume velocity sources are discussed, and the volume velocity source used for the experiments in this thesis is detailed. Chapter 4 begins the experimental results

chapters, starting with an investigation conducted on a simply supported beam model created using Matlab software. The SVD approach is used to evaluate the structural modes of the measured beam. Transfer functions containing the contribution of a lone singular value, Ξ , are introduced. The evaluation of the Ξ transfer function method for the separation of modal contribution of structures using a simulated beam is conducted, detailing how response position sampling density affects the outcomes of the singular value decomposition technique for the evaluation of vibrating structures Chapter 5 details an experiment using a measured steel beam with 17 response and excitation positions, where the Ξ transfer functions are constructed and evaluated. In Chapter 6, a similar evaluation is made using a real plate, with velocities measured using a scanning laser vibrometer. The data collected is used to evaluate mode shapes of the plate, and how the Ξ transfer functions relate to the structural modes of the plate. The data is manipulated to show how sampling resolutions affect the measured data when processed using SVD. Chapters 7 and 8 are concerned with an extensive case study. A plate with multiple vibration sources, excitations, and external responses is analysed. Chapter 7 concerns a traditional transfer path analysis method for noise prediction using the volume velocity source, which compares the prediction of radiated noise using direct impact hammer excitations with the volume velocity source reciprocally measured vibro-acoustic transfer functions. In Chapter 8, the Location vs Frequency (LvF) SVD is applied to the volume velocity transfer function, where the radiation modes of the plate are built into individual Ξ transfer functions for the prediction of contributions from particular modes or combinations of modes included in each singular value. Chapter 9 details the conclusions of the thesis and suggests options for further development of the methods covered.

2 THEORY

The basis of this novel Singular Value Decomposition theory developed from Operational Modal Analysis (OMA) and Experimental Modal Analysis (EMA) methods, and builds on the knowledge that mode shapes can be described using the ‘ U ’ output matrix of the SVD algorithm, with a small number of modes actually contributing to radiated noise. This SVD algorithm is commonly used in OMA. The significance of these modes are theoretically displayed in the diagonal of the ‘ S ’ output matrix, while the frequency response of these modes are shown in the ‘ V ’ output matrix. Combining these assumptions with the blocked forces method, it is proposed that a method for extracting parts of the equation can be used to optimise the blocked force prediction. The method is based on using transfer functions as opposed to other input data, such as power. By extracting the singular values from the diagonal matrix, new transfer functions can be constructed containing only a single singular value, giving the blocked force prediction for the contribution of a single mode or set of modes. This analysis should allow for prediction of radiated noise, and at which frequency, given the structure is sufficiently instrumented for characterisation.

2.1 Transfer Functions

Transfer functions are essentially the ratio of input to output due to the effects of some system, for example a metal beam as used in this thesis. The data Acquisition System employs the use of FFT analysis and windowing to calculate the cross-spectra, also known as the Cross Power Spectral Density (CPSD), and autospectra, or Power Spectral Density (PSD), of the excitations and responses as described in [122], giving G_{AA} as the autospectra for the input, G_{BB} as the autospectra for the output, and G_{AB} as the crossspectra of the two (as a function of frequency):

$$G_{AA}(f) = \frac{1}{n} \sum |A(f)|^2 \quad (1)$$

$$G_{BB}(f) = \frac{1}{n} \sum |B(f)|^2 \quad (2)$$

$$G_{AB}(f) = \frac{1}{n} \sum A^*(f) \cdot B(f) \quad (3)$$

A complex transfer function H is given as:

$$H(f) = \frac{A(f)}{B(f)} \quad (4)$$

And can be calculated in two ways, giving:

$$H_1(F) = \frac{A^*(f)B(f)}{A^*(f)A(f)} = \frac{G_{AB}(f)}{G_{AA}(f)} \quad (5)$$

$$H_2(F) = \frac{B^*(f)B(f)}{B^*(f)A(f)} = \frac{G_{BB}(f)}{G_{AB}^*(f)} \quad (6)$$

Defining H_1 as the crossspectra divided by the autospectra of the input, and H_2 as the autospectra of the output divided by the complex conjugate of the crossspectra. If there is no noise present in the measurement, the two calculations will yield identical results. For instances where noise is uncorrelated with the input, that is, noise is present on the output, H_1 is the preferred transfer function, and the opposite is true for H_2 , where noise is present on the input and uncorrelated to the output. In experimental modal analysis, the H_1 transfer function is generally used for impact hammer measurements, and H_2 for noise sources such as shakers. FRFs are a type of transfer function used in vibro-acoustic testing, and are defined as

the frequency-dependent ratio of the motion-response Fourier transform to the Fourier transform of the excitation force of a linear system [19].

The coherence between the signals is monitored during experimental testing to ensure accurate measurements, which is calculated by:

$$Coh(f) = \frac{\sqrt{\frac{H_1(f)}{H_2(f)}}}{\sqrt{\frac{|G_{AB}^2|}{G_{AA} \cdot G_{BB}}}} \quad (7)$$

This produces a value between 0 and 1 at each frequency, where 1 indicates complete correlation between the signals, and a complete absence of correlation is indicated by a value of 0 [122]. When conducting modal testing, accurate impact hammer hits should garner a correlation of 1 across the frequency range, with few discrepancies.

2.2 In-Situ Blocked Forces: Matrix Inversion Method

The blocked forces of the system are the force which would need to be applied to prohibit any vibration at that particular point on the system. The blocked forces method used in this thesis is the in-situ matrix inversion method. The matrix inversion transfer path analysis method, or source path contribution method, uses inverse force synthesis in order to find the operational forces at work on the interface between the vibrating source and the receiver of an assembly [123].

Inverse force synthesis [17], or the matrix inversion method, is preferred to other methods, such as the dynamic stiffness method, as it has been shown to be more reliable, especially over a wide frequency range [123]. The method does not require the separation of source and receiver and, as no assumption is required for the behaviour of the receiver structure, the in-situ method is most likely more reliable than the previous TPA approaches [38]. Another

advantage of the in-situ approach is that the operational blocked forces are independent of the receiver structure, meaning that they remain valid for different assemblies by re-measuring or modelling the transfer function for the complete new assembly. This property is not shared by the conventional approach as the contact forces measured in that method can vary significantly between receiver structures [13].

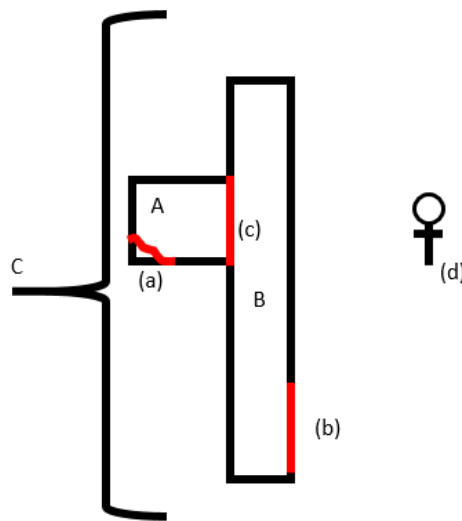


Figure 2.1: Schematic of source receiver structure, consisting of vibration source 'A', which is coupled to a receiver structure 'B'. When operational, the source creates multiple forces at '(a)', which are then transmitted through the interface '(c)' to the receiver structure 'B'. The receiver '(d)' is the point at which a combination of the radiated sound from the receiver 'B' and airborne radiated sound from the source 'A' are measured as sound pressures. 'C' denotes the assembly as a coupled structure, and '(b)' the vibration velocities on the plate, which are the quantities use in this method.

Consider that the receiver *B* in Figure 2.1 has been discretised into a grid consisting of m positions. A matrix of frequency response functions $y_{mn}(\omega)$ is constructed, containing FRFs of acceleration due to force. Source *A* is then made operational, and the blocked forces of the system *C* due to excitation from source *A* can be described as:

$$\begin{bmatrix} \dot{\bar{f}}_{A,C_1(\omega)} \\ \vdots \\ \dot{\bar{f}}_{A,C_i(\omega)} \\ \vdots \\ \dot{\bar{f}}_{A,C_n(\omega)} \end{bmatrix} = \begin{bmatrix} y_{C_{11}(\omega)} & \cdots & y_{C_{1i}(\omega)} & \cdots & y_{C_{1n}(\omega)} \\ \vdots & \ddots & \vdots & \ddots & \vdots \\ y_{C_{i1}(\omega)} & \cdots & y_{C_{ii}(\omega)} & \cdots & y_{C_{in}(\omega)} \\ \vdots & \ddots & \vdots & \ddots & \vdots \\ y_{C_{m1}(\omega)} & \cdots & y_{C_{mi}(\omega)} & \cdots & y_{C_{mn}(\omega)} \end{bmatrix} \begin{bmatrix} \dot{v}_{C_1(\omega)} \\ \vdots \\ \dot{v}_{C_i(\omega)} \\ \vdots \\ \dot{v}_{C_m(\omega)} \end{bmatrix} \quad (8)$$

Where $\dot{\bar{f}}_{A,C_i(\omega)}$ is the blocked force at position i of n response positions; the elements of Y_C

Are FRFs of mobility, measured using a force hammer at each accelerometer position, and

the elements of \dot{v}_C are complex velocities at measurement locations (b) on assembly C , whilst

the source A is operational.

This can be seen as:

$$\dot{\bar{f}}_{A,c} = Y_{C,cc}^{-1} \dot{v}_{C,c} \quad (9)$$

Where:

$$\dot{\bar{f}}_{A,c} = -\dot{f}_{A,c} \Big|_{\dot{v}_{A,c}=0} \quad (10)$$

Upper-case subscripts are the structure elements A - source, B - receiver, C – coupled

elements; lower case are measurement locations (a), (b), (c), (d); dot denotes that the source

is operational, and bar denotes the blocked force. Subscripts are arranged as row (response)

then column (excitation): $Y_{C,cc}$ is a matrix of frequency response functions of velocities due to

force/ mobility [76], [124] .

Assuming the direct sound pressure at (d) radiated from source A during measurement is

negligible, the sound pressure due to the structure-borne noise radiated by the coupled

assembly is defined as:

$$\dot{P}_{C,d} = H_{C,db} \dot{\bar{F}}_{A,c} \quad (11)$$

Where $H_{C,dc}$ is the measured transfer function for the coupled assembly C . This transfer function can be measured in multiple ways. In this thesis, the transfer function for $H_{C,dc}$ will be measured in two ways: using a force hammer, which will be referred to as H_{pf} - sound pressure due to force;

$$\dot{P}_{C,d} = H_{pf} \ddot{F}_{A,c} \quad (12)$$

Which is equivalent to Equation 51, and reciprocally with a volume velocity source, which will be referred to as H_{vq} - surface velocities due to volume velocity, which is equivalent to:

$$\dot{P}_{C,d} = H_{C,bd} \ddot{F}_{A,c} \quad (13)$$

2.2.1 Volume Velocity Source

The reciprocal volume velocity transfer function is obtained by utilizing a reference microphone located a distance away from the assembly, and is calculated using:

$$H_{aq} = \frac{a}{q_1} = \frac{a}{P_2} \times \frac{j\rho_0 e^{j(\omega t - kr)}}{2\lambda r} \quad (14)$$

$$H_{vq} = \frac{H_{aq}}{j\omega} \quad (15)$$

$$\dot{P}_{C,d} = H_{vq} \ddot{F}_{A,c} \quad (16)$$

Where $\frac{a}{q_1}$ is the transfer function between the accelerometers and the volume velocity source,

P_2 is the sound pressure at the reference microphone, $\frac{a}{P_2}$ is a transfer function between the

accelerometers and the pressure at the reference microphone, $\rho_0 =$ air density, $e = 2.71$, $\omega = 2$

* π * frequency, $t =$ time = 1, $k =$ wavenumber, r is the distance between the volume velocity source and the reference microphone, and $\lambda =$ wavelength [125].

The volume velocity source is activated at each of the microphone positions to gain a vector of transfer function for each response position: these positions are equivalent to multiple (d) in Figure 2.1; to the accelerometer excitation positions on the plate (b).

2.3 Reciprocity

A system is reciprocal when a transfer function for transmission of a quantity from Position 1 to Position 2 is the same as the transfer function from Position 2 to Position 1 [126], [127].

Reciprocity theory within acoustical systems was first proposed by Helmholtz in 1860 [128], before the theorem was extended to include linear dynamic systems of multiple types, becoming the General Reciprocity Theorem, by Lord Rayleigh in 1873 [129], [130].

Extensive research in reciprocity for acoustics and mechano-acoustical systems has been carried out by Ten Wolde and Verheij since the early 1970s. The volume velocity source is a reciprocal method, as the excitations occur at the external microphone response positions, with the responses taken at the discretised surface of the source.

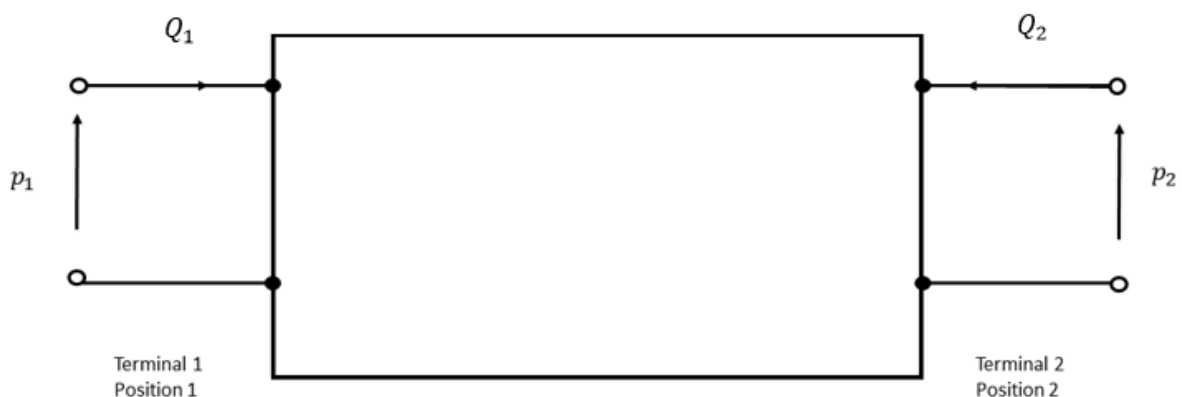


Figure 2.2: 4- pole representation in an acoustical system. Volume velocity Q and sound pressure p at positions 1 & 2, positive directions of these quantities denoted by arrows, figure based on [127]

The reciprocal relationships for the transfer functions of the four sound transmission paths from position 1 to position 2 can be seen as:

$$\left(\frac{p_2'}{Q_1'}\right)_{u_2'=0} = \left(\frac{p_1''}{Q_2''}\right)_{u_1''=0} \quad (17)$$

$$\left(\frac{p_2'}{p_1'}\right)_{Q_2'=0} = -\left(\frac{Q_1''}{Q_2''}\right)_{p_1''=0} \quad (18)$$

$$\left(\frac{Q_2'}{Q_1'}\right)_{p_2'=0} = -\left(\frac{P_1''}{P_2''}\right)_{Q_1''=0} \quad (19)$$

$$\left(\frac{Q_2'}{p_1'}\right)_{p_2'=0} = \left(\frac{Q_1''}{p_2''}\right)_{p_2''=0} \quad (20)$$

Where the first equation is Helmholtz's classical derivation [128], followed by the three other valid relationships in an acoustical system [131]. Reciprocity as a concept in linear algebra is also applicable to the FRF matrices of accelerances:

$$A_{i,j} = A_{j,i} \quad (21)$$

Where A is a matrix of accelerances and i, j are the off-diagonal elements of the matrix. This can be used to check the quality of data, as reciprocity should be apparent between the corresponding positions [46].

2.4 Singular Value Decomposition

Principal Component Analysis is a method of data analysis used to find the most important elements of a dataset based on the maximum variance from the full data matrix [132]. This

process is used in a vast array of applications for many types of data processing. The main method under investigation in this project is the Singular Value Decomposition.

Singular Value Decomposition, or ‘SVD’, is a method of factorising a matrix, commonly used in linear algebra-based operations. As with other forms of PCA, the applications of SVD are varied, and are used in a wide range of signal processing methods.

As shown in Numerical Mathematics [133] a real $m \times n$ matrix A can be shown as:

$$A = USV^T \quad (22)$$

Where $U^T U = V^T V = VV^T = I_n$ and $S = \text{diag}(\sigma_1, \dots, \sigma_n)$.

U is a matrix consisting of n orthonormalised eigenvectors which are associated with the n largest eigenvectors of AA^T and V contains the orthonormalised eigenvectors of $A^T A$. The elements on the diagonal of S are the singular values; the non-negative square roots of the eigenvalues of $A^T A$. It is assumed that

$$\sigma_1 \geq \sigma_2 \geq \dots \sigma_n \geq 0 \quad (23)$$

If the rank of $A = r$, $\sigma_{r+1} = \sigma_{r+2} = \dots = \sigma_n = 0$ the decomposition is called the SVD.

The main applications of the SVD in this project is that the SVD can be applied in a manner of location versus frequency, with all frequencies analysed at once, as opposed to frequency by frequency. The values of U give the shapes of the modes in an order of their significance. V shows the frequency response of the mode, and the diagonal of S contains the strength, or contribution, of the individual mode. The relationship between the elements of U and S are that U is weighted by the elements of S , which are magnitude coefficients of the modes. when a surface is adequately sampled spatially for a number of modes, that amount of modes will have singular values on the diagonal of S of significantly higher magnitude than the lower value elements of S , usually shown by a ‘knee’ or large drop off in the singular values. This

indicates that the modes of U , associated with the singular values of a higher magnitude, are sufficiently spatially described [134]. It is described in the literature that between 5 and 10 elements per wavelength are desirable for the accurate description of modes [135], [136], with a sample rate twice the maximum frequency of interest [137], [138].

2.5 Singular Value Extraction Method for Construction of a Transfer Function Containing a Single Mode: LvF Method

The Peak Picking (PP) method described in the literature is compared to the alternative approach proposed in this thesis, the Location by Frequency (LvF) method which evaluates all frequencies at once. The PP method is a frequency by frequency method which calculates for each frequency separately. When referring to the PP method, this will be defined as:

$$[\mathbf{H}_{(\omega)}] = [\mathbf{U}_{(\omega)}] [\mathbf{S}_{(\omega)}] [\mathbf{V}_{(\omega)}]^T \quad (24)$$

Where \mathbf{H} is an input matrix of transfer functions. This is used at some points to describe the data. However, the main method being investigated is the location vs frequency algorithm, which is conducted on a transfer function, and new individual transfer functions containing only a single singular value are constructed, for the purpose of extracting single modes or groups of modes. An LvF SVD is conducted over all frequencies simultaneously:

$$[\mathbf{H}_{(\omega)}] = [\mathbf{\Psi}] [\mathbf{\Sigma}] [\mathbf{\Phi}]^T \quad (25)$$

From which a new transfer function representing a single mode can be constructed. H_{vq} is:

$$\begin{bmatrix} \mathbf{H}_{vq_1(\omega)} \\ \vdots \\ \mathbf{H}_{vq_i(\omega)} \\ \vdots \\ \mathbf{H}_{vq_n(\omega)} \end{bmatrix} = \begin{bmatrix} \psi_{1,1} & \cdots & \psi_{1,i} & \cdots & \psi_{1,m} \\ \vdots & \ddots & \vdots & \ddots & \vdots \\ \psi_{i,1} & \cdots & \psi_{i,j} & \cdots & \psi_{i,m} \\ \vdots & \ddots & \vdots & \ddots & \vdots \\ \psi_{n,1} & \cdots & \psi_{n,i} & \cdots & \psi_{n,m} \end{bmatrix} \begin{bmatrix} \sigma_1 & 0 & 0 & 0 & 0 \\ 0 & \ddots & 0 & 0 & 0 \\ 0 & 0 & \sigma_i & 0 & 0 \\ 0 & 0 & 0 & \ddots & 0 \\ 0 & 0 & 0 & 0 & \sigma_n \end{bmatrix} \begin{bmatrix} \phi_{1,1} & \cdots & \phi_{1,i} & \cdots & \phi_{1,m} \\ \vdots & \ddots & \vdots & \ddots & \vdots \\ \phi_{i,1} & \cdots & \phi_{i,j} & \cdots & \phi_{i,m} \\ \vdots & \ddots & \vdots & \ddots & \vdots \\ \phi_{n,1} & \cdots & \phi_{n,i} & \cdots & \phi_{n,m} \end{bmatrix}^T \quad (26)$$

Where \mathbf{H}_{vq} is $n \times m$, Ψ is the $m \times m$ matrix containing elements ψ which portray the mode shapes; Σ is the $m \times n$ diagonal matrix containing the singular values σ on the diagonal, and Φ^T is $n \times n$ and contains the frequency response, or temporal behaviour, of the modes ϕ .

For $1:n$, the singular values are discarded:

$$\xi_i = \begin{bmatrix} \mathbf{0} & \mathbf{0} & 0 & \mathbf{0} & 0 \\ \mathbf{0} & \mathbf{0} & \mathbf{0} & \mathbf{0} & \mathbf{0} \\ 0 & \mathbf{0} & \sigma_i & \mathbf{0} & 0 \\ \mathbf{0} & \mathbf{0} & \mathbf{0} & \mathbf{0} & \mathbf{0} \\ 0 & \mathbf{0} & 0 & \mathbf{0} & 0 \end{bmatrix} \quad (27)$$

The diagonal Σ matrix is replaced by ξ_i , to calculate the transfer function $\mathbf{E}_{i(\omega)}$ containing the contribution for only mode i :

$$\begin{bmatrix} \mathbf{E}_{1(\omega)} \\ \vdots \\ \mathbf{E}_{i(\omega)} \\ \vdots \\ \mathbf{E}_{n(\omega)} \end{bmatrix} = \begin{bmatrix} \psi_{1,1} & \cdots & \psi_{1,i} & \cdots & \psi_{1,m} \\ \vdots & \ddots & \vdots & \ddots & \vdots \\ \psi_{i,1} & \cdots & \psi_{i,j} & \cdots & \psi_{i,m} \\ \vdots & \ddots & \vdots & \ddots & \vdots \\ \psi_{n,1} & \cdots & \psi_{n,i} & \cdots & \psi_{n,m} \end{bmatrix} \begin{bmatrix} 0 & 0 & 0 & 0 & 0 \\ 0 & 0 & 0 & 0 & 0 \\ 0 & 0 & \xi_i & 0 & 0 \\ 0 & 0 & 0 & 0 & 0 \\ 0 & 0 & 0 & 0 & 0 \end{bmatrix} \begin{bmatrix} \phi_{1,1} & \cdots & \phi_{1,i} & \cdots & \phi_{1,m} \\ \vdots & \ddots & \vdots & \ddots & \vdots \\ \phi_{i,1} & \cdots & \phi_{i,j} & \cdots & \phi_{i,m} \\ \vdots & \ddots & \vdots & \ddots & \vdots \\ \phi_{n,1} & \cdots & \phi_{n,i} & \cdots & \phi_{n,m} \end{bmatrix}^T \quad (28)$$

This singular transfer function is then multiplied by the blocked forces of the system in order to describe the contribution to radiated noise at the receiver position:

$$P_{\mathbf{E}i} = \mathbf{E}_i \ddot{\mathbf{F}}_{A,c} \quad (29)$$

Because:

$$H_{vq(\omega)} = \sum_{i=1}^n \mathbf{E}_{i(\omega)} \quad (30)$$

Multiple transfer functions containing combinations of modes can be constructed and evaluated, which could potentially improve the prediction of radiation noise by discarding values which do not contain information about the radiation modes and instead contain noise or other extraneous data.

The proficiency of this method, as with other OMA methods, is likely to depend on spatial sampling and frequency resolution. Throughout this thesis, this approach will be investigated using models and measured data. Modal information for the structure or device under test is also available in the columns of Ψ , in which the mode shapes are described. The relationship between these modes and the singular values is explored.

In order to explore how the \mathcal{E} transfer function works, an initial beam model experiment is conducted, before moving on to a more complex plate.

2.6 Modes in Beams

The work in thesis concentrates on a single degree of freedom in the beam experiments, neglecting the beam rotations. The beam model used is a free-free Euler- Bernoulli beam [139], with the real experimental suspended by elastic cords to mimic free-free boundary conditions. Many variations of procedure for calculating beam modes exist in the literature.

The modal frequencies of the beam are calculated using:

$$f_i = \frac{i^2 \pi^2 \sqrt{EI}}{2L^2 \rho A} \quad (31)$$

where f_i is frequency of mode number i , i is the mode number representing how many half wavelengths fit in the beam, E is elasticity in GPa, I is moment of inertia in m^4 , L is length in m, ρ is density kg/m^3 and A is the area of the beam in m^2 [140]–[143].

Wavenumber k is approximated by [142]:

$$k = \frac{i\pi}{L} \quad (32)$$

Where i is a positive integer corresponding to mode number and L is the length of the beam.

The wavelength λ of each mode can be approximated by [144]:

$$\lambda = \frac{2L}{i} \quad (33)$$

The node positions of the modes spatially along the beam can be approximated by [145]:

$$x_i = \frac{L(1 - (2i - 1))}{2i} \quad (34)$$

Where x is the nodal position.

2.7 Modes in Plates

To calculate the frequencies of modes in a simply supported plate [143],

$$f_{i,j} = \frac{\lambda_{i,j}^2}{2\pi L_x^2} \left[\frac{Eh^3}{12\rho(1 - \theta^2)} \right]^{1/2} \quad (35)$$

Where ρ is density of the plate, E is the Young's modulus of elasticity, L_x is the plate length, h is the plate thickness, and θ is Poisson's ratio. $\lambda_{i,j}^2$ is a dimensionless frequency parameter, and i, j are the mode index numbers. $\lambda_{i,j}^2$ is given by:

$$\lambda_{i,j}^2 \approx i^2 + j^2 \left(\frac{L_y}{L_x} \right)^2 \quad (36)$$

Where L_y is the plate length in the y - direction [143].

The wavenumber k for a frequency of wavelength λ be calculated by [125]:

$$k_i = \frac{2\pi}{\lambda_i} \quad (37)$$

The nodal lines, or eigenfunctions, for a simply supported plate are given by [134],

[146][147]:

$$\check{\Phi}_{x,y} = \sin\left(\frac{m\pi x}{L_x}\right) \sin\left(\frac{n\pi y}{L_y}\right) \quad (38)$$

m and n are the mode numbers, L_x and L_y are the dimensions of the plate in the x and y directions, respectively, x and y are the coordinates of a point on the plate, and $\Phi_{i,j}$ is the eigenfunction for the $(i,j)^{\text{th}}$ mode.

The nodal points are located at the intersections of the nodal lines. The position of the $(i,j)^{\text{th}}$ nodal point is given by:

$$x_i = \frac{L_x i}{m+1}; y_j = \frac{L_y j}{n+1} \text{ where } i = 1, 2, \dots, m \text{ and } j = 1, 2, \dots, n. \quad (39)$$

Where m and n are the number of divisions of the plate.

The bending wavelengths as a property of the plate are given by:

$$\lambda_n = \frac{2L}{n} \quad (40)$$

Where n is the mode number and L is the length of the plate in either the x or y direction.

The critical frequency of a plate is the frequency at which its radiation is at the maximum to the surrounding body [148]. Up to this frequency the radiation increases, and from this frequency the radiation decreases. This is the frequency at which the wavenumber in the plate meets the wavenumber of the surrounding fluid or air. The critical frequency of the plate is given by:

$$f_c = \frac{\sqrt{\frac{E}{\rho} / 1 - \theta^2}}{2/L_x} \quad (41)$$

The damping ratio of the plate is a value which defines the damping behaviour of the plate. It can be approximated for a second order system, such as a plate, using the half power bandwidth method [149], [150]:

$$\zeta = \frac{\Delta f}{f_{ave}} \quad (42)$$

Where ζ represents the damping ratio. Δf is defined as :

$$\Delta f = \frac{f_2}{f_1} \quad (43)$$

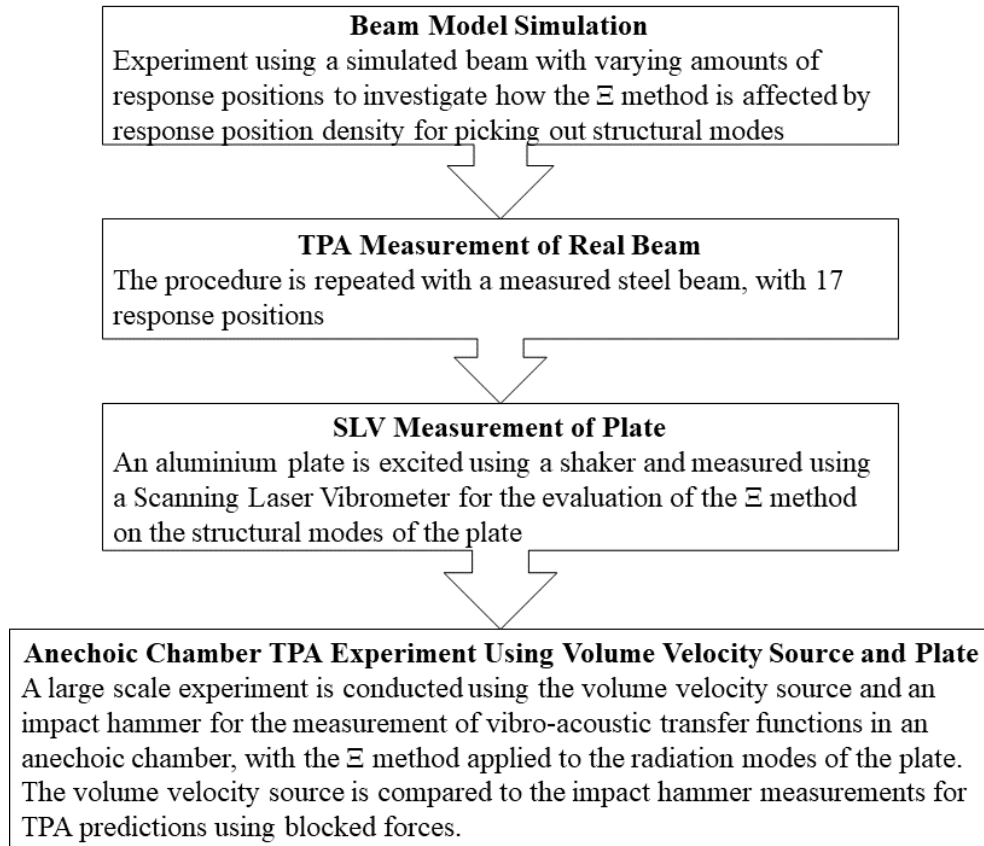
Where f_1 is the lower frequency boundary, where the magnitude drops to -6 dB of the peak, and f_2 is the upper frequency boundary, where the magnitude drops to -6 dB of the peak on the other side. f_{ave} is the average frequency between the two boundary frequencies. The loss factor of the plate is then given by:

$$\eta = \frac{\zeta}{2\pi} \quad (44)$$

Which is a dimensionless parameter between 0 and 1, where 0 indicates perfectly un-damped conditions and 1 represents perfectly damped conditions.

3 Methodology

In this chapter, an overview of the methodologies applied for each of the experiments is given. Description is given for the equipment and hardware used, and the volume velocity source is detailed in terms of its function and characteristics.



The thesis is based around a series of experiments of increasing complexity, beginning with an idealised simply supported beam model experiment. The benefit of beginning with a simple beam is that the modes in a beam are well separated, as opposed to the more complex plate structure, which has overlapping modes and more complex behaviour. The beam model is used to experiment with varying spatial sampling positions and the effects on the modal descriptions from the LVF and PP methods are discussed.

Following on from the idealised beam model, a real beam is measured. This will allow demonstration of the method when encountering realistic constraints, such as frequency response and noise of equipment, whilst still being a simple structure.

Building in complexity, a plate is next used. A shaker is used as an excitation and a scanning laser vibrometer is used to capture the velocities across 247 positions on the surface of the plate. The transfer functions across the plate are calculated using a voltage reference taken from the shaker. This experiment is classed as having high spatial sampling, as it would be unusual in practice to have 247 accelerometers on a surface of this size, due to constraints of physical spacing and mass loading of the plate. As the method is aiming for realistic applications which have machinery instrumented with accelerometers, this laser experiment is purely to provide a highly sampled version of the plate, for the purposes of investigating limitations in terms of spatial sampling. The larger dataset is used for a series of reductions in spatial sampling and the effects on the frequency content of the single singular value transfer functions Ξ due to this are investigated. A final large scale experiment is then detailed, which uses 24 accelerometers on the same plate. This experiment was conducted in an anechoic chamber, and a shaker is again used as an operational excitation source. A baffle is added to maintain the integrity of the noise from the surface of the plate by reducing the direct transmission from the shakers used to excite the plate. The Vibro-acoustic Frequency Response Functions of the plate are measured using the volume velocity source and an impact hammer.

3.1 Volume Velocity Source

Volume velocity sources are used for reciprocal excitation of the structure, with the responses on the plate being excited by the volume velocity source at the receiver position. Transfer functions are garnered between the pressure at the volume velocity source and the discretised

grid of accelerometers on the receiver. These are then calibrated and converted into reciprocal pressure due to volume velocity transfer functions using a method based on [125], with a reference microphone measurement taken from a distance from both the excitation and response positions.

3.1.1 Design

The volume velocity source operates by producing a burst of pressurised air, using a manual trigger to release. The frequency response of source can be altered by using different sized pipes, which would also affect the directivity of the source. In this thesis, a single pipe is used, with a diameter of 2cm and a length of 19.5cm.

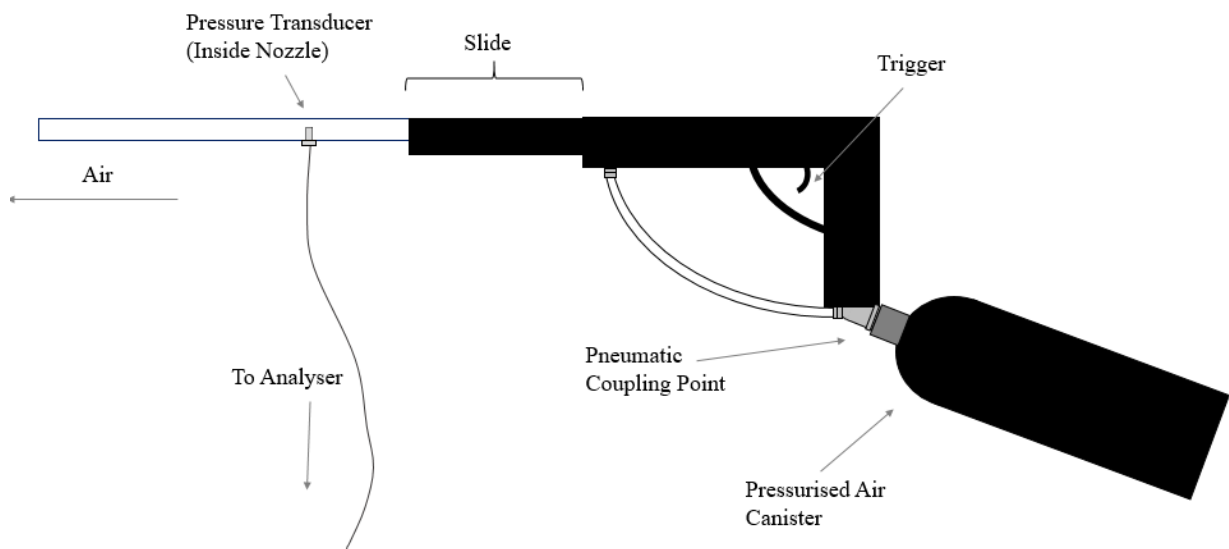


Figure 3.1: Schematic diagram of volume velocity source. At the left, the nozzle from which the burst of air produced; the pressure transducer is inside, which is connected to the analyser. On the right is the canister of pressurised air, which is coupled to the body. The slide is used to arm the volume velocity source, and the trigger is used to release the air from the body after the slide has been cocked.

The volume velocity source is shown in Figure 3.1. It consists of a canister of pressurised air, which is coupled to the body via a pneumatic coupling point. A slide on the body is used to arm the source, after which the trigger is used to release the burst of air from the nozzle. A

pressure sensor is located inside the nozzle, which can be used to calculate the transfer function between the source and the receiver.



Figure 3.2: PCB piezoelectronics 113B21 pressure transducer

The pressure sensor mounted in the source nozzle is a PCB piezoelectronics 113B21, pictured in Figure 3.2. This sensor is high frequency piezoelectric pressure sensors, containing a quartz sensing element [151]. It has a measurement range of 1380kPa, with an over-range of 2758 kPa, resonant frequency at ≥ 500 kHz, and a sensitivity of 3.6mV/kPa [152]. The maximum pressure is 6895 kPa with a resolution of 0.007kPa, and $\leq 1\%$ non-linearity [152]. A reference microphone is used to calibrate the source and convert from a direct to a reciprocal transfer function. This method of volume velocity source measurement requires a reference microphone for the calculation of the reciprocal transfer functions from the directly measured.

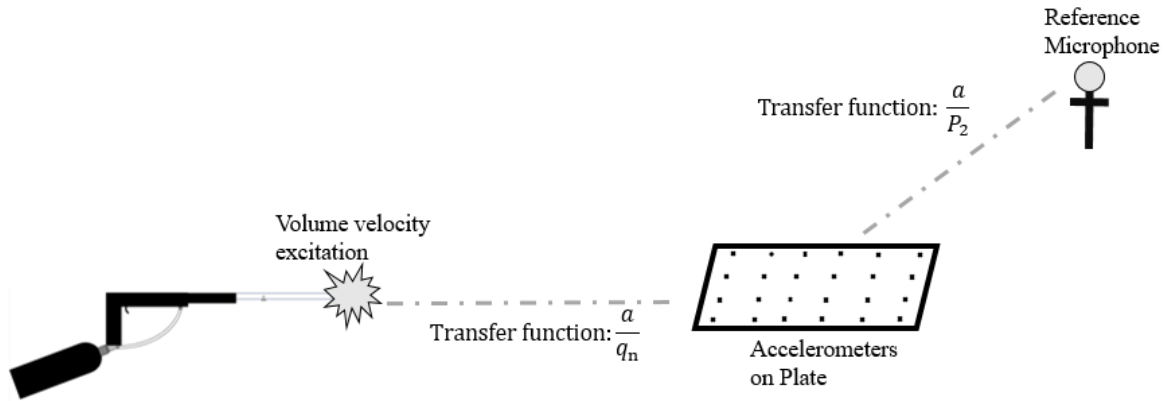


Figure 3.3: diagram showing transfer functions used in calculation for volume velocity transfer function. The transfer function $\frac{a}{q_n}$ is that between the pressure sensor in the nozzle of the volume velocity source and the accelerometer array on the plate, and the transfer function $\frac{a}{P_2}$ is that between the accelerometers on the plate and the reference microphone.

Figure 3.3 shows visually how the transfer functions are measured for the individual parts of the volume velocity calculation shown in Chapter 2.1.1.

In terms of transfer function, both H1 and H2 were calculated and compared to determine which was most suitable for the volume velocity source.

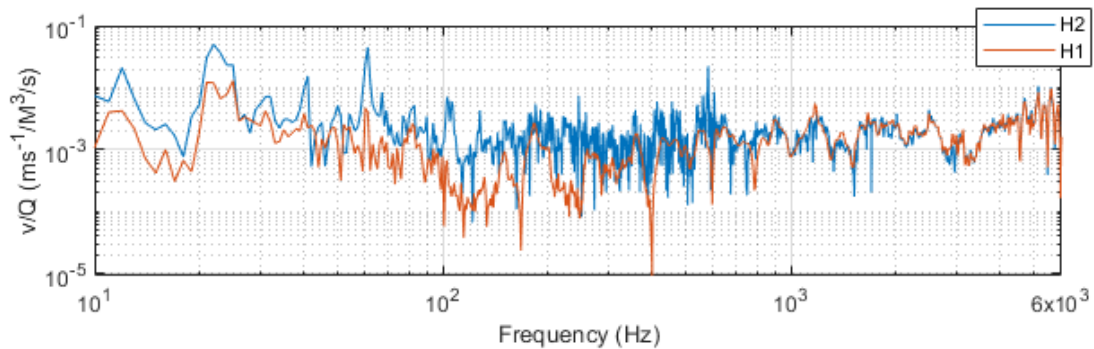


Figure 3.4: Comparison between H1 and H2 for the volume velocity source, measured at a single accelerometer mounted to a plate. Shown in blue is the H2 transfer function, and shown in red is the H1 transfer function.

It can be seen from Figure 3.4 that the H1 transfer function looks far less noisy than the H2 transfer function, indicating that noise is correlated with the output rather than the input. For this reason, the H1 transfer function is used for the volume velocity source.

3.1.1.1 Signal to Noise Ratio

To verify that the volume velocity produces an adequate signal to be prominent above the noise floor, it can be compared to the ambient noise in the anechoic chamber:

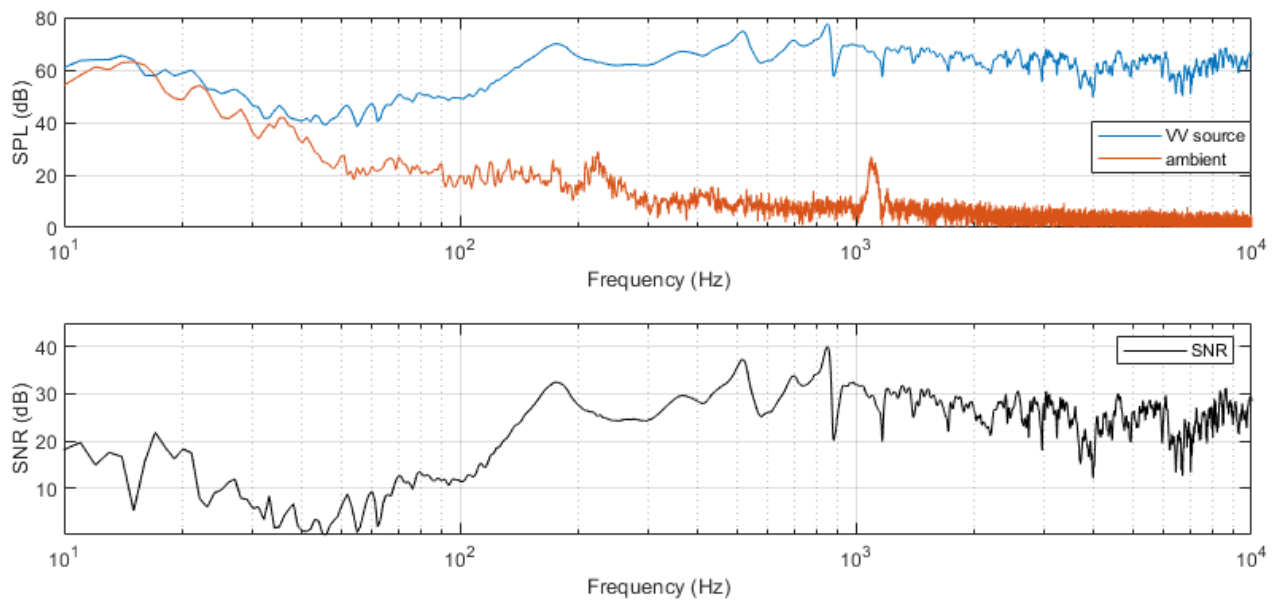


Figure 3.5: In the upper frame, the measured dB SPL at a microphone due to volume velocity source excitation is shown in blue, with the ambient background noise SPL of the anechoic chamber shown in red. The lower frame shows the signal to noise ratio between the volume velocity source signal and the ambient anechoic chamber. The x axes are between 10 Hz and 10 kHz.

Figure 3.5 shows in the upper plot a comparison in Pascals of the pressure at the response microphone due to the volume velocity source excitation, in blue, compared to the ambient noise of the anechoic chamber in red. Below 40 Hz, the volume velocity source is fairly close to the noise floor, indicating that it produces a lower velocity excitation. At around 15 Hz, it seems the volume velocity source is in the noise floor. However, above 40 Hz the volume velocity source is considerably higher pressure than the background noise, indicating that the signal is clear and uncontaminated by background noise.

3.1.2 Comparison Between *Hpf* and *Hvq* at Accelerometer Positions on the Plate and Microphone Positions

In order to ensure that the volume velocity source produces accurate data, the transfer functions between the volume velocity source and response positions on the plate are evaluated against those for the hammer source for positions on the plate with respect to microphone positions.

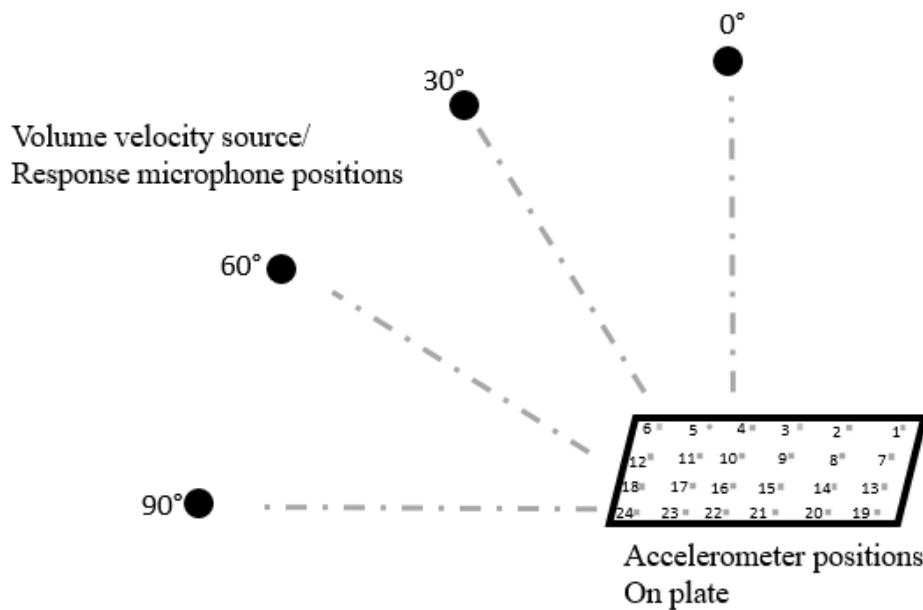


Figure 3.6: diagram showing the angles of the response at the microphone positions, which are also the volume velocity excitation positions (black circles). The numbered accelerometer positions on the plate are excitation positions for the hammer transfer functions, and response positions for the volume velocity excitations.

Figure 3.6 shows the microphone positions in the anechoic chamber and accelerometer positions on the plate. These positions are selected in order to provide different acoustic profiles of the plate, as the radiation behaviour of the plate varies in terms of frequency composition, depending on the observation position.

The volume velocity transfer function is measured reciprocally, from the volume velocity source at each of the microphone positions to each of the accelerometers on the plate. As this transfer function is between the pressure at the volume velocity source and the

accelerometers, it is converted to velocity due to volume velocity with the aid of a reference microphone located in the anechoic chamber. The transfer function measured was taken as an average over 5 impulses.

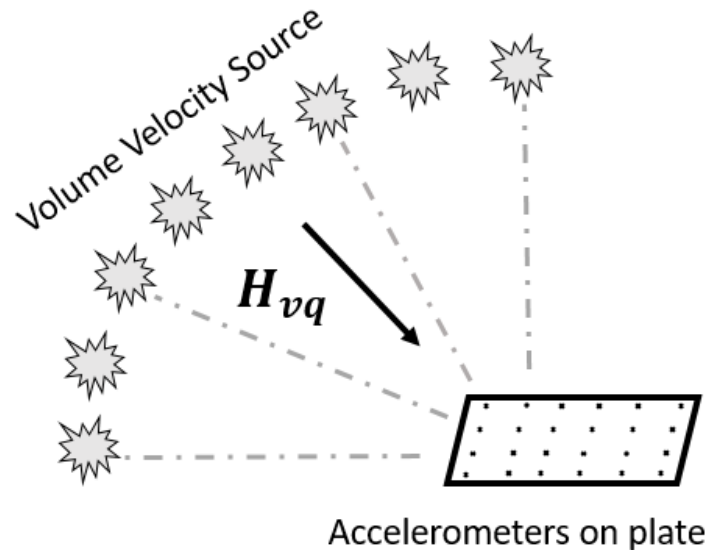


Figure 3.7: Visual representation of transfer function for plate radiation measured reciprocally, using the volume velocity source, for which measurements were taken at each microphone position to garner responses at each accelerometer position

Shown in Figure 3.7 is a visual representation of the measurement of the reciprocal volume velocity source transfer function. The two transfer functions are compared for accuracy, and to validate the use of the volume velocity for the use of these measurements within the blocked forces procedure. An advantage of the volume velocity source is that it excites the receiver reciprocally, meaning direct interaction with the structure is unnecessary. For complex structures which are difficult to excite manually, this may be a preferred method. As long as the structure has an initial characterisation successfully, gaining the mobilities of the system, a volume velocity source can be used for the airborne characteristics for the system in interchanging environments.

For the prediction of radiated noise, the transfer functions between the discretised segments of the plate and response positions are required. These are measured directly using the impact

hammer: a measurement was taken at each of the accelerometer positions with the force hammer, with the transfer function calculated for each of these points to each microphone, depicted in Figure 3.8.

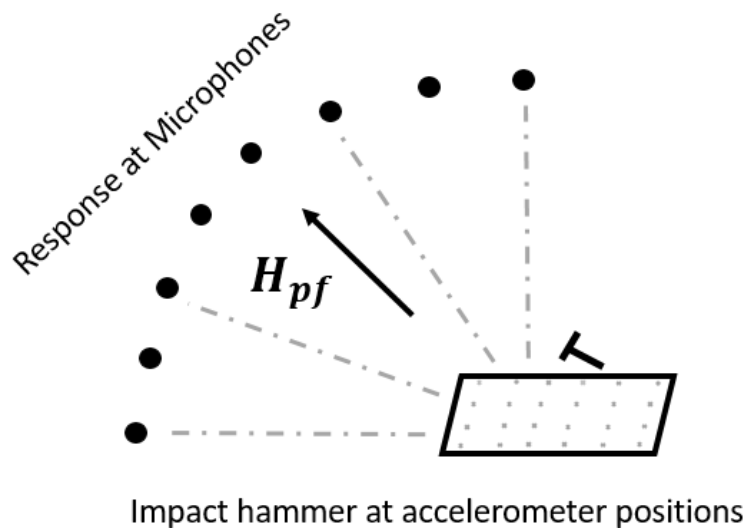


Figure 3.8: Visual representation of transfer function for plate radiation measured directly, using impact hammer, for which measurements were taken at each accelerometer position to garner responses at each microphone position

An average over 3 impulses was taken to calculate the transfer function, which is common practice, to ensure good coherence and frequency response. During these measurements, a metal hammer tip was used. This allows for a cleaner impulse and higher frequency range to be measured. Because the accelerometers were not included in this measurement, overloading of sensors was not an issue, which allows for a louder impulse to be created, which would hopefully lead to cleaner transfer function, lifted above the noise floor. This transfer function will be multiplied by the blocked forces of the plate to create the prediction.

In order to ensure that the volume velocity source produces accurate data, the transfer functions between the volume velocity source and response positions on the plate are evaluated against those for the hammer source for positions on the plate with respect to microphone positions. A range up to 6 kHz is shown, due to the upper reliable frequency of the accelerometers.

3.1.3 For microphone position at 0°

For the microphone response and volume velocity source excitation normal to the plate, the responses are shown for accelerometers, 2, 10, 14, and 22:

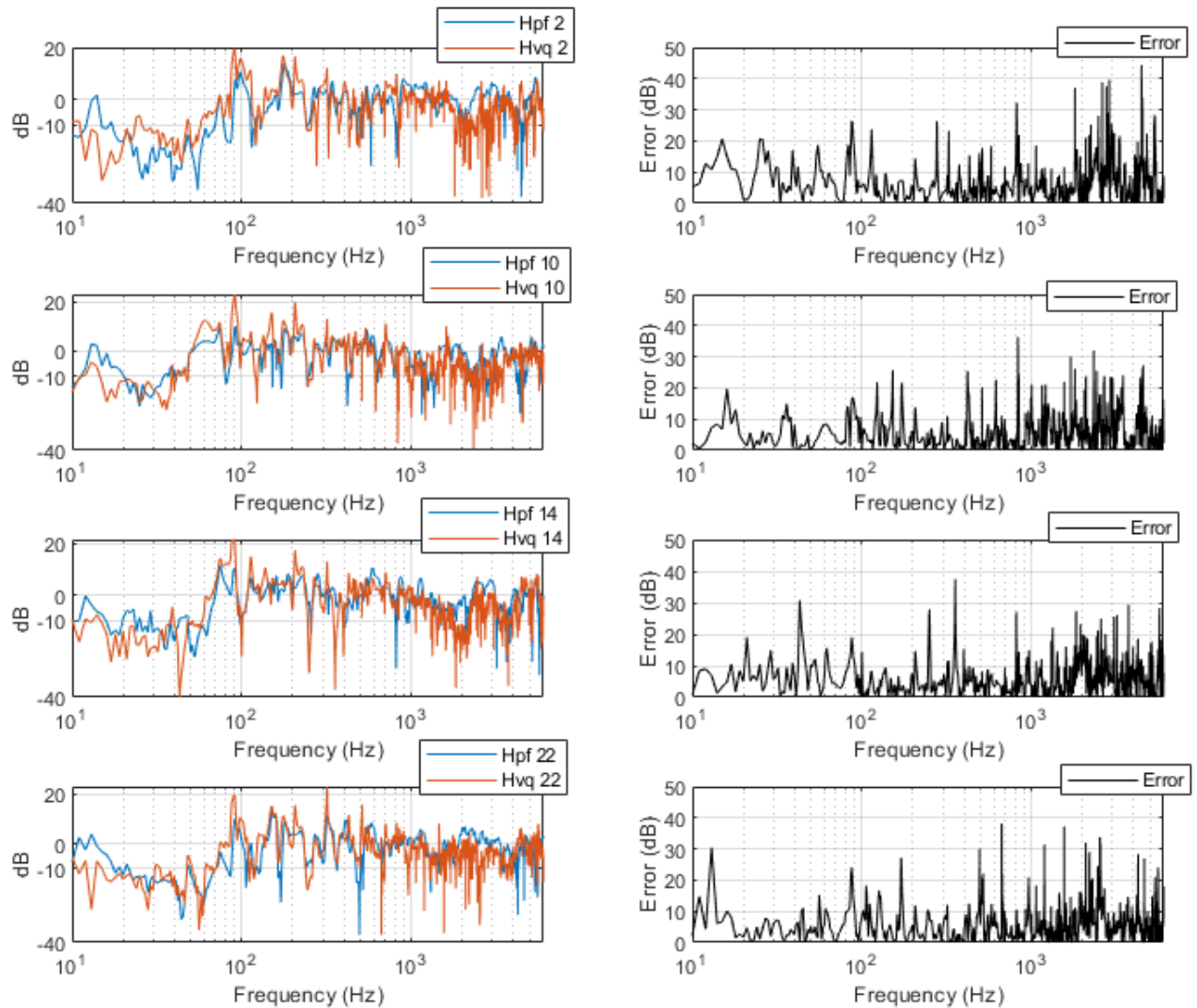


Figure 3.9: Comparison between H_{pf} , pressure due to force in blue, and H_{vq} , velocity due to volume velocity, shown in red, for response microphone at 0° . In the left hand side frames, the y-axis is dBs, and the x-axis is frequency in Hertz, ranging between 10 Hz and 6 kHz. From top to bottom on the left, the responses at accelerometer positions 2, 10, 14, and 22 respectively. The right hand frames show the difference error in dB between the two transfer functions for the accelerometer positions on the left: from top to bottom, positions 2, 10, 14, and 22.

Shown in blue in Figure 3.9 is the transfer function created by exciting the plate at the accelerometer positions with the force hammer, with response at the microphone positioned at 0° . In red, the transfer functions between the volume velocity source excitation at the 0°

microphone position and the response at the accelerometers in terms of velocity. In the first frame, accelerometer position 2 is shown with the second frame showing position 10, the third position 14, and the fourth position 22. In general there are some significant errors at resonances between, the H_{vq} transfer function and the H_{pf} transfer function for the 0° microphone position. The differences are likely to have been exacerbated by a difficulty in making the reciprocal measurement with the volume velocity source.

3.1.4 For microphone position at 30°

For the microphone response due to the hammer on the plate, and volume velocity source excitation, at 30°, responses are shown for accelerometer positions 2, 10, 14, and 22 on the plate:

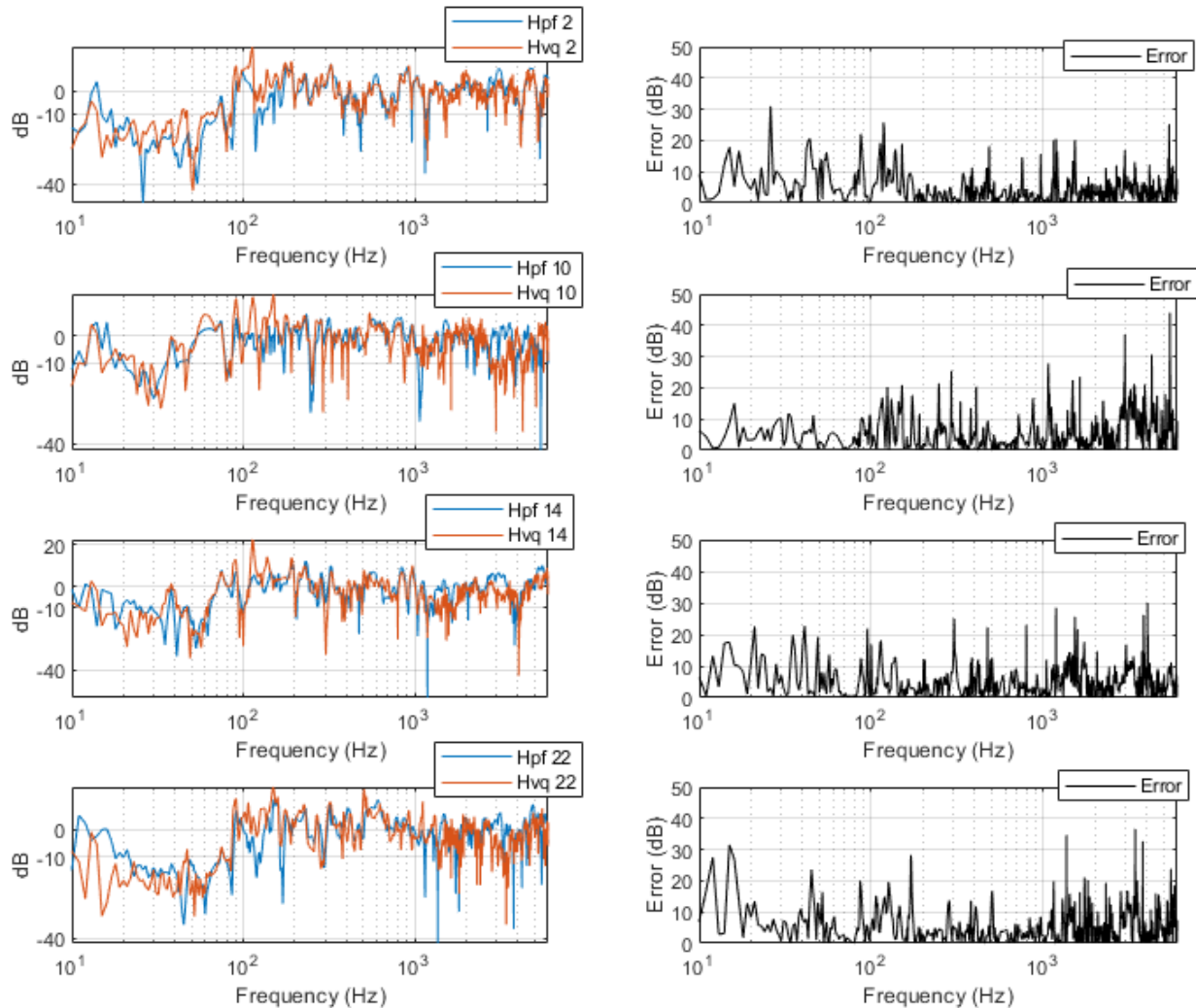


Figure 3.10: Comparison between H_{pf} , pressure due to force in blue, and H_{vq} , velocity due to volume velocity, shown in red, for response microphone at 30°. In the left hand side frames, the y-axis is dBs, and the x-axis is frequency in Hertz, ranging between 10 Hz and 6 kHz. From top to bottom on the left, the responses at accelerometer positions 2, 10, 14, and 22 respectively. The right hand frames show the difference error in dB between the two transfer functions for the accelerometer positions on the left: from top to bottom, positions 2, 10, 14, and 22.

In Figure 3.10, in red, is the H_{vq} reciprocal volume velocity transfer function, and in blue, the directly measured H_{pf} transfer function. The upper frame shows accelerometer position 2, the

second frame accelerometer position 10, the third frame shows accelerometer position 14, and the fourth frame shows accelerometer position 22. The transfer functions have somewhat closer agreement, with lower magnitude errors, than those shown in Figure 3.9, with overall errors tending to be under 30dB apart from 2 errors in the higher range of accelerometer position 10 and 3 instances in the higher range of accelerometer position 22.

3.1.5 For microphone position at 60°

For the microphone and volume velocity source excitation at 60°, responses are shown for accelerometer positions 2, 10, 14, and 22 on the plate:

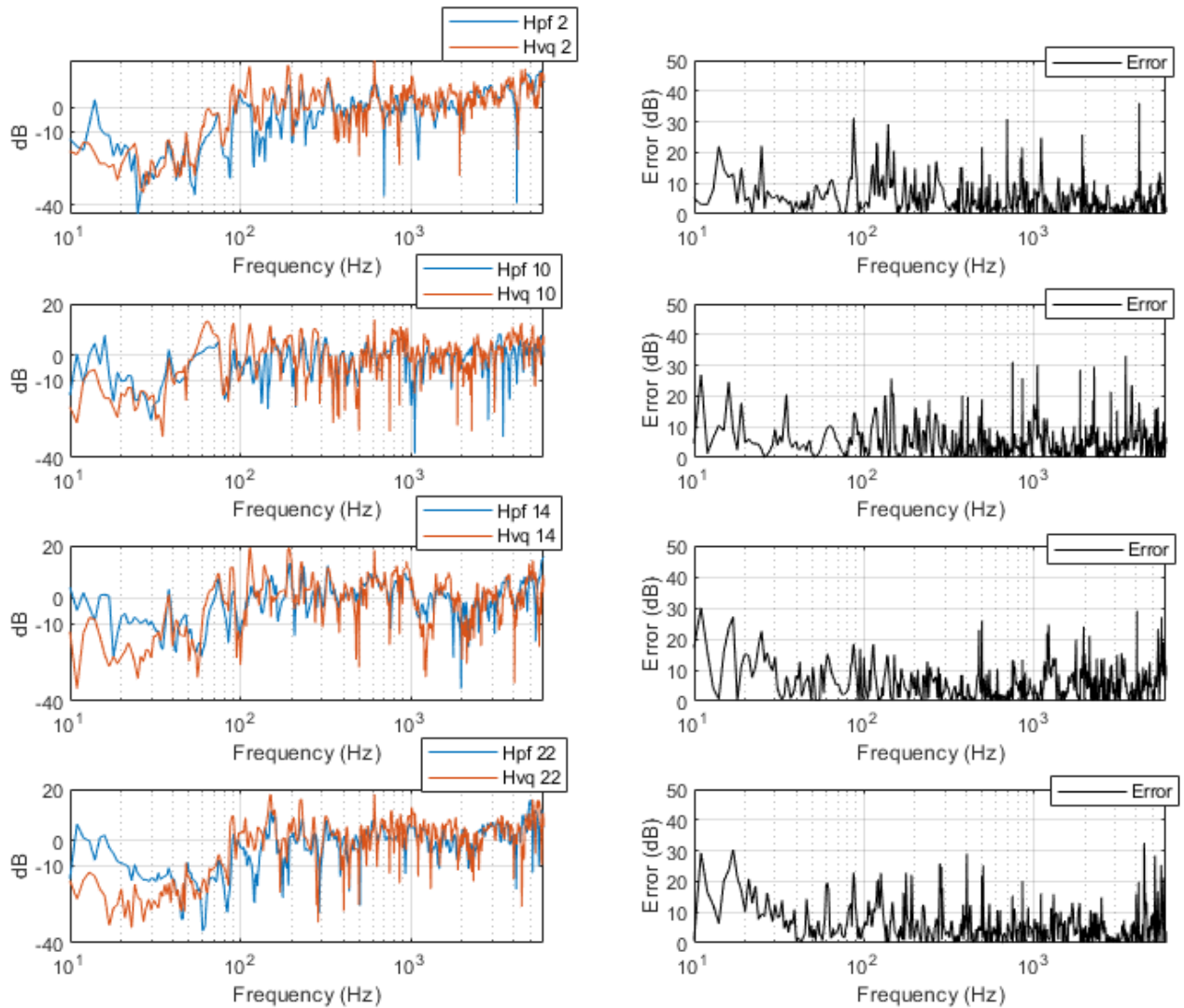


Figure 3.11: Comparison between H_{pf} , pressure due to force in blue, and H_{vq} , velocity due to volume velocity, shown in red, for response microphone at 60°. In the left hand side frames, the y-axis dBs, and the x-axis is frequency in Hertz, ranging between 10 Hz and 6 kHz. From top to bottom on the left, the responses at accelerometer positions 2, 10, 14, and 22 respectively. The right hand frames show the difference error in dB between the two transfer functions for the accelerometer positions on the left: from top to bottom, positions 2, 10, 14, and 22.

Shown in blue in Figure 3.11 is the directly measured H_{pf} transfer function, and in red the reciprocally measured H_{vq} transfer function. In the first frame accelerometer position 1 is

shown, in the second frame accelerometer 10, in the third frame is accelerometer 14, and in the fourth frame accelerometer 22 is shown. An improvement on the 0° and 30° plots, there is an instance of error around 35dB in position 2 and for position 22, though the rest of the errors stay below a 30 dB threshold. There is good correlation between the two transfer functions across the frequency range shown, with anti-resonances described at the same frequencies in both transfer functions. However, the magnitudes of the anti-resonances appear to be unaligned, as shown by the errors or around 30dBs at many of the anti-resonances.

3.1.6 For microphone position at 90°

For the microphone and volume velocity source excitation at 30°, responses are shown for accelerometer positions 1, 10, 14, and 22 on the plate:

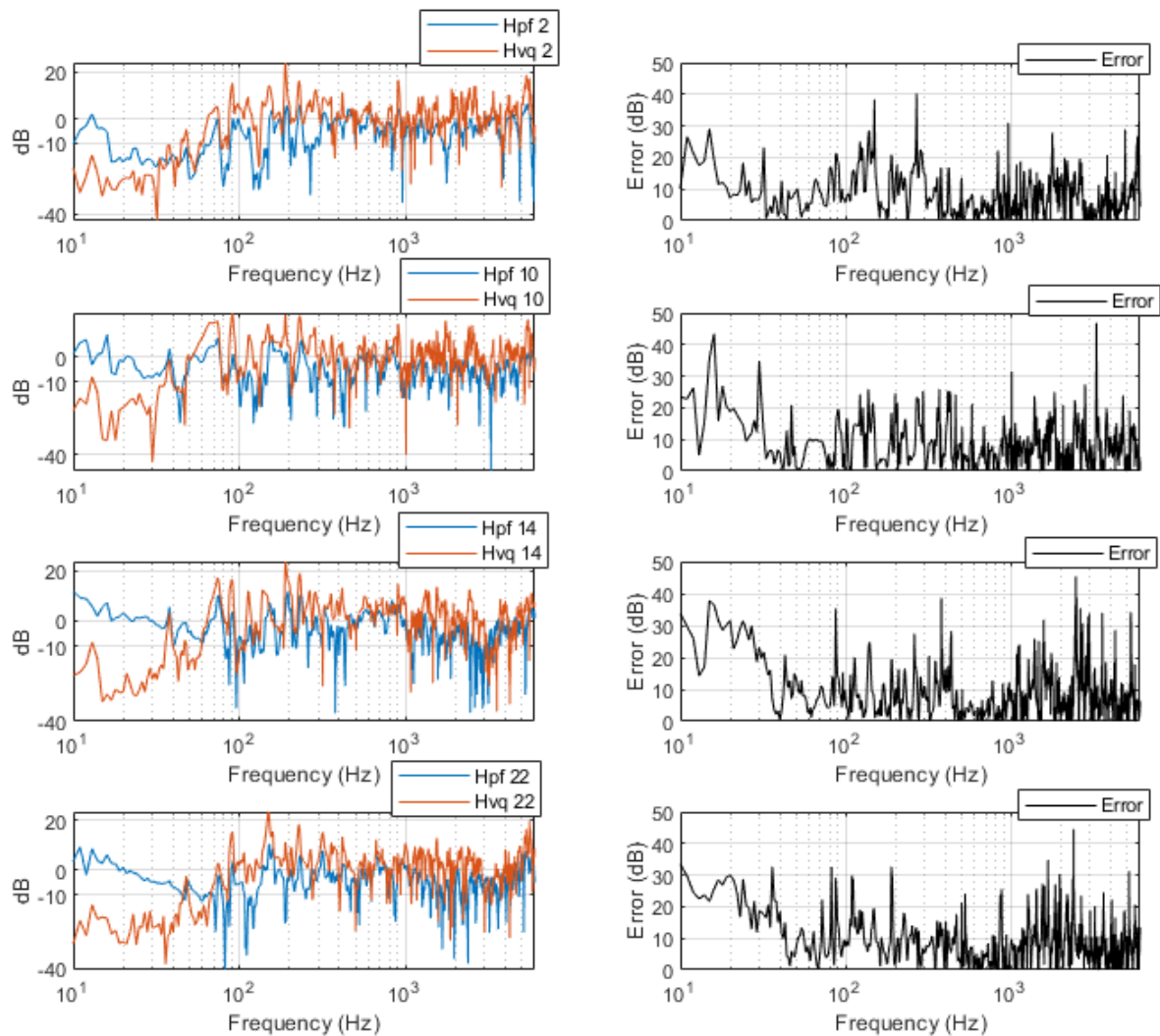


Figure 3.12: Comparison between H_{pf} , pressure due to force in blue, and H_{vq} , velocity due to volume velocity, shown in red, for response microphone at 90°. In the left hand side frames, the y-axis is dBs, and the x-axis is frequency in Hertz, ranging between 10 Hz and 6 kHz. From top to bottom on the left, the responses at accelerometer positions 2, 10, 14, and 22 respectively. The right hand frames show the difference error in dB between the two transfer functions for the accelerometer positions on the left: from top to bottom, positions 2, 10, 14, and 22.

In Figure 3.12, In blue is the directly measured H_{pf} transfer function, and in red the reciprocally measured H_{vq} transfer function. Accelerometer position 2 is shown in the first frame, accelerometer position 10 is shown in the second frame, accelerometer position 14 is shown in the third frame, and accelerometer position 22 is shown in the fourth frame. Agreement is worse for the 90° microphone shown in Figure 3.12 than for the microphone positions shown in Figure 3.9, Figure 3.10, and Figure 3.11, as the transfer functions do not align as well as they do in the previous figures. This is likely due to the right angle placement of the response/ excitation position to the plate. The plate radiates differently from this angle and the two measurement methods likely excite slightly differently due to the presence of the enclosing frame around the edge of the plate. In the H_{pf} transfer functions, there appears to be some comb filtering effects at higher frequencies. As this transfer function is between a single excitation and single response, this must be due to reflection. As the testing was conducted in an anechoic chamber, part of the test rig must be causing this. As the plate frame is slightly wider than the plate, it is possible that this has caused some reflection. Potentially, the plate itself may have caused some reflection. Another option may be that the metal arc upon which the microphones are mounted could also contribute towards some reflection. Alternatively, this could be the actual frequency response, as the metal hammer tip is likely to excite a higher frequency range than the volume velocity source. It could also be due to an insufficient or substandard measurement.

3.1.6.1 Directivity

The directivity of the volume velocity source was measured in the anechoic chamber, by rotating the volume velocity source about the horizontal axis with respect to the response microphones. A reference microphone at 0° was used, whilst the volume velocity source was activated pointing at 0°-180° with intervals of 10°.

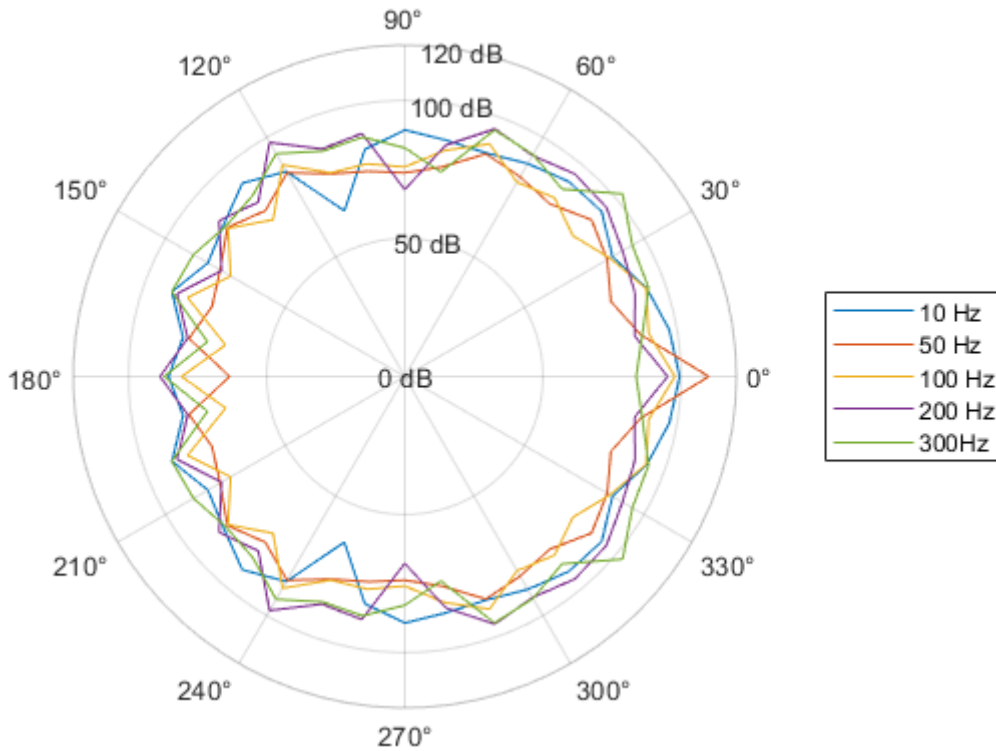


Figure 3.13: Radiation pattern of the volume velocity source in dB with reference to a microphone at 0°. At the top of the plot is 90°, with 0°/360° to the right of the plot. Shown in blue is radiation for 10 Hz, shown in red is 50 Hz, in yellow 100 Hz, in purple 200 Hz, and in green 300 Hz. The radial axis is between zero and 120 dB.

The directivity of the volume velocity source is converted to decibels from the measured transfer functions using $20\log_{10}$ with a reference to $2e^{-5}$. Figure 3.13 shows the directivity for the volume velocity source at frequencies of 10 Hz, 50 Hz, 100 Hz, 200 Hz, and 500 Hz. In this range, it appears that 50 Hz is more directional than the other frequencies, with a peak at the 0° node. Overall, there is an average range of 30 dB difference for each frequency in terms of the directivity for each frequency. The frequencies in this range cover a dynamic range from 63 dB, the minima of 10 Hz, and 110 dB, the maxima of 50 Hz.

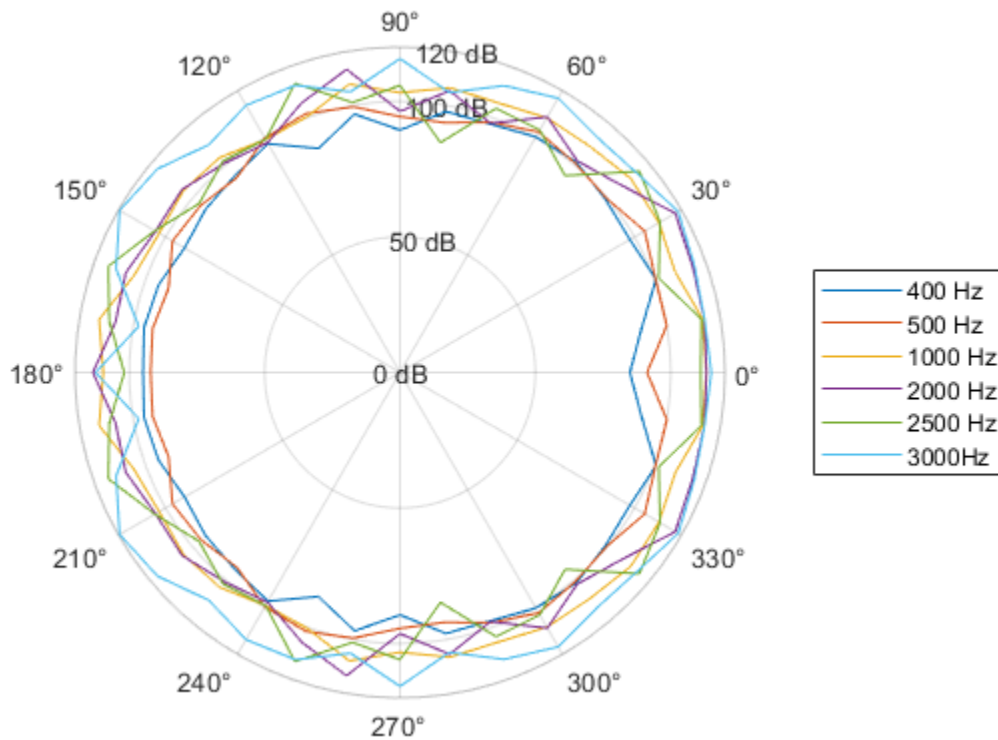


Figure 3.14: Radiation pattern of the volume velocity source in dB with reference to a microphone at 0°. At the top of the plot is 90°, with 0°/360° to the right of the plot. Shown in dark blue is radiation for 400 Hz, shown in red is 500 Hz, in yellow 1000 Hz, in purple 2000 Hz, in green 2500 Hz, and in light blue 3000 Hz. The radial axis is between zero and 120 dB.

The directivity of frequencies 400 Hz, 500 Hz, 1 kHz, 2 kHz, 2.5 kHz, and 3 kHz is shown in Figure 3.14. The overall dynamic range in this group of frequencies is from 85 dB at 0° for 400 Hz, to 120 dB at 150° for 3 kHz. The magnitude increases with frequency, as does the omni-directionality. From 1 kHz, the source becomes more consistent at the varying angles, with a range of under 20 dB for rotational angles at the higher frequencies. Compared to Figure 3.13, an increase of around 20 dB is apparent for all the frequencies.

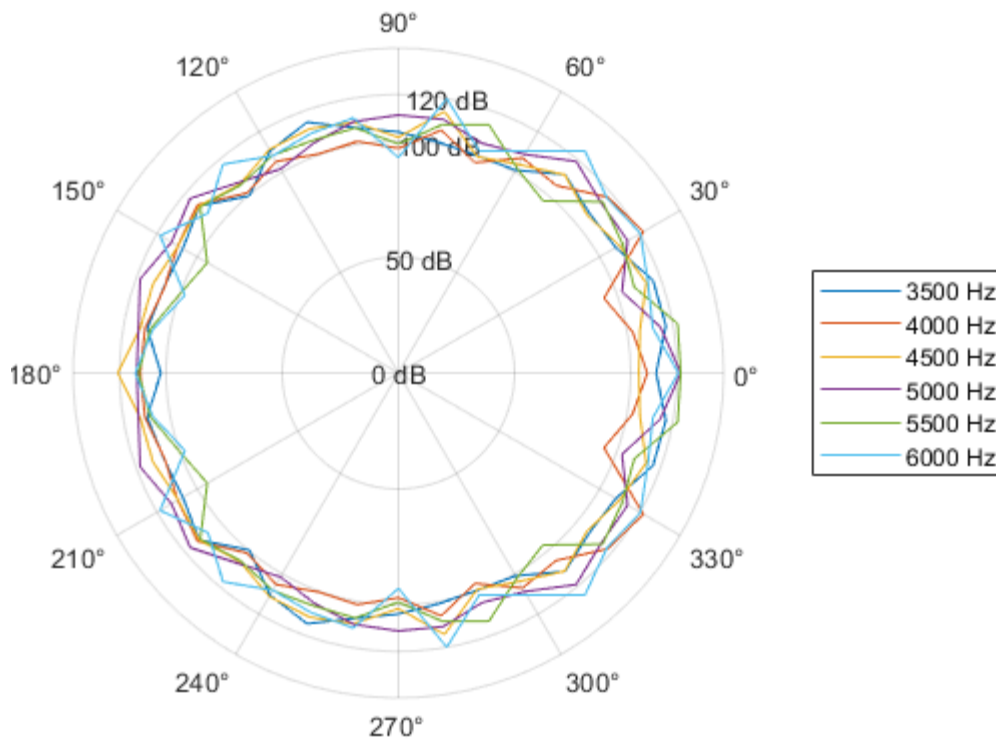


Figure 3.15: Radiation pattern of the volume velocity source in dB with reference to a microphone at 0°. At the top of the plot is 90°, with 0°/360° to the right of the plot. Shown in dark blue is radiation for 3500 Hz, shown in red is 4000 Hz, in yellow 4500 Hz, in purple 5000 Hz, in green 5500 Hz, and in light blue 6000 Hz. The radial axis is between zero and 130 dB.

Figure 3.15 shows the directivity of the source at frequencies of 3.5 kHz, 4 kHz, 4.5 kHz, 5 kHz, 5.5 kHz, and 6 kHz. Like with Figure 3.14, when compared to Figure 3.13, an increase of around 20 dB is apparent for all the frequencies. This indicates a stabilisation of magnitude across frequency when reaching mid-range, as the lower frequencies were of a lesser magnitude. However, the difference in magnitude remains around 30 dB, with the lowest magnitude apparent at 95 dB 5.5 kHz at 150° and the highest magnitude at 124 dB at 50° and 6 kHz.

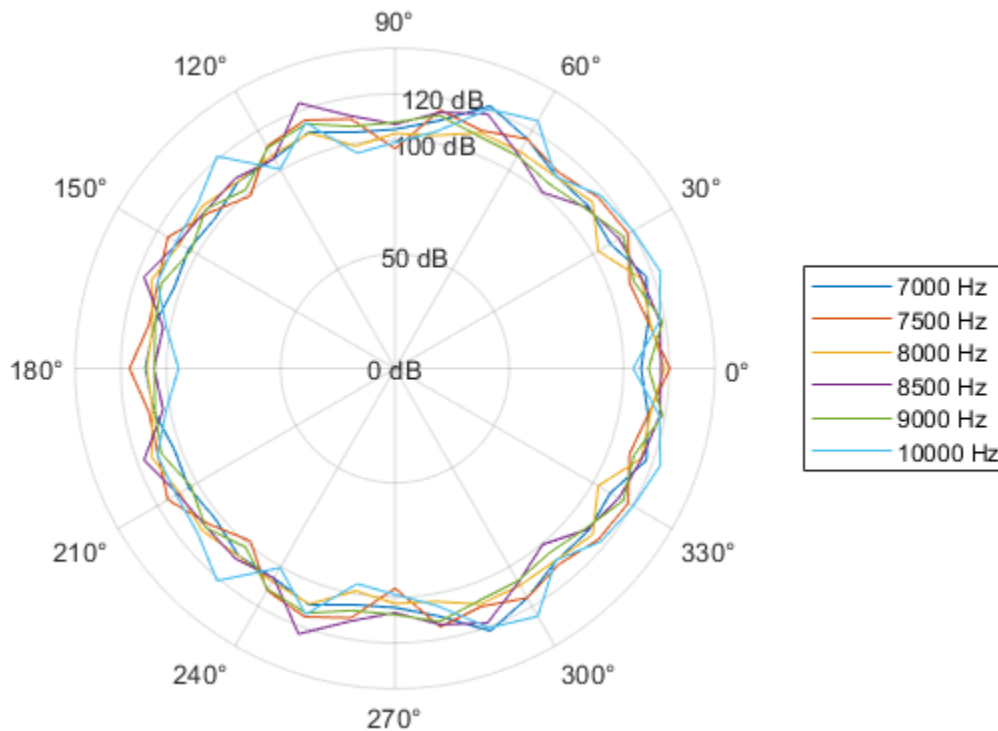


Figure 3.16: Radiation pattern of the volume velocity source in dB with reference to a microphone at 0° . At the top of the plot is 90° , with $0^\circ/360^\circ$ to the right of the plot. Shown in dark blue is radiation for 7000 Hz, shown in red is 7500 Hz, in yellow 8000 Hz, in purple 8500 Hz, in green 9000 Hz, and in light blue 10000 Hz. The radial axis is between zero and 130 dB.

Similar to the frequencies shown in Figure 3.15 the frequencies of 7 kHz, 7.5 kHz, 8 kHz, 8.5 kHz, 9 kHz, and 10 kHz, are largely between 100 dB and 120 dB for the varying degrees of radiation, as shown in Figure 3.16. The maxima and minima of the range in magnitude at these frequencies are both attributed to 10 kHz, with a maxima of 125 dB at 60° and a minima of 95 dB at 180° . These results show that the source directivity from 400 Hz to 10 kHz ranges between 20 to 30 dB. The source is somewhat omni-directional, however 20-30 dB is a rather large range which may in practice prove problematic for non-direct excitations.

3.1.6.2 Volume velocity source summary

The nature of the volume velocity source has been described, in terms of its construction, function, and use in practice. A comparison for suitability between the H1 and h2 transfer functions has been conducted, with the decision to use H1 for the excitation due to noise apparent with H2, indicating noise is correlated with the output. The reciprocal transfer functions have been compared to transfer functions measured directly using a hammer. The directivity of the source has been measured, and the signal to noise ratio has been observed compared to the ambience in an anechoic chamber. Overall, it can be seen that the volume velocity source is effective and accurate for collecting reciprocal vibro-acoustic transfer functions. When compared to the directly measured transfer functions using a metal hammer tip at the accelerometer positions, there is a similar response across frequency. The volume velocity transfer functions appear to be clear across the frequency range shown. As there may be some degree of interaction between the plate and the enclosing frame, it is positive that the edge and corner positions of the plate are in agreement, despite these areas potentially having slightly different excitation requirements in terms frequency, due to non-exact boundary conditions in practice. The volume velocity source appears to correlate well with the hammer measurements for all microphone positions, which given the difficulties measuring the 0° transfer function reciprocally is encouraging for the further data analysis. The directivity of the source has been shown to have around 20 dB discrepancy when considered in terms of a horizontal directivity. The data shown here informs the suitability for the use of the H_{vq} transfer function in place of H_{pf} for blocked forces predictions, the results of which are discussed in Chapter 7. Suggestions on further investigation and improvement on the volume velocity source are discussed in Chapter 9.

3.2 Experimental Equipment

In this section, the equipment used throughout the testing is detailed. An overview of the physical tools used for the experiments such as the impact hammer, accelerometers and other transducers are discussed, and brief description of the Data Acquisition System and post-processing software is given.

3.2.1 Scanning Laser Vibrometer (SLV)

The SLV used in the experiments detailed in Chapter 7 was a Polytec PSV 400. The PSV 400 consists of a Class 2 633 nm helium-neon (HeNe) laser.

This SLV has a maximum measurement frequency of 40 kHz with a maximum vibration velocity of 10m/s, and a spatial range of 10 to 1000 mm s⁻¹/V.



Figure 3.17: PSV 400 scanning laser vibrometer in-situ for plate experiment detailed in Chapter 6

The PSV 400 SLV is shown in Figure 3.17 in-situ as it was during the measurements taken, the results of which are shown in Chapter 6.

3.2.2 Measurement Microphones

For the anechoic chamber experiment, detailed in Chapters 7 and 8, an array of 8 measurement microphones were used, along with a reference microphone for the volume velocity source. The microphones used were Bruel & Kjaer Type 4966 ½“ prepolarised free-field microphones.



Figure 3.18: Bruel and Kjaer ½” prepolarised free-field microphone Type 4966. Figure taken from product datasheet [153].

Shown in Figure 3.18, the microphone is a high sensitivity measurement microphone, with a sensitivity of 50nV/Pa, a frequency range of 5Hz to 20 kHz, and a dynamic range of 14.6 to 144 dB [153]. The microphones were used with Bruel& Kjaer Type 1706 high temperature CCLD microphone preamplifiers [154].

3.2.3 Impact Hammer

Impact hammers are widely used tools in transfer path and modal analysis, for which their utility is usually to measure the Frequency Response Functions (FRFs) of a surface or system by manual excitation at points on the structure. In this thesis, these positions correspond to the accelerometer positions on the beam and plate, and the direct vibro-acoustic FRFs measured between the plate and microphones. The hammer contains a force transducer,

which is used to calculate the transfer function between itself and the accelerometer. It is standard practice to produce a number of impacts, usually 3 or 4, and calculate the transfer function from an average across the impacts. The coherence of the impacts is observed during testing to ensure that excitations are consistent across the frequency range. This requires the impacts to be near identical. The data can be corrupted by mistakes such as allowing a double hit to occur within the window of measurement, or hitting the surface with a different force, meaning that frequencies are not excited uniformly across the hits.



Figure 3.19: Impact Hammer by Bruel & Kjaer, type 8206-001. Figure taken from the product datasheet [155]

The hammer used in the experiments detailed in Chapters 5, 7, and 8 of this thesis, shown in Figure 3.19, is a Bruel & Kjaer type 8206-001, which has a sensitivity of 10.41mV/N [156]. The frequency response of the hammer is dependent upon the material used for the tip. Impact hammers are supplied with tip surfaces to excite at different magnitudes and frequency ranges.

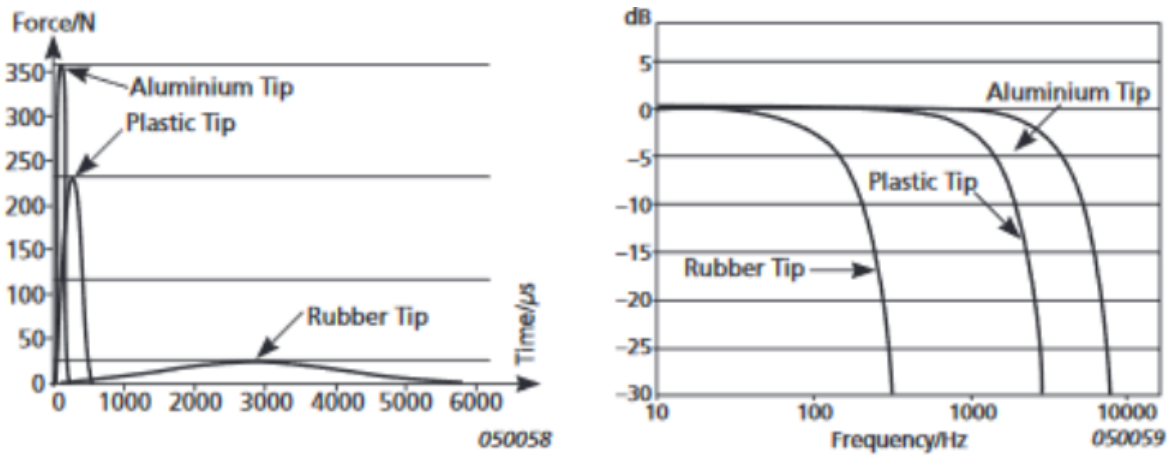


Figure 3.20: Shown left are the impulse shapes, pulse decay, and peak value for the three types of hammer tip as a function of time, shown right are the force spectra for the three hammer tips for an impact on an aluminium plate. Figure from product datasheet [155].

The three types of hammer tips available for this model are rubber, plastic, and aluminium. The left frame of Figure 3.20 shows the peaks and decay of the impulse for the three types of tip, whereas the right frame shows the frequency response. The hammer tips lend themselves to different applications based on the needs of the user in terms of frequency range and impulse magnitude.



Figure 3.21: Impact hammer in case with tips shown in upper left of photograph. The left tip is the metal tip, the middle shows the side which is screwed into the hammer of another metal tip, and the right tip is the plastic tip. The bottom right element is a weight or extender which can be added to the hammer.

Figure 3.21 depicts the hammer used in its case with the tips supplied. In this thesis, a metal hammer tip was used for the experimentally measured beam described in chapter 5, allowing for a frequency range up to around 6 kHz when the limitations of the accelerometers is considered. A plastic hammer tip was used for the measurement of FRFs on the plate. As the impacts are forced at the accelerometer positions, a smaller force input was required to avoid overloading of the accelerometers, due to the plate being physically thin. This was not an issue for the beam as it was thicker, meaning that a higher force could be tolerated by the accelerometers. For the plate experiment, this then renders a reliable frequency range up to 5 kHz. For the measurement of the vibro-acoustic FRFs between the accelerometer positions and the remote microphones, the aluminium hammer tip was used, as the accelerometers

were not active during the measurement of these FRFs. This allowed stronger impacts in terms of force, which translate to a higher acoustic pressure measured at the microphones, therefore ensuring a more desirable signal to noise ratio. The transfer function H1 is used for the measurements with hammer, as any noise is assumed to be uncorrelated to the input. The impact hammer was used for the physical beam experiment detailed in Chapter 5, and for the anechoic chamber experiment in Chapters 7 and 8.

3.2.4 Accelerometers and Force Transducers

The type of accelerometers used in this thesis are piezoelectric sensors used to measure the acceleration at positions on a surface, containing an extremely thin quartz crystal upon which the input force is enacted. The accelerometers were Bruel & Kjaer type 4507, which have a frequency range of 0.3 Hz to 6 kHz and a sensitivity of 50mV/ms⁻². These are a relatively high sensitivity accelerometer suitable for measuring wide frequency ranges from <1 Hz, up to around 20 kHz [157]. The input force is converted to a voltage which is analogous to the acceleration, which is then interpreted by the data acquisition system.



Figure 3.22: Bruel & kjaer Type 4507 accelerometer

Shown above in Figure 3.22 is one of the accelerometers used in the testing. Accelerometers must be mounted correctly to ensure the frequency response is preserved, with a close contact

between the accelerometer and the surface of the device under test, with guidelines provided in BS ISO 5348-1998 Mechanical vibration and shock - Mechanical mounting of accelerometers [158],[46], [159]. Commonly used substances used to attach accelerometers in experiments are beeswax and superglue. Beeswax has the advantage of being easier to remove from the surface after testing, but does not have as strong adherence as superglue, meaning accelerometers can become loose. Superglue was used to attach accelerometers for the experiments described in this thesis to ensure the accelerometers remained in place. These accelerometers were used for the physical beam experiment detailed in Chapter 5, and for the anechoic chamber experiment in Chapters 7 and 8.

A force transducer was used to measure the force at each of the shakers in the anechoic chamber experiment (Chapters 7& 8). These force transducers were Sinocera CL-YD-303 compression only force transducers. The transducer's flat surface was glued to the plate to hold the shakers in position using superglue, and the male thread was attached to the shaker using a screw adaption.



Figure 3.23: Sinocera CL-YD-303 2kN Compression only force transducer

One of the two force transducers used is pictured in Figure 3.23. The CL-YD-303 transducers have a sensitivity of 4pC/N and a linear range of 0 to 2kN [160]. They were each used in conjunction with a Sinocera YE5857A remote charge amplifier [161].

3.2.5 Shakers

Two different types of shakers were used for the experiments in this thesis: for the SLV experiment shown in chapter 6, a Bruel & Kjaer Ling Dynamic Systems V101 permanent magnet shaker was used.



Figure 3.24: Bruel & Kjaer LDS V101 permanent magnet shaker

Shown in Figure 3.24, the LDS V101 shakers have a usable frequency range of 5 Hz to 12 kHz, a peak to peak displacement of 2.5mm, resonance at 12 kHz, and a moving element mass of 0.0065kg [162]. In the laser experiment, the shaker was supported by a spur attached to the plate frame.

In order to attach shakers to the plate for the anechoic chamber experiment without the use of a supporting element, smaller, lightweight shakers were needed. The shakers used were unbranded, 4 Ω 25W shakers.

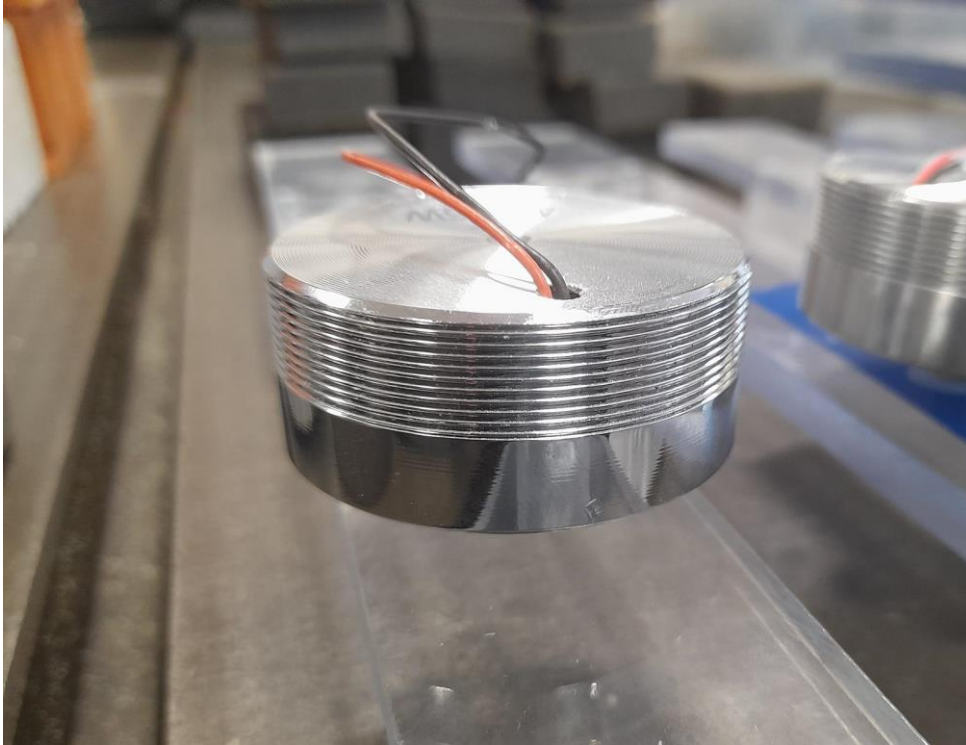


Figure 3.25: Unbranded 4 Ω , 25W shakers used in anechoic chamber experiment, detailed in chapters 7 and 8.

The shakers, shown in Figure 3.25, have a resonance frequency of 60 Hz at 1V, an output SPL of 86 dB and a maximum frequency of 20 kHz [163].

3.2.6 Data Acquisition and Analysis

The data acquisition system used in the experiments was Dewesoft SIRIUS hardware, which is a modular system allowing for the daisy-chaining of separate units to allow flexibility in the number of channels used. One of the units used is pictured below in Figure 3.26.



Figure 3.26: Dewesoft SIRIUS Data Acquisition System Interface

The associated software for controlling the DAQ, Dewesoft X, has myriad features for acquisition and analysis of data, and allows for post-measurement calculation of required parameters. Dewesoft X allows the operator to export data as a .mat file for ease of transition to Matlab for further data analysis. The analysis in this thesis has been conducted using Matlab software, which is named thusly as a portmanteau of ‘Matrix laboratory’. Matlab software is an analysis software for handling matrices and large datasets, and has a vast range of applications for data analysis across disciplines.

3.3 Experimental Methodology

In this section, an overview of the methodology for each of the experiments conducted is provided.

3.3.1 Beam Model Experiment

A free- free beam model was used to simulate a 0.555m length beam with responses captured at intervals of 0.0084m (67 points along the beam) with a frequency range of 20 kHz and a frequency resolution of 1 Hz. A beam was chosen for the initial experimental structure due to the fact that the modes are well separated. The dimensions were defined as 0.555m x 0.038m x 0.01m, with a density of 7850Kg/m³ and Young’s modulus of 190GPa (average for steel).

A loss factor of 0.009 was chosen to emulate the damping of a real steel beam of these dimensions. Together, these parameters give a realistic frequency response function, in line with that expected for a real beam. The rotations of the beam were not included to allow for a single degree of freedom model containing only the bending modes of the beam.

The beam model was used to form a mobility matrix Y with dimensions $67 \times 67 \times 20000$ and a $67 \times 1 \times 20000$ vector of input forces was created. Multiplication of this force vector by the mobility matrix then gave the velocity response of the beam when excited by the applied force. For the results presented, the force is applied at the first response position on the beam model, located at 0m from the left hand side (end) of the modelled beam. The resulting $67 \times 1 \times 20000$ vectors of vibration velocities obtained by multiplying the mobility matrix by the input forces represents the ‘operational’ vibration of the beam structure. This matrix was then reshaped to form a 67×20000 matrix with rows corresponding to the response coordinates and columns to frequency before an SVD was performed.

The SVD resulted in three new matrices: where the columns of Ψ (67×67) give the mode shapes of the beam, Φ (20000×20000) gives the frequency response of the mode, and the diagonal of Σ (67×20000) gives the singular values, corresponding to the ‘significance’ or ‘strength’ of each ‘operational’ mode. This mode was compared to models with reduced spatial sampling in order to observe the modal content of the constructed transfer functions Ξ . The other model presented in the chapter is of 20 kHz frequency range with 17 response positions spaced at 0.034m, in order to compare the effects of the reduced sampling positions.

3.3.2 Measured Beam Experiment

The experiments conducted using the beam model were used to inform a further test conducted using a real steel beam. Transfer functions containing the contribution for a single mode are going to be constructed using the location vs frequency method. The beam approximately meets the physical conditions of those in the model, having the same physical

dimensions of 0.555m x 0.038m x 0.01m, with assumed density of 7850Kg/m³ and Young's modulus of 190GPa, which are average values for steel. The data acquisition was conducted using a sample rate of 32775 Hz and 16384 frequency lines, allowing for a frequency resolution Δ of 1Hz and range of 16384 Hz, in accordance with the basic state of the model in Chapter 4. The frequency range of interest is between 100 Hz and 6 kHz, which should account for the low damping of the system by having a relatively high sample rate compared to range of interest.



Figure 3.27: Experimental steel beam. 17 accelerometers are mounted on the bottom side of the beam at interval of 3.2cm. The beam was excited using an instrumented force hammer at each of the same positions on the upper face of the beam.

In the real experiment, sensor and excitation sampling density are limited by physical conditions, with the experiment using 17 response and excitation positions, and a sampling interval of 3.2cm, as shown by Figure 3.27.

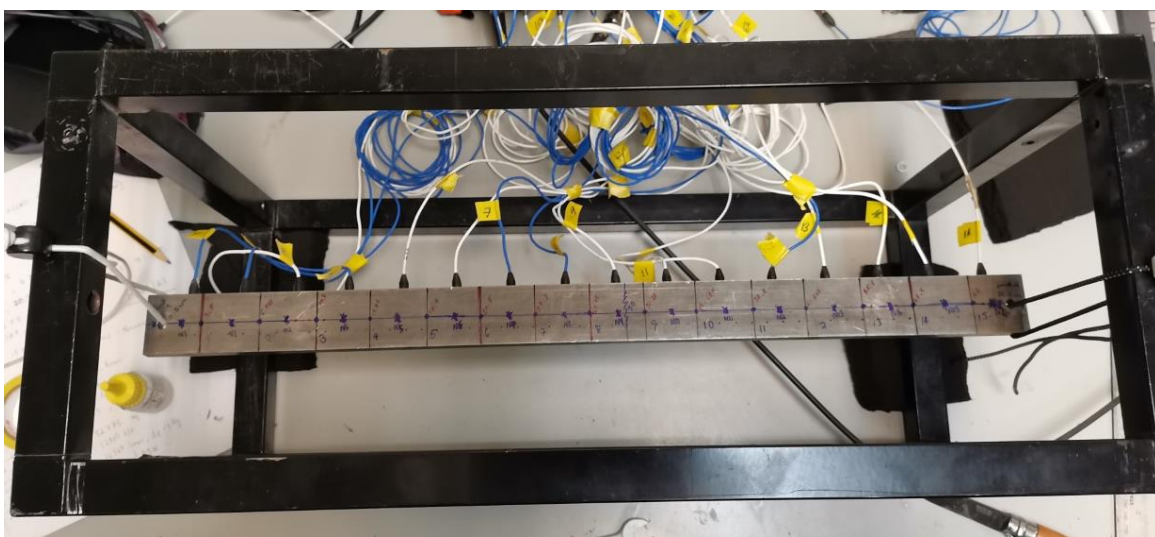


Figure 3.28: Beam in testing position. The beam has been suspended using elastic bungee cords in order to approximate free-free boundary conditions.

The beam was suspended from a metal frame, using elastic cords to simulate a free-free boundary condition. The suspension frame was placed on pieces of foam to mitigate any vibration interference from the surface underneath. The accelerometers were mounted on the underside of the beam, and at each of the accelerometer positions of the upper side, the force hammer was used to measure the transfer functions at each position. The measurement positions can be seen marked on the upper side of the beam in Figure 3.28. The accelerometers were mounted in the centre of the beam, as only the bending modes were observed.

The acceleration due to force transfer functions in the mobility matrix were converted to velocity, to aid mode shape description in the SVD procedure. The data was then analysed using SVD, with transfer functions Ξ containing a single singular value being constructed. The beam experiments were conducted to provide a simple structure with well separated modes, before a more complex plate experiment was conducted.

3.3.3 Scanning Laser Vibrometer Experiment

The structural modes of a real plate are determined using the Peak Picking SVD method, before the LvF method is employed to construct transfer functions containing the contribution of a single singular value element. As seen in the beam model experiment, a high sampling resolution is needed to gain the state where only a single mode is described by a singular value. The experiment was conducted using a 900mm x 700mm x2.5mm plate set in a lightweight frame, isolated with foam inside the contact points to emulate simply supported boundary conditions.



Figure 3.29: Plate mounted in-situ. The surface of the plate has been coated with a non-metallic matte white paint in order to reduce reflections, allowing the laser to take clearer measurements.

Figure 3.29 shows the plate mounted in-situ. The surface of the plate has been sprayed matte white in order to provide a non-reflective surface, as reflections can cause noise in the measurements. The plate is resting on a thick wadded material to protect from ground-borne vibrations and to provide a simply supported boundary condition, along with elasticated cords to hold the plate in position, emulating simply supported boundary conditions.

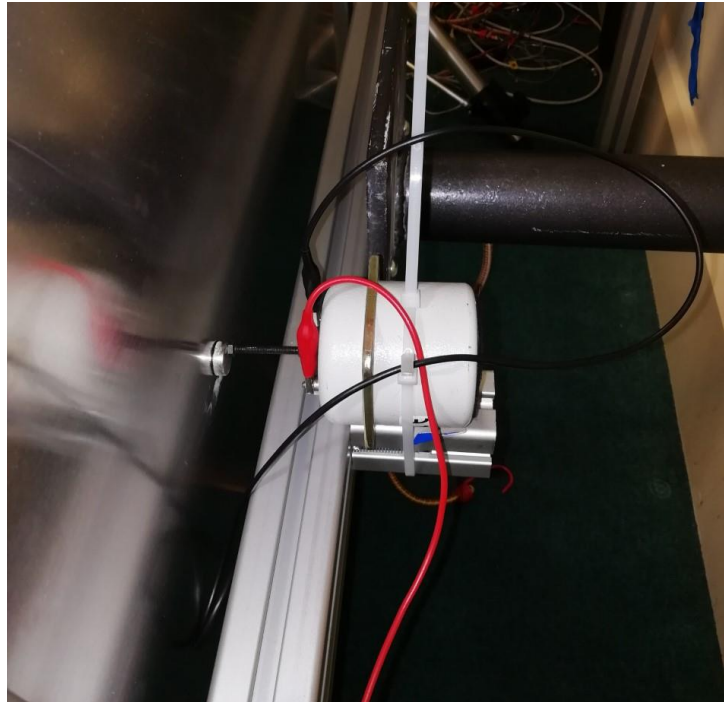


Figure 3.30: Shaker in-situ for measurement of plate.

The Bruel & Kjaer LDS V101 shaker was mounted on the plate 22 cm from the left edge and 49.5 cm from the bottom edge of the plate, as seen from the rear surface. A short stinger was used to translate the excitation and reduce shocks, with a small magnet used to keep the stinger in place, as shown in Figure 3.30.

The Scanning Laser Vibrometer (SLV) was used to collect data for 247 points, arranged in a 13x19 point grid of FRFs. This is the highest resolution of grid possible with the laser within the optimal range of distance from the plate surface. These are then built into a matrix of FRFs. The modes of the plate are picked out using the PP method, before the single transfer functions \bar{E} are extracted and evaluated. The associated modes in the columns of Ψ are shown for the individual transfer functions, before the original transfer function matrix is reduced from 13 to 6 rows, to observe how this affects the mode shapes and the \bar{E} functions. A further reduction is conducted, to 3 remaining rows, and the effects are observed.

3.3.4 Anechoic Chamber Experiment

As one of the aims of the thesis is to investigate the method for application in scenarios with relatively sparse accelerometer arrays for the measurement of vibration, a larger scale experiment was conducted in an anechoic chamber using a sparsely sampled plate. Further to this, the experiment was conducted in order to investigate the use of the volume velocity source for capturing FRFs, which were then compared to the equivalent transfer functions measured using an impact hammer.

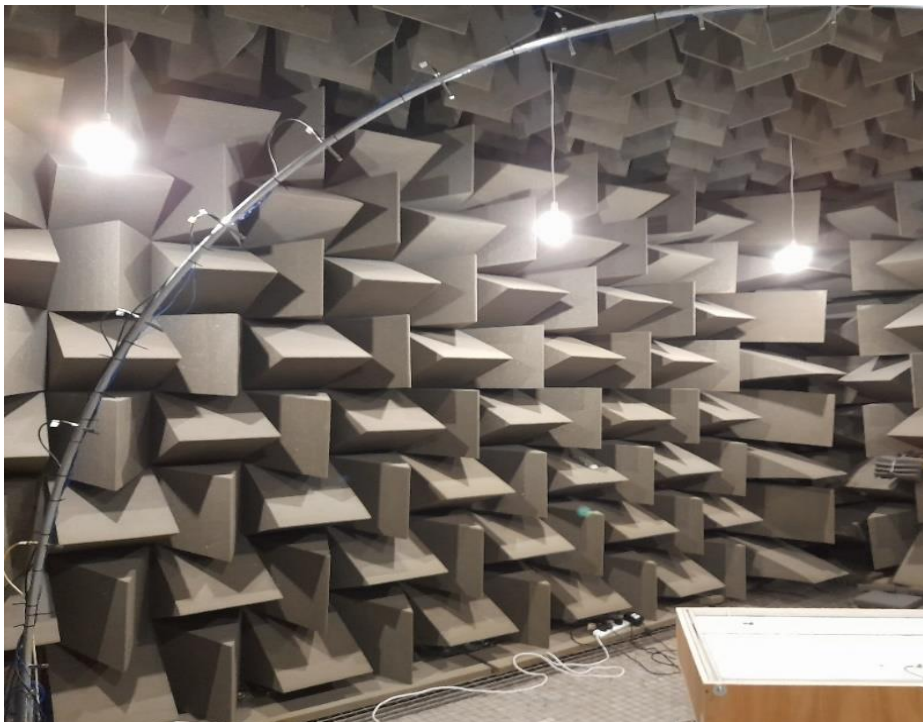


Figure 3.31: Baffled plate installed in an anechoic chamber. An array of response microphones are arranged on an arc-shaped frame, allowing for the collection of frequency response functions and measured transfer functions at multiple degrees of radiation from the plate.

Conducted in anechoic chamber with a temperature stable around 21°C, an array of microphones at 0°, 10°, 30°, 50°, 60°, 70°, 80°, 90°, mounted on a metal arc, were used to measure the directivity of the radiated sound of a plate loaded with 2 small vibrating shakers, as seen above in Figure 3.31.

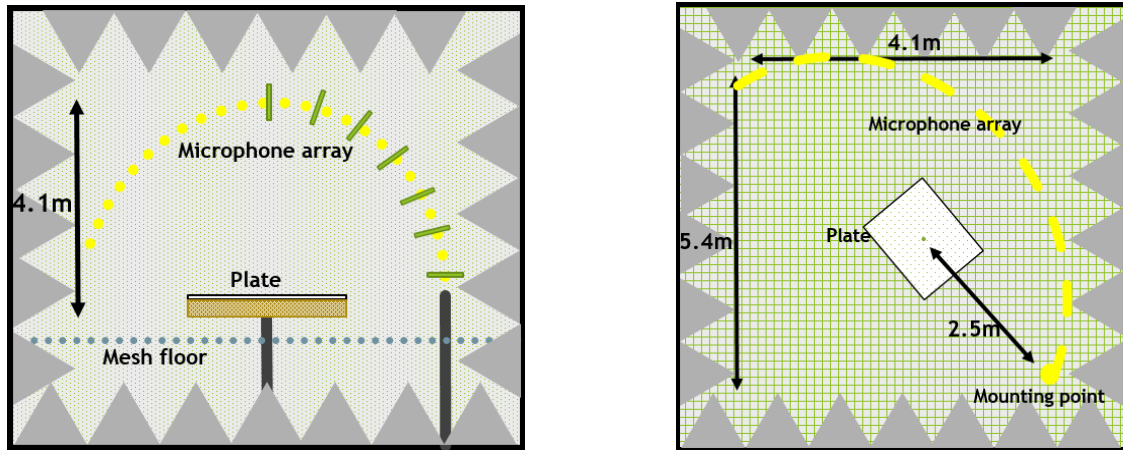


Figure 3.32: Schematic diagrams of the plate in the anechoic chamber: on the left, a view from the side, and on the right; a view from above.

Figure 3.32 shows the layout and position of the test set up in the anechoic chamber, with the left frame showing a schematic view from the side, and the right frame showing a schematic layout from above. Eight condenser microphones were arranged in an arc above the plate, capturing multiple radiation angles. The plate was rotated about its x-axis at angles of 0° , 45° , and 90° .

The same plate used for the laser mode shapes experiment, an aluminium plate of dimensions 900mm x 700mm, with a thickness of 2.5mm, was used in this experiment. The plate is again mounted in a frame with soft foam coating the contacting surfaces in the frame, emulating simply supported boundary conditions.



Figure 3.33: Interior of plate baffle showing acoustic foam

In order to maintain the integrity of the radiated sound received at the microphone positions from the surface of the plate, a wooden baffle 21cm deep was used to enclose the back, mitigating spill from the shakers mounted on the rear side. This baffle was lined with acoustic foam as seen in Figure 3.33, in an attempt to reduce reflection from the baffle internally back to the plate.



Figure 3.34: Rear side of plate showing damping application

Damping in the form of non-rigid vinyl panels were mounted on the underside of the plate, shown in Figure 3.34. This was added due to considerable overlapping and degenerate modes apparent in the plate from the scanning laser vibrometer experiment, with the intention to increase the separation of modes in the anechoic chamber experiment.

Two unbranded 4 Ω , 25 Watt shakers were used to excite the plate with white noise and pink noise. As viewed from the rear or underside of the plate, Shaker 1 was located 33cm from the top and 18 cm from the left edge, and shaker 2 23.5 cm from the bottom and 14cm from the right edge shown in Figure 3.35:

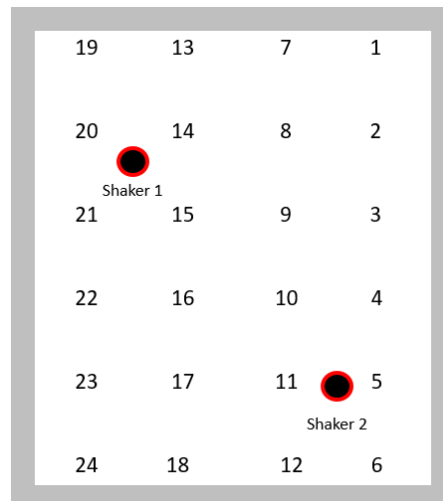


Figure 3.35: Schematic diagram of the plate, shown from the rear, where the number grid denotes accelerometer positions. Two shakers are mounted on the plate, and a reference accelerometer is mounted on the other side of the plate where each shaker is attached as a further reference quantity.

The plate had been discretised into a grid of 24 accelerometers, as seen in Figure 3.35, which are used to measure accelerations on the plate. Using an instrumented force hammer, the vibro-acoustic FRFs are collected for construction into a mobility matrix for the characterisation of the surface of the plate. A plastic hammer tip was used for these measurements, due to the accelerometers overloading in previous experiments using the plate. References were measured in the form of force transducers mounted between each shaker and the plate, and a voltage reference was taken from the excitation source, which drove the shakers with white and pink noise. An accelerometer was also attached to the plate at each shaker position to allow a direct acceleration measurement from each shaker. When the shakers are operational, a vector of transfer functions between the accelerometers and

each shaker is constructed, using the force transducers mounted between the shaker and the plate, and the further reference taken from the input voltage to the shakers.

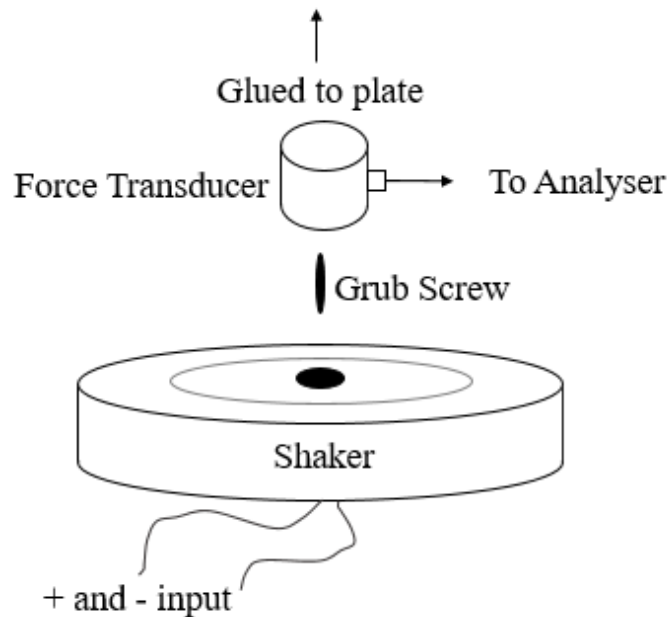


Figure 3.36: Schematic diagram of shaker. The shaker is rated as 4Ω , 25W, and is powered by a signal generator running through an amplifier. The shaker has been slightly modified, with the original coupling plate removed for a force transducer to be attached instead. A small grub screw is used to attach the shaker to a force transducer, which has an output to the analyser system. The face of the force transducer is superglued to the plate.

Both shakers used are 4Ω impedance, 25W power shakers with an iron coil, essentially like a small loudspeaker, as shown in Figure 3.36. The shaker input of white noise came from a signal generator, input through an amplifier, and connected to the shaker input wires. The original coupling face of the shaker was removed to allow a grub screw to be used to attach the shaker to a force transducer. The force transducer was then attached to the plate using superglue, with an M3 coaxial cable output to the side of the force transducer for connection

to the analyser. The transfer functions measured are H2, with acceleration due to voltage, and acceleration due to force, which is standard for noise sources such as shakers.

The data from this experiment is used in chapters 7 and 8. Chapter 7 uses the measurements to compare the prediction of radiated noise using the in-situ blocked forces approach [19] for a direct impact hammer measurement of the vibro-acoustic FRF to the prediction using the reciprocal vibro-acoustic FRF measured using the volume velocity source. Chapter 8 will detail the outcome of using the LvF of SVD for the construction of \bar{E} transfer functions, built by decomposing the volume velocity source FRFs to determine the contribution of radiation modes to radiated noise of the plate.

4 MODAL DECOMPOSITION METHOD USING SINGULAR VALUE DECOMPOSITION ON A BEAM MODEL

In order to explore how the \bar{E} transfer function, which is weighted to the modes by extracting and isolating a single singular value, is affected by measurement parameters, a beam model is used to investigate the properties of the LvF method to inform further experimental testing. Mode shapes produced in the columns of the Ψ matrix are compared to the mode shapes picked from the peaks using the PP method described in the literature review. Varying spatial sampling resolutions were looked at to find how the LvF method is affected for dense and sparse sensor arrays. This is done using the beam due to the distinct spacing of modes and the simplicity of the modal behaviour of beams compared to a plate. An Euler- Bernoulli beam model with free-free boundary conditions, made available at the University of Salford, was implemented in Matlab software [164]. The rotations of the beam were disregarded and only the bending modes observed. The model was then used to investigate different frequency ranges, response resolutions, and the effects of adding noise in order to determine the influence of these parameters on the resulting SVD outputs. As described in the theory, a matrix of velocities was analysed using the SVD algorithm: Y (input matrix) $=USV^T$ Peak Picking approach, and $Y = \Psi \Sigma \Phi^T$ for the LvF approach. This modelling exercise was used to inform a further test using a real beam, measured using a force hammer and accelerometers to obtain the real mobility. The beam model was matched to the realistic parameters of a real beam by tuning the variables used to construct the model. In this section, the LvF method is used to construct transfer functions containing details of a single mode. The reason for this case study using a modelled beam is that it is unconstrained by limitations of frequency range and spatial sampling, due to the nature of the accelerometers and other equipment, and represents an idealised circumstance in the first instance, to which alterations are made to

observe the effects of these changing parameters on the SVD outcomes. Many variations of the model were constructed, however the models shown here effectively portray the effects of spatial sampling on the output parameters of the SVD, informing the effect of spatial sampling on the construction and content of the \mathcal{E} single singular value transfer functions. Firstly, a 67 response position model is investigated, before a model with 17 response positions is detailed. The bending wavelengths of the modes in the beam, and the nodes of the modes (excluding the end points of the beam), are calculated using Equations (33,34).

Mode	λ_B (m)	Nodes
1	1.1	0.275
2	0.55	0.1833, 0.3667
3	0.367	0.1375, 0.275, 0.4125
4	0.275	0.11, 0.22, 0.33, 0.44
5	0.22	0.0917, 0.183, 0.275, 0.37, 0.46
6	0.18	0.079, 0.16, 0.24, 0.31, 0.39, 0.47
7	0.157	0.069, 0.14, 0.2, 0.28, 0.34, 0.41, 0.48
8	0.138	0.061, 0.12, 0.18, 0.24, 0.3, 0.36, 0.43, 0.49
9	0.122	0.055, 0.11, 0.165, 0.22, 0.275, 0.33, 0.385, 0.44, 0.495
10	0.11	0.05, 0.1, 0.15, 0.2, 0.25, 0.3, 0.35, 0.4, 0.45
11	0.1	0.046, 0.09, 0.14, 0.18, 0.23, 0.28, 0.38, 0.36, 0.41, 0.46, 0.5
12	0.09	0.04, 0.085, 0.13, 0.17, 0.2, 0.25, 0.3, 0.34, 0.38, 0.42, 0.47, 0.5
13	0.085	0.039, 0.078, 0.12, 0.157, 0.196, 0.2, 0.28, 0.31, 0.35, 0.39, 0.43, 0.47, 0.51
14	0.079	0.037, 0.073, 0.11, 0.15, 0.18, 0.22, 0.26, 0.29, 0.33, 0.37, 0.4, 0.44, 0.48, 0.51
15	0.072	0.034, 0.069, 0.103, 0.14, 0.17, 0.206, 0.24, 0.275, 0.309, 0.344, 0.378, 0.4125, 0.447, 0.481, 0.516

Table 4.1: mode number, bending wavelength, and node positions for the first 15 modes of the beam

There are the same amount of nodes as the mode number, as shown in Table 4.1. Considering the theory that 6-10 positions per wavelength is needed to give an accurate description of modes, with the peaks and troughs of the mode described using 2 elements, based on the sampling positions being accurately situated [76], there should be at least 10 modes accurately described in the 67 response position model.

4.1 67 Response Position Model

A beam model with 67 response positions at 0.0084m and frequency range of 20 kHz, with an excitation at the first position along the beam at 0m from the left end, is modelled. Firstly, the outcomes of the LvF SVD are shown and compared to matrices using a frequency by frequency SVD, as in the Peak Picking Approach.

4.1.1 SVD matrices of 67 response position model

Using the LvF SVD on the beam model, the three output matrices can be seen in terms of their relationship to modes. On the diagonal of Σ , the singular values σ align to give the weighting coefficient of each mode, or group of modes.

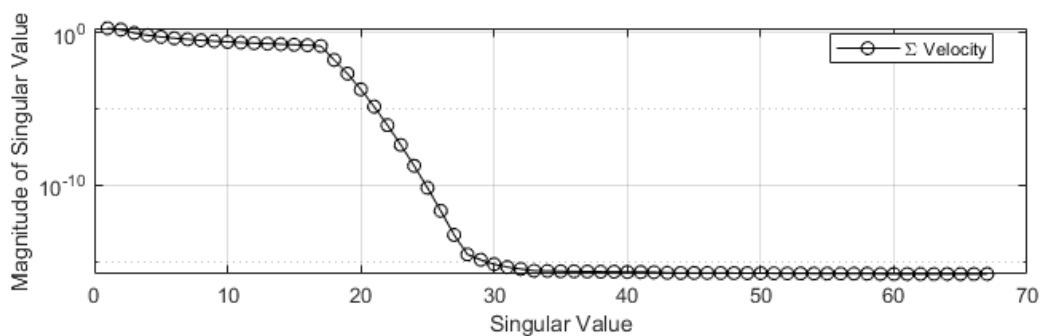


Figure 4.1: Diagonal of singular value matrix Σ . Each circle on the graph corresponds to a singular value ' σ ' for 67 response position model

Figure 4.1 shows the singular values σ in terms of magnitude, which are the elements on the diagonal of the Σ matrix. There are 17 singular values above a magnitude of 0.1, indicating there are 17 significant modes or groups of modes in the beam. The knee or drop-off observed suggests that the beam is sufficiently sampled to capture the significant modes.

In the case that the spatial sampling resolution is sufficient, each significant singular value corresponds to a mode.

The Φ matrix contains eigenvalues which correspond to the frequency response of each mode or group of modes described by the corresponding singular value and mode shape Ψ . This matrix is not used for the construction of transfer functions, but for illustrative purposes, the first 9 columns of Φ are shown below in Figure 4.2: Columns of Φ , representing temporal behaviour or frequency response, of modes 1 to 9, with respect to frequency from 10 Hz to 20 kHz in frame 1 to show the rigid body mode, and 100 Hz to 20 kHz

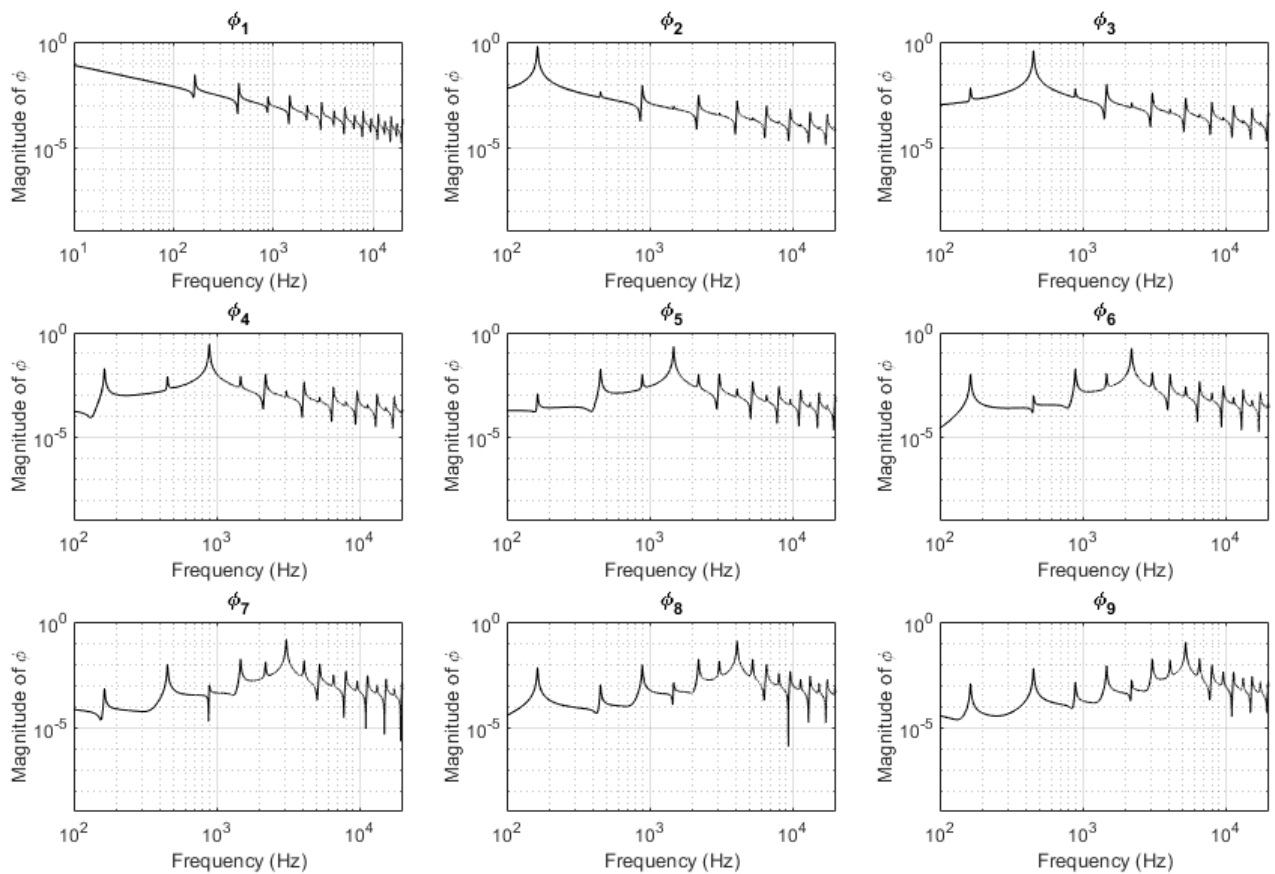


Figure 4.2: Columns of Φ , representing temporal behaviour or frequency response, of modes 1 to 9, with respect to frequency from 10 Hz to 20 kHz in frame 1 to show the rigid body mode, and 100 Hz to 20 kHz for the other frames, for 67 response position model.

Reading from left to right across, the top row of Figure 4.2 shows the first 3 columns of Φ , the second row columns 4 to 6, and the bottom row columns 7 to 9. As the beam has free-free boundary conditions, the first mode, the rigid body mode, has a frequency of 0 Hz [165]. The response of this mode is shown in frame 1. Moving through the frames of Figure 4.2, the peaks move up in frequency and correspond to the resonances of the beam.

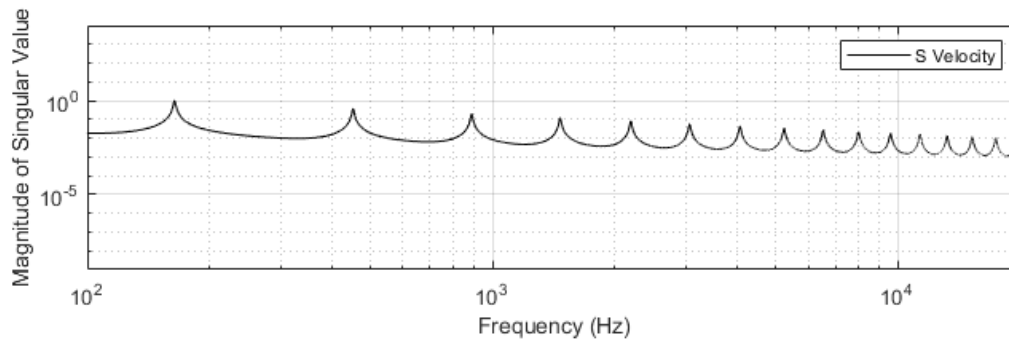


Figure 4.3: Singular value from PP method, showing mode frequencies at peaks for 67 response position model.

Figure 4.3 shows the diagonal of the S matrix, from the PP method SVD. The peaks correspond to the modes of the beam, and the frequencies are picked out of the FRF matrix in order to compare the mode shapes to those of the columns of Ψ :

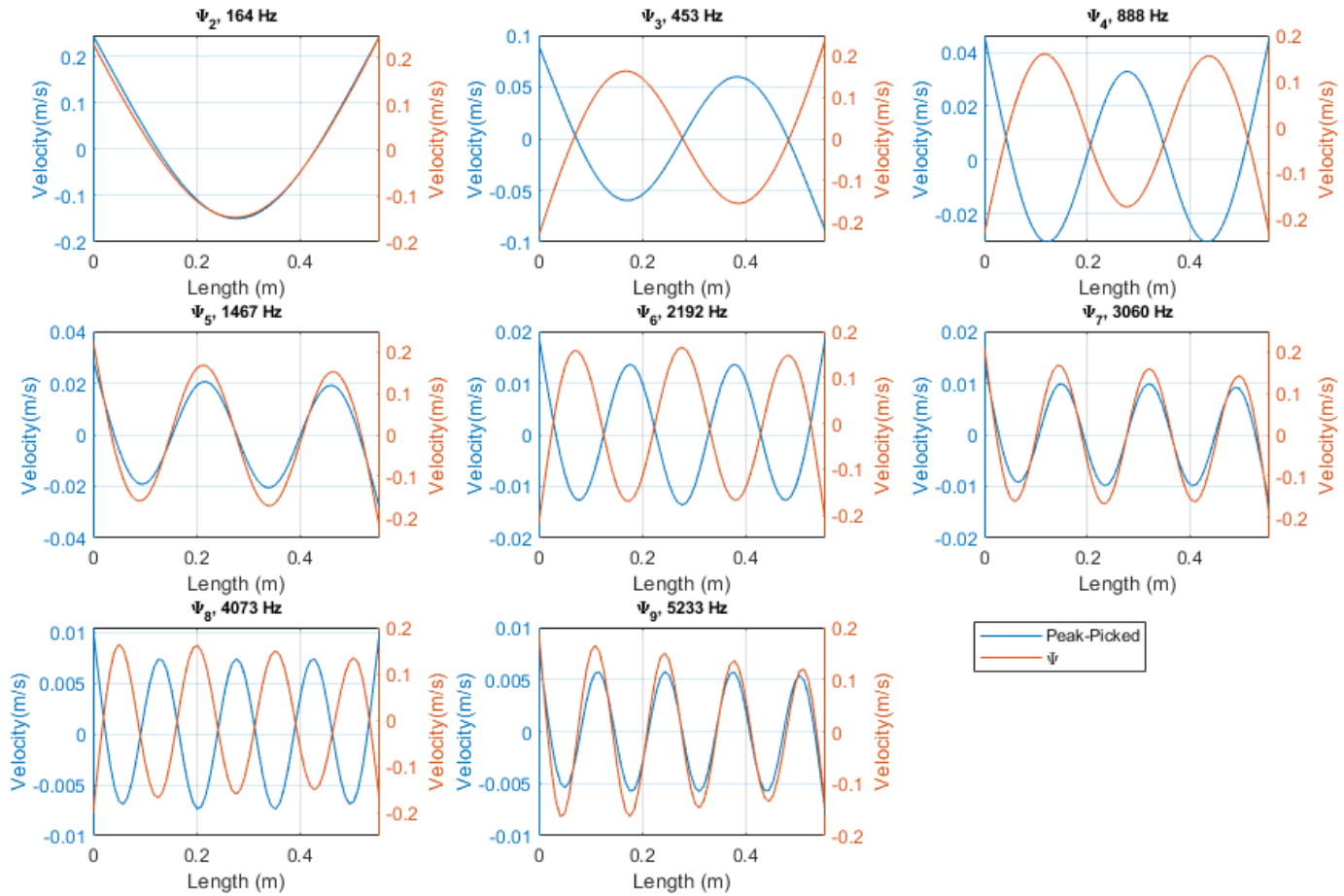


Figure 4.4: Mode shapes ψ 2-9 from the columns of Ψ are shown in red, compared to the modes peak picked from the diagonal of S , shown in blue. The x-axis is the length of the beam from 0m to 0.555m, and the two y-axes are velocity.

Neglecting ψ_1 , which corresponds to the rigid mode at 0 Hz, the columns of Ψ can be seen to correspond to the mode shapes of the beam from the peak picked from the diagonal of the S matrix, shown in Figure 4.4. There are separate left and right y-axes, as the two methods produce mode shapes of different magnitudes. This is due to the fact that the singular values of the Σ matrix provide the weighting coefficients to the modes of Ψ , and these mode shapes are therefore scaled differently to the FRFs of the beam. The mode shapes can be compared to determine they are of the same order. Frame 1, showing ψ_2 and the mode at 164 Hz shows almost exact agreement, with negligible difference. Frames, 4, 6, and 8 clearly show the same modes, with a slight disagreement in the dynamic range, as they are not aligned at the

peaks. Frames 2, 3, 5, and 7 show the same modes but in anti-phase. The order of modes, that is how many peaks and troughs are present, agrees for each of the modes. This suggests that the spatial sampling is sufficient to characterise these modes of the beam.

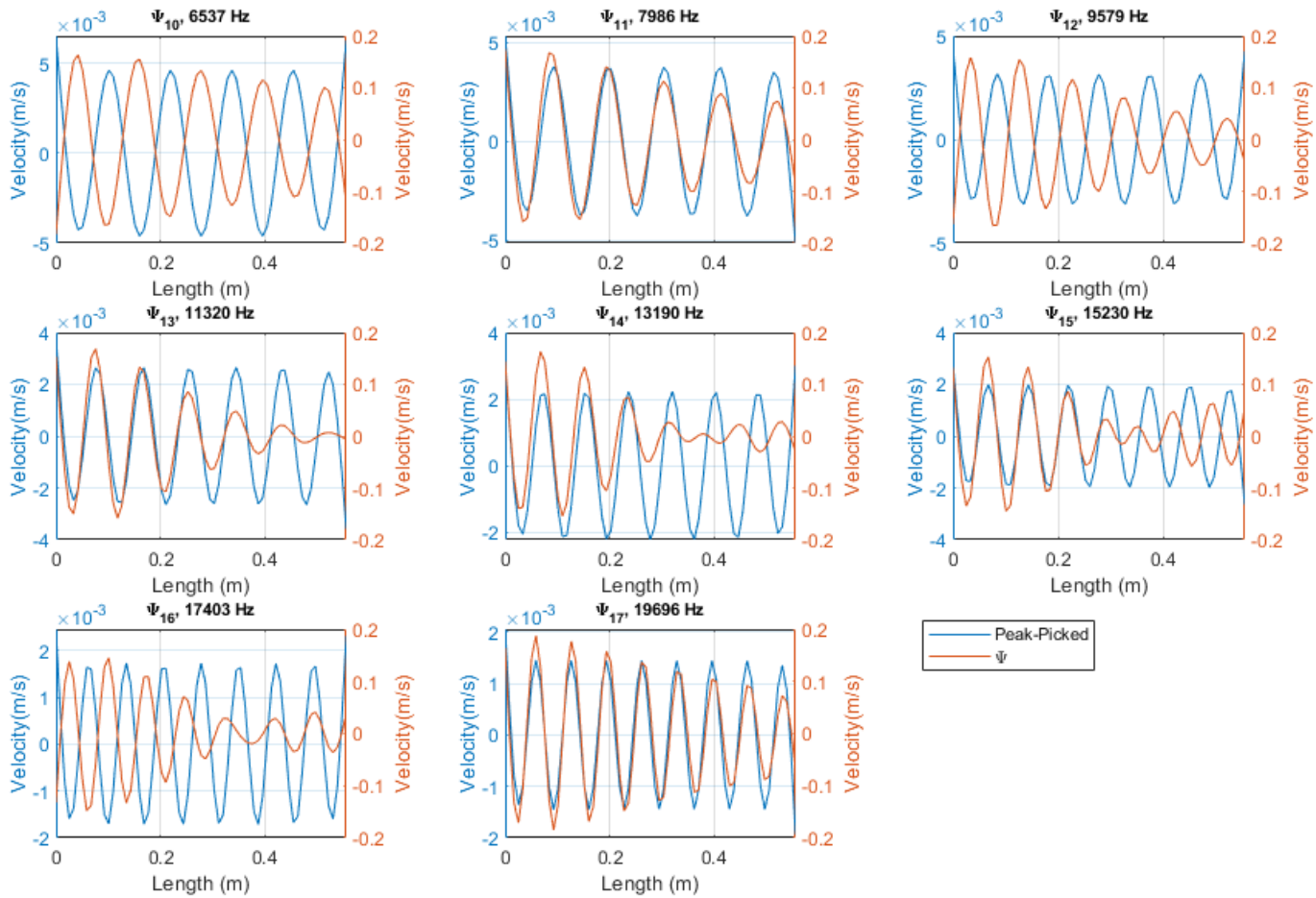


Figure 4.5: Mode shapes ψ 10-17 from the columns of Ψ are shown in red, compared to the modes peak picked from the diagonal of S , shown in blue. The x-axis is the length of the beam from 0m to 0.555m, and the two y-axes are velocity.

The next group of modes, leading to the upper frequency limit of 20 kHz, are shown in Figure 4.5. The modes again are of the same order, however a decay in the mode shapes of Ψ can be observed in terms of length across the beam. However, the peaks and troughs are accurately represented, as the spatial sampling is sufficient, the highest mode characterised having 8 full cycles in the beam. With the highest mode being characterised with 8 sampling positions per wavelength, this is to be expected. To the left hand side of the plots, where the

force is input, the magnitude is higher for the modes of Ψ . This is again likely due to the lack of scaling due to the absence of the singular value. In the FRF trace, the mode shape is made up of all three matrices, rendering the actual mode response, whereas for the Ψ modes shapes only the eigenfunctions are present.

4.1.2 67 response position Ξ transfer functions

The singular values can be isolated by repeatedly performing an SVD and discarding all but one singular value, before reconstructing the FRFs Ξ_i containing one singular value, for each of the 67 values. This results in 67 Ξ , each containing only one singular value: the first transfer function Ξ_1 contains only the first singular value; the second Ξ_2 contains only the second singular value; et cetera. This weights the transfer functions to the individual modes of the beam when spatial sampling is sufficient. Presented below are these beam models, compared to the original model containing all singular values:

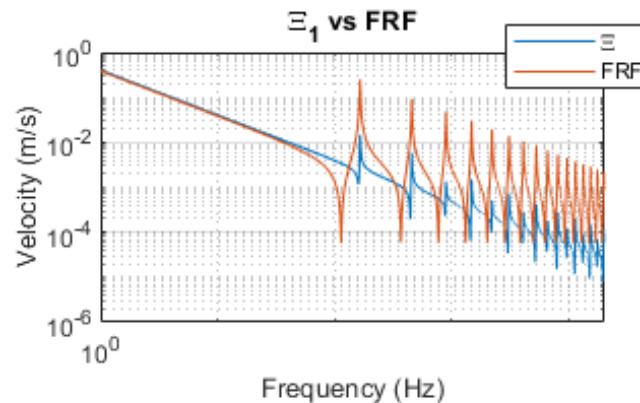


Figure 4.6: Single singular value transfer function Ξ_1 plotted against full FRF for 67 response position, 20 kHz range beam model. Shown in red is the original FRF and shown in blue is the isolated singular value transfer function. The x-axis is between 1 Hz and 20 kHz, as the rigid body mode is below 100 Hz.

The first singular value Ξ_1 aligns perfectly with the rigid body mode of the FRF, with some small amounts of detail present at the resonant peaks moving up in frequency, which can be seen in Figure 4.6. As the rigid body mode starts at 0 Hz, this is seen separately to the other

transfer functions, which are observed over a range from 100 Hz to 20 kHz in Figure 4.7 and

Figure 4.8:

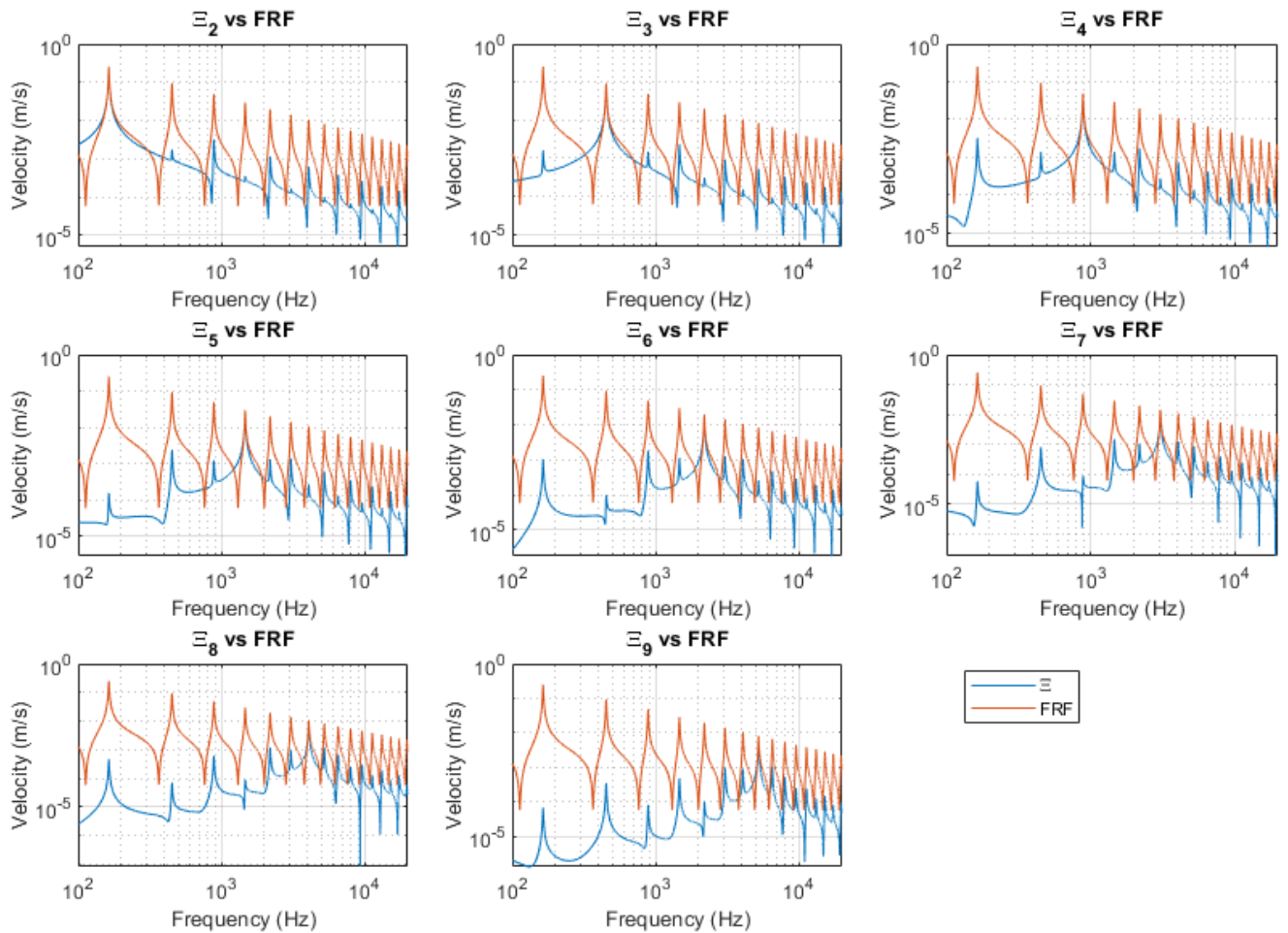


Figure 4.7 Reading from left to right, single singular value transfer functions Ξ_2 to Ξ_9 plotted against full FRF for 67 response position, 20 kHz range beam model. Shown in red is the original FRF and shown in blue is the isolated singular value model. The x-axis is between 100 Hz and 20 kHz.

As to be expected for a sufficiently sampled beam, the resonances of the original FRF are met by resonances in the Ξ transfer function, going up in order through the frames of Figure 4.7 from mode 2 to mode 9. With reference to the rigid body mode being mode 1, and Ξ_1 in alignment, Ξ_2 aligns with the mode 2 of the beam, and so on. These transfer functions contain the contribution to the overall FRF from each of the modes described.

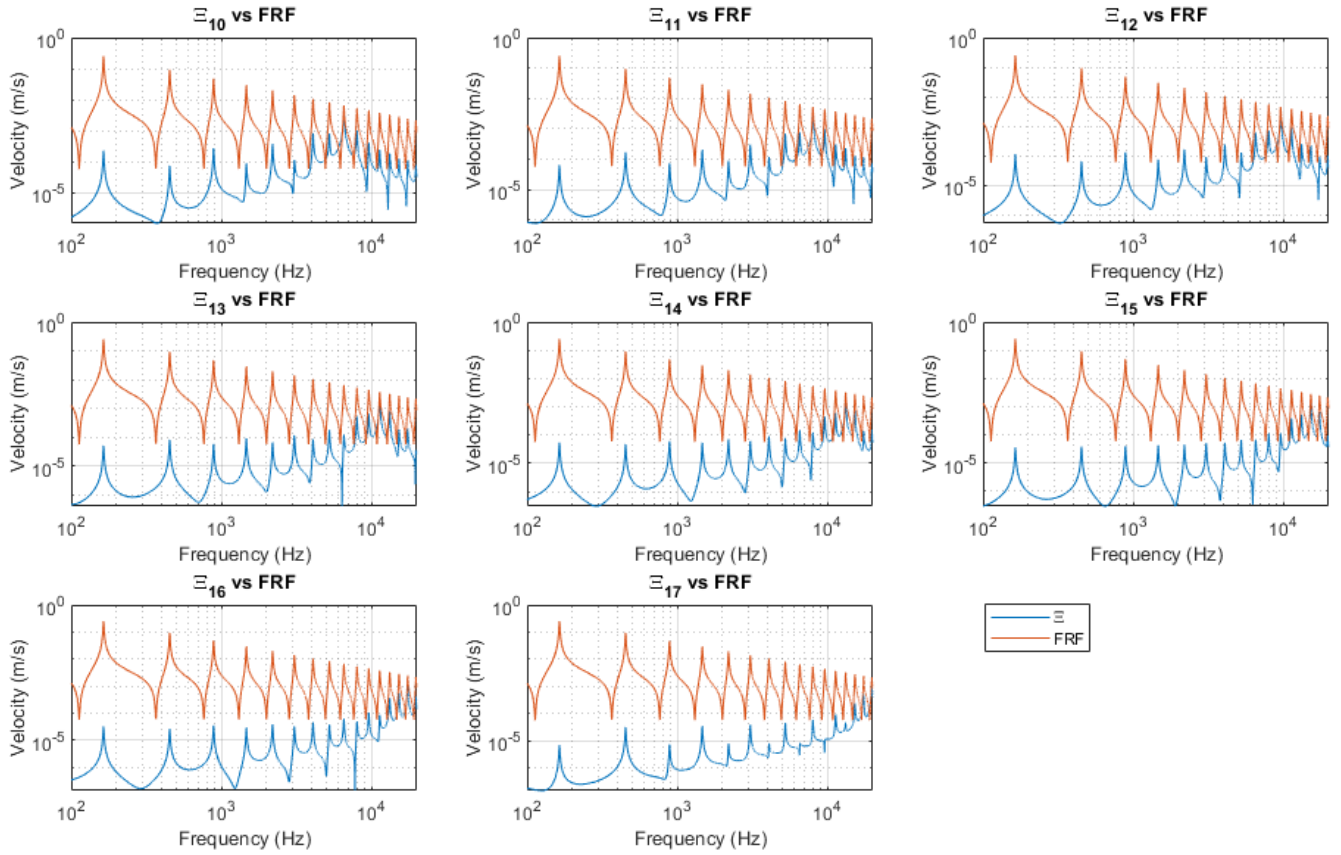


Figure 4.8: Reading from left to right, single singular value transfer functions Ξ_{10} to Ξ_{18} plotted against full FRF for 67 response position, 20 kHz range beam model. Shown in red is the original FRF and shown in blue is the isolated singular value model. The x-axis is between 100 Hz and 20 kHz.

Moving up through the modes, Ξ_{10} to Ξ_{17} are shown in Figure 4.8. The same pattern is seen, with each resonance of the Ξ lining up successively with the resonances of the original beam FRF.

All of the modes within the covered frequency range have now been described by singular values, and as seen in Figure 4.1, the singular values now drop significantly in magnitude after the 17th value. Continuing up through the singular values, the effect of this drop in magnitude can be seen in the further Ξ transfer functions:

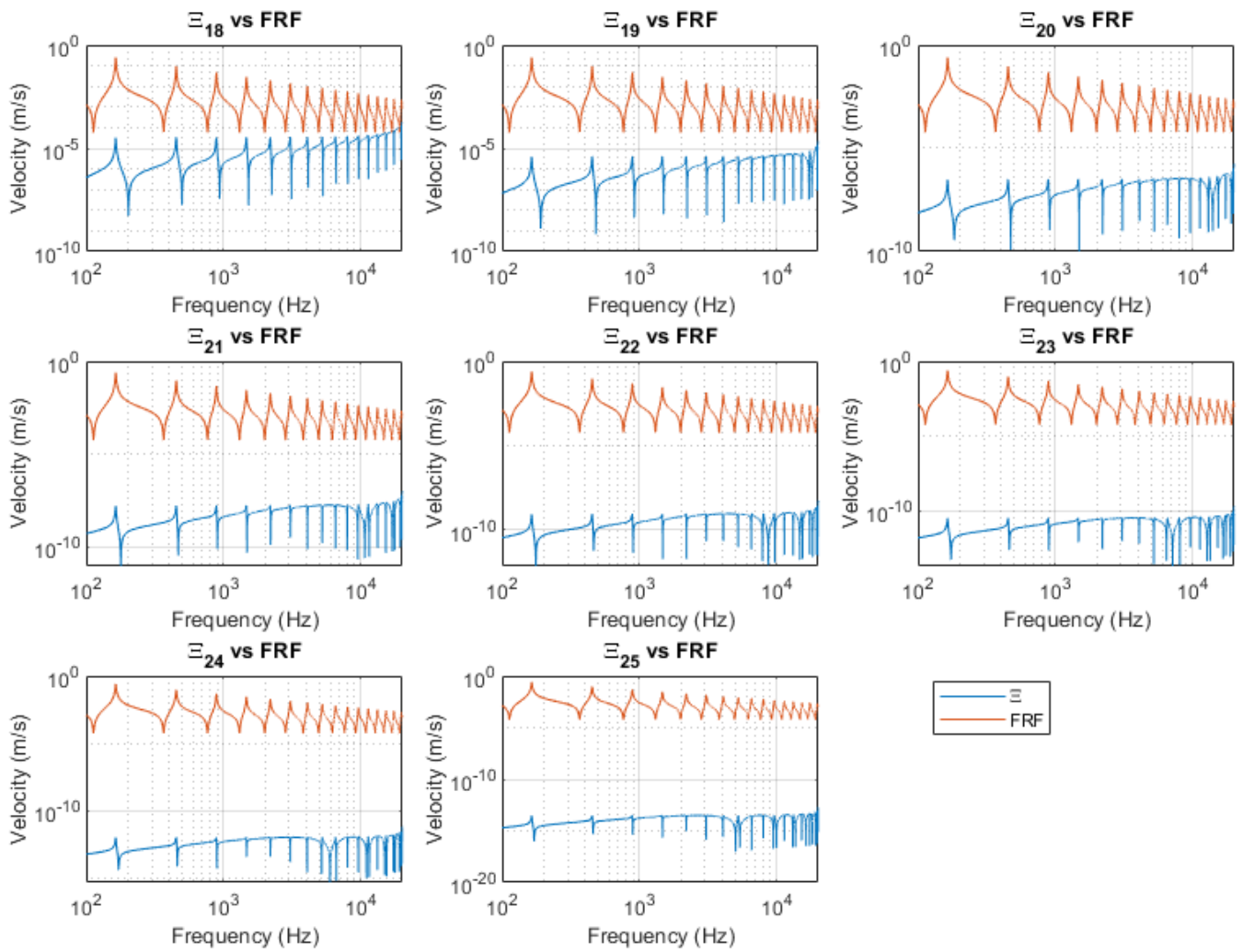


Figure 4.9: Reading from left to right, single singular value transfer functions Ξ_{18} to Ξ_{25} plotted against full FRF for 67 response position, 20 kHz range beam model. Shown in red is the original FRF and shown in blue is the isolated singular value model. The x-axis is between 100 Hz and 20 kHz.

The first frame of Figure 4.9 shows that Ξ_{18} ends the pattern of peaks aligning with modes, with the subsequent plots showing a continual drop in magnitude away from the original FRF. This indicates that from the 18th singular value, Ξ_{18} , onwards, there is little modal information present.

Summing the first 17 Ξ and plotting the FRF results in an accurate reconstruction of the FRF:

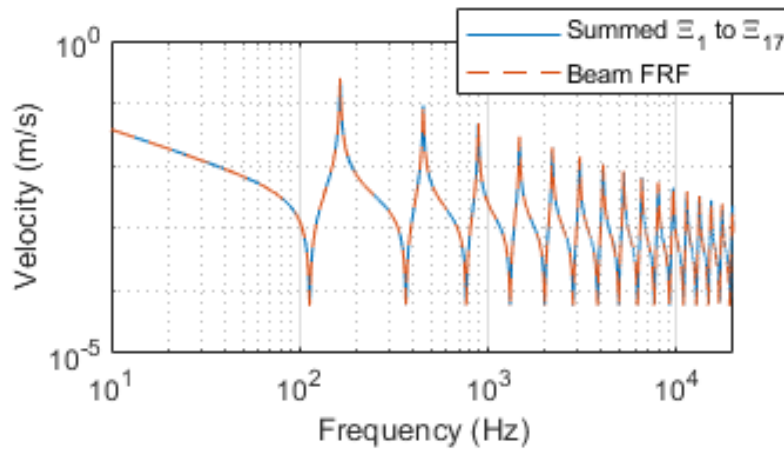


Figure 4.10: Reconstructed FRF built by adding Ξ_{1-17} versus the complete model FRF for 67 response positions and a frequency range of 20 kHz. Shown in the solid line is the original model FRF and shown in the dashed red line is the reconstructed Ξ FRF.

Complete alignment can be seen between the summation of the Ξ functions and the original, full singular value model in Figure 4.10. This implies that no information has been lost by neglecting to include the singular values beyond the first 17. Continuing from this densely sampled beam model, and inspired by the dominance of the first 17 singular values, a model is next investigated using 17 response positions.

4.2 17 response Position Model

As the 67 response position beam model indicates that the first 17 singular values are significant and contain modal information, a model with 17 response positions is investigated. The responses are spaced at 0.036m along the beam, with a simulated force input at the first position, at the left end of the beam, as with the 67 position beam.

4.2.1 SVD matrices of 17 response position model

As with the 67 response position model, the singular values are observed.

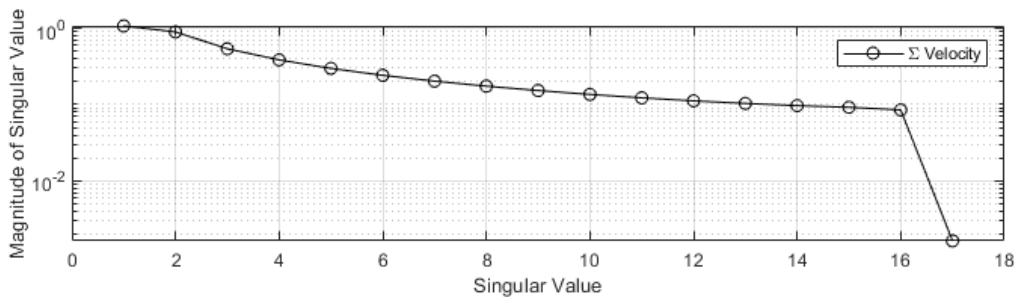


Figure 4.11: Diagonal of singular value matrix Σ . Each circle on the graph corresponds to a singular value ' σ ' for 17 response position model.

Figure 4.11 shows the singular values on the diagonal of matrix Σ . When compared to the singular values of the 67 response position model shown in Figure 4.1, the singular values are all of a similar magnitude, with no distinctive knee or drop off present, until the 17th element, which falls significantly in magnitude. This could indicate that the beam is under-sampled with respect to the modelled frequency range, as the presence of a significant drop in singular values, with many values much lower magnitude than the those of the highest magnitude, indicates sufficient or oversampling for the description of modes [76].

The modes of the beam can be observed in the diagonal of the S matrix, using the frequency by frequency SVD for the PP method:

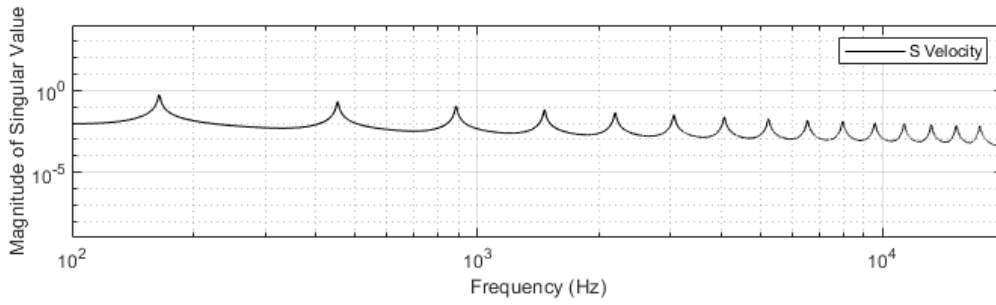


Figure 4.12: Singular value from PP method, showing mode frequencies at peaks for 17 response position model.

As to be expected, performing the frequency by frequency SVD on the 17 response position model, shown in Figure 4.12, conveys the same modal resonances present in the S matrix for the 67 response position model, shown in Figure 4.3.

The mode shapes of Ψ are examined next. As with the 67 response position model, the rigid body mode is present in the first column of Ψ :

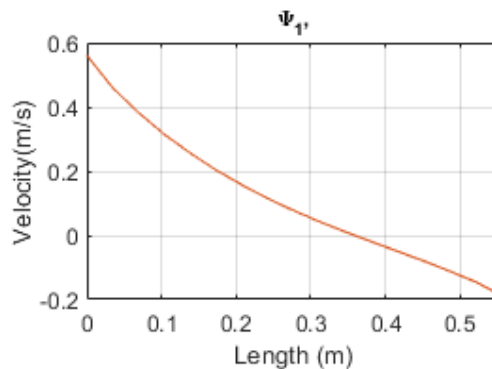


Figure 4.13: First column of Ψ , showing rigid body mode of beam in terms of velocity with respect to length

As with the 67 response position model, the rigid body mode is present in the first column of Ψ , as shown by Figure 4.13. The following columns of Ψ are compared to the beam modes present in the peaks of the S matrix:

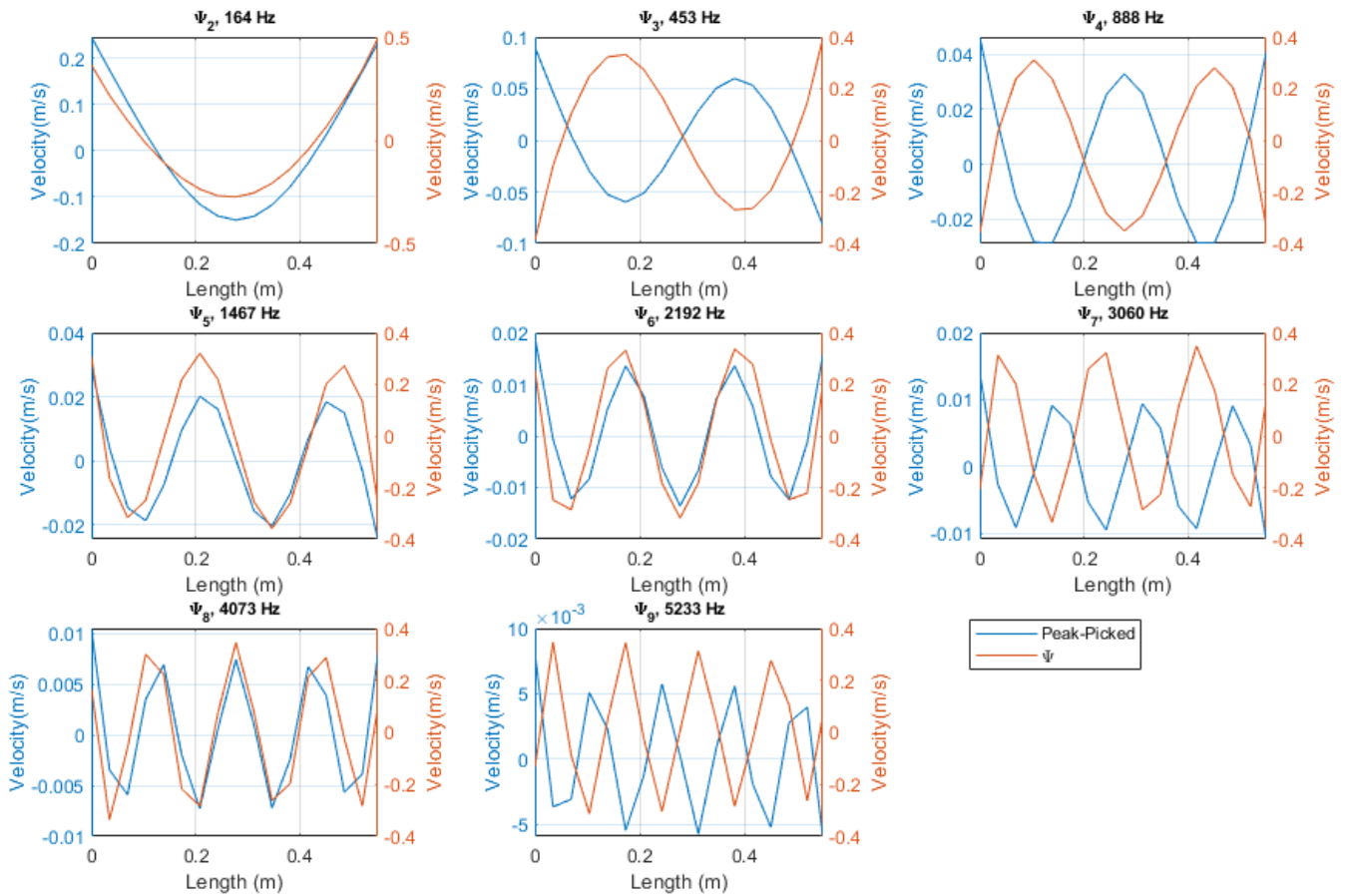


Figure 4.14: Mode shapes ψ 2-9 from the columns of Ψ are shown in red, compared to the modes peak picked from the diagonal of S , shown in blue. The x-axis is the length of the beam from 0m to 0.555m, and the two y-axes are velocity.

When compared to the mode shapes in the columns of Ψ produced by the 67 response position model, there are significant differences seen for the 17 response position model. Figure 4.14 compares the 2nd – 9th columns of Ψ to the modes of the beam corresponding to the peaks present in S shown in Figure 4.12. When compared to the columns of Ψ for the 67 response position model shown in Figure 4.4, ψ_2 shown in the first frame has an exaggerated misalignment in terms of a shift in position and a lack of agreement at the peak. The mode picked from the velocity of the beam shows the extremity of the trough halfway along the beam, as would be expected for the 2nd mode, whereas the mode described by Ψ appears slightly shifted along the beam, with a slightly wider width. The 3rd and 4th modes appear very much the same, with the 3rd Ψ mode having a slightly larger magnitude than seen in the

67 position model. From the 4th mode, the shapes start to become angular for both the peak picked modes and the Ψ modes, indicating that the sampling resolution is becoming insufficient to describe the modes. This is due to the sensors being too far apart to include the curvature detail of the modes, whilst still being able to describe the peaks and troughs.

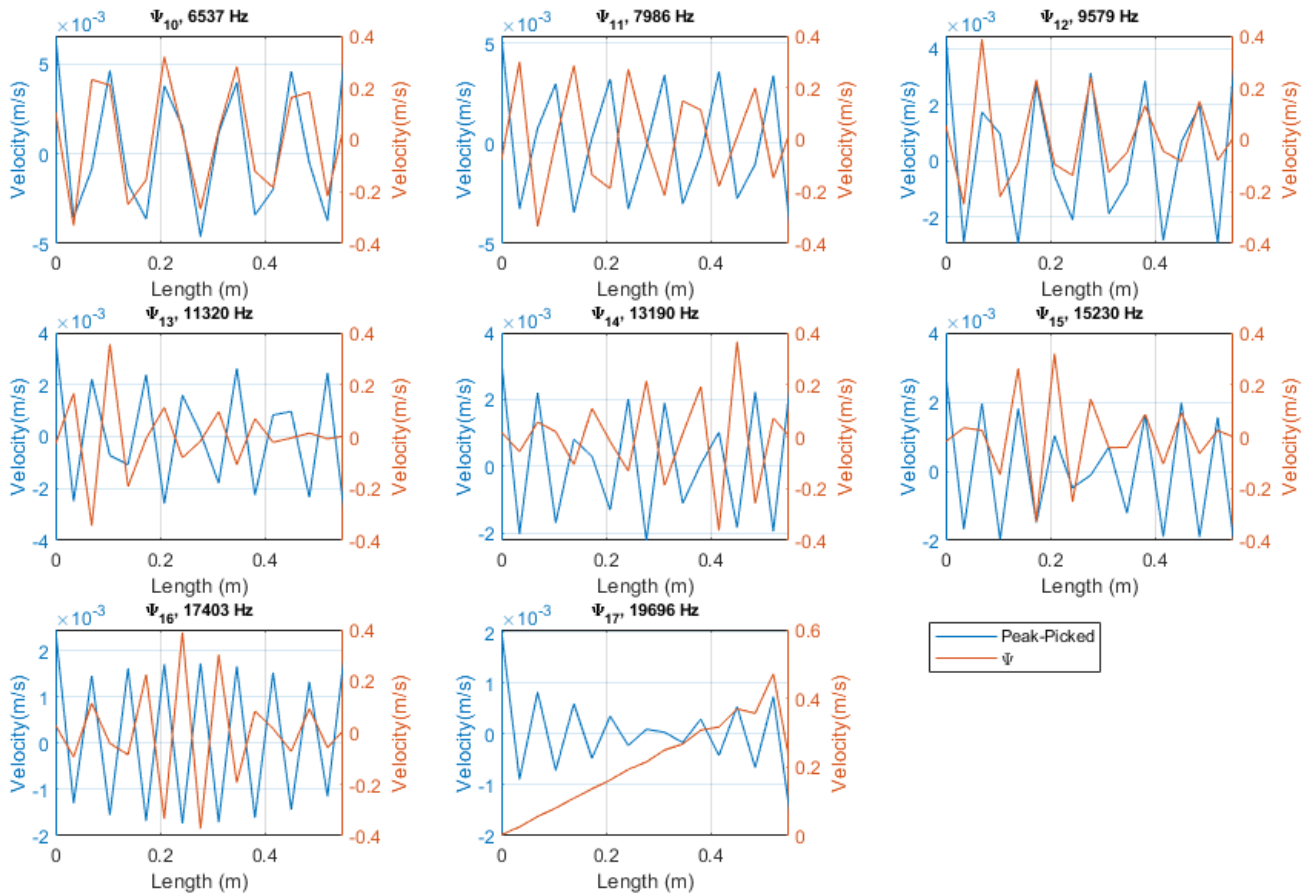


Figure 4.15: Mode shapes ψ 10-17 from the columns of Ψ are shown in red, compared to the modes peak picked from the diagonal of S , shown in blue. The x-axis is the length of the beam from 0m to 0.555m, and the two y-axes are velocity.

Continuing up through frequency, Figure 4.15 shows that the mode shapes continue to become more angular, becoming completely disturbed by the 17th Ψ mode. The 10th, 11th, and 12th Ψ modes show some degree of similarity to the peak picked modes, then from the 13th mode onwards there is no agreement, with the peak picked modes no longer resembling modes. The beam is under-sampled to describe the modes above 10 kHz. The last mode

shape which could reasonably be interpreted as a mode is at 6537 Hz, with 4 cycles in the beam, giving 4.25 spatial samples per bending wavelength.

4.2.2 17 Response Position Ξ Transfer Functions

As with the 67 response position model, the singular values are isolated by repeatedly performing an SVD and discarding all but one singular value, before reconstructing the FRFs Ξ_i containing one singular value, for each of the 17 values.

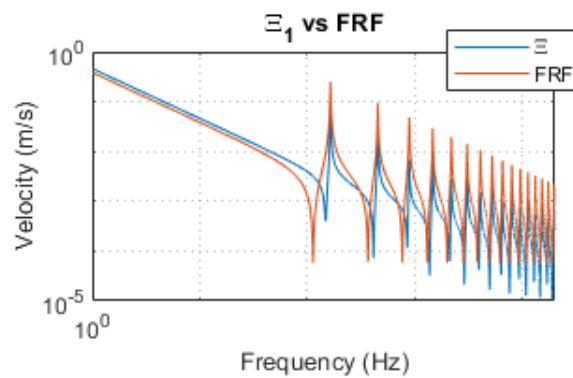


Figure 4.16: Single singular value transfer function Ξ_1 plotted against full FRF for 17 response position, 20 kHz range beam model. Shown in red is the original FRF and shown in blue is the isolated singular value transfer function. The x-axis is between 1 Hz and 20 kHz, as the rigid body mode is below 100 Hz.

As with the 67 response position model, Ξ_1 aligns with the rigid body mode of the beam, as seen in Figure 4.16. When compared to the 67 response position model rigid body mode transfer function shown in Figure 4.6, there is a slight disagreement to the original beam FRF. The peaks of the resonances going up in frequency have a higher magnitude in Ξ_1 when compared to the 67 position model. Overall, the 17 position Ξ model resembles the original beam FRF far more closely than the 67 position model, indicating that each of the singular values contain information about a higher number of modes.

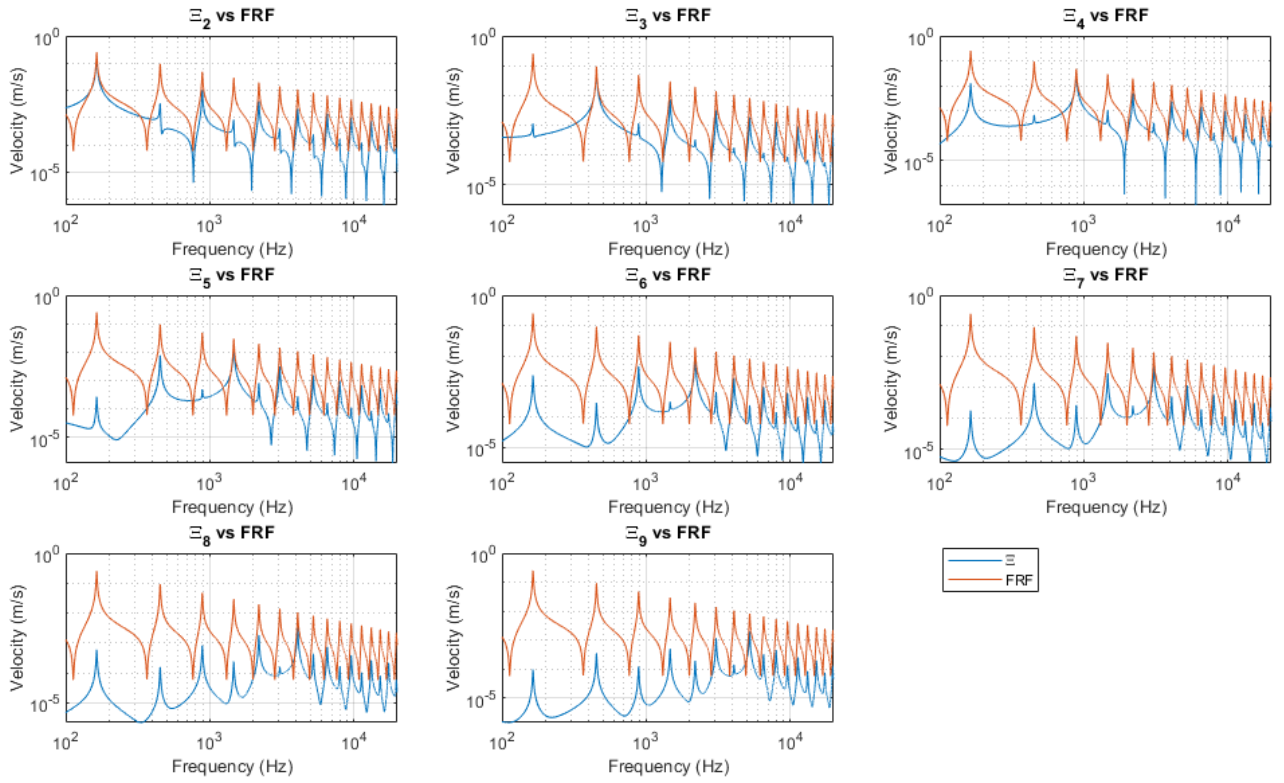


Figure 4.17: Reading from left to right, single singular value models Ξ_{2-9} plotted against full FRF for 17 response position, 20 kHz range beam model. Shown in red is the original FRF and shown in blue is the isolated singular value transfer function.

As determined by Figure 4.16, Figure 4.17 reinforces that there is more than one mode associated with each Ξ_i transfer function. However, the resonances are described in order of frequency moving up through the frequency range. The first resonance is described by Ξ_2 , the second resonance is shown by Ξ_3 and this continues, albeit with other resonances present.

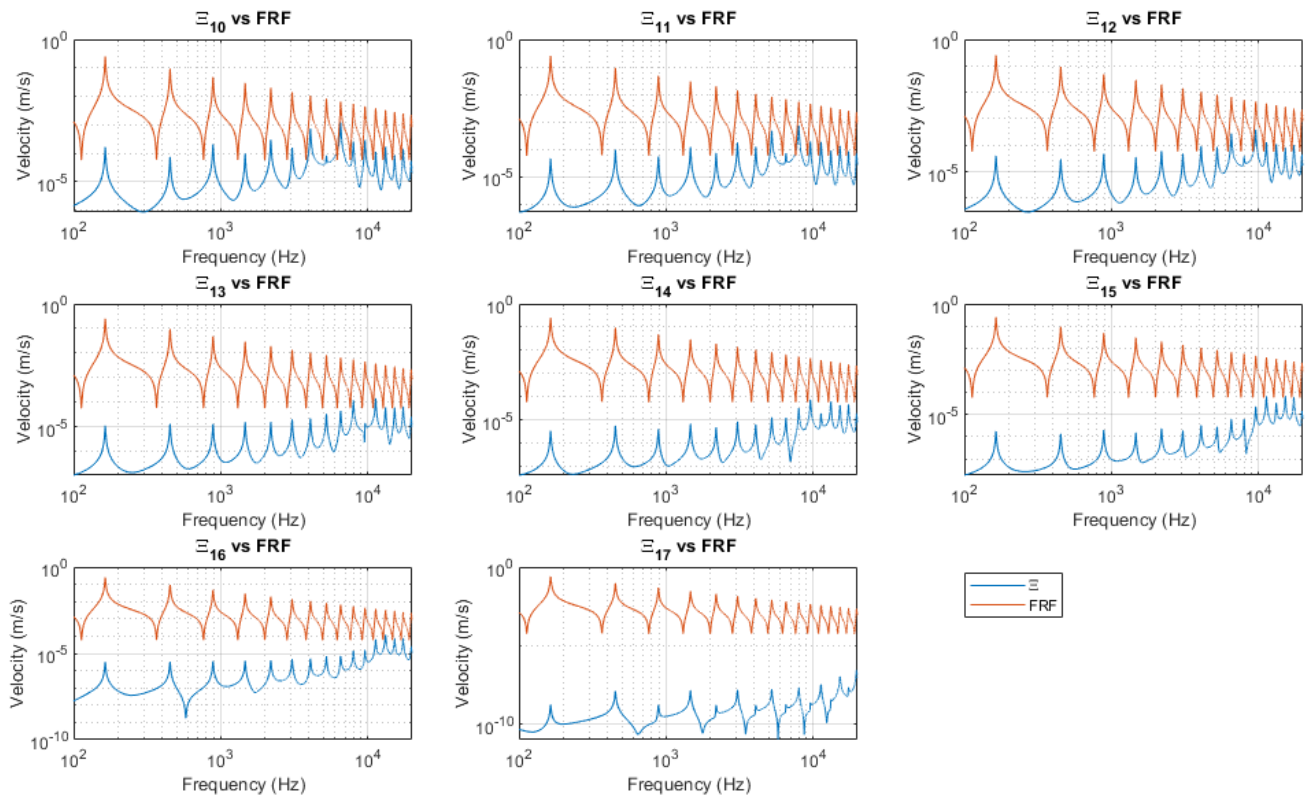


Figure 4.18: Reading from left to right, single singular value models Ξ_{10-17} plotted against full FRF for 17 response position, 20 kHz range beam model. Shown in red is the original FRF and shown in blue is the isolated singular value transfer function.

Shown in Figure 4.18 are the 10th to 17th Ξ transfer functions. Continuing up through the resonances, the Ξ transfer functions decline in magnitude far before the Ξ transfer functions for the 67 response position model. By Ξ_{14} , there is no overlap between the FRF and the single singular value transfer function. This implies that from the 14th singular value, modes are no longer being described.

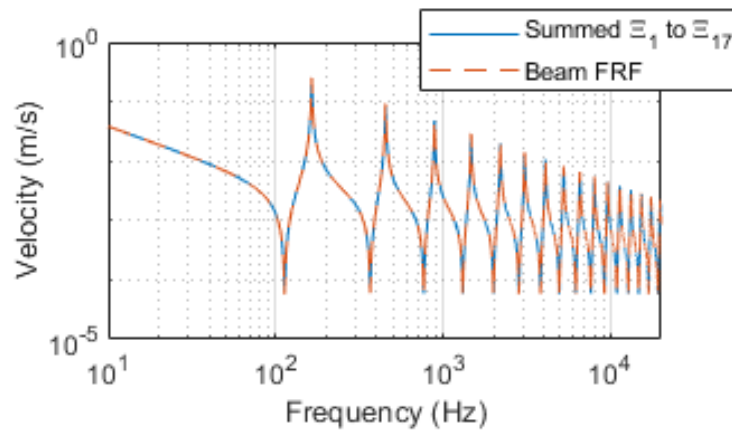


Figure 4.19: Reconstructed FRF using the all 17 singular value Ξ_i models versus the complete model FRF for 17 response positions and a frequency range of 20 kHz. Shown in the solid line is the original model FRF and shown in the dashed red line is the reconstructed FRF.

Shown in Figure 4.19, all of the Ξ_i transfer functions are needed to reconstruct the FRF, whereas in the 67 position beam model, only the first 17 were needed. Some information is retained even in Ξ_{17} , which does not appear to contain any useful information in the plots of Ξ compared to the original beam FRF, but must contain some magnitude information when related to the other Ξ_i functions.

4.3 Discussion

A method for isolating the modal contributions to an FRF was investigated using a beam model, due to the simple harmonic behaviour of a beam in terms of well separated modes. The rotations of the beam were neglected, and only the bending modes analysed. A 67 response position beam model was evaluated using the LvF SVD method. The mode shapes of the beam were found to be described by the columns of Ψ , which were compared to the modes of the beam found using the PP method. Only the first 17 singular values were of significant value, indicating that the spatial sampling resolution of the beam was sufficient to describe the modes of the beam up to a frequency of 20 kHz, with more than 6 elements per wavelength for the highest mode. The singular values were used to construct artificial transfer functions containing the contribution of single mode to the overall FRF, $\bar{\varepsilon}$. These were seen to align with each of the modes in the beam in turn, going up in frequency. Past the 17th singular value, the $\bar{\varepsilon}$ transfer functions no longer had any agreement with the original beam FRF, implying that they do not contain modal information.

Due to these findings, a beam model with 17 response positions was analysed using the same procedure. The singular values were found to all be significant apart from the 17th singular value. In terms of the modes described by the columns of Ψ , the 17 response position model had less success than the 67 position model, with only the modes under 3 kHz well described in terms of curvature, and under 10 kHz for maintaining the peaks and troughs. The highest mode which could be considered characterised was of 4.25 sampling positions per bending wavelength. However, as an experimental beam would be restricted to a maximum frequency of 6 kHz, the results lead to 17 response positions being sufficient for sampling the modes of the beam up to this frequency.

The effects of sparse and dense response positions on the content of the \mathcal{E}_i transfer functions has been investigated. It has been shown that when the spatial sampling resolution is high, the singular value transfer functions \mathcal{E}_i contain only a single mode, and as long as the frequency range is wide enough to capture the modes of the system, the modes can be described by individual \mathcal{E}_i functions. Where the spatial sampling resolution is sufficient, some \mathcal{E}_i functions do not contain any modal information, and when the \mathcal{E}_i functions are summed, the original input FRF can be reconstructed without including some non-significant \mathcal{E}_i . As stated in the literature review, along with other methods using SVD, the efficiency of the method is likely to be dependent on spatial sampling resolution.

Reducing the frequency range only reduces the amount of resonances observed, and does not allow for increased mode separation in the \mathcal{E}_i transfer function when the sampling resolution is low. The frequency range does not affect the content of the \mathcal{E}_i functions.

Though it is usually accepted to keep the sample rate at 1 Hz for ease of analysis when conducting modal tests [66], an investigation was conducted into the effects of lowering the frequency resolution. It was found not to affect the mode shape prediction until it became an extreme reduction in resolution, which would be unrealistic in practice. However, for a free-free beam, the damping is assumed to be very low. Similarly, an investigation into adding simulated spectral noise was conducted, which similarly yielded no effects on the SVD outputs. Overall, these modelling exercises are used to demonstrate a scenario which is not limited to realistic constraints of spatial sampling and frequency range and compare it to two examples which are more realistic in practice, a measured beam and a measured plate, in order to investigate how the extraction of singular values is affected by the spatial sampling resolution and frequency range in the experiments.

These results inform the further testing stages of the project, leading toward the aim of decomposing a vibro-acoustic FRF for the prediction to radiated noise of a single mode or group of modes. It is apparent that spatial sampling resolution is key to the separation of modes in the \mathcal{E}_i transfer functions, and the efficiency of the method may depend on ensuring substantial discretisation of the device under test. For the beam described by the model, the first 17 singular values appear to contain the significant modes, indicated by the drop-off or knee seen in the singular values plot of the 67 position model. However, the reduction of spatial sampling positions to 17 reduced the amount of modes accurately described in the columns of Ψ , and therefore the modal coefficients in Σ . This indicates that the frequency range of interest must be reduced when sampling resolution is low, which holds towards the discussion of a minimum of 6 spatial responses per wavelength for the accurate and detailed characterisation of modes. For a rough estimation of the mode shapes, the results show that the mode shape can be described, albeit with little detail, with less sampling positions. This will be further investigated in the next chapter, using a beam measured in the laboratory. The columns of Ψ for the 17 response position model had accuracy up to around 10 kHz, whereas the laboratory experiment will use a frequency range up to 6 kHz. Considering the spatial resolution of the 9th mode at 5233 Hz, there are 9 nodes, or points where the beam velocity is zero. The implication of this is that 17 response positions should be sufficient to detail these points, and the peaks and troughs in the velocity. In the next chapter, the use of the \mathcal{E}_i method for extraction of modes is applied to a real measured beam, which corresponds to the 17 response position model described in this chapter.

5 MODAL DECOMPOSITION METHOD USING SINGULAR VALUE DECOMPOSITION ON A MEASURED BEAM

Following on from the modelled beam experiments, a real steel beam is measured in a laboratory. There are 17 response and excitation positions, used to build a matrix of velocities of the beam. These are then analysed using the LvF and PP SVD algorithms, in the same way as the modelling experiments.

5.1 SVD matrices of 17 Response Position Model

As only the mobility of the beam was measured, with no operational measurement, a single row of responses is taken from the mobility matrix. The first row is taken, as in the beam model experiments, and the simulated input force was at the first position, at the end of the beam and a position of 0m.

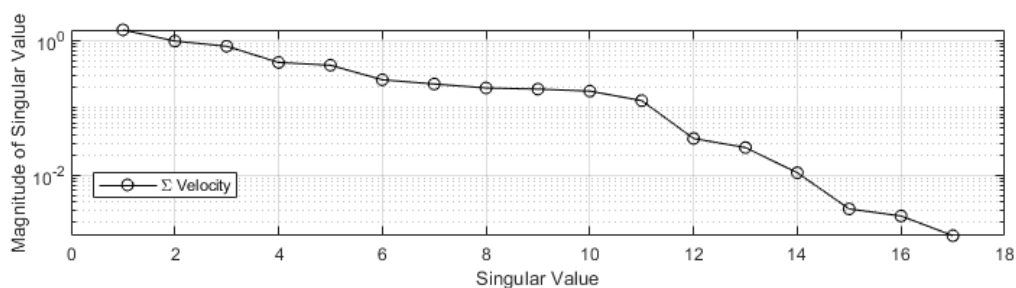


Figure 5.1 Diagonal of singular value matrix Σ for measured beam. Each circle on the graph corresponds to a singular value ' σ ' for the 17 response position measured beam.

The singular values from the diagonal of the Σ matrix are shown in Figure 5.1. When compared to the singular values of the 17 response position model, shown in Figure 4.11, there is a distinct sloping in magnitude of the singular values. Unlike the model, there are not multiple singular values above 0.1, but a gradual reduction in magnitude from the first singular value. This implies that the individual singular values do not correspond wholly to the modes of the beam due to sampling resolution being insufficient.

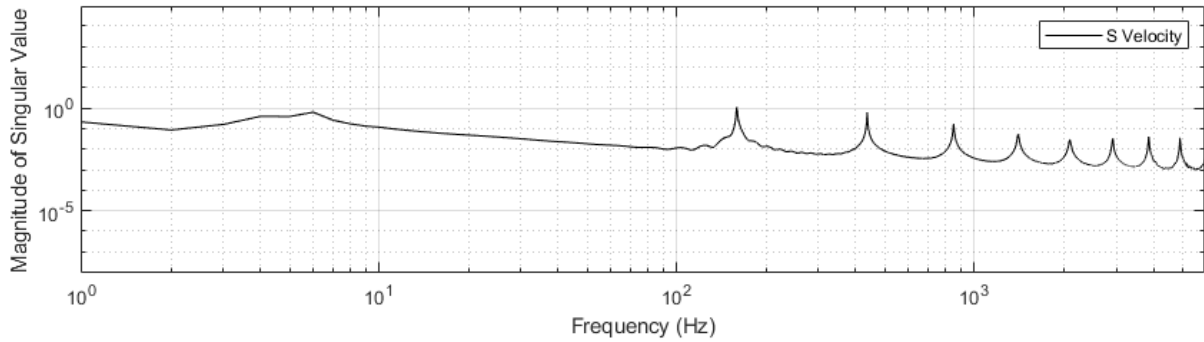


Figure 5.2: Singular values from the ‘S’ matrix obtained from the Peak Picking SVD method, with a single force input at the first position along the beam. The SVD has been conducted on the velocity due force transfer functions, which have been converted to velocity from the measured quantity of acceleration by dividing by $j\omega$. The x-axis goes from 1 Hz to 6 kHz.

By evaluating the S matrix from the conventional frequency by frequency SVD approach, the resonances of the beam illustrate the frequencies of modes. The resonance peaks of the highest magnitude are seen at 159 Hz, 437 Hz, 853 Hz, 1406 Hz, 2107 Hz, 2912 Hz, 3857 Hz, and 4909 Hz, in Figure 5.2. The rigid body mode of the beam can be seen at around 6 Hz, indicating that the boundary conditions of the beam are not free at both ends as intended. Returning to the LvF SVD, the picked peaks from the PP approach are compared to the mode shapes found in the Ψ matrix.

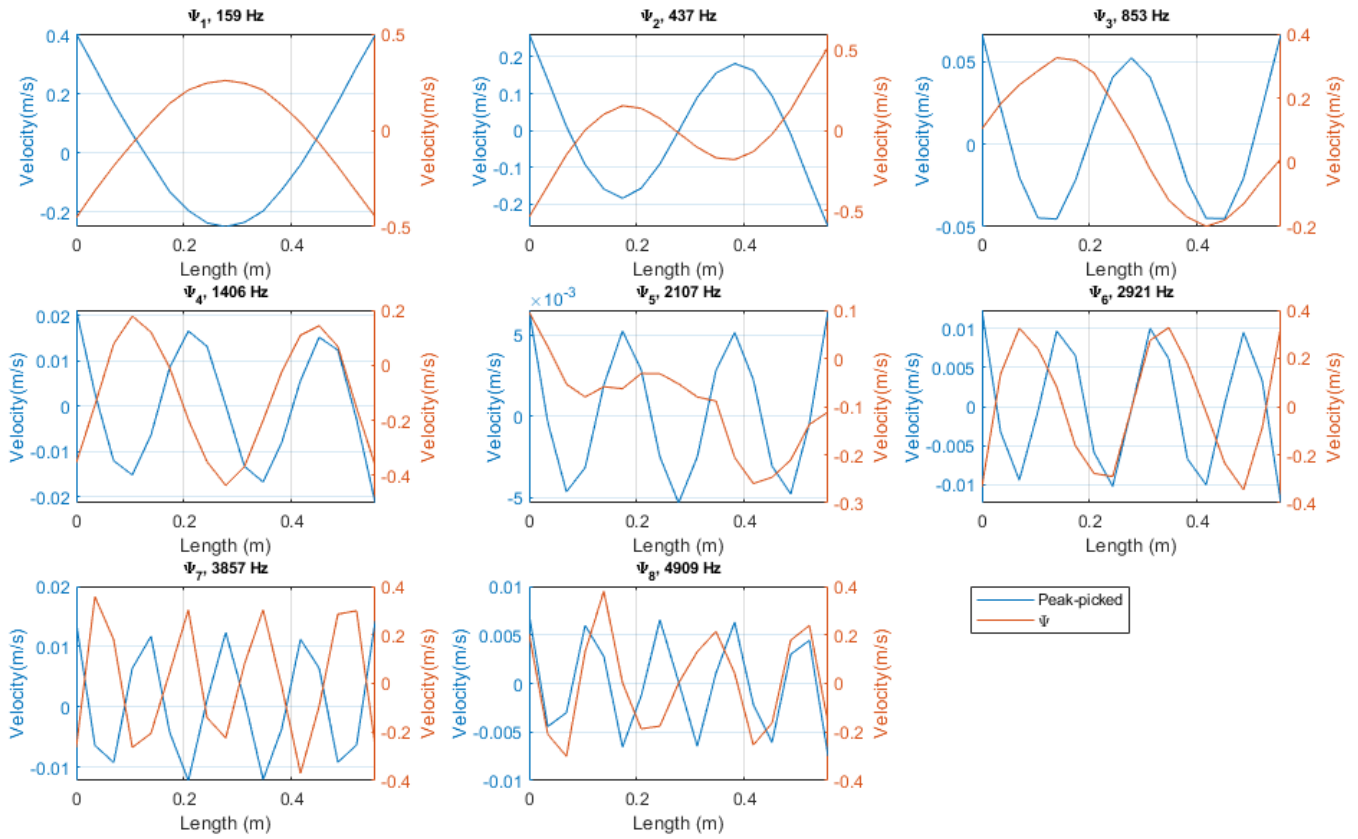


Figure 5.3: Mode shapes picked from the matrix of velocities at the frequency peaks shown in in the S plot, shown in black; and the mode shapes taken from the columns of Ψ , shown in grey. Shown here are Ψ 1- Ψ 18, showing picked modes up to 6 kHz.

In Figure 5.3, the mode shapes manually picked from the PP method and plotted from the beam mobility are shown in blue, and the mode shapes from the LvF algorithm which gives the mode shapes in the columns of the Ψ matrix are shown in red. The first few modes which are at lower frequency appear to have been sufficiently sampled, with a curved shape indicating adequate spatial sampling resolution. As the frequency increases, the mode shapes become more angular and jagged in appearance; this suggests that the sampling resolution is insufficient for the characterisation of the modes at these higher frequencies. Overlooking the difference in phase, the first two modes at 159 Hz and 437 Hz appear to be the same mode in each method. However, the 3rd and 4th columns of Ψ do not align with the picked modes. The picked modes show the expected order of modes, whereas the modes of Ψ diverge. This

indicates that there is a combination of modes described in the columns of Ψ , as well as the magnitude of the modes not decreasing linearly from the fundamental mode, which was seen in the beam model. The central frame of Figure 5.3 shows in red the 5th column of Ψ , which appears to relate to the rigid body mode. By observing the magnitude of the peaks in Figure 5.2, it can be seen that the resonant frequencies do not neatly reduce in magnitude as the frequency increases, as was seen in the modelled beams S matrices in Figure 4.3 and Figure 4.12. This leads to the assumption that the singular values do not correspond in order of mode, that is, the 5th singular value does not necessarily convey the weighting of the 5th order mode of the beam. The implication of this is that the singular values contain the coefficients of a combination of modes.

5.2 Single Mode Contribution Transfer Functions Ξ for Measured Beam

In this section, the Singular value transfer function method described in the beam model chapter will be applied to the measured beam. The Ξ transfer functions are compared to the complete FRF. A comparison can be made between the modelled and measured data, to observe how real experiment parameters effect the method.

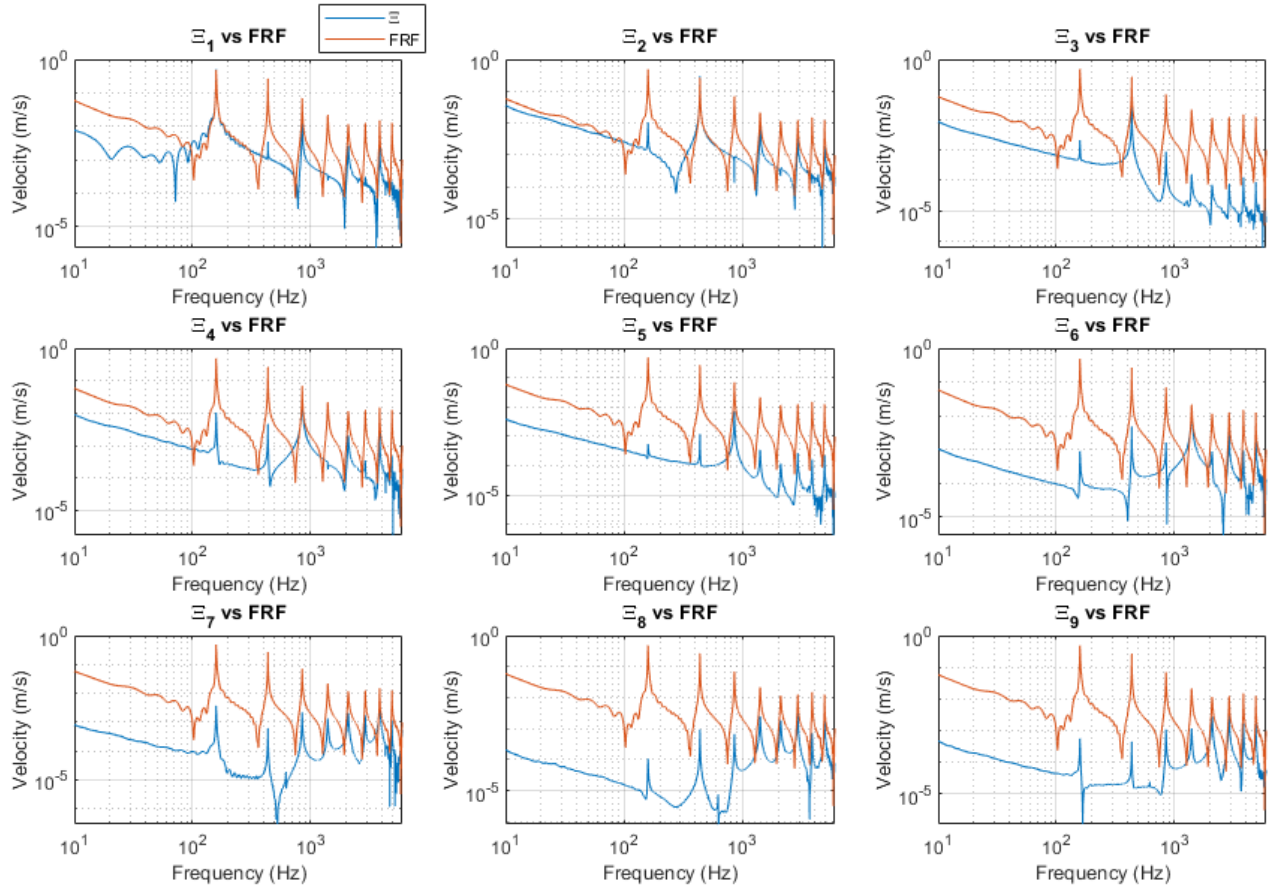


Figure 5.4: Transfer functions Ξ_1 to Ξ_9 constructed using single singular values picked from the diagonal of Σ , compared to the mobility of the beam. The assembled transfer functions containing a single mode are shown in blue, and the unchanged mobility of the beam is shown in red. These are plotted as velocity, on the y-axis, against frequency on the x-axis, between 10 Hz and 6 kHz.

As with the 17 response position beam model, each extracted singular value transfer function Ξ_i contains the information for more than one mode. Shown in the Figure 5.4 are Ξ_1 to Ξ_9 , compared to the mobility of the beam. The Ξ_i transfer functions are shown in blue, and the unaltered beam FRF is shown in red. For the beam model with 17 response positions shown in Figure 4.16, the first singular value contained the rigid body mode, and was aligned with the low frequency range of the transfer function. This alignment can be seen in the second frame of Figure 5.4, showing the second singular value transfer function Ξ_2 . In the modelled beam, the resonances were described in order moving up through frequency, with each resonance described in turn, albeit with other peaks present in the Ξ_i transfer functions, until

around \mathcal{E}_7 . This is somewhat evident in the measured beam, though from around the 5th \mathcal{E} there are multiple peaks in the higher frequency range. This indicates that multiple modes are being described by the singular values, giving a combined contribution from several modes.

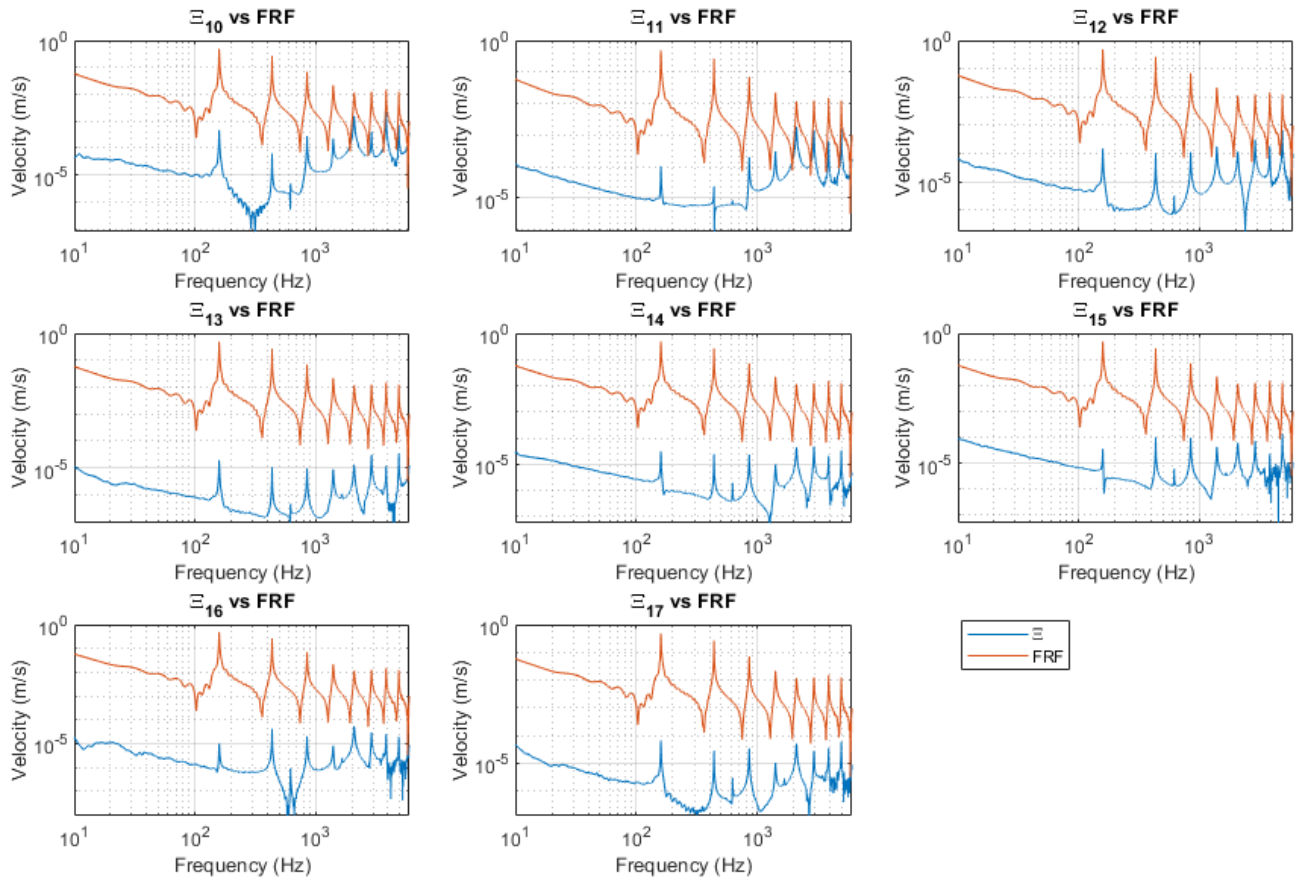


Figure 5.5: Transfer functions \mathcal{E}_{10} to \mathcal{E}_{17} constructed using single singular values picked from the diagonal of Σ , compared to the mobility of the beam. The assembled transfer functions containing a single mode are shown in blue, and the unchanged mobility FRF of the beam is shown in red. These are plotted as velocity, on the y-axis, against frequency from 10 Hz to 6 kHz on the x-axis.

The 10th to 17th \mathcal{E} transfer functions are shown in Figure 5.5. Moving up through the transfer functions, \mathcal{E}_{10} , \mathcal{E}_{11} , and \mathcal{E}_{12} appear to overlap on the FRF, whereas the transfer functions \mathcal{E}_{13} to \mathcal{E}_{17} no longer correspond to any of the original FRF. With reference to the values of Σ shown in Figure 5.1, this corresponds to the 13th -17th singular values being of extremely low magnitude in comparison to the other singular values. However, as with the 17 response

position model, all 17 Ξ are needed to accurately reconstruct the original FRF, shown in Figure 5.6.

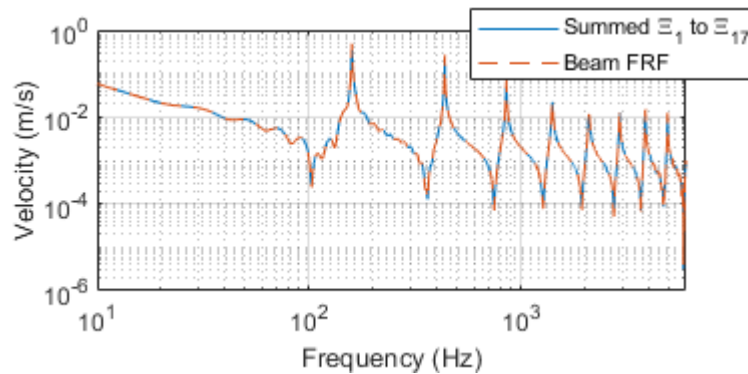


Figure 5.6: Reconstructed FRF using the all 17 singular value Ξ_i models versus the complete model FRF for 17 response positions and a frequency range of 10 Hz to 6 kHz. Shown in the solid line is the original model FRF and shown in the dashed red line is the reconstructed FRF.

This indicates that even though the higher order singular values do not appear to correspond to modes, they still act as coefficients for weighting the columns of Ψ in the original FRF.

5.3 Discussion

Following on from the beam model experiment detailed in the previous chapter, the mobility matrix of a real beam has been measured in a laboratory experiment. The beam was measured with 17 response and excitation positions, with the excitation at the first position used to perform a frequency by frequency SVD, from which the matrices U , S and V were produced. The S matrix from this SVD was used to conduct a Peak Picking methodology of evaluating the resonances displayed. A location vs frequency SVD was then performed, resulting in the matrices Ψ , Σ , and Φ . The values of Σ did not show the same pattern as the beam model singular values, with all singular values showing a gradual decline in magnitude. This implies that the beam is under-sampled [76]. The mode shapes described by the columns of Ψ were then compared to the mode shapes at the frequencies picked from the peaks of the S matrix. The mode shapes were shown to be of the same order for the initial lower frequency modes,

but soon became inconsistent with the modes picked from the peaks of S . At some frequencies, the mode shapes from the columns of Ψ do not appear clearly as actual mode shapes, indicating an insufficient spatial sampling resolution. This is further shown by the angularity of the higher frequency mode shapes, which appear jagged in the mode shapes described by both methods. This is contrary to the beam model with 17 response positions, which indicated that modes up to 6 kHz could be sufficiently sampled with 17 response positions. The modes from the PP method appear in order of frequency, whereas the mode shapes picked from Ψ do not, due to the magnitude of the modes being ‘out of order’ in terms of frequency. In the beam model, the modes were seen to descend in magnitude from the rigid body mode, whereas the measured beam had irregular magnitudes of modes. This leads to the implication that individual modes are not being described, but combinations of modes, as there may be overlapping modes due to a lack of damping. Individual values of σ_i were then extracted, and used to construct 17 new transfer functions $\bar{\mathcal{E}}_i$ describing the FRF associated with each mode. Due to under-sampling, more than one mode appears to be present in each new transfer function when compared to the original FRF of the beam. This is comparable to the beam model with 17 response positions, which also showed multiple modes in each $\bar{\mathcal{E}}$, but to a lesser extent. The implications of this case study are that the SVD method suffers when used in a real laboratory measurement, likely due to factors such as mass loading from accelerometers and non-idealised boundary conditions, which were not an issue for the modelled beam. These effects change the resonance of the beam, and considerations for these aspects can be made for the next experiment. These beam experiments lead to the more complex case of a plate. In the next chapter, data measured from a discretised plate using a contactless Scanning Laser Vibrometer is analysed using the same methods as used for the modelled and measured beam.

6 MODAL DECOMPOSITION OF A PLATE MEASURED USING A SCANNING LASER VIBROMETER

In this chapter, the structural modes of a real plate are determined using the Peak Picking SVD method, before the LvF method is employed to construct transfer functions containing the contribution of a single singular value element. As seen in the beam model experiment, a high sampling resolution is needed to gain the state where only a single mode is described by a singular value. The experiment was conducted using a 900mm x 700mm x 2.5mm plate set in a lightweight frame, with simply supported boundary conditions. A scanning laser vibrometer was used to collect data for 247 points, arranged in a 13x19 point grid of FRFs, up to a maximum frequency of 6400 Hz. These are then built into a matrix of FRFs. The modes of the plate are picked out using the PP method, before the individual singular value transfer functions \bar{E} are extracted and evaluated. The associated modes in the columns of Ψ are shown for the individual transfer functions. As 247 was the maximum measurable response positions, the original transfer function matrix is reduced from 13 to 6 rows, to observe how this affects the mode shapes and the \bar{E} functions. A further reduction is conducted, to 3 remaining rows, and the effects are observed. This experiment aimed to determine the effect of reducing the spatial sampling on the content of the \bar{E} functions for the case of a thin, simply supported plate with low damping. Using Equations (42-44), the damping ratio ζ is estimated as 0.02, which divided by 2π gives a loss factor η of 0.0032. These are calculated using an f_1 of 193 Hz and an f_2 of 201 Hz, with a centre frequency of 196 Hz. These values indicate that the plate is significantly underdamped.

The scanning tests were performed whilst the plate was excited by a shaker, mounted on the back of the plate. A piece of thick wadding was used to isolate the plate from the floor and

protect the measurements from ground-borne excitations, whilst the plate was suspended using elasticated cords to maintain it in an upright position. The frame is excluded from these measurements, with just the surface of the plate measured.

The sampling positions are located at 0.05m in the x direction and 0.047m in the y direction.

The bending wavelengths of the plate in either direction are calculated using Equation (40):

Mode x-axis	$\lambda_{B,x}$ (m)	Mode y-axis	$\lambda_{B,y}$ (m)	Mode y-axis	$\lambda_{B,y}$ (m)
1	1.4	1	1.8	15	0.12
2	0.7	2	0.9	16	0.113
3	0.47	3	0.6	17	0.106
4	0.35	4	0.45	18	0.1
5	0.28	5	0.36	19	0.095
6	0.24	6	0.3	20	0.09
7	0.2	7	0.257		
8	0.175	8	0.225		
9	0.16	9	0.2		
10	0.14	10	0.18		
11	0.13	11	0.164		
12	0.12	12	0.15		
13	0.11	13	0.135		
14	0.1	14	0.129		

Table 6.1: Modenumber and bending wavelength

The bending wavelengths for the modes down to twice the spatial sampling interval in the x-direction are shown in column 2 and for the y-direction in columns 4 and 6 of Table 6.1:

Modenumber and bending wavelength For there to be 6 sampling positions per wavelength, this will approximately correspond to mode 5 in the x-direction and mode 6 in the y-direction. It is unlikely that modes with smaller wavelengths will be accurately described,

though some detail may be present with intervals as small as 0.1m, as few as 2 intervals per wavelength can sometimes be enough to detect frequency [136].

The modes of the plate were calculated using Equation (35) and the nodal positions using Equation (39). The calculations were made using standard values for aluminium, with a density ρ of 2710 kg/m³, Young's modulus E of 70 GPa, and Poisson's ratio θ of 0.3. The speed of sound c in aluminium is taken as 6420 m/s.




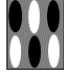

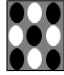
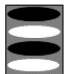
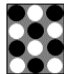
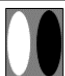
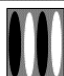
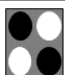

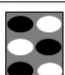
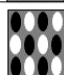
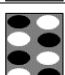
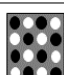
Mode	Frequency (Hz)	Eigen-functions	Nodes (m)	Mode	Frequency (Hz)	Eigen-functions	Nodes (m)
$f_{1,1}$	14.12		X: 0.35 Y: 0.45	$f_{3,1}$	28.45		X: 0.175, 0.35, 0.525 Y: 0.45
$f_{1,2}$	24.05		X:0.35 Y: 0.3, 0.6	$f_{3,2}$	34.44		X: 0.175, 0.35, 0.525 Y: 0.3, 0.6
$f_{1,3}$	34.74		X:0.35 Y: 0.225, 0.45, 0.675	$f_{3,3}$	42.6		X: 0.175, 0.35, 0.525 Y: 0.225, 0.45, 0.675
$f_{1,4}$	45.67		X:0.35 Y: 0.18, 0.36, 0.54,0.72	$f_{3,4}$	51.9		X: 0.175, 0.35, 0.525 Y: 0.18, 0.36, 0.54,0.72
$f_{2,1}$	20.73		X: 0.234, 0.467 Y: 0.45	$f_{4,1}$	36.63		X: 0.14, 0.28, 0.42, 0.56 Y: 0.45
$f_{2,2}$	28.4		X: 0.234, 0.467 Y: 0.3, 0.6	$f_{4,2}$	41.45		X: 0.14, 0.28, 0.42, 0.56 Y: 0.3, 0.6
$f_{2,3}$	37.9		X: 0.234, 0.467 Y: 0.225, 0.45, 0.675	$f_{4,3}$	48.44		X: 0.14, 0.28, 0.42, 0.56 Y: 0.225, 0.45, 0.675
$f_{2,4}$	48.1		X: 0.234, 0.467 Y: 0.18, 0.36, 0.54,0.72	$f_{4,4}$	56.8		X: 0.14, 0.28, 0.42, 0.56 Y: 0.18, 0.36, 0.54,0.72

Table 6.2: Mode frequencies, eigenfunctions, and nodes for the first 4 modes of each order of the plate.

The eigenfunctions, or mode shapes, of the plate are shown with the corresponding calculated frequency and node positions in Table 6.2. The first subscript number on f indicates the number of nodes in the x-axis and the second number the nodes in the y-axis. The mode shapes of the plate are predicted to appear at these frequencies and at harmonics of these frequencies. For example, the breathing mode at $f_{1,1}$ should appear at $2f_{1,1}$, $3f_{1,1}$, $4f_{1,1}$, etc.

The critical frequency of the plate is calculated as 3.8 kHz. As the plate has not had any damping applied, it is likely there will be degenerate modes in practice, where multiple mode

shapes share the same frequency, and overlapping modes, where different frequencies share very similar mode shapes. The lower order mode shapes presented are likely to be described at the harmonic frequencies, though higher order modes are likely to be undersampled.

6.1 Mode Shapes from Peak Picking Method

The laser scan was conducted using the maximum resolution and frequency range with respect to the highest spatial sampling possible, over a frequency range of 6400 Hz with 1.56Hz resolution, and 13x 19 grid resolution. The FRFs of velocity due to voltage was measured, which is a matrix consisting of transfer functions of velocity measured by the laser at discretised points on the plate surface due to voltage measured for the shaker. A frequency by frequency SVD was conducted on the data in order to pick the peaks from the diagonal of the S matrix.

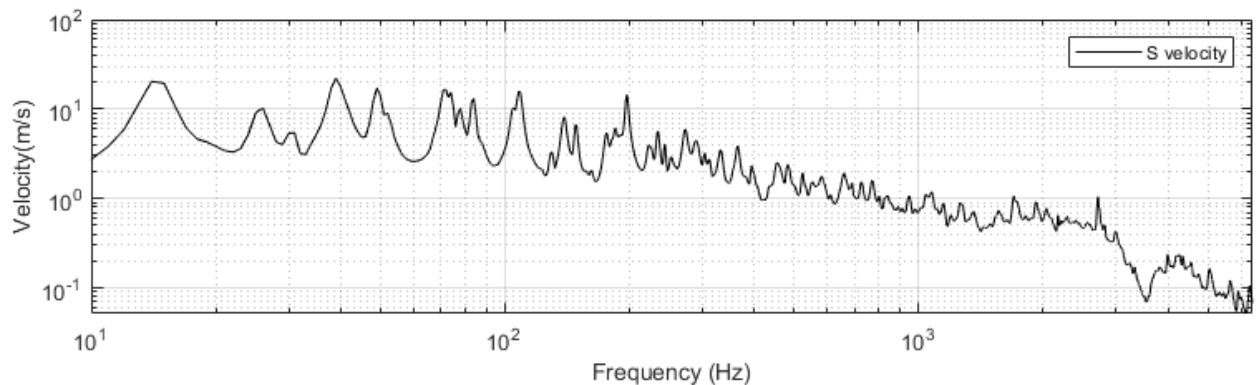


Figure 6.1: Diagonal of S matrix from SVD conducted on the velocity due to voltage transfer function matrix in a frequency- by-frequency loop for the PP method. The x-axis is frequency between 10 and 6400 Hz and the y-axis is velocity from 1 to 100 m/s. From this plot, the peaks are manually picked in order to determine the modes of the plate.

From the peaks present in S , shown in Figure 6.1, the mode shapes of the plate are extracted. As the scanning laser vibrometer was used to measure a dense grid of response positions, there should be considerably better mode resolution than that seen with the measured beam.

The first nine peaks of the S plot are present at 14 Hz, 26 Hz, 31 Hz, 39 Hz, 49 Hz, 72 Hz, 84 Hz, 108 Hz, and 139 Hz, which can be plotted spatially to determine their modal patterns:

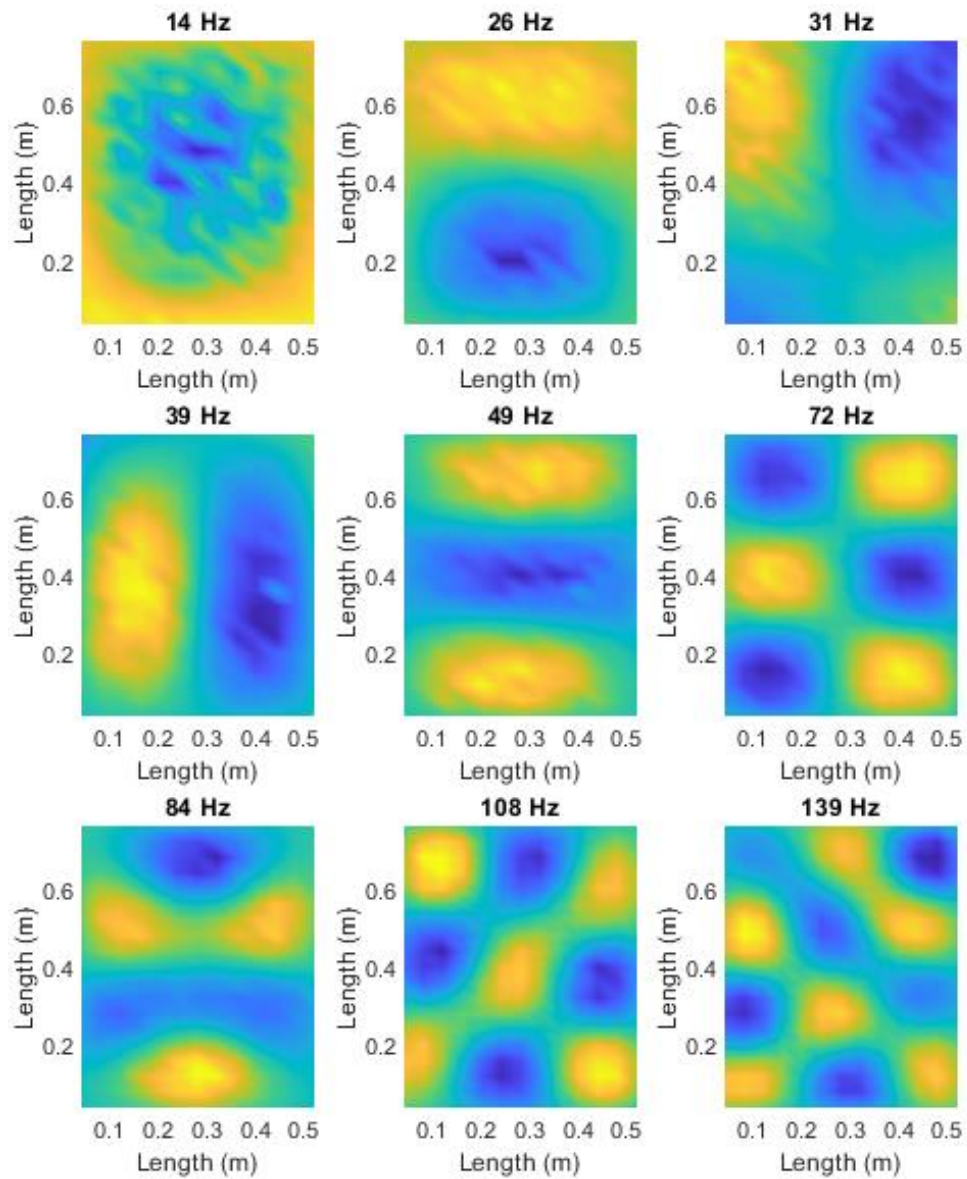


Figure 6.2: First nine mode shapes extracted using the Peak Picking Method. Seen in the first frame is the first mode of the plate, at 15 Hz. Reading left to right, the mode shapes increase in frequency. These are plotted by the dimensions of the plate in the x and y axes.

The first nine mode shapes picked out from the peaks of S show modal shapes are shown in Figure 6.2. The first mode shown appears to be the fundamental or breathing mode, with the mode shapes increasing by order as the frequency increases. This should indicate that when the LvF SVD is performed, the singular value transfer functions constructed with extracted

singular values should describe a small amount of modes, as it is likely these mode shapes contain more than one mode as they are not all exact representations of modes. $f_{1,1}$ is apparent at 14 Hz, $f_{1,2}$ at 26 Hz, $f_{2,1}$ at 39 Hz, $f_{1,3}$ at 49 Hz, and $f_{2,3}$ at 72 Hz. Comparing to the calculated frequencies in Table 6.1: Modenumber and bending wavelength these mode shapes appear at almost the same frequency or double the frequency, indicating a harmonic. 108 Hz appears to be close to $f_{3,3}$, which was calculated to be 42.6 Hz. As $2f_{3,3}$ would be 85.2 Hz, and $3f_{3,3}$ 127.8 Hz, it is likely that the mode shape picked using the PP approach is a combination of modes, causing the asymmetry visible. The peaks picked at 84 Hz and 139 Hz do not appear as clear mode shapes, indicating overlapping modes.

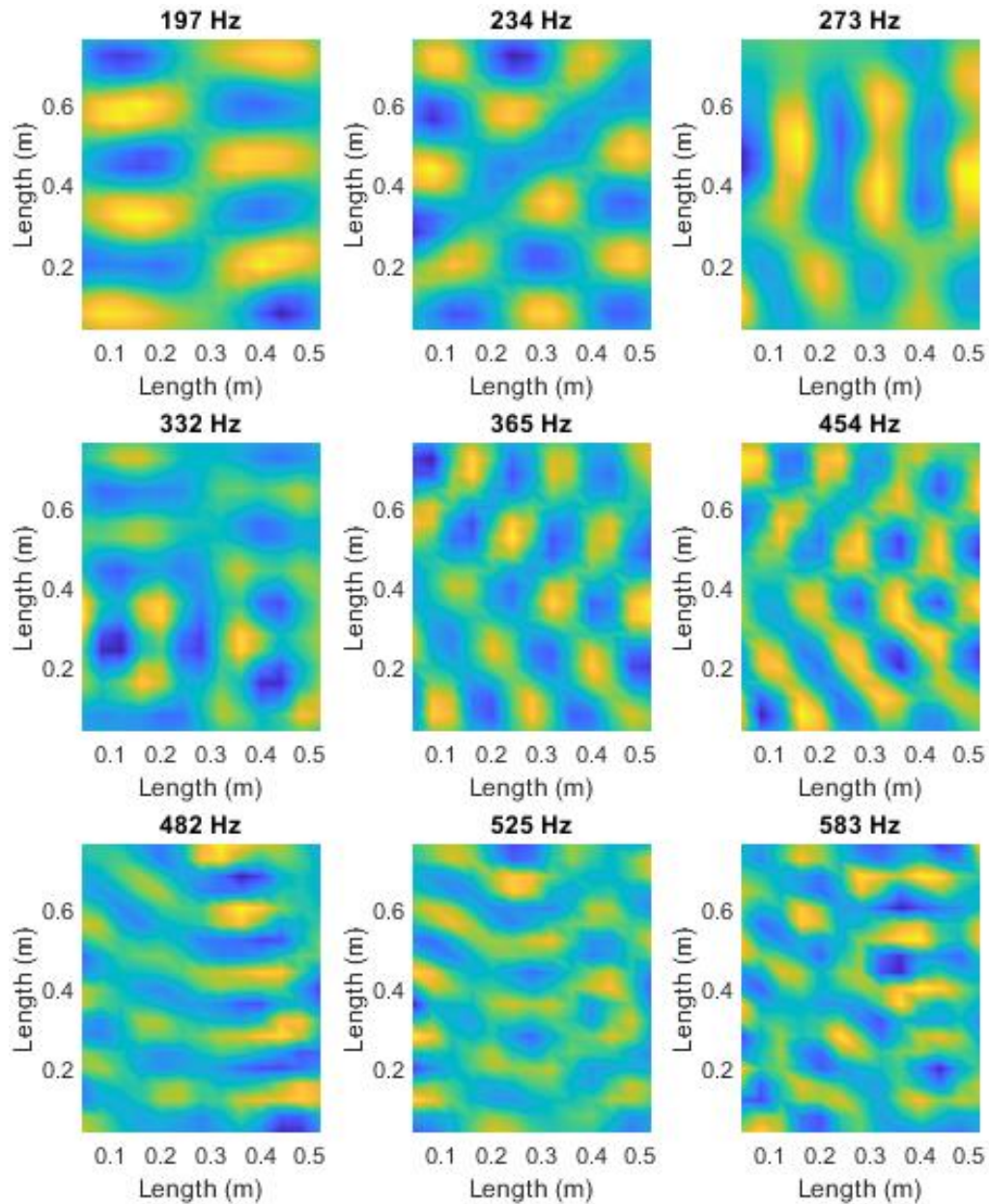


Figure 6.3: mode shapes 10 to 18 extracted using the Peak Picking Method. Seen in the first frame is the 10th mode of the plate, at 197 Hz. Reading left to right, the mode shapes increase in frequency. These are plotted by the dimensions of the plate in the x and y axes.

The next 9 peaks are present at 197 Hz, 234 Hz, 273 Hz, 332 Hz, 365 Hz, 454 Hz, 482 Hz, 525 Hz, and 583 Hz, and shown in Figure 6.3. Mode shapes can be seen for $f_{2,6}$ at 197 Hz, which was calculated as 69.5 Hz. The 3rd harmonic for the calculated frequency would appear at 208 Hz, which allowing for discrepancy between the calculated estimates and the measurements indicates this should be the actual mode at the 3rd harmonic position. The next

mode shape visible is $f_{3,6}$ at 234 Hz. The calculated frequency for this mode is 72.15 Hz, giving the 3rd harmonic at 216.5Hz. The peak is dominated by this mode shape, but has some disturbance, indicating the influence of another mode. An approximation to $f_{5,5}$ is shown for 365 Hz. $f_{5,5}$ was calculated as being 71 Hz, with the closest harmonic to 365 being 355 at $5f_{5,5}$. Though there are 3 fairly representative mode shapes seen here, the mode shapes begin to look more disturbed and break down in this frequency range. This suggests that the sampling resolution is beginning to become insufficient to describe the modes. The highest mode shape approximated is $f_{5,5}$, giving a bending wavelength of 0.28m in the x-direction and 0.36m in the y-direction. The node positions in the x-direction are at 0.12m, 0.24m, 0.35m, 0.47m, and 0.58m. The node positions in the y-direction are 0.15m, 0.3m, 0.45m, 0.6m, and 0.75m, giving 5 nodes in either direction. As there are 13 sampling positions in the x-direction, this gives 2.6 sampling positions per node, and in the y-direction, 3.8 sampling positions per node. Modes with more than 5 nodes are therefore unlikely to be described. This may indicate that when the singular values are extracted, the transfer functions are likely to include overlapping modes, due to the spatial sampling resolution being insufficient to capture the higher frequency modes.

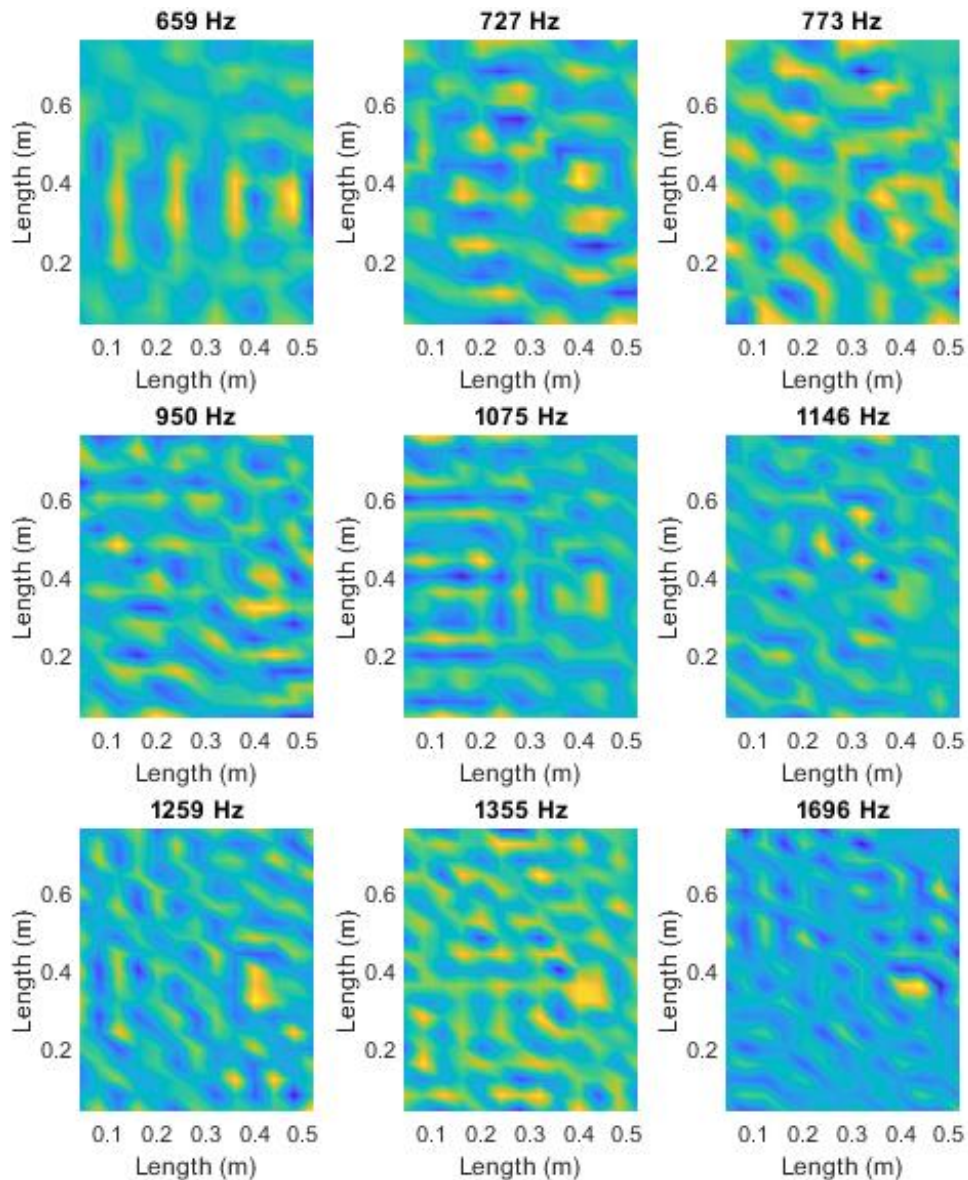


Figure 6.4: mode shapes 19 to 27 extracted using the Peak Picking Method. Seen in the first frame is the 19th mode of the plate, at 659 Hz. Reading left to right, the mode shapes increase in frequency. These are plotted by the dimensions of the plate in the x and y axes.

The next set of modes are at 659 Hz, 727 Hz, 773 Hz, 950 Hz, 1075 Hz, 1146 Hz, 1259 Hz, 1355 Hz, and 1696 Hz. However, due to insufficient resolution and overlapping of modes, these do not appear as mode shapes, as shown in Figure 6.4. As seen in the higher frequencies of the previous figure, the results are no longer resembling modes and are likely to be noise. From 1259 Hz, an artefact can be seen around the shaker position on the right of the frames, indicating the velocities elsewhere on the plate have reduced considerably. The remaining

peaks picked at frequencies above 1696 Hz also do not appear as clear mode shapes and have not been included here.

6.2 Decomposed Transfer Functions Ξ

As with the beams in the previous chapters, new transfer functions containing a single singular value are constructed, which in theory will describe the transfer function of a single mode, or group of modes depending on spatial sampling resolution. These are presented with the corresponding column of Ψ , which contains a mode shape associated with the singular value used to construct Ξ .

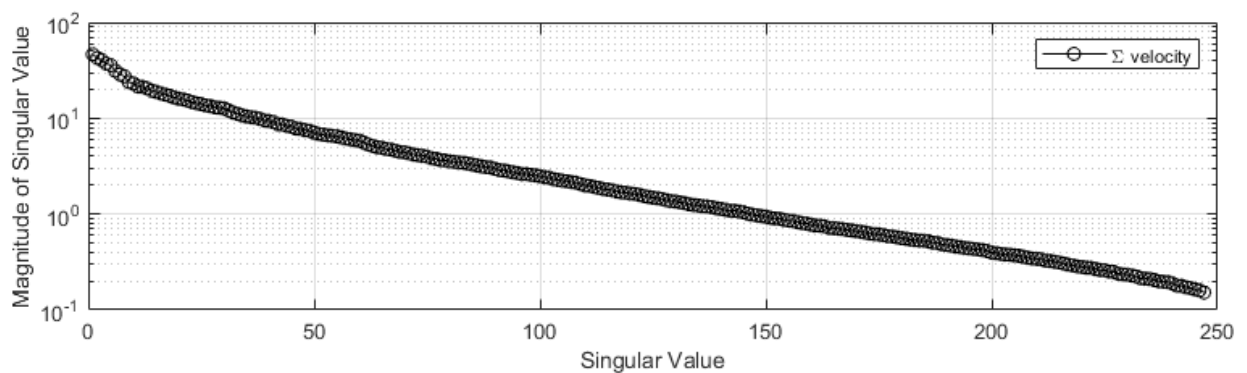


Figure 6.5: Singular values on the diagonal of Σ

Figure 6.5 shows the singular values on the diagonal of Σ . As there are 247 sampling positions, there are 247 singular values. Unlike the 67 response position beam model, there is no distinct knee or drop off in magnitude as the order of singular value increases, with instead a smooth downward slope. This indicates that although the higher number singular values contain less modal information than the lower numbers, there is not a clear separation in modes which are dominant, leading towards multiple modes being described by the singular values.

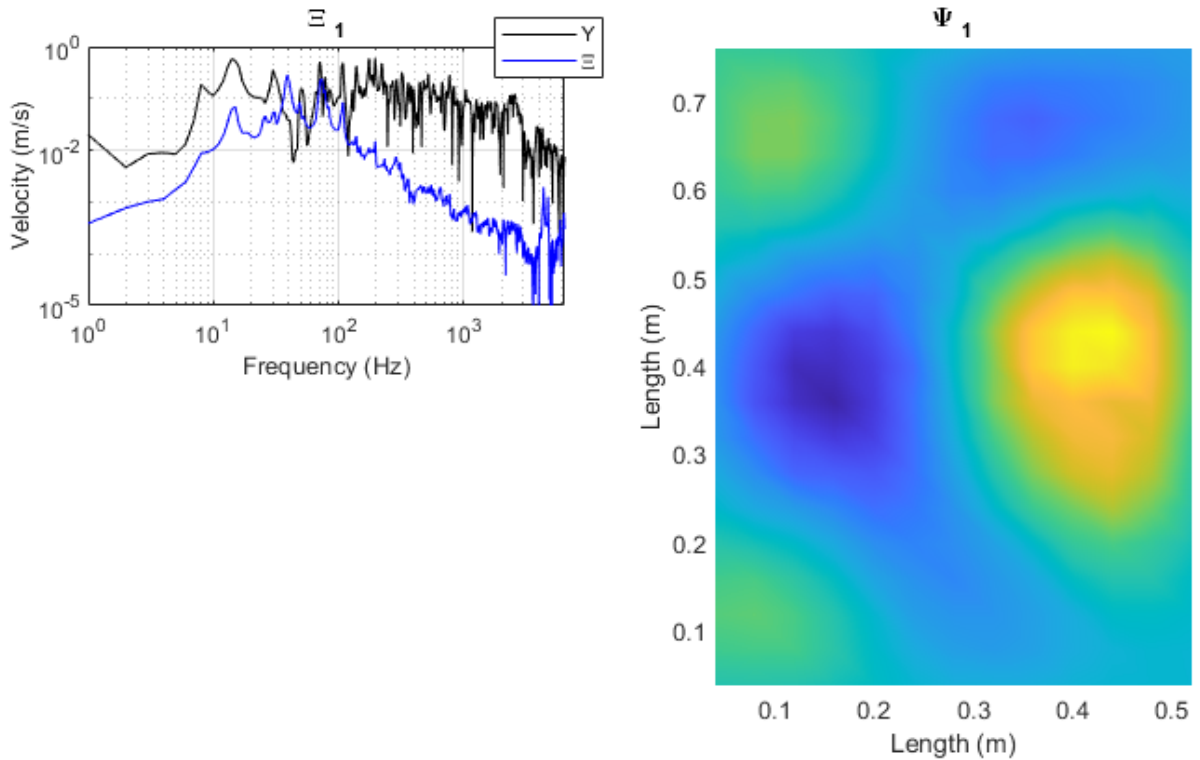


Figure 6.6: Singular transfer function Ξ_1 and Ψ_1 . The left hand plot shows Ξ_1 plotted against Y , with Ξ in blue and Y in black. The x-axis is velocity in metres per second and the y-axis is frequency in Hertz. The right hand plot shows the associated mode with the Ξ transfer function, Ψ_1 , plotted by the plate dimensions.

On the left of Figure 6.6 is the constructed transfer function Ξ_1 in black, and Y , the original transfer function in grey, with frequency on the x-axis and velocity on the y-axis. It can be seen that two peaks are included in the Ξ_1 transfer function which overlap with Y , at approximately 35 and 55 Hz. By looking at the associated mode shape on the right, a clear shape can be seen. However, this does not look like an exact mode shape as there is asymmetry, and considering the two peaks present in Ξ_1 , likely depicts a combination of two modes. A peak is present in Ξ_1 at around 15 Hz, however this does not overlap with the original transfer function. The shape described in Ψ resembles a combination of modes. An approximate reconstruction of Ψ mode shape can be built by extracting the plate mode shapes at the frequencies of 40 Hz and 70 Hz.

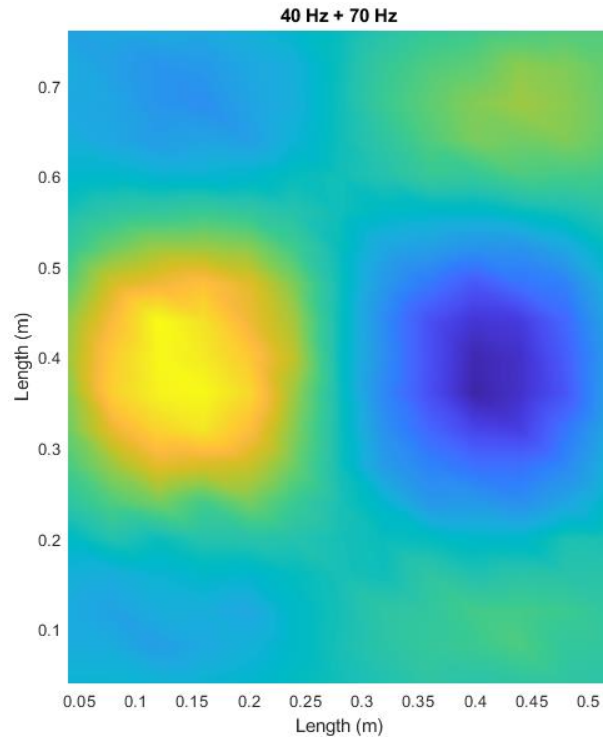


Figure 6.7: reconstruction of SVD mode by adding the two peak frequencies in the Ξ transfer function

Evaluating the differences between Figure 6.6 and Figure 6.7, it can be seen that the phase is reversed. This implies that the discarded singular values contain phase information. The reconstructed mode shape appears more defined, which leads to there being more than the two peak modes interacting in the Ψ mode. Therefore, the first singular value contains more than the 2 peak modes.

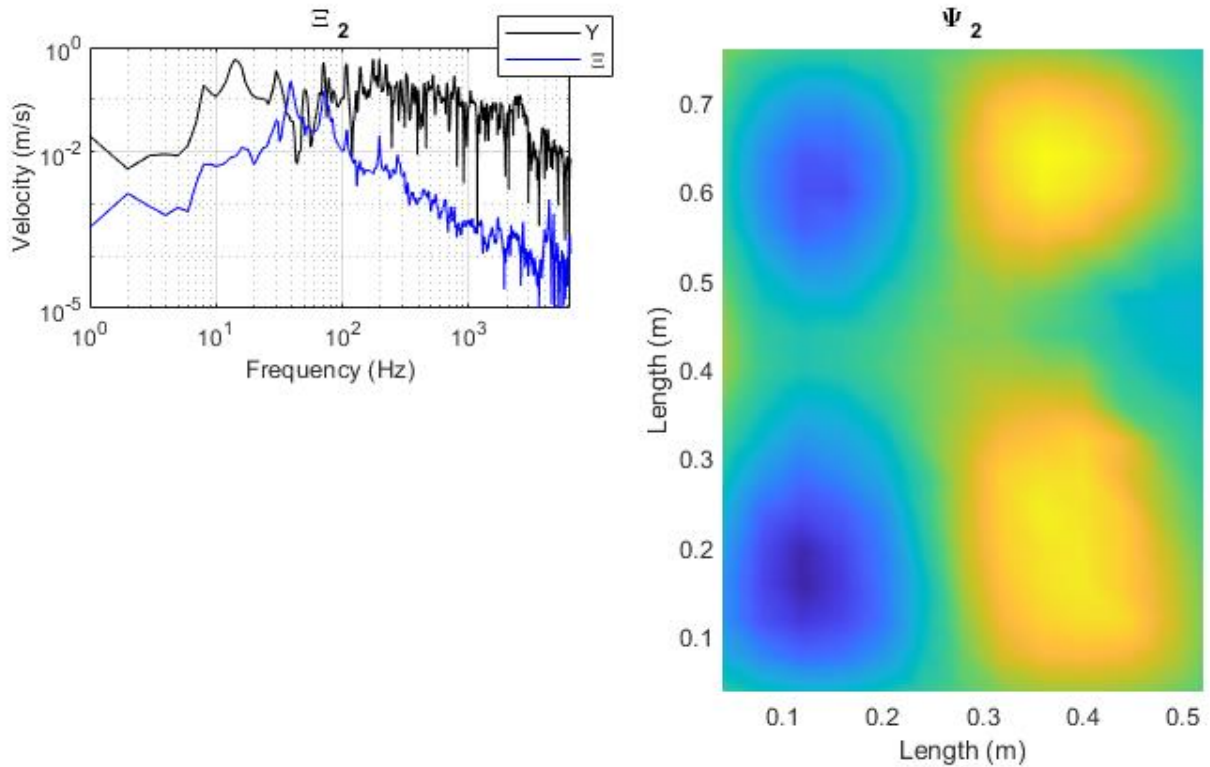


Figure 6.8: Singular transfer function Ξ_2 and Ψ_2 . The left hand plot shows Ξ_2 plotted against Y , with Ξ in blue and Y in black. The x-axis is velocity in metres per second and the y-axis is frequency in Hertz. The right hand plot shows the associated mode with the Ξ transfer function, Ψ_2 , plotted by the plate dimensions.

Shown in Figure 6.8 are the second Ξ transfer function against the original FRF, and the associated Ψ mode shape. The peaks present in Ξ_2 appear to be at the same frequencies as Ξ_1 , however the peak at around 35 Hz may be of very slightly higher magnitude. There is also no peak present around 15 Hz. This exact mode was not extracted from the peaks of S . Although resembling a mode shape, this could actually be a combination of modes which happen to add together to resemble a 4th order mode, or it could be a degenerate mode appearing at more than one frequency.

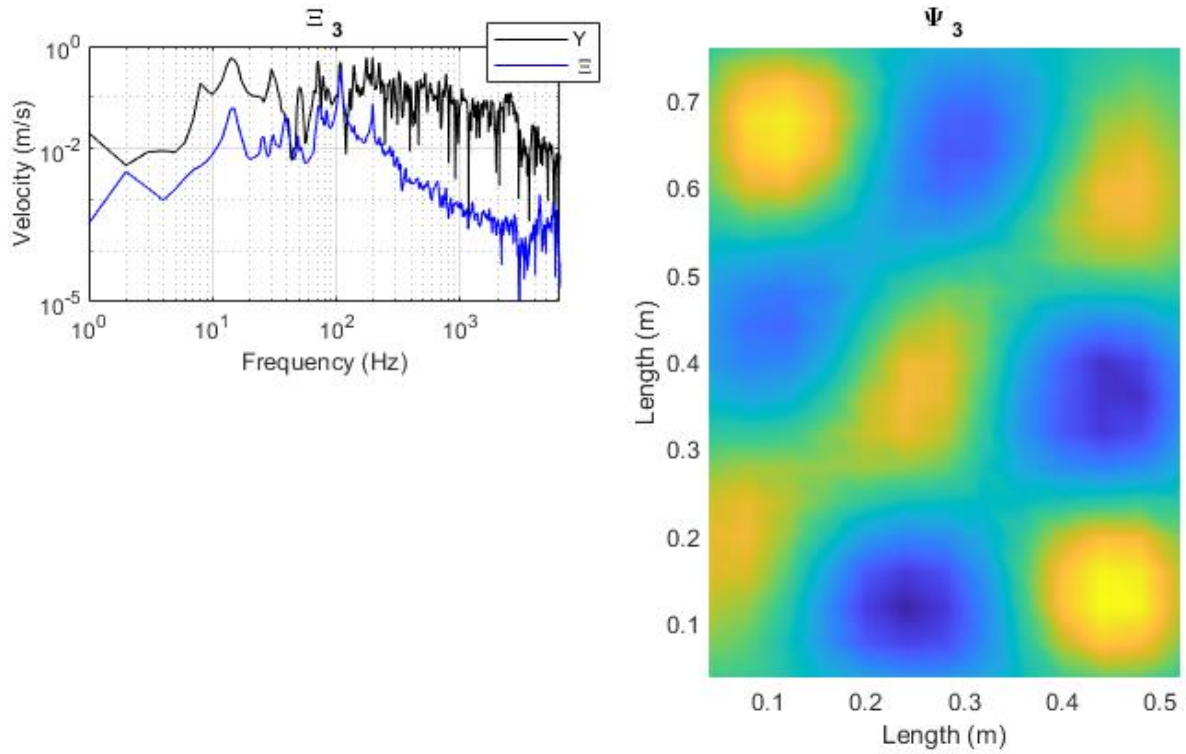


Figure 6.9: Singular transfer function Ξ_3 and Ψ_3 . The left hand plot shows Ξ_2 plotted against Y , with Ξ in blue and Y in black. The x-axis is velocity in metres per second and the y-axis is frequency in Hertz. The right hand plot shows the associated mode with the Ξ transfer function, Ψ_2 , plotted by the plate dimensions.

Ξ_3 has a much clearer single peak overlapping the original transfer function at 108 Hz, as shown by Figure 6.9. Though there are other peaks in Ξ_3 , there is only one of significant magnitude. This implies that the clear mode shape seen in Ψ_3 is undisturbed, and is a true description of the plate behaviour at 108 Hz. Looking at the mode shapes picked from S , this mode is very similar with the mode picked at 108 Hz, with slight smearing detail due to the influence of the remaining data for the other frequencies.

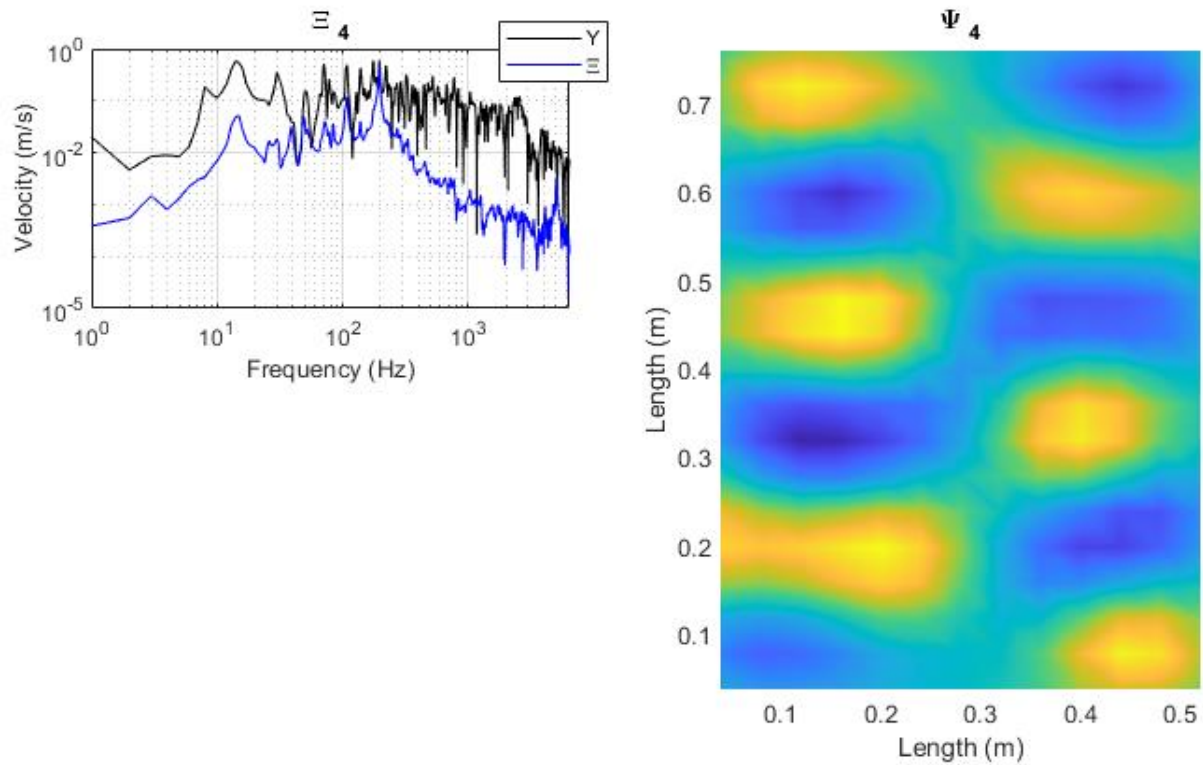


Figure 6.10: Singular transfer function Ξ_4 and Ψ_4 . The left hand plot shows Ξ_4 plotted against Y , with Ξ in blue and Y in black. The x-axis is velocity in metres per second and the y-axis is frequency in Hertz. The right hand plot shows the associated mode with the Ξ transfer function, Ψ_4 , plotted by the plate dimensions.

Figure 6.10 depicts Ξ_3 and Ψ_3 , which appear to be corresponding to a clear modal peak at 198 Hz. This corresponds to the peak picked from S at 197 Hz. There is some asymmetry visible in Ψ_3 which indicates contribution from the lesser peaks in Ξ_3 , as there is overlap in some of the resonances between 15 Hz and 100 Hz. These results are leading to some modes being described individually by the Ξ transfer functions.

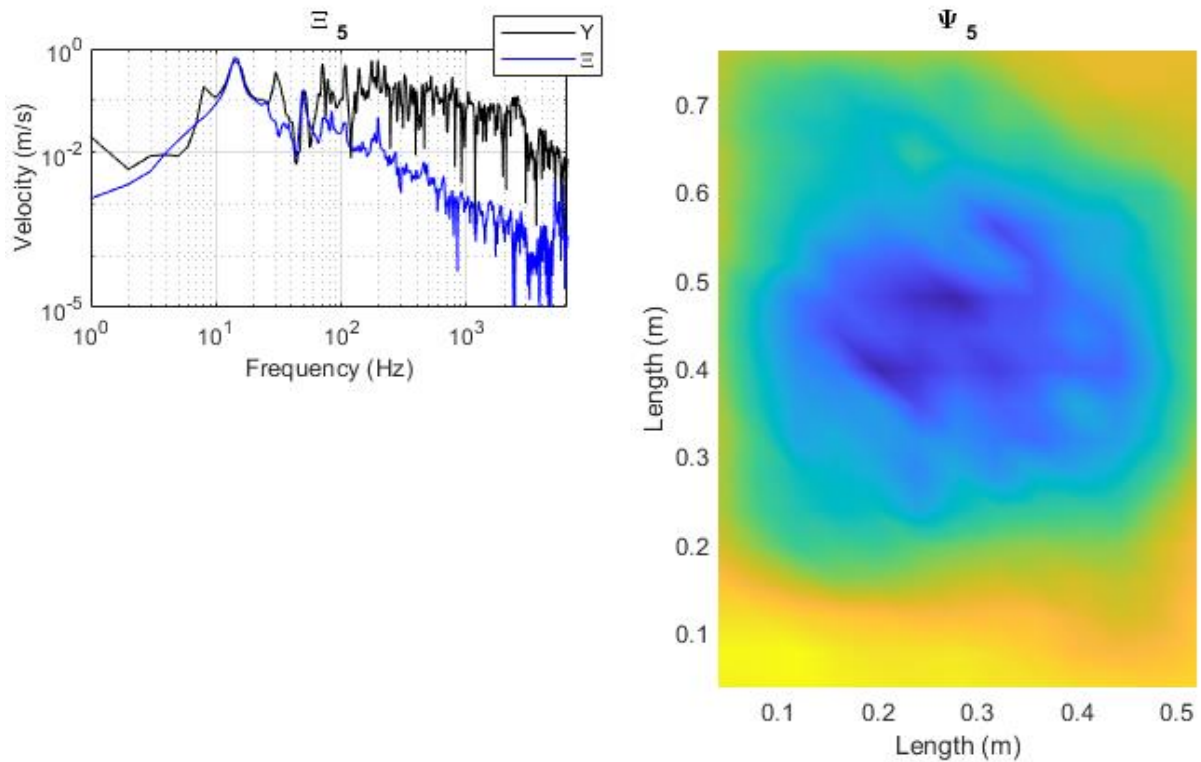


Figure 6.11: Singular transfer function Ξ_5 and Ψ_5 . The left hand plot shows Ξ_5 plotted against Y , with Ξ in blue and Y in black. The x-axis is velocity in metres per second and the y-axis is frequency in Hertz. The right hand plot shows the associated mode with the Ξ transfer function, Ψ_5 , plotted by the plate dimensions.

Ξ_5 and Ψ_5 very clearly show the contribution of the first mode, at around 15 Hz, in Figure 6.11. The shading in Ψ_5 has some disturbance, indicating some involvement of other modes, which can be seen in Ξ_5 . There is a peak visible at 50 Hz which overlaps with the original transfer function, suggesting that the singular value contains some contribution from this mode as well as the first order mode at 15 Hz. From S , a peak was picked at 14 Hz, which resembles this mode. This indicates that the breathing mode dominates in the Ξ_5 transfer function.

For brevity, a selection of further Ξ_i transfer functions are presented in Figure 6.12.

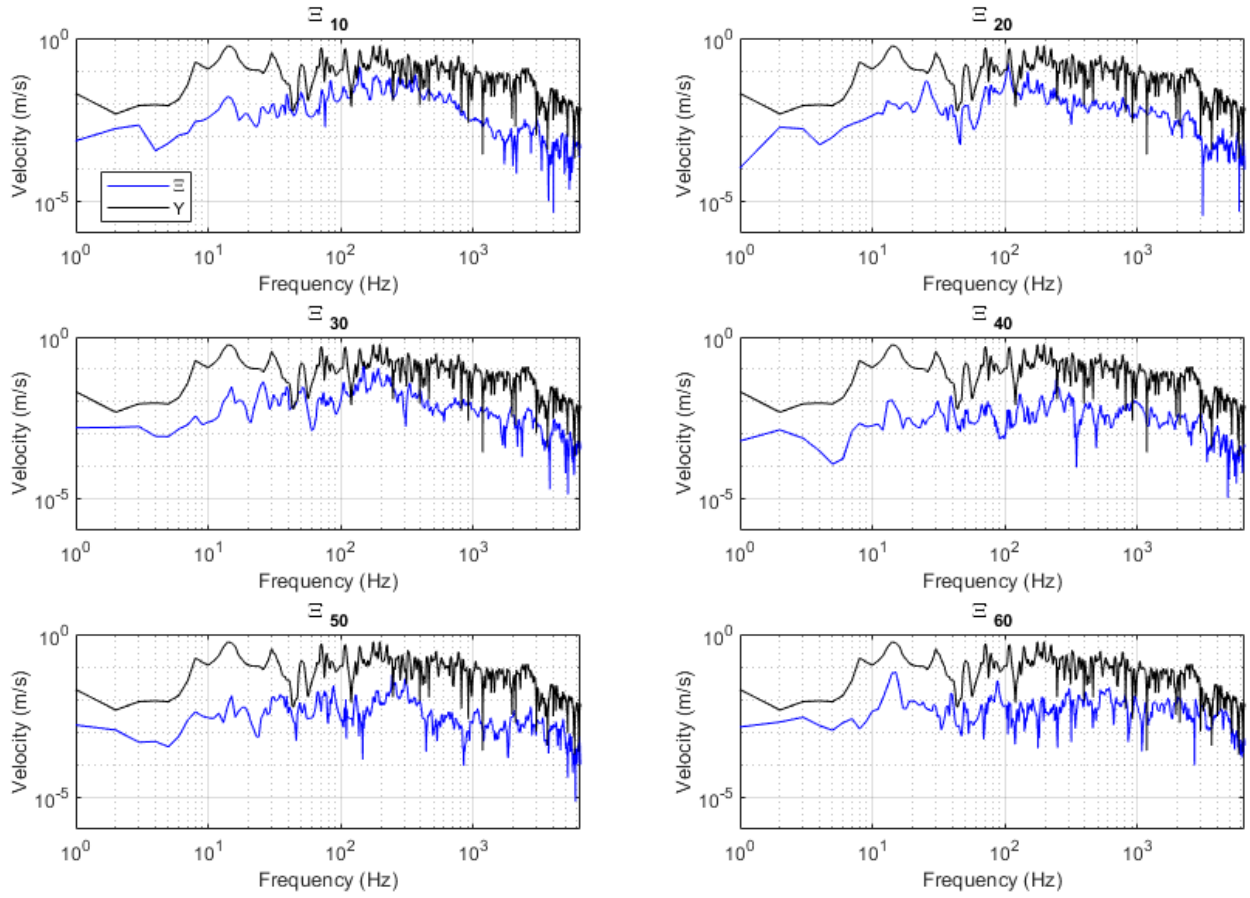


Figure 6.12: Singular transfer functions Ξ_{10} , Ξ_{20} , Ξ_{30} , Ξ_{40} , Ξ_{50} , and Ξ_{60} compared to Y . The constructed singular value transfer functions Ξ are shown in blue, and the original unaltered mobility of the plate is shown in black.

The x -axes are frequency in Hertz and the y -axes are velocity in metres per second.

The singular values on the diagonal of Σ get smaller as the number increases, meaning that in theory, as i tends towards n , where n is the number of response positions, Ξ_i contains less and less significant singular values, until eventually they do not contain modal information.

However, all of the Ξ transfer functions were required to reconstruct the original FRF, unlike with the highly sampled beam model, where the smaller singular values became insignificant.

The better spatial sampling resolution, the more modes can be described, with the measured frequency range dictating how many modes are present. Once all modes are described, the remaining values would contain no information. As i increases, there is less overlap between Ξ_i and Y . Though Ξ_{20} does appear to have an overlapping peak at around 100 Hz, looking at

the associated mode shape in Figure 6.13 indicates that Ξ_{20} contains insignificant modal information:

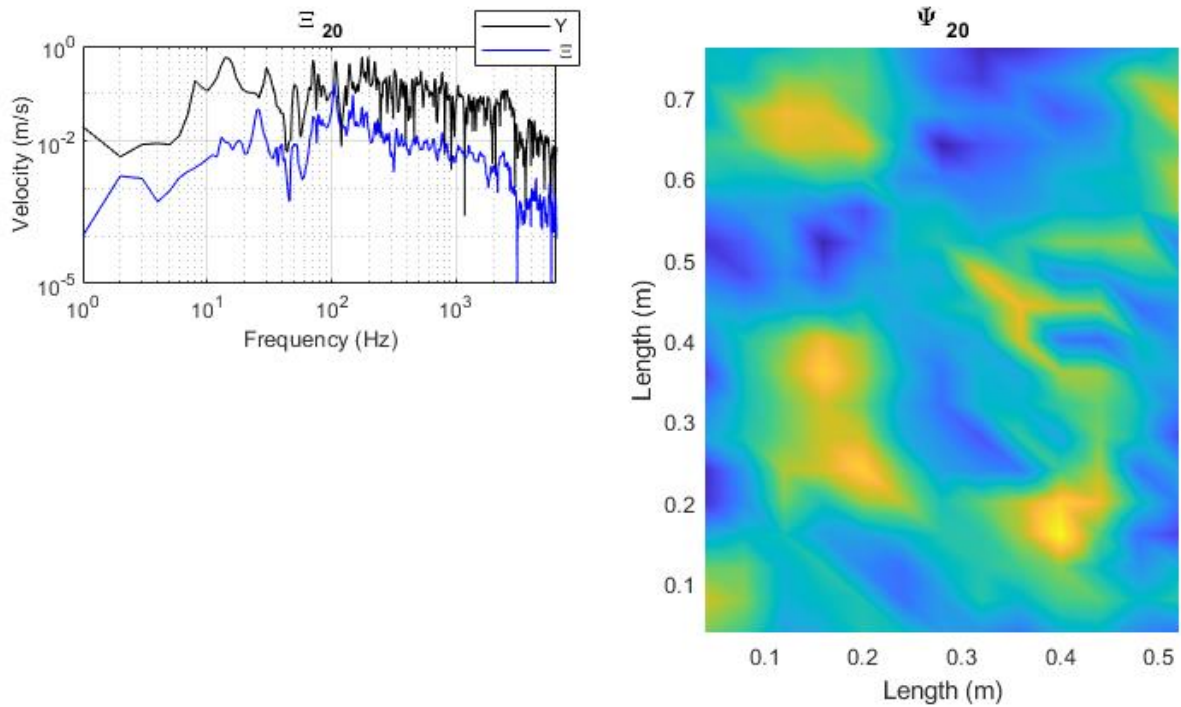


Figure 6.13: Singular transfer function Ξ_{20} and Ψ_{20} . The left hand plot shows Ξ_{20} plotted against Y , with Ξ in blue and Y in black. The x-axis is velocity in metres per second and the y-axis is frequency in Hertz. The right hand plot shows the associated mode with the Ξ transfer function, Ψ_{20} , plotted by the plate dimensions.

A clear mode shape is not described in Ψ_{20} , which suggests that Ξ_{20} either contains the contributions of multiple overlapping modes, or no actual modal information, as shown by Figure 6.13. There is no resemblance to a peak picked from S . This indicates that only the first few singular values can clearly describe contributions of modes, with some interference still present. By looking at Ψ , these mode shapes, or mode-like shapes, are evident in the first 5 columns, depicted in Figure 6.14.

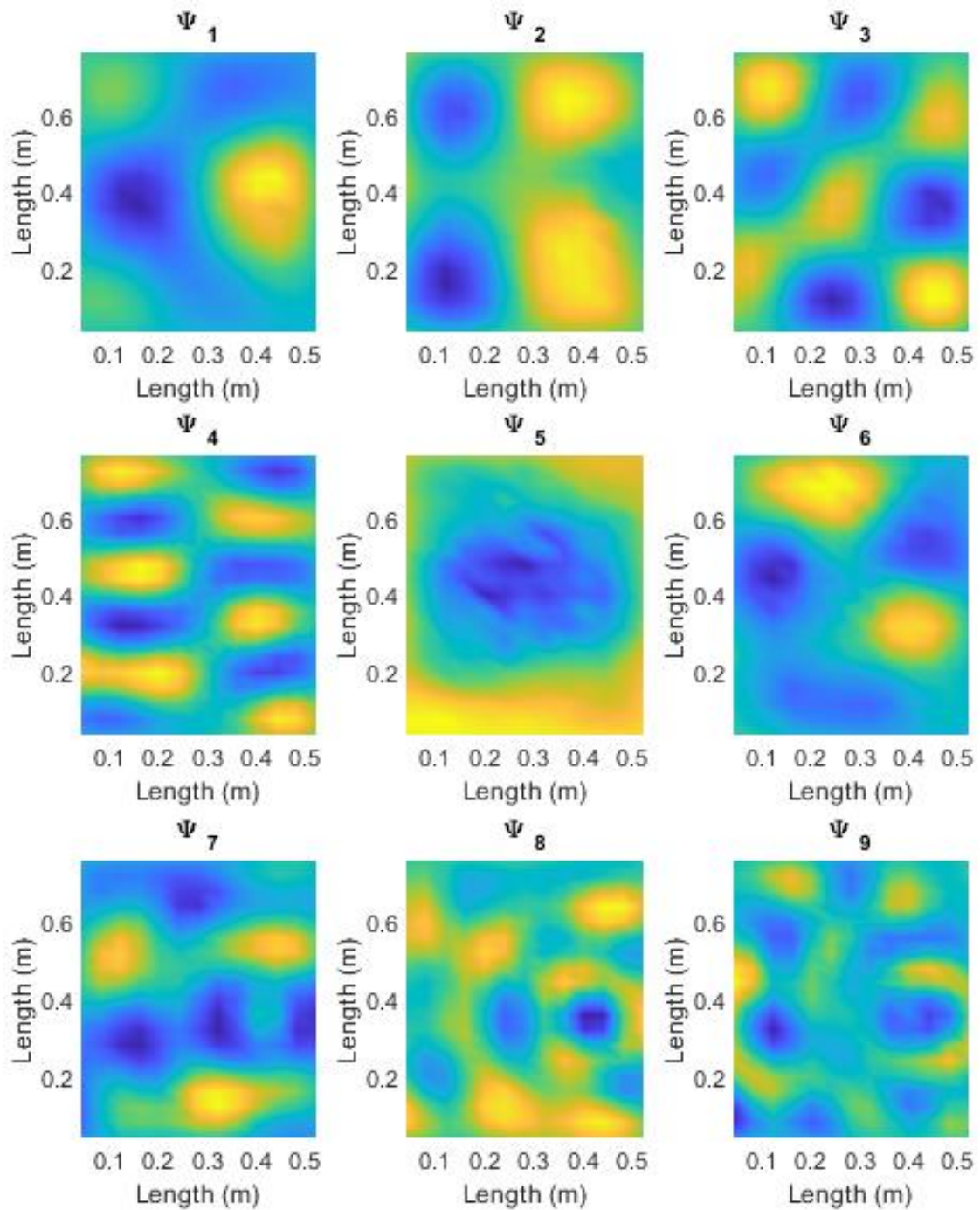


Figure 6.14: Ψ_1 to Ψ_9 mode shapes, plotted in terms of plate dimensions. There are modal shapes present in the first 5 frames

In the first 5 columns of Ψ , there are modal shapes present. However from Ψ_6 onwards, these shapes have become disturbed, and do not particularly resemble clear mode shapes like the initial 5 Ψ plots. When compared to the peaks picked from S , there are some shapes which are undescribed in the PP method. This suggests that the columns of Ψ are containing more than

1 mode, with a small number of modes dominant in the smaller singular values. The shapes seen from the columns of Ψ_6 onwards are likely to be combinations of multiple modes seen in the Peak Picking method. The singular value transfer functions Ξ associated with these higher order frequencies contain contributions from multiple modes. This is likely due to overlapping and degenerate modes, as there is a lack of damping, as well as an under-sampling in terms of ratio of spatial sampling positions to bending wavelength.

6.2.1 Influence of reduction in grid resolution

As seen in the beam experiments, insufficient spatial resolution renders poorly described mode shapes and multiple mode involvement in the singular values, resulting in multiple peaks in Ξ_i . As the plate has been well described, with sampling positions at 0.05m in the x direction and 0.047m in the y direction which have allowed a fairly good description of a number of mode shapes in Ψ , the data has been reduced to contain less sampling positions. This will give information as to how the method will be affected by a sparser spatial sampling.

6.2.1.1 6 remaining rows

7 of the 13 rows of the transfer function matrix have been removed, leaving rows 2, 4, 6, 8, 10, and 12, and giving 114 response positions across the plate.

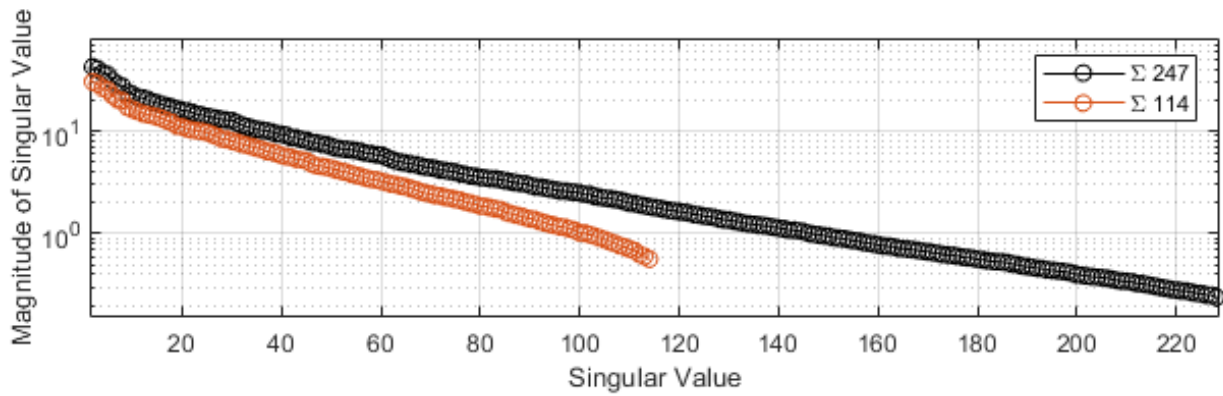


Figure 6.15: Diagonal of Σ , showing singular values for full dataset of 247 response positions, and with 6 remaining rows, giving 114 response positions, in red.

Figure 6.15 compares the diagonal of Σ for the original full dataset in black, and for the 6 row dataset in red. There are 114 singular values on the diagonal of Σ for the 114 response position case. When compared to the full dataset, there is a slight reduction in magnitude, with a steeper slope down to the last singular value.

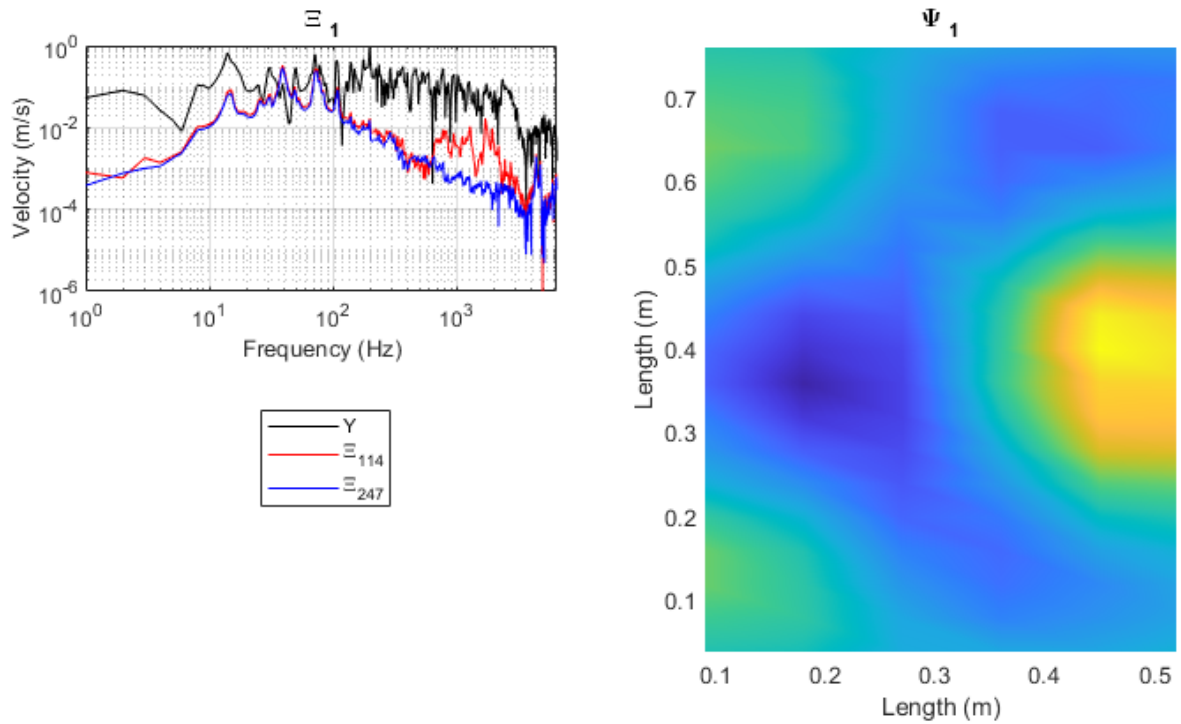


Figure 6.16: Singular transfer function Ξ_1 and Ψ_1 for reduced Y with 6 remaining rows of responses. The left hand plot shows Ξ_1 plotted against Y , with Ξ for 114 responses in red, Ξ for 247 responses in blue, and Y in black. The x-axis is velocity in metres per second and the y-axis is frequency in Hertz. The right hand plot shows the associated mode with the Ξ transfer function, Ψ_1 , plotted by the plate dimensions.

Very little difference can be seen in the first transfer function Ξ_1 for 6 remaining rows when compared to the full dataset in Figure 6.16. There is a stronger anti-resonance at approximately 5 kHz in the Ξ_1 function, and there is an increase in velocity between 900 Hz and 3 kHz. The overlapping peaks are the same, and though Ψ_1 for 6 remaining rows appears slightly less detailed, there is still a clear description of the shape seen for the full dataset.

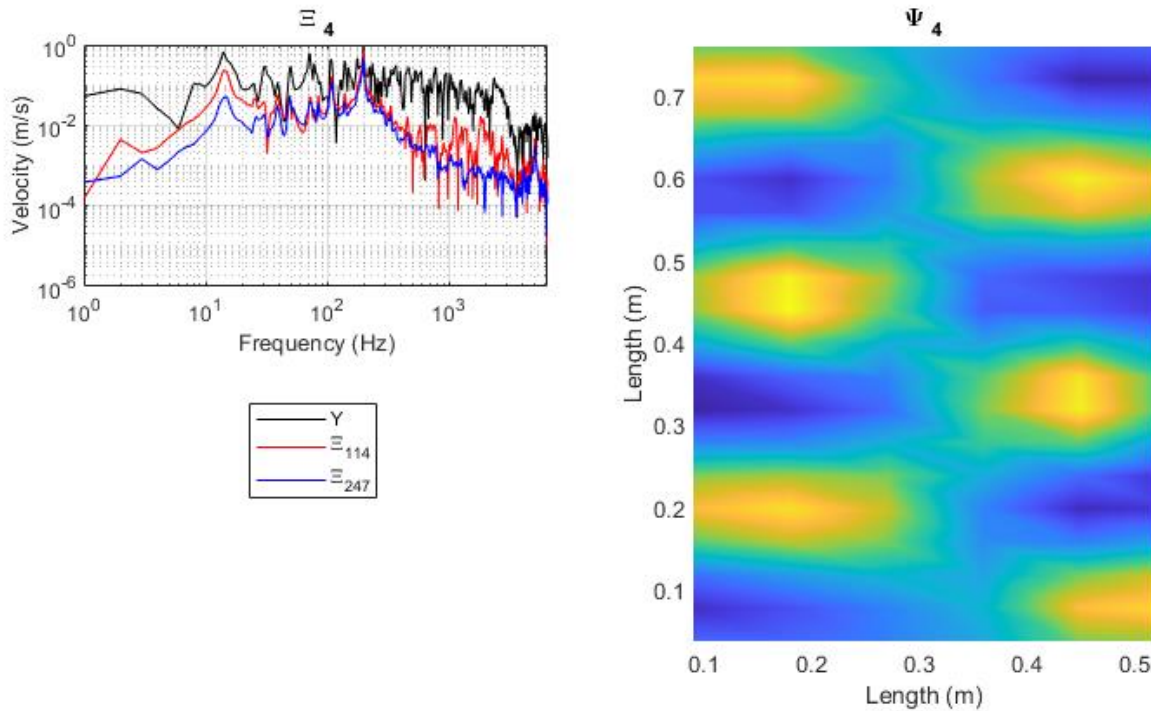


Figure 6.17: Singular transfer function Ξ_4 and Ψ_4 for reduced Y with 6 remaining rows of responses. The left hand plot shows Ξ_4 plotted against Y , with Ξ for 114 responses in red, Ξ for 247 responses in blue, and Y in black. The x-axis is velocity in metres per second and the y-axis is frequency in Hertz. The right hand plot shows the associated mode with the Ξ transfer function, Ψ_4 , plotted by the plate dimensions.

In Figure 6.17, the singular transfer function Ξ_4 , with the associated mode shape Ψ_4 also show strong similarities to the complete dataset with 13 rows. When compared to the Ξ_4 for the complete dataset, the peak at around 15 Hz is closer to that of Y in this case, with slightly higher velocity shown at the frequencies between 10 Hz and 50 Hz. In the higher frequencies, there appear to be more anti-resonances in the 6 row Ξ_4 , further indicating that there is more modes or frequencies associated with the singular values for the reduced Ξ functions. The mode shape described by Ψ_4 here is the same order mode seen for the complete dataset, though it has a smeared appearance, indicating that the lower spatial sampling resolution is not defining the mode sufficiently, with potentially more involvement from other frequency elements included in the Ξ function.

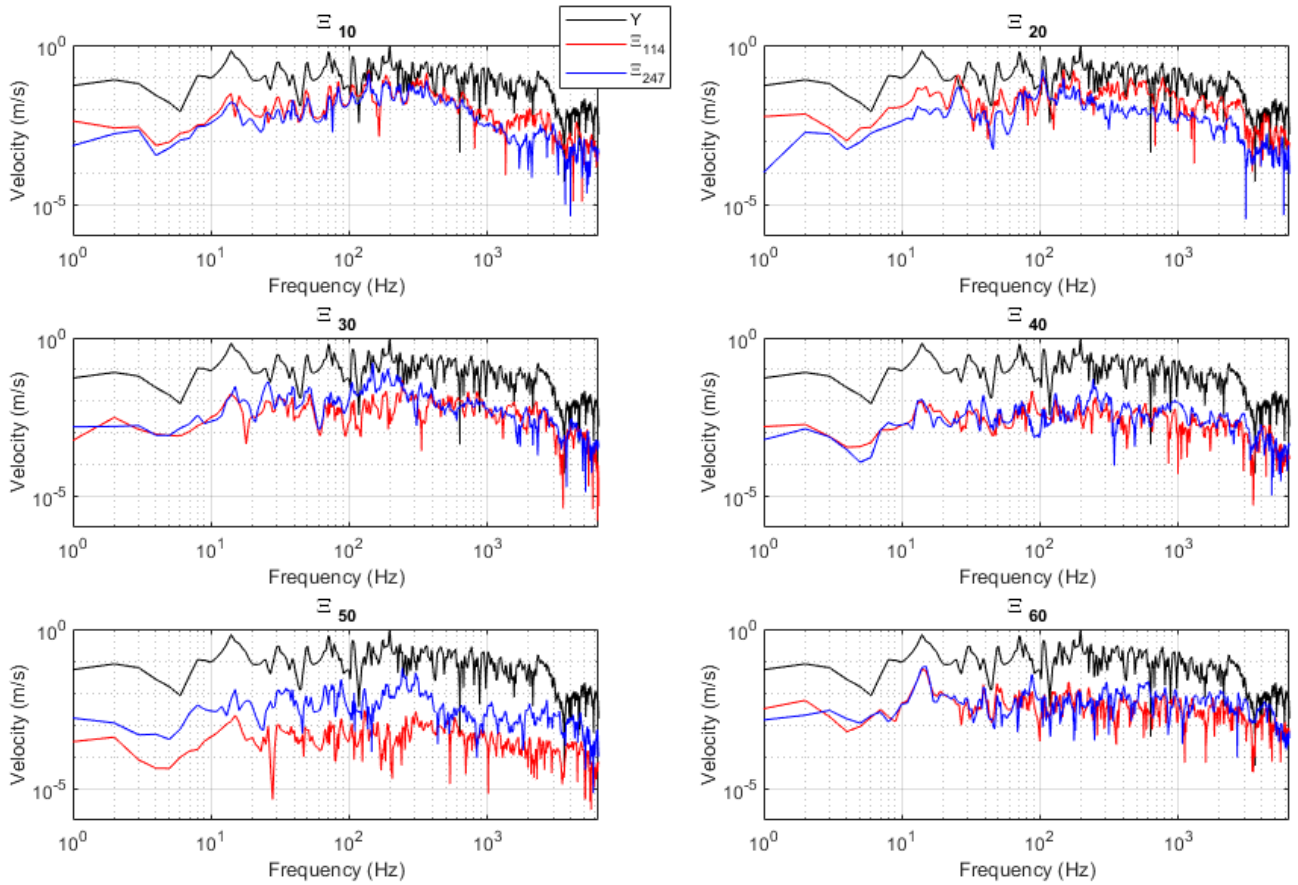


Figure 6.18: Singular transfer functions Ξ_{10} , Ξ_{20} , Ξ_{30} , Ξ_{40} , Ξ_{50} , and Ξ_{60} compared to Y for a reduction to 6 rows remaining in Y , with Ξ for 114 responses in red, Ξ for 247 responses in blue, and Y in black. The x-axes are frequency in Hertz and the y-axes are velocity in metres per second.

There are some subtle differences when looking at this sample of Ξ functions and comparing to the full dataset Figure 6.18. Ξ_{50} has very little connection with Y , with only very slight overlap at anti-resonances at around 55 Hz and 4 kHz, whereas there were more overlaps for the complete dataset at lower magnitude anti-resonances.

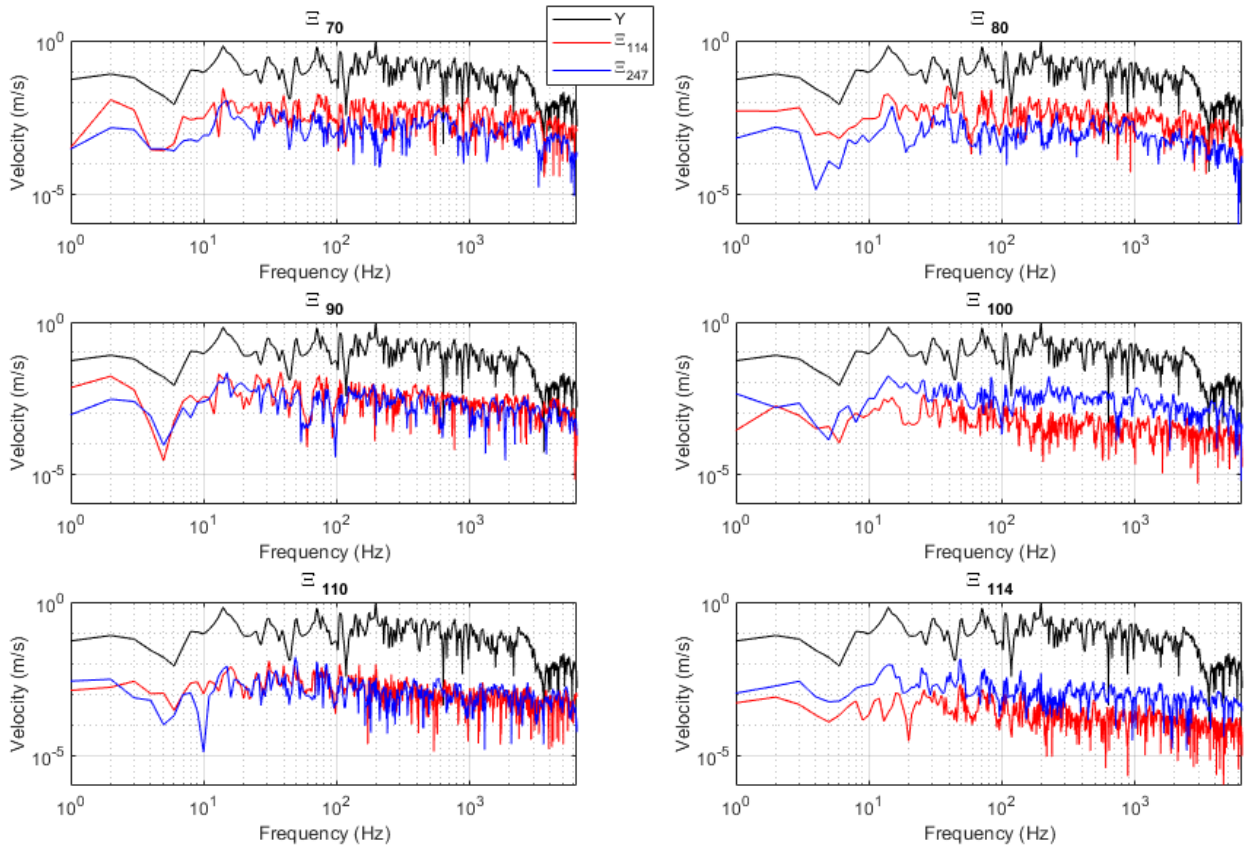


Figure 6.19: Singular transfer functions Ξ_{70} , Ξ_{80} , Ξ_{90} , Ξ_{100} , Ξ_{110} , and Ξ_{114} compared to Y for a reduction to 6 rows remaining in Y , with Ξ for 114 responses in red, Ξ for 247 responses in blue, and Y in black. The x-axes are frequency in Hertz and the y-axes are velocity in metres per second.

Looking at the Ξ functions containing the smaller singular values Figure 6.19, a larger separation between Y and Ξ is visible. This is because there are now less singular values, and the singular values contain more modal information than for the complete dataset. The smaller singular values become less significant sooner, but retain necessary information. The final transfer function Ξ_{114} still retains some necessary information, where it overlaps with Y at around 4 kHz. When checking the data, all of the Ξ functions are required to reconstruct the original FRF, whereas in the beam chapter, not all of Ξ were needed when the sampling resolution was high.

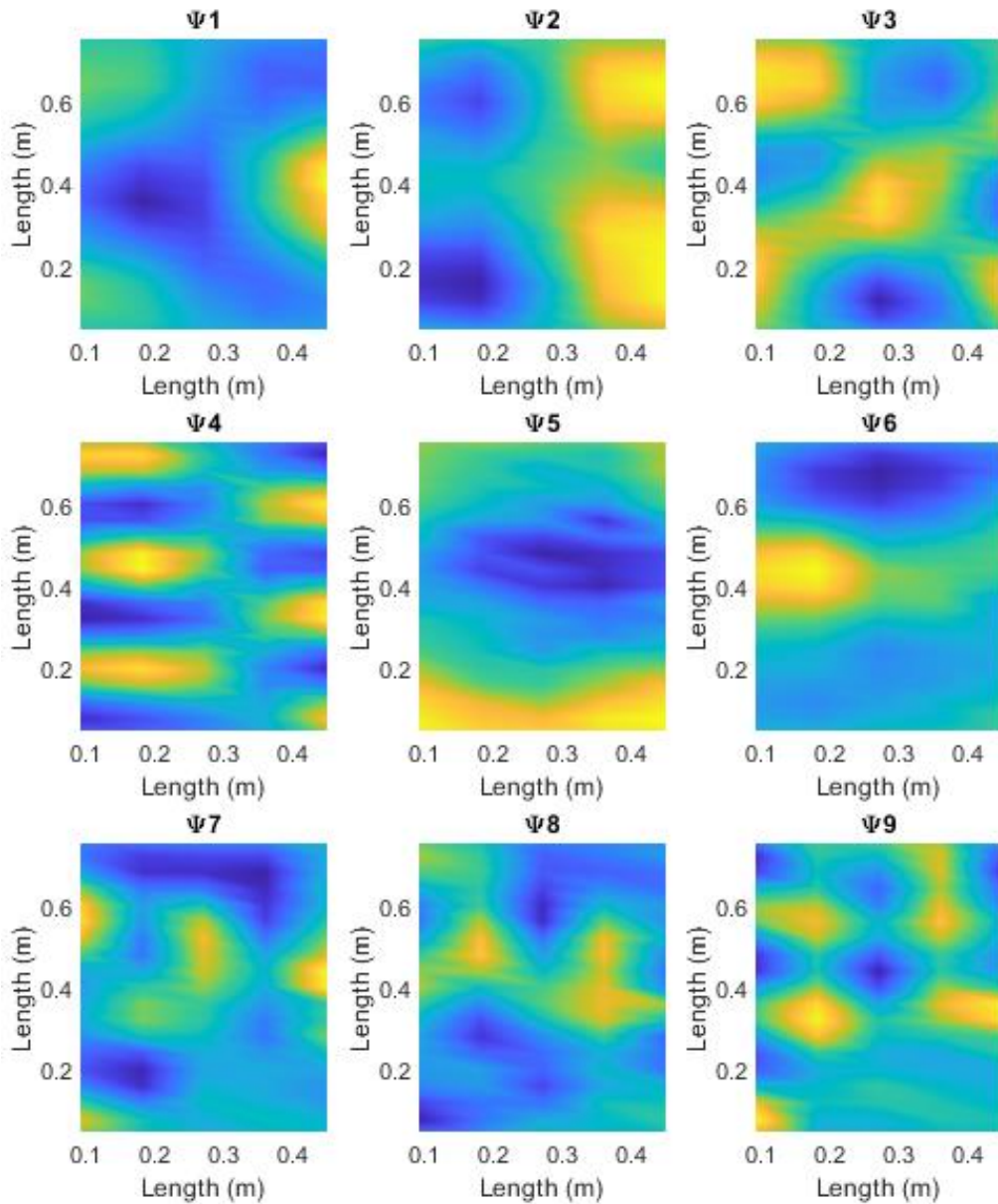


Figure 6.20 Ψ_1 to Ψ_9 mode shapes, plotted in terms of plate dimensions for 114 response positions

The first 5 mode shapes of Ψ for 114 in Figure 6.20 show a great resemblance to the Ψ mode shapes for the full dataset shown in Figure 6.14. Ψ_3 and Ψ_4 appear to be undescribed at the edges, however the general shape remains the same. Above Ψ_5 , like with the full dataset, there are no longer modal shapes present. A reduction to 6 rows does not seem to have made a huge difference to the SVD outcomes compared to the original 13 row data.

6.2.1.2 3 remaining rows

Following from the 6 remaining row investigation, the data is further reduced to contain only three rows of 19 responses, giving a total of 57 response positions on the plate. The rows remaining are rows 2, 6, and 10, allowing a degree of coverage across the upper, middle, and lower regions of the surface of the plate spatially, however there are now only 3 columns of 19 sensors, which is likely to have a significant effect on the content of the singular values.

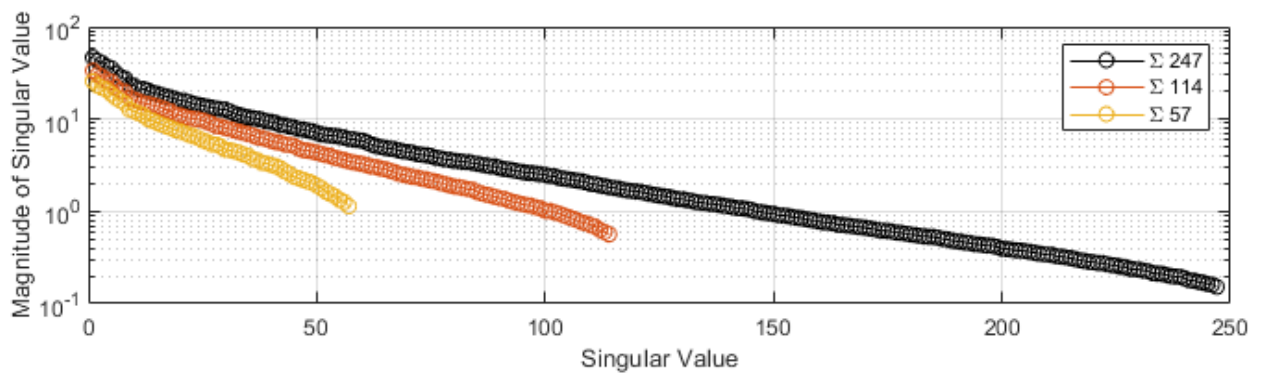


Figure 6.21: Diagonal of Σ , showing singular values for full dataset of 247 response positions, with 6 remaining rows, giving 114 response positions, in red, and with 3 remaining rows giving 57 positions, in yellow.

As with the reduction in sampling positions to 114, the singular values on the diagonal of S show a further reduction in magnitude, and a steeper drop towards the last singular values for the 57 position case, shown in Figure 6.21. There is therefore more modal information contained in each singular value.

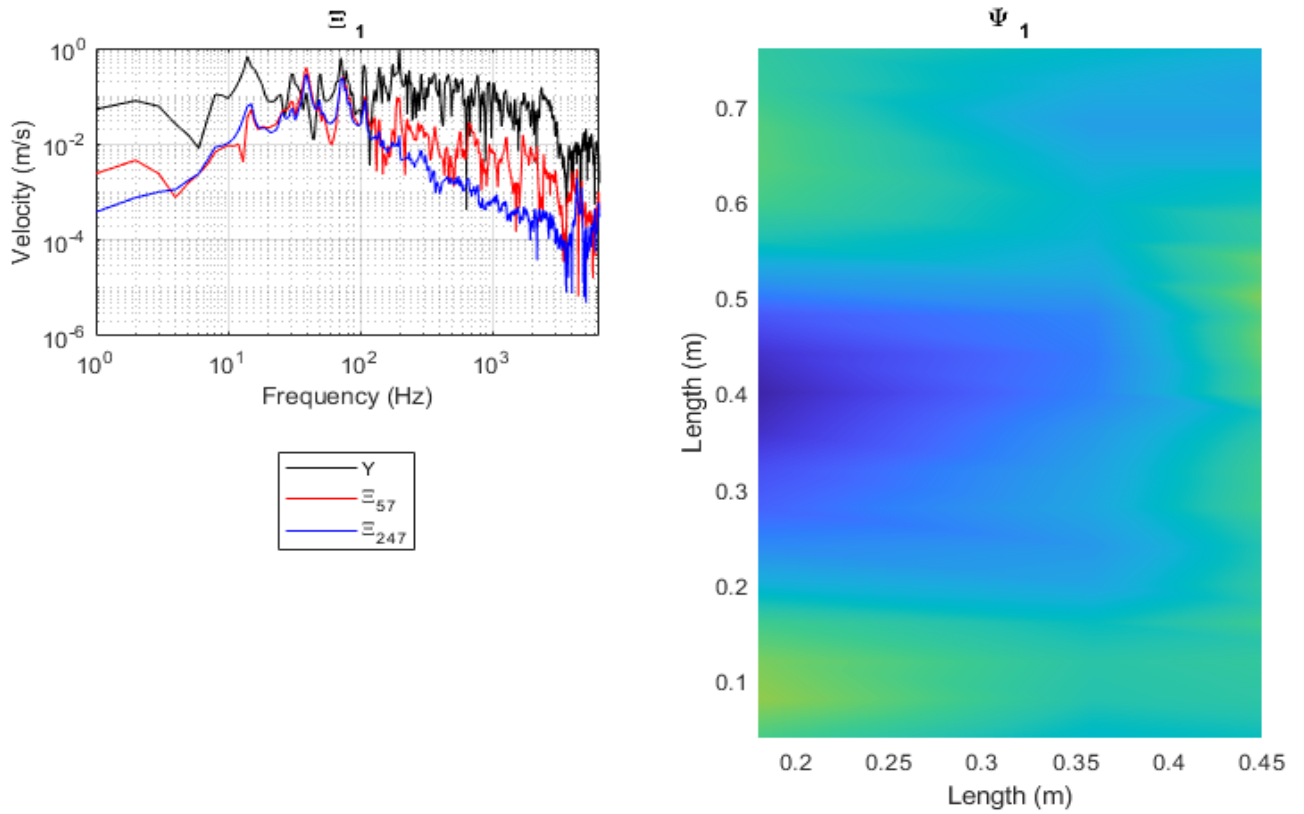


Figure 6.22: Singular transfer function Ξ_1 and Ψ_1 for reduced Y with 3 remaining rows of responses. The left hand plot shows Ξ_1 plotted against Y , with Ξ for 57 responses in red, Ξ for 247 responses in blue, and Y in black. The x-axis is velocity in metres per second and the y-axis is frequency in Hertz. The right hand plot shows the associated mode with the Ξ transfer function, Ψ_1 , plotted by the plate dimensions.

At first glance of Figure 6.22, Ξ_1 far more resembles Y than the complete dataset and the 6 remaining row results. There is obviously a considerable amount of the transfer function information in Ξ_1 , which is further reinforced by Ψ_1 . When compared to the previous Ψ_1 results, there is some visual resemblance, but there is not a clear mode shape present. This is indicative of under-sampling the plate surface; the spatial resolution is not fine enough for the mode shape, and there is more than one mode contained in the column of Ψ_1 .

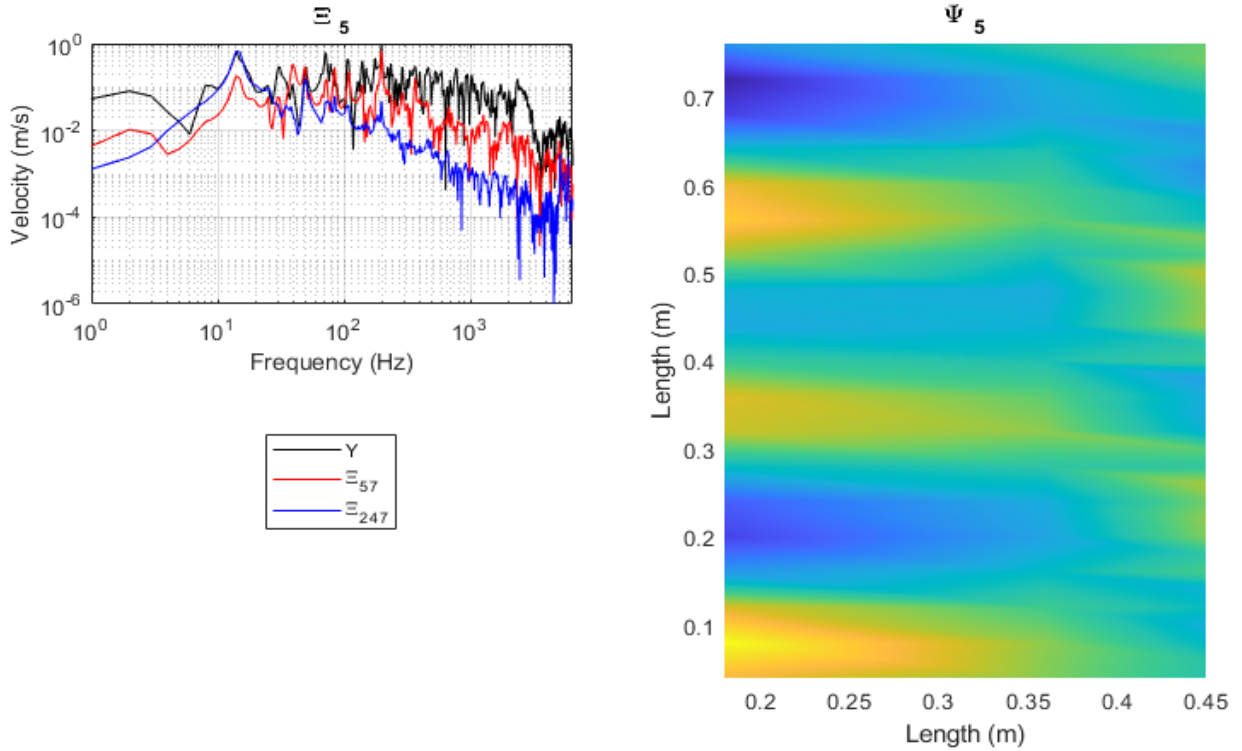


Figure 6.23: Singular transfer function Ξ_5 and Ψ_5 for reduced Y with 3 remaining rows of responses. The left hand plot shows Ξ_5 plotted against Y , with Ξ for 57 responses in red, Ξ for 247 responses in blue, and Y in black. The x-axis is velocity in metres per second and the y-axis is frequency in Hertz. The right hand plot shows the associated mode with the Ξ transfer function, Ψ_5 , plotted by the plate dimensions.

Whereas with the 114 position Ξ_5 and Ψ_5 results the first mode of the plate was visible, Ψ_5 has a very unclear approximate mode shape of a higher order for the 57 response positions, seen in Figure 6.23. Again, a significant amount of the original FRF is present in the transfer function Ξ_5 , which shows there is little to no separation of modes happening for the 3 row dataset.

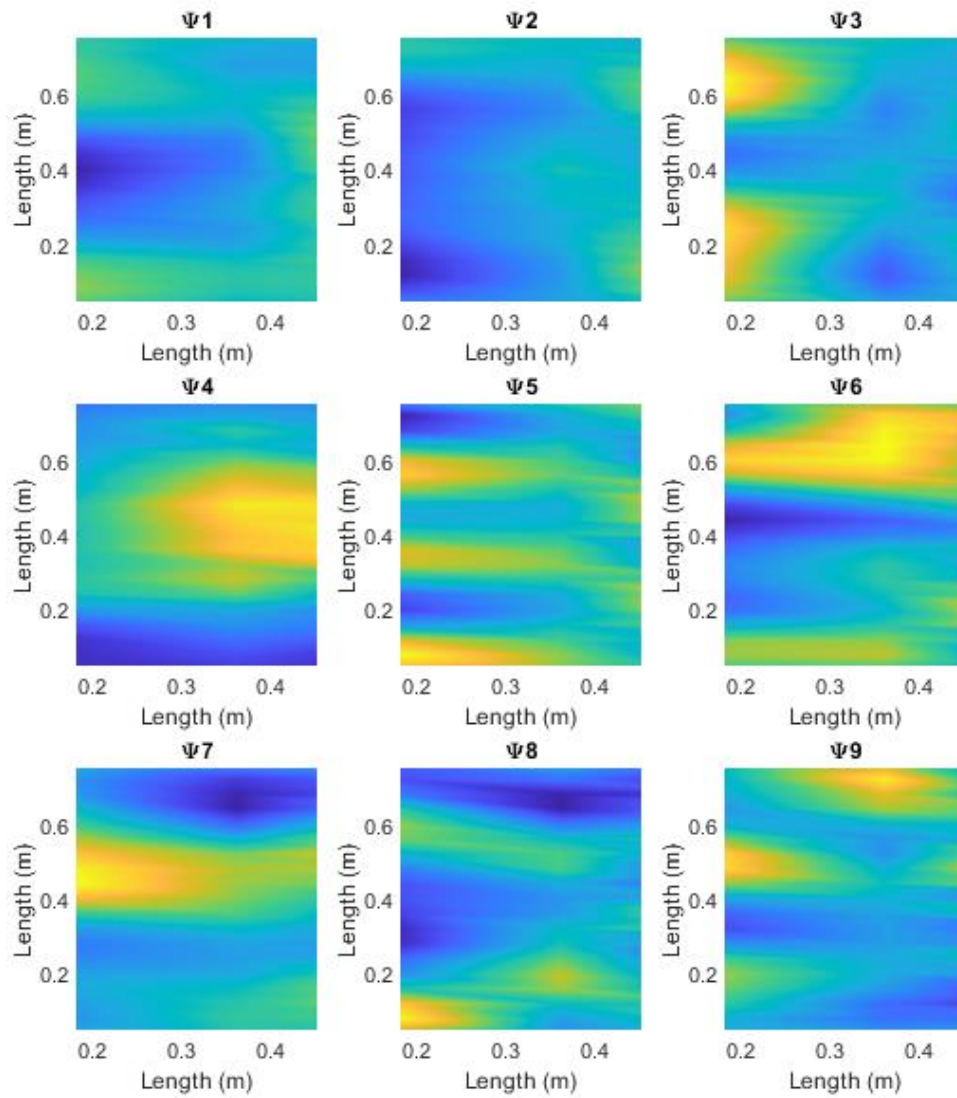


Figure 6.24: Ψ_1 to Ψ_9 mode shapes, plotted in terms of plate dimensions for 57 response positions

Compared to the Ψ mode shapes seen for the 247 and 114 response position cases, the columns of Ψ do not resemble modes at all for the 57 response position case, shown in Figure 6.24. This indicates that modal separation has not been achieved for any of the modes with the 3 row dataset. Potentially, Ψ_1 could be regarded as depicting the first mode of the plate, however there is not enough detail to render it a successful mode shape. Compared to the bending wavelength, this would indicate only the first mode can be characterised in the x-direction, with 3 sensors, which follows from 2.6 sensors per half wavelength determination.

6.3 Discussion

A scanning laser vibrometer has been used to characterise a plate in terms of transfer functions of velocity due to voltage for a single shaker excitation. A Peak Picking method using frequency by frequency SVD was used to determine the plate modes from the peaks given by the S matrix. New transfer functions containing the contribution of a single singular value have been constructed using a Location vs Frequency SVD, and the dataset has been altered to reduce the spatial sampling resolution to observe the effects of insufficient surface discretisation on the modal separation in the singular values. Though the surface was discretised by a 13x19 grid of 247 response positions, there still appeared to be multiple modes present in the new transfer functions \mathcal{E} . However, clear mode shapes were evident in the columns of Ψ , suggesting that despite there being more than one mode in the singular value, the initial modes of the system could be described up to $f_{5,5}$, with 2.6 sampling positions per node in the x-direction, and in the y-direction, 3.8 sampling positions per node. This relates to the literature in that 2 elements per wavelength are needed to capture the nodes, though 6 to 10 are needed for the complete separation of modes using SVD [76], [166].

When the dataset was altered to contain only 6 rows of responses, giving 114 response positions. The effect on the mode shapes described by Ψ were not significant, though the mode shapes became slightly smeared in appearance. From \mathcal{E} , it could be seen that the transfer functions contained slightly more FRF information than for the complete dataset. When the data was further reduced to 3 remaining rows leaving 57 response positions, the mode shapes described by the columns of Ψ are destroyed. Despite there being the same samples per wavelength in the y-direction, the reduction to only 3 samples in the x-direction rendered all shapes non-existent, with the exception perhaps of the first mode. The \mathcal{E} transfer functions contain considerably more frequency peaks, with no distinctive singular modal

behaviour evident. To conclude, the experiment detailed here suggests that even at 257 response positions, the plate is not discretised sufficiently for the Ξ transfer functions to contain only a single mode. However, the poor results given by the 57 response position data is significantly less detailed than the 114 response position data. The 114 response position data, with 6 remaining rows of the original FRF matrix, does not have extremely different mode shapes present in Ψ than the full dataset. The results produced in this chapter will be used to make considerations for the experiment detailed in the next two chapters, with specific attention to adding damping to the plate in an effort to aid the separation of modes. As the next experiment aims to use a sparse grid resolution, as will be the case in the intended application, it is likely that very few modes will be accurately described by the columns of Ψ . Similarly, seeing as the comparatively dense sampling position resolutions described in this chapter did not show a significant drop-off or knee in the singular values, it is likely that the separation of modes may not be successful. The rearrangement of the grid will be explored in Chapter 8, with an array of 6 columns of 4 sensors. Potentially, the redistribution of sensors over the surface, rather than having densely sampled columns, may improve on the 3 row laser case. However, with only 4 sensors in the x-direction, there may only be the first order mode shape accurately described.

7 PREDICTION OF RADIATED SOUND USING THE BLOCKED FORCES METHOD AND VOLUME VELOCITY SOURCE

7.1 Introduction

In this chapter, the blocked forces/ pressures of the aluminium plate are used in conjunction with the vibro-acoustic transfer functions to predict the radiated noise from the plate to the various microphones, using both the hammer and the volume velocity source. To maintain the integrity of the signal between the plate surface and the response microphones, a baffle lined with acoustically absorbent panels has been added. However, due to the compliance of the baffle, it has increased the radiation of the plate at low frequencies. This is most likely due to insufficient isolation between the frame and the baffle, with effects of flanking. For that reason, the results in the next two chapters neglect frequencies below 100 Hz, as these frequencies are deemed to be under the influence of the baffle rather than a true description of the radiated pressure from the surface of the plate. The plate has had damping added, as shown in Chapter 2, with the aim to increase the separation of modes. Due to this damping, the damping ratio ζ of the plate has been recalculated as 0.3653, with the loss factor η now being 0.0581. These values, though more damped than the laser experiment, still render the plate with relatively little damping. This is based on the half bandwidth method described in Equations (42- 44), with a centre frequency of 787 Hz, f_1 as 737 Hz, and f_2 of 1312 Hz. The critical frequency of the plate is recalculated to 3.5 kHz to account for the damping using $f_{c,D} = f_c \sqrt{1 - \zeta^2}$, where f_c is the un-damped critical frequency of the plate at 3.8 kHz.

The shakers were mounted on the plate with considerations for their distance from the edges and proximity to accelerometers within the accelerometer array. Attaching the shakers too

near to the accelerometers may have induced overload during the operational measurements, and compromised the signal to noise ratio. The shakers were positioned non-symmetrically on either half of the plate, with the hopes that these positions would allow for the excitation of different plate modes. The force reference is used in these transfer functions, as opposed to the voltage reference. This was chosen due to it producing more resonances on the plate, as the voltage reference did not appear to maintain resonances present in the measurements. As there is not significant differences in the results using the different shakers, or combinations of shakers, only Shaker 1 is analysed in this thesis.

7.2 Blocked Forces Method for the Prediction of Radiated Sound

As described in Chapter 2.2, these are the product of the inverse accelerance matrix of force to accelerometer transfer functions, and the operational shaker vector of force to acceleration transfer functions. These are multiplied by the vibro-acoustic transfer functions for each method of excitation to predict the radiated noise. Presented are a selection of results which describe the accuracy of the blocked forces predictions using the reciprocal volume velocity source compared to the direct hammer excitations.

Shaker 1 is located centre-right of the face of the plate when viewed from the upper surface. The radiated noise predictions using the directly measured hammer transfer functions and the reciprocally measured volume velocity source transfer functions are compared to the measured transfer functions for Shaker 1 to the microphone positions to the plate. Firstly, determination of the valid frequency range must be conducted.

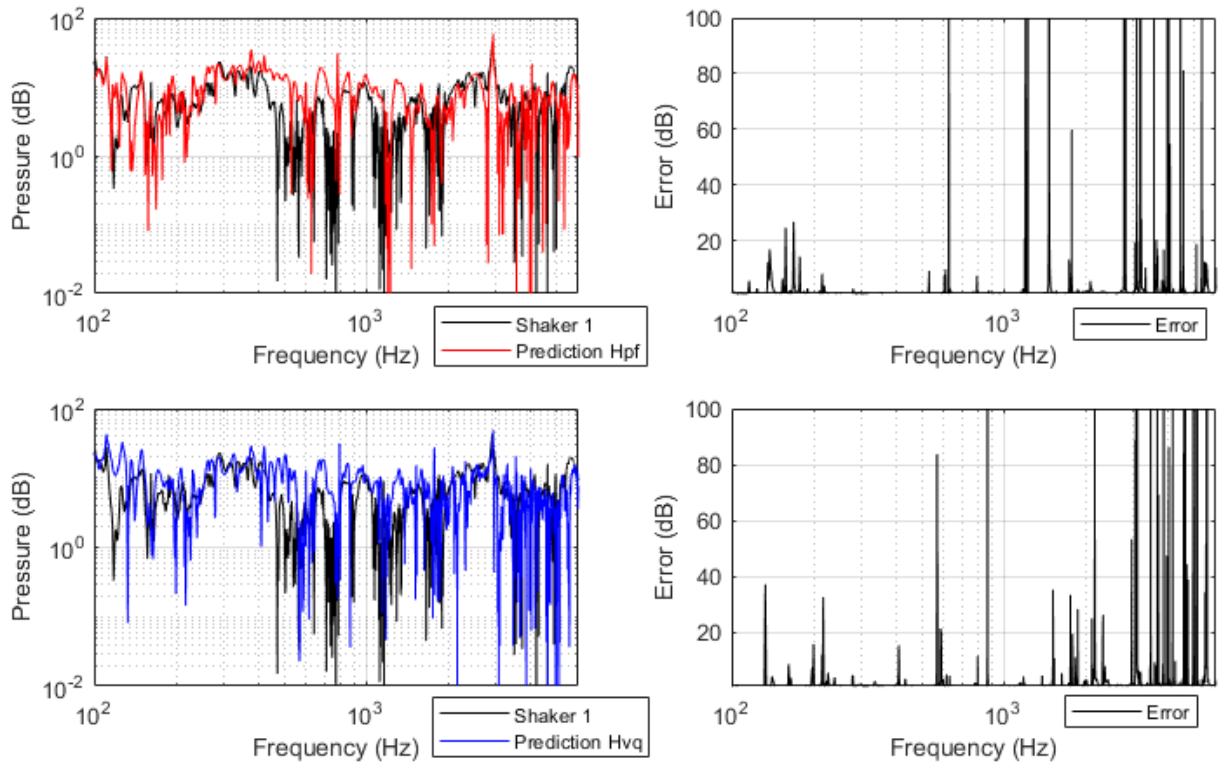


Figure 7.1: Predicted radiated pressure for H_{pf} and H_{vq} , plotted against measured pressure for Shaker 1 at microphone positioned at 30° . The x-axis shows frequency in Hertz between 10 Hz and 6 kHz, and the y-axis shows pressure in dB, of the magnitude of the transfer functions. The upper plots show the measured shaker response in black and the predicted pressure calculated using H_{pf} in red, with the error in second frame. The lower plots show the measured shaker response in black and the pressure calculated using H_{vq} in blue, with the error in the final plot

The predictions of radiated sound for H_{pf} and H_{vq} , shown in dBs of the transfer functions of pressure due to force in Figure 7.1, show most accuracy between 100 Hz and 1.5 kHz. Above 1.5 kHz, there are significant errors, though the peak at 3 kHz is described by each prediction. There is a considerable under-prediction for anti-resonances with both methods. As neither source shows accuracy above 1.5 kHz, the following results will show predictions for between 100 Hz and 1.5 kHz.

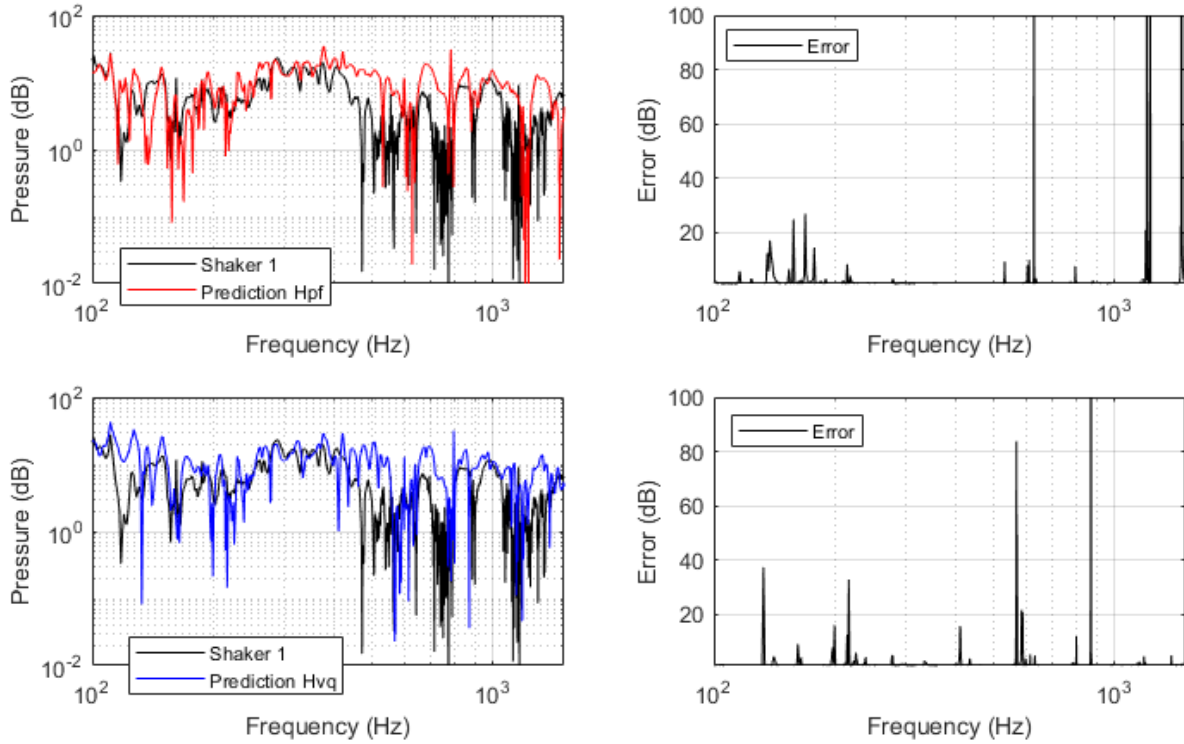


Figure 7.2: Predicted radiated pressure for H_{pf} and H_{vq} , plotted against measured pressure for Shaker 1 at microphone positioned at 30° . The x-axis shows frequency in Hertz between 100 Hz and 1.5 kHz, and the y-axis shows pressure in dB. The upper plots show the measured shaker response in black and the predicted pressure calculated using H_{pf} in red, with the error in second frame. The lower plots show the measured shaker response in black and the pressure calculated using H_{vq} in blue, with the error in the final plot.

The frequency range for the 30° position has been reduced to 100 Hz- 1.5 kHz in Figure 7.2.

In this range, the majority of errors are below 20 dB, with some anti-resonances over-predicted below 500 Hz, and unaligned anti-resonances above 800 Hz. The errors are comparable for both methods of excitation. Overall, there are 4 errors over 20 dB in the volume velocity source prediction, and 5 in the hammer prediction.

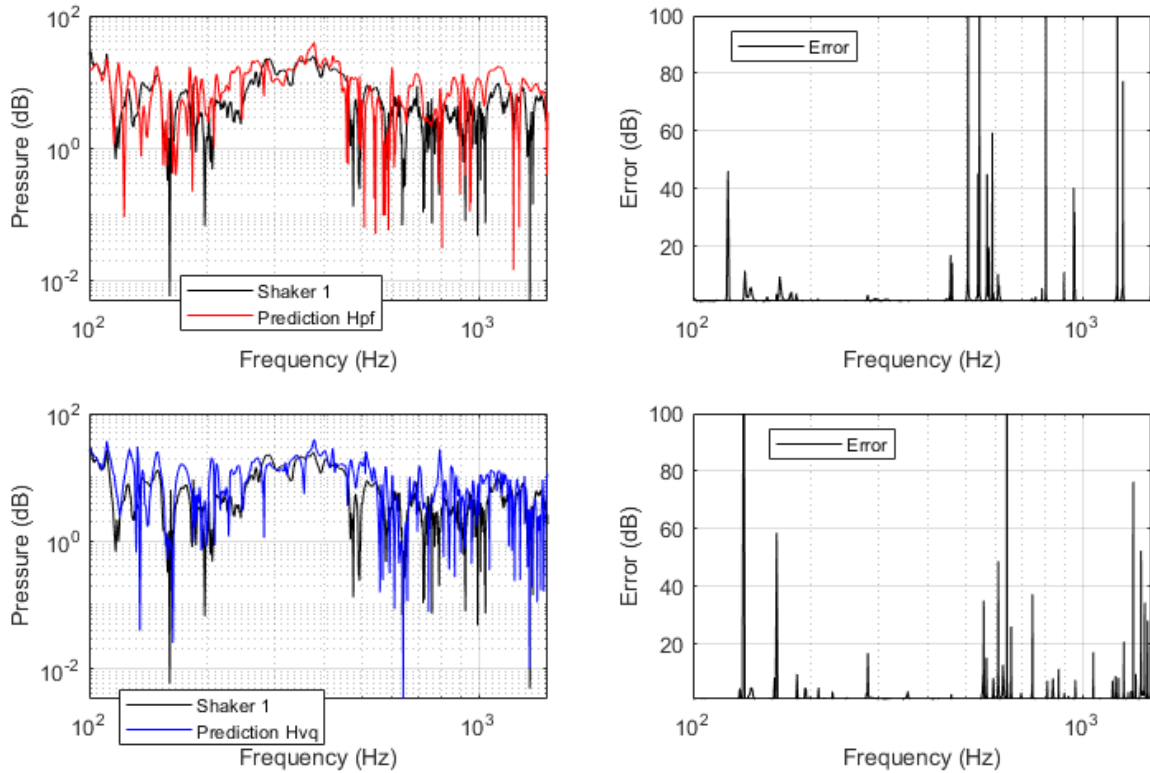


Figure 7.3: Predicted radiated pressure for H_{pf} and H_{vq} , plotted against measured pressure for Shaker 1 at microphone positioned at 0° . The x-axis shows frequency in Hertz between 100 Hz and 1.5 kHz, and the y-axis shows pressure in dB. The upper plots show the measured shaker response in black and the predicted pressure calculated using H_{pf} in red, with the error in second frame. The lower plots show the measured shaker response in black and the pressure calculated using H_{vq} in blue, with the error in the final plot.

For the 0° position, the results are again comparable for the two excitation methods, shown by Figure 7.3. There is a large error in both methods in the region of 120 Hz to 200 Hz, where the volume velocity source prediction contains a significant antiresonance not present in the measured response. The antiresonance at 160 Hz has been slightly missed by the volume velocity source prediction, with the anti-resonance in the prediction at 163 Hz. The anti-resonance has not been fully characterised by the hammer prediction, but has a less significant error. There are significant errors in both plots above 500 Hz. This is potentially due to some of the structural modes radiating highly to the 0° microphone from the surface of the plate, despite them not being adequately excited by the hammer and volume velocity source. The radiation of the modes increases as frequency approaches f_c the critical

frequency, which despite being outside the measurement range, the effect is that of some frequencies radiating from the surface of the plate more strongly when excited by the shaker are evident for the 0° microphone when approaching the critical frequency. This may also be due to non-linearities in the shaker excitation, which would be more obvious at this response position, normal to the plate.

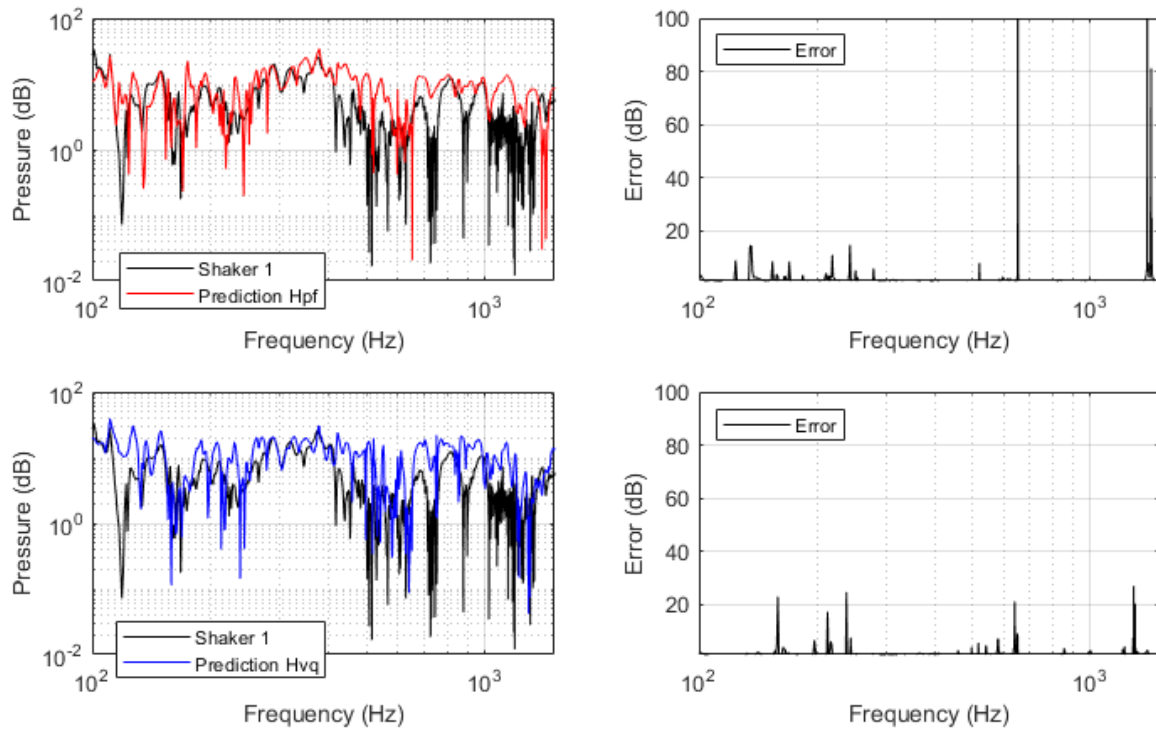


Figure 7.4: Predicted radiated pressure for H_{pf} and H_{vq} , plotted against measured pressure for Shaker 1 at microphone positioned at 60° . The x-axis shows frequency in Hertz between 100 Hz and 1.5 kHz, and the y-axis shows pressure in dB. The upper plots show the measured shaker response in black and the predicted pressure calculated using H_{pf} in red, with the error in second frame. The lower plots show the measured shaker response in black and the pressure calculated using H_{vq} in blue, with the error in the final plot.

The predictions for the 60° position are improved for both methods, as shown by Figure 7.4. There are 2 significant errors of high magnitude in the hammer prediction, with the remaining errors below 20 dB. There are 4 errors just above 20dB in the volume velocity source prediction, however overall the volume velocity source has the closer prediction.

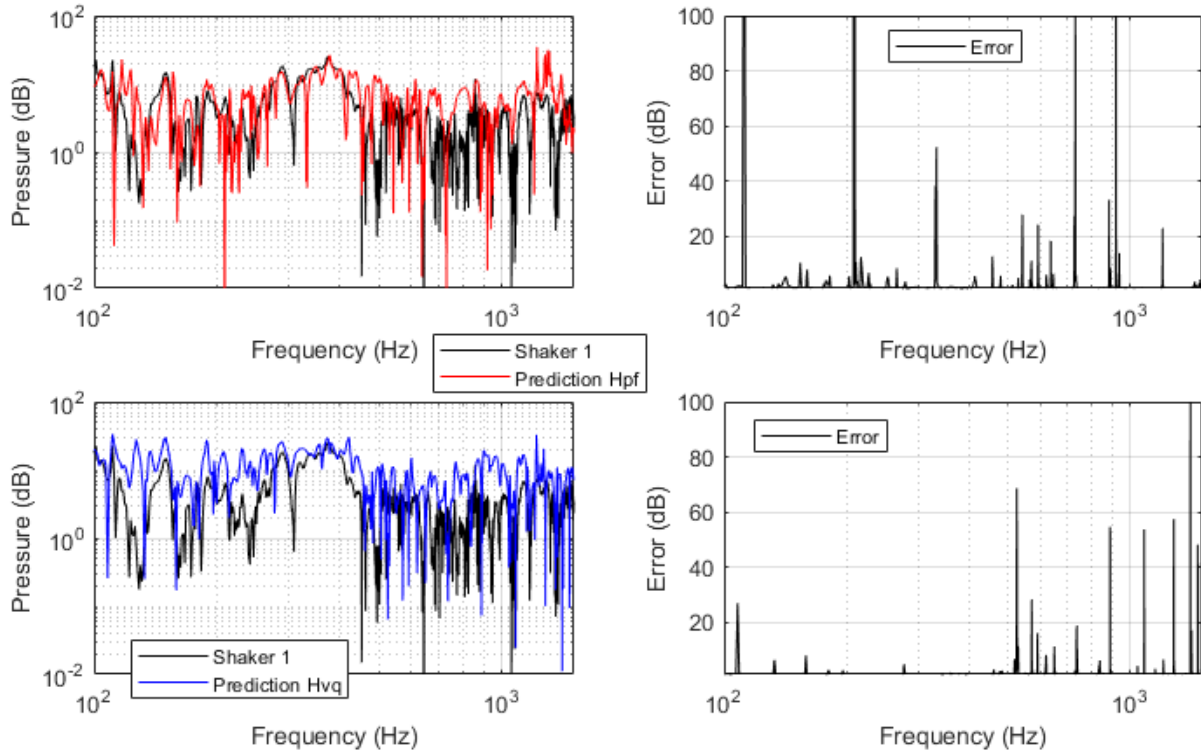


Figure 7.5: Predicted radiated pressure for H_{pf} and H_{vq} , plotted against measured pressure for Shaker 1 at microphone positioned at 90° . The x-axis shows frequency in Hertz between 100 Hz and 1.5 kHz, and the y-axis shows pressure in dB. The upper plots show the measured shaker response in black and the predicted pressure calculated using H_{pf} in red, with the error in second frame. The lower plots show the measured shaker response in black and the pressure calculated using H_{vq} in blue, with the error in the final plot.

Finally, the predictions for the microphone position at 90° is shown in Figure 7.5. There are some significant errors in both methods. However, the volume velocity source has the best agreement up to 500 Hz, with errors across the frequency range for the hammer prediction. As this microphone was pointing at the side of the plate, there is potential that radiation from the baffle has caused interference to the measured pressure, and perhaps also to the hammer artificial excitation, if the hits were strong enough to excite the baffle.

7.3 Discussion

The blocked forces method has been shown for the prediction of radiated noise from the plate excited by a shaker to multiple response microphones in an anechoic chamber, for which a comparison was made between the predictions using the directly measured H_{pf} transfer

function from a metal hammer tip at the accelerometer positions on the plate, and the reciprocally measured transfer function H_{vq} , using a volume velocity source at the receiver positions.

The results show that the volume velocity source is of comparable accuracy when used in this manner, and can be deemed suitable for collecting the airborne vibro-acoustic transfer functions when conducting noise prediction using the blocked forces method. Both excitations are most accurate between 100 Hz and 1.5 kHz, rendering the volume velocity source a comparable alternative to the impact hammer for these measurements.

There are many instances in the literature where the blocked forces method has been used to predict the radiated sound from a structure, with the results generally being presented over a relatively limited frequency range. For example, a range of 10 Hz to 1kHz is shown to have errors up to 20 dB in one study [123], with another study exhibiting 20 dB errors over a range of just 250 Hz to 700 Hz [167]. It is also most likely these two methods employed regularisation through singular value discarding, which removes the smallest singular values from a matrix to improve predictions, whereas no regularisation has been used in this thesis. Therefore, the results are deemed comparable to those in the literature, considering the wider frequency range analysed.

Further refinement of the volume velocity source design may result in improvement and further agreement between the two methods. Overall, depending on access limitations to the device under test, the volume velocity source could provide an alternative to the modal hammer method for the vibro-acoustic transfer function measurement. An advantage of this would be that once the blocked forces of the system have been measured, the volume velocity source could be used instead of a direct measurement on the actual assembly for the airborne aspect of the prediction. As the volume velocity source is activated at each of the remote response positions, rather than the positions on the device, this may be a more efficient

method. In the case of a heavily discretised assembly, with a single remote response position, this would mean a single measurement from the response position rather than a full set of transfer functions needing to be individually excited with a modal hammer. This has implications for reduced fatigue for the operator, and also may allow for those with less modal testing experience to gain satisfactory results, as the volume velocity source operation requires less practice and experience than making accurate and clear modal hammer excitations. With regards to the damping of the plate, one would expect better results at a somewhat higher frequency range, with less severe anti-resonances, which suggests that the damping is insufficient.

In the next chapter, the volume velocity source will be used for prediction of individual singular value contributions to the radiated noise using the LvF SVD to decompose H_{vq} , with the decomposed transfer functions used in place of H_{vq} in the blocked forces noise prediction equation. As the 60° excitation position provided the least error in the blocked forces predictions, this angle will be used for the next chapter.

8 PREDICTION OF RADIATED NOISE USING AN SVD APPROACH TO THE BLOCKED FORCES METHOD

8.1 Introduction

In this chapter, the \mathcal{E} transfer function method discussed in Chapters 4, 5, and 6 is applied to a vibro-acoustic FRF. This decomposed FRF is then used in place of the undecomposed transfer function in the blocked forces prediction. The volume velocity source is used to measure the FRF reciprocally. As the least error was seen in the H_{vq} predictions for the 60° position, this FRF will be used in these predictions. As Chapter 7 determined that the most accurate frequency range was between 100 Hz and 1.5 kHz, this range will again be used.

8.2 Decomposed Transfer Functions \mathcal{E}

From the SVD on H_{vq} , the matrices of Ψ and Σ can be used as an indication of the contents of the \mathcal{E} transfer functions. Firstly, the singular values on the diagonal of Σ are evaluated.

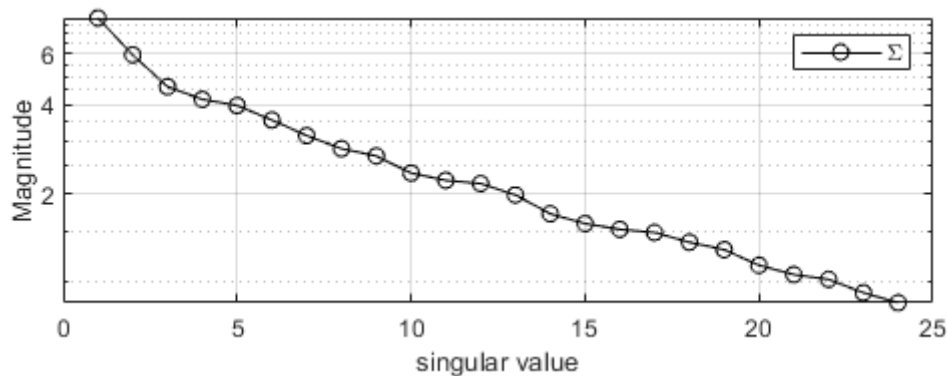


Figure 8.1: Plot of the singular values σ on the diagonal of singular value matrix Σ . The y-axis is magnitude and the x-axis is σ

Looking at the singular values on the diagonal of Σ in Figure 8.1, a steady decline in magnitude is evident, which explains that as the position of each singular value increases, it contains less information than the previous singular value. For σ_{24} , the magnitude is at zero,

suggesting no contribution has been made in terms of picking out any significant information. There is no distinct drop-off indicating sufficient description and separation of the dominant modes. The first singular value is of the highest magnitude, indicating that potentially only the first mode of the plate is described, which with respect to the bending wavelength, would have 4 samples per half wavelength in the x direction and 6 samples in the y.

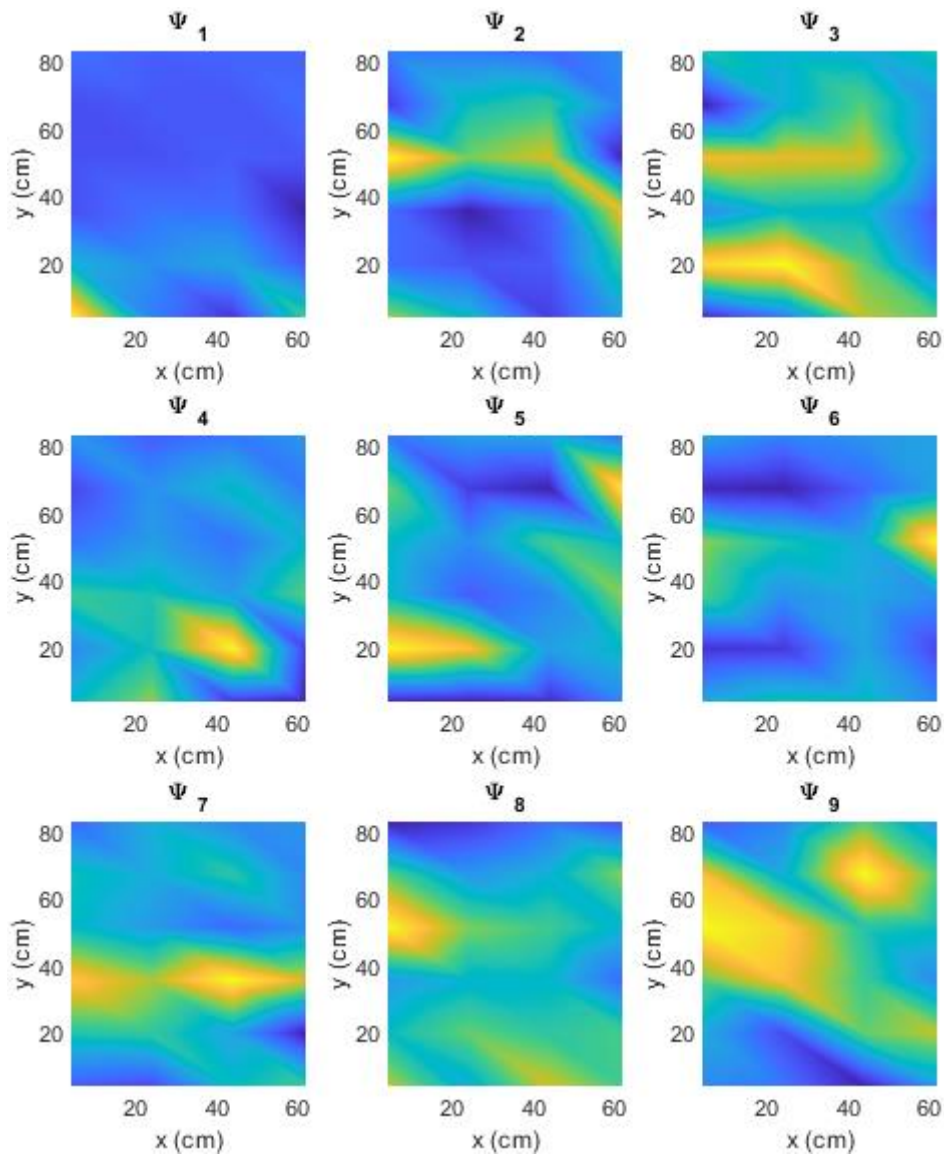


Figure 8.2: First 9 Columns of Ψ which should contain the mode shapes of the plate, plotted in terms of plate dimensions. Shown are the shapes of Ψ for the volume velocity source at an angle of 60° . Due to under-sampling, the shapes are disturbed.

Seen in Figure 8.2 are the columns of Ψ , from Ψ_1 to Ψ_9 . Like the results seen in the reduced laser experiments, the mode shapes are not clearly described. As indicated by the dominant

1st singular value, Ψ_1 could reasonably be interpreted as the breathing mode of the plate. Due to the spatial resolution, none of the further modes appear.

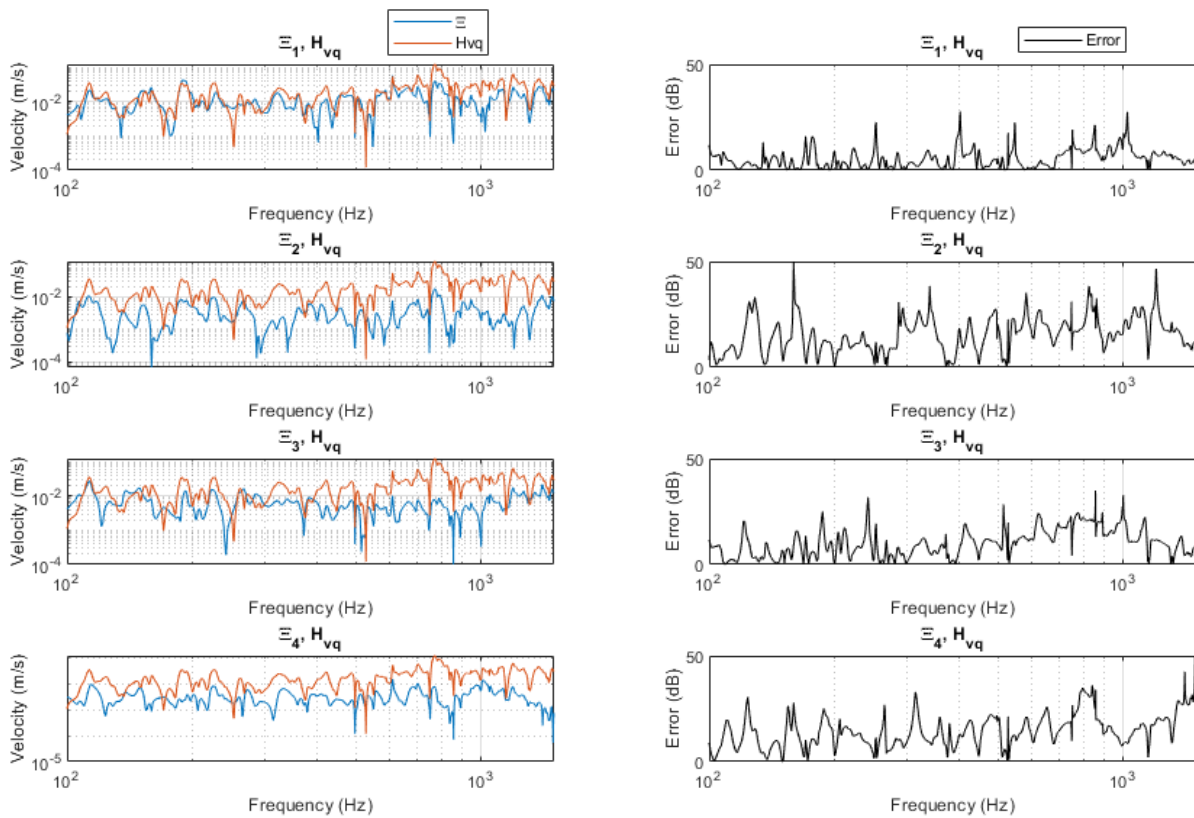


Figure 8.3: The left hand frames depict the single singular value transfer functions Ξ_1 to Ξ_4 , plotted against the original, unchanged H_{vq} transfer function. The x axis is frequency in Hertz and the y axis is velocity in metres per second. The right hand frames show the difference error in dB for the corresponding Ξ with respect to H_{vq} .

The first 4 Ξ transfer functions quite clearly contain more than one modal element of the H_{vq} transfer function in Figure 8.3. Looking through the transfer functions, it can be seen that the first 4 Ξ are far more dynamic than the well separated out modes seen in the previous experiments which have higher surface discretisation resolution. Ξ_1 bears the most similarity to H_{vq} , indicating the substantial modal information described by the 1st singular value. The dB error for the 2nd Ξ onwards is relatively similar across the frequency range, further indicating the lack of modal separation. The large errors visible across the frequency range are due to the lack of information for those particular frequencies included in the singular values.

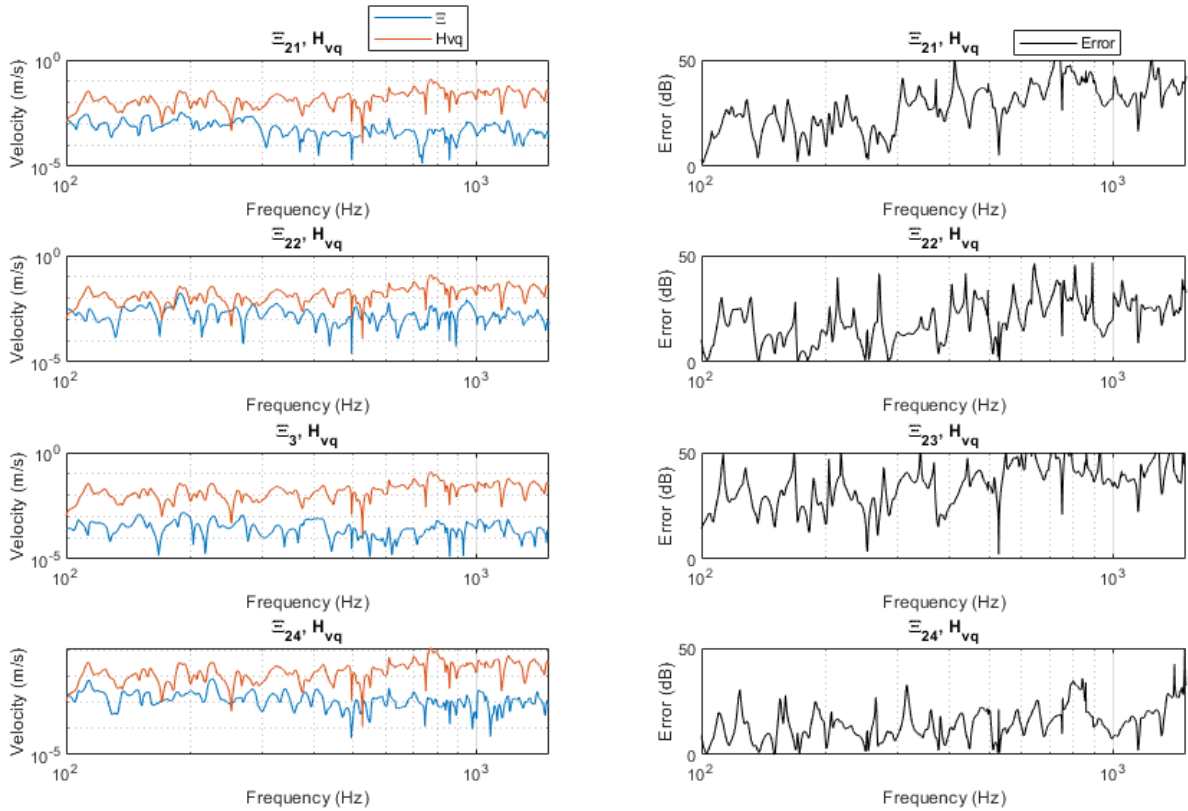


Figure 8.4: The left hand frames depict the single singular value transfer functions Ξ_{21} to Ξ_{24} , plotted against the original, unchanged H_{vq} transfer function. The x axis is frequency in Hertz and the y axis is velocity in metres per second. The right hand frames show the difference error in dB for the corresponding Ξ with respect to H_{vq} .

Looking at Ξ_{21} to Ξ_{24} in Figure 8.4, the significant divergence between the original FRF and the single singular value FRF seen in previous experiments for the transfer functions constructed using the smallest singular values is not evident. The general shape of the Ξ transfer functions remain fairly consistent, with little differentiation between them. The method has clearly been unsuccessful in separating out individual modal contributions from H_{vq} . The error in dB remains fairly consistent for both groups of Ξ shown, with the exception of the 1st Ξ , which bears the most resemblance to H_{vq} .

8.3 Blocked Force Predictions Using Ξ

A selection of results are shown here using the Ξ transfer function multiplied by the blocked forces, to give the contribution to radiated pressure associated with the individual singular value. As the plate is under-sampled, more than one mode is present in each singular value. Shown are a selection of results for the microphone/ volume velocity position at 60° , to the side of the plate. The plate is excited by Shaker 1.

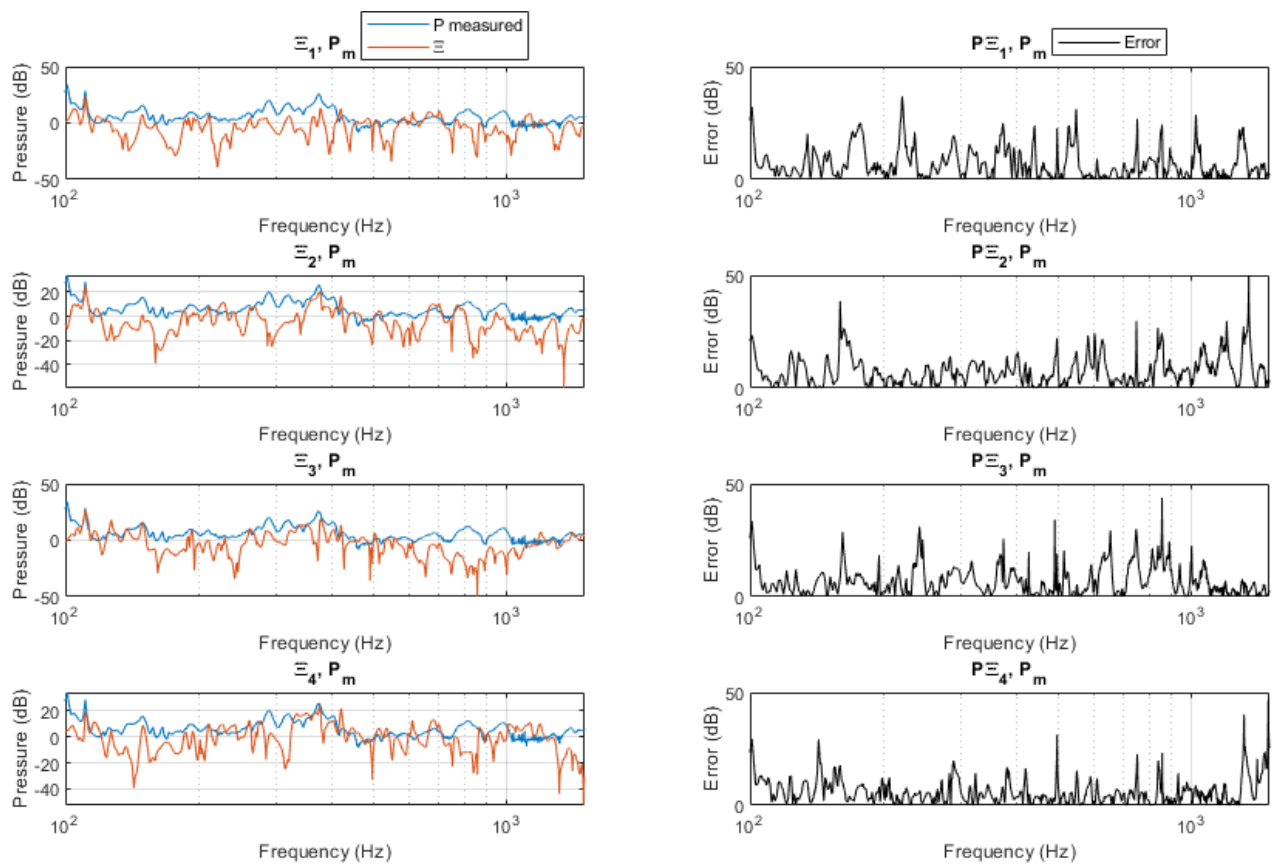


Figure 8.5: Predictions of radiated pressure contributions from singular value transfer functions Ξ_1 to Ξ_4 , for the microphone response and volume velocity excitation at the 60° position to the plate. The left hand frames show in blue is the original measured transfer function of pressure due to force for the operational shaker response., and plotted in red is the blocked force prediction using the constructed singular value transfer function Ξ_i . The x-axis is frequency in Hertz and the y axis is pressure in dBs. The right hand frames show the error in dB between the prediction and the measured response in black.

There are minimal differences in the pressure predictions made using each decomposed function Ξ . Shown above in Figure 8.5 are the predictions using the singular value transfer

functions Ξ_i multiplied by the blocked forces of the plate. Each prediction looks very similar to the other predictions, which is relatively close to the measured pressure. This indicates that the singular values contain multiple modes, and any contribution from a single mode has been obscured by the inclusion of the other modes in each singular value. There are areas of the Ξ where the error between the prediction and measured is under 20 dB, however there are no substantial bands of frequency which precisely coincide with the measured pressure. In the case of success, it would be expected that areas of the predictions would overlap at certain frequencies, indicating those frequencies are described singularly by that particular Ξ , as seen in the Ξ for the laser measurements in Chapter 7.

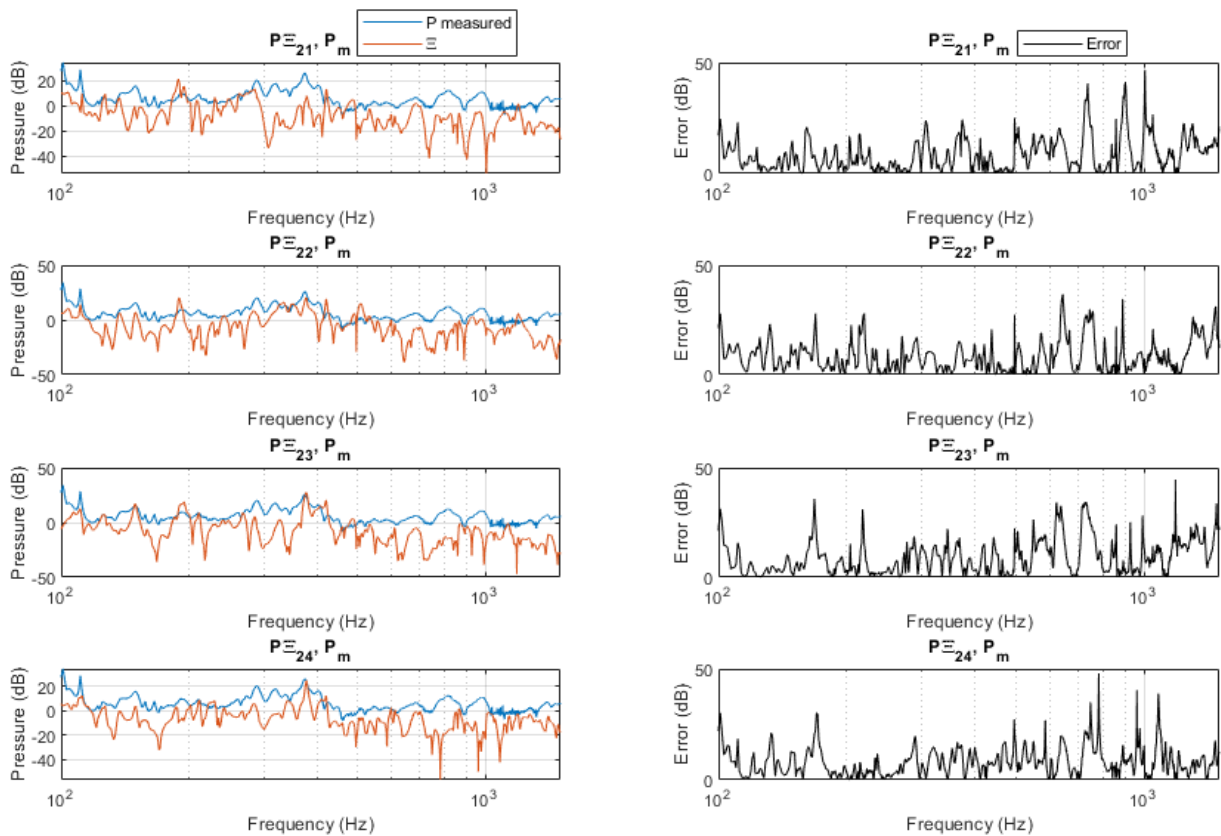


Figure 8.6: Predictions of radiated pressure contributions from singular value transfer functions Ξ_{21} to Ξ_{24} , for the microphone response and volume velocity excitation at the 60° position to the plate. The left hand frames show in blue is the original measured transfer function of pressure due to force for the operational shaker response., and plotted in red is the blocked force prediction using the constructed singular value transfer function Ξ_i . The x-axis is frequency in Hertz and the y axis is pressure in dBs. The right hand frames show the error in dB between the prediction and the measured response in black.

Continuing from the first 4 predictions using $\bar{\mathcal{E}}$ transfer functions, the predictions using $\bar{\mathcal{E}}_{21}$ to $\bar{\mathcal{E}}_{24}$ look similar in appearance, as depicted in Figure 8.6. These results are unsurprising considering the failure of the larger singular values to contribute significant modal information. As the transfer functions tend towards containing smaller and smaller singular values, the prediction begins to resemble the blocked force. This indicates that the $\bar{\mathcal{E}}$ transfer functions are no longer contributing any significant modal information.

8.4 Discussion

A method for predicting the contribution of a group of dominant modes to the measured radiation of a plate has been investigated using a plate instrumented with 24 accelerometers and the volume velocity source. Due to insufficient discretisation of the plate surface, the method has not been successful, with each decomposed transfer function $\bar{\mathcal{E}}$ containing the contribution of many frequencies. This was confirmed by the lack of clarity seen in the columns of Ψ , which if sufficient spatial sampling had been used would contain the mode shapes of the plate, as described in the scanning laser vibrometer experiments. It is assumed that with a more detailed discretisation of the surface, the method would provide more specific modal contributions, as evidenced by the higher amount of spatial sampling positions in the laser tests. It is likely that the spatial sampling resolution must have intervals at less than half of the wavelength of the frequency of the target mode, which in this particular case is only applicable for the first mode of the plate. Despite efforts to increase the damping of the plate, it is also likely that degenerate and overlapping modes are an issue. One way this could be further investigated is using a non-metal panel, such as polyethylene, which would have innately better damping, leading to superior separation of modes. Alternatively, heavily discretising the surface of the metal plate with accelerometers, to a resolution higher than 57 response positions as indicated by the laser testing, would allow for a more complete description of the surface.

9 CONCLUSIONS

The main aim of the thesis was to develop a method of decomposing frequency response functions using singular value decomposition, for the prediction of far-field radiated noise from vibrating structures. By combining the decomposed frequency response functions with blocked forces, the intention was to identify the contribution of individual modes, or small groups of modes, to the overall radiated noise. As opposed to other methods, the decomposition used in this thesis was novel as it was conducted in terms of location vs frequency, rather than frequency by frequency. Blocked forces have also not yet been used in combination with decomposed frequency response functions, and the work in this thesis may inspire further developments using blocked forces with operational modal analysis techniques. Using the blocked forces, or blocked surface pressures, rather than other parameters, is advantageous over other quantities, as these are inherent properties of the structure, as that they remain valid when the receiver is changed. As the blocked force parameters may be quantified before the structure is deployed, this could lead to a streamlined real-time analysis procedure, which may be less computationally expensive than current methods.

An in-situ transfer path analysis approach was conducted as a baseline, whereby a discretised surface has a blocked pressure assigned to each element. This discretised surface is then treated as the source, and the surrounding fluid as the receiver. This is a relatively new technique, though has been previously proposed by other researchers. The novel application of singular value decomposition of the vibro-acoustic frequency response functions measured reciprocally, by which the radiation modes of the structure should be extracted, is then used to replace the non-decomposed transfer function usually used in the blocked forces prediction. The decomposed individual singular value frequency response functions are

multiplied by the blocked forces, which in an ideal case would give a prediction of radiated noise contribution for an individual mode. As the experiment was under-sampled, the decomposed transfer functions do not represent modes, but rather whole sections of the frequency response function. This led to the results not offering an improvement on the baseline in-situ transfer path analysis in this thesis.

Based on the results shown in this thesis, with adequate spatial sampling, modally separating the frequency response functions can be achieved, as shown by the heavily discretised beam experiment. However, this depth of resolution is impractical experimentally. With a 17 response position beam model, the highest mode which could be considered characterised was of 4.25 sampling positions per bending wavelength.

Similarly, when conducted on a plate with a relatively dense spatial sampling, transfer functions were constructed containing a small number of modes, though complete separation of individual modes was not achieved. When attempted with a more sparsely discretised plate, the method has been unsuccessful. The modes are not separated due to each singular value containing multiple modes. Therefore, the method can only be shown to work with heavy discretisation of the surface.

Due to the fact that the volume velocity source does not require the operator to directly excite the assembly, the volume velocity source could be considered an advantageous alternative to the direct measurement for the measurement of vibro-acoustic frequency response functions. It offers itself as an alternative to those already available, with advantages in being lower cost, more portable, and easier to use than sources already established. In the case where an assembly is heavily discretised with a limited number of remote response positions, the novel volume velocity source would allow for the assembly to be measured far more efficiently than with a hammer. As the in-situ blocked force transfer path analysis method allows for the characterisation of the source independently from the environment, a single evaluation of the

blocked forces could be conducted, and assuming the instrumentation of the assembly remains in place, the vibro-acoustic frequency response functions can then be evaluated reciprocally. These frequency response functions measure the radiation from the surface of the radiating structure, which can then be decomposed to give the radiation modes. The reciprocal frequency response functions were shown to be comparable to the directly measured frequency response functions measured using the hammer, rendering them a suitable alternative method of measurement, with the added advantages associated with the reciprocal measurement.

9.1 Further Work

An appropriate starting point to continue the work would be with a Finite Element Analysis model, with which modelling of the blocked pressures on the surface of the modelled structure could be used to evaluate exactly how many discretised positions are necessary for the separation of modes, and to ascertain how the desired frequency range can be characterised. It is assumed that with specific attention to the positioning of discrete response positions, it may be that a number of modes of interest can be captured without an exceedingly dense sensor array.

Relatively small test structures have been evaluated in the thesis, whereas the method is more likely to be functional in very large structures, as the wavelengths of the resonances will be much longer. This may allow for a comparatively sparse sensor array to be sufficient at low frequencies. An investigation into this, perhaps using a model, would be pertinent.

In terms of the volume velocity source, improvements could be made to its directivity by modifications to the aperture of the barrel, such as adding a dispersive nozzle. Varying the barrel in terms of length would affect the frequency response, whilst using a different

diameter would affect the directivity. The excitations may be increased in amplitude by using different amounts of pressure, which could be achieved by replacing the regulator.

BIBLIOGRAPHY

- [1] T. ten Wolde and G. Gadefelt, "Development of Standard Measurement Methods for Structureborne Sound Emission," *Noise Control Eng. J.*, vol. 28, no. 1, p. 5, 1987.
- [2] A. T. Moorhouse, A. S. Elliott, and T. A. Evans, "In situ measurement of the blocked force of structure-borne sound sources," *J. Sound Vib.*, 2009.
- [3] L. Zhang, R. Brincker, and P. Andersen, "An overview of operational modal analysis: Major development and issues," in *Proceedings of the 1st International Operational Modal Analysis Conference, IOMAC 2005*, 2005.
- [4] B. Peeters and G. De Roeck, "Stochastic system identification for operational modal analysis: A Review," *J. Dyn. Syst. Meas. Control. Trans. ASME*, 2001.
- [5] M. V. van der Seijs, D. de Klerk, and D. J. Rixen, "General framework for transfer path analysis: History, theory and classification of techniques," *Mech. Syst. Signal Process.*, vol. 68–69, pp. 217–244, Feb. 2016.
- [6] G. J. O'hara, Z. * Zjk, and Zlv, "1121/1.1915605 The Mobility Method of Computing the Vibration of," *Mech. Immittance-and Transm. Concepts J. Acoust. Soc. Am.*, vol. 41, p. 4199, 1967.
- [7] P. Gardonio and M. J. Brennan, "On the origins and development of mobility and impedance methods in structural dynamics," *J. Sound Vib.*, vol. 249, no. 3, pp. 557–573, 2002.
- [8] F. A. Firestone, : By, and F. A. Frv, "1121/1.1916217 The Mobility Method of Computing the Vibration of," *A New Analog. between Mech. Electr. Syst. J. Acoust. Soc. Am.*, vol. 4, p. 5, 1933.
- [9] F. V Hunt, "Electroacoustics The Analysis of Transduction and Its Historical

- Background,” 1954.
- [10] I. J. Busch-Vishniac, *Electromechanical Sensors and Actuators*. Springer Science and Business Media, 1999.
- [11] A. D. Pierce and P. W. Smith, “Acoustics: An Introduction to Its Physical Principles and Applications,” *Phys. Today*, vol. 34, no. 12, pp. 56–57, 1981.
- [12] H. C. Pusey, “Progress in Shock and Vibration Technology Over 80 Symposia,” Springer, New York, NY, 2011, pp. 533–543.
- [13] A. Elliott, “Characterisation Of Structure Borne Sound Sources In-Situ,” University Of Salford, Greater Manchester, 2009.
- [14] J. R. Meggitt, “On In-situ Methodologies for the Characterisation and Simulation of Vibro-Acoustic Assemblies,” University of Salford, 2017.
- [15] “International Organisation for Standardisation. BS EN ISO 3741 : 2010 Acoustics - Determination of sound power levels and sound energy levels of noise sources using sound pressure - Precision methods for reverberation test rooms (ISO 3741:2010).” .
- [16] “International Organisation for Standardisation. BE EN ISO 5136 : 2009 Acoustics - Determination of sound power radiated into a duct by fans and other air-moving devices - In-duct method.”
- [17] B. J. Dobson and E. Rider, “A Review of the Indirect Calculation of Excitation Forces from Measured Structural Response Data,” *Proceedings of the Institution of Mechanical Engineers, Part C: Journal of Mechanical Engineering Science*. 1990.
- [18] International standards organisation, “ISO 9611: Acoustics—characterisation of sources of structure-borne sound with respect to sound radiation from connected structures—measurement of velocity at the contact points of machinery when

- resiliently mounted,” 1996.
- [19] International Organization for Standardization, “ISO 20270:2019 Acoustics - Characterization of Sources of Structure-Borne Sound and Vibration - Indirect Measurement of Blocked Forces,” 2019.
- [20] A. T. Moorhouse, “On the characteristic power of structure-borne sound sources,” *J. Sound Vib.*, vol. 248, no. 3, pp. 441–459, Nov. 2001.
- [21] H. Lee and Y. S. Park, “Error analysis of indirect force determination and a regularisation method to reduce force determination error,” *Mech. Syst. Signal Process.*, vol. 9, no. 6, pp. 615–633, 1995.
- [22] Plunt Juha, “Finding and Fixing Vehicle NVH Problems with Transfer Path Analysis,” *Sound Vib.*, vol. 39, pp. 12–17, 2005.
- [23] A. Diez-Ibarbia *et al.*, “Comparison between transfer path analysis methods on an electric vehicle,” *Appl. Acoust.*, vol. 118, pp. 83–101, 2017.
- [24] J. Plunt, “Finding and Fixing Vehicle NVH Problems with Transfer Path Analysis.”
- [25] T. AN and D. Thompson, “The quantification of structure-borne transmission paths by inverse methods. Part 2: Use of regularization techniques,” *J. Sound Vib.*, vol. 264(2), 2003.
- [26] A. Thite and D. Thompson, “The quantification of structure-borne transmission paths by inverse methods. Part 1: Improved singular value rejection methods,” *J. Sound Vib.*, vol. 264(2), 2003.
- [27] M. H. A. Janssens and J. W. Verheij, “A pseudo-forces methodology to be used in characterization of structure-borne sound sources,” vol. 61, pp. 285–308, 2000.
- [28] M. H. A. Janssens and J. W. Verheij, “Two applications of the pseudo-forces method

- for characterizing the source strength for structure-borne sound,” in *Internoise, Liverpool, UK, 1996*.
- [29] M. H. A. Janssens, J. W. Verheij, and D. J. Thompson, “The use of an equivalent forces method for the experimental quantification of structural sound transmission in ships,” *J. Sound Vib.*
- [30] J. W. Verheij, “Inverse and Reciprocity Methods for Machinery Noise Source Characterization and Sound Path Quantification Part 1: Sources,” *Int. J. Acoust. Vib.*, vol. 2, no. 1, pp. 11–20, 1997.
- [31] M. Ohlrich and A. Crone, “An equivalent force description of gear-box sources applied in prediction of structural vibrational in wind turbines. Proceedings of Inter-noise 88, 1988.”
- [32] S. Laugesen and M. Ohlrich, “The vibrational source strength descriptor using power input from equivalent forces: a simulation study,” *Acta Acust.*, 1994.
- [33] B. M. Gibbs, N. Qi, and A. T. Moorhouse, “A practical characterisation for vibro-acoustic sources in buildings,” *Acta Acust. united with Acust.*, vol. 93, no. 1, pp. 84–93, 2007.
- [34] A. T. Moorhouse and B. M. Gibbs, “Measurement of structure-borne sound emission from resiliently mounted machines in situ,” *J. Sound Vib.*, vol. 180, no. 1, pp. 143–161, 1995.
- [35] A. Moorhouse and A. Elliott, “The ‘round trip’ theory for reconstruction of Green’s functions at passive locations,” *J. Acoust. Soc. Am.*, vol. 134, no. 5, pp. 3605–3612, Nov. 2013.
- [36] A. T. Moorhouse, T. A. Evans, and A. S. Elliott, “Some relationships for coupled structures and their application to measurement of structural dynamic properties in

- situ,” *Mech. Syst. Signal Process.*, vol. 25, no. 5, pp. 1574–1584, Jul. 2011.
- [37] D. Lennström, M. Olsson, F. Wullens, and A. Nykänen, “Validation of the blocked force method for various boundary conditions for automotive source characterization,” *Appl. Acoust.*, vol. 102, pp. 108–119, Jan. 2016.
- [38] A. S. Elliott, J. W. R. Meggitt, and A. T. Moorhouse, “Blocked forces for the characterisation of structure borne noise,” in *Conference Proceedings of Internoise and Noise-Con Congress*, 2015, vol. 250, no. 1.
- [39] H. K. Lai, A. Moorhouse, and B. Gibbs, “Experimental round-robin evaluation of structure-borne sound source force-power test methods,” no. November 2015, 2016.
- [40] G. Banwell and R. Faventi, “Assessment of experimental techniques to characterise the vibration source strength of a motor radially mounted with resilient elements.”
- [41] F. J. Fahy and J. Walker, *Advance Applications in Acoustics, Noise and Vibration*. Spoon press, 2004.
- [42] J. W. R. Meggitt and A. T. Moorhouse, “On the completeness of interface descriptions and the consistency of blocked forces obtained in situ,” *Mech. Syst. Signal Process.*, vol. 145, Nov. 2020.
- [43] D. De Klerk, “Dynamic response characterization of complex systems through operational identification and dynamic sub-structuring,” TU Delft, 2009.
- [44] H. Lai, “Alternative test methods for measuring structure-borne sound power,” in *Internoise, Honolulu, Hawaii, USA*.
- [45] Y. I. Bobrovnikskii, “A theorem on the representation of the field of forced vibrations of a composite elastic system,” *Acoust. Phys.*, vol. 47, no. 5, pp. 507–510, Sep. 2001.
- [46] A. A. Abohnik, “In situ blocked force measurement in gearboxes with potential

- application for condition monitoring,” no. February, 2018.
- [47] T. Marwala, “Condition monitoring using computational intelligence methods: applications in mechanical and electrical systems.,” *Springer Sci. Bus. Media.*, 2012.
- [48] S. Ghodake, A. Mishra, and A. Deokar, “A Review on Fault Diagnosis of Gear-Box by Using Vibration Analysis Method,” *IPASJ Int. J. Mech. Eng. IJME*, vol. 4, no. 1.
- [49] L. S. Dhamande and M. B. Chaudhari, “An Overview of Fault Detection Methods for Transmission System Components using Vibration Analysis,” vol. 2, no. 4, pp. 360–368, 2014.
- [50] T. Hoshi, “Damage Monitoring of Ball Bearing.”
- [51] A. A. Abohnik, “In Situ Blocked Force Measurement in Gearboxes With Potential Application for Condition Monitoring,” University of Salford, 2018.
- [52] R. Brincker and C. E. Ventura, *Introduction to Operational Modal Analysis*. 2015.
- [53] M. A. Biot, “A Mechanical Analyser for the Prediction of Earthquake Stresses,” 1941.
- [54] M. A. Biot, “Analytical and Experimental Methods in Engineering Seismology,” New York, 1943.
- [55] M. Biot, “Geometry of the Heat Equation: First Paper,” 1932.
- [56] M. Trifunac and B. Westerno, “Ground Motion on Magnitude, Epicentral Distance, Geological Conditions at the Recording Station and Frequency of Motion,” *Univ. South. Calif.*, 1976.
- [57] M. D. Trifunac, “Early History of The Response Spectrum Method,” 2007.
- [58] P. Van Overschee and B. De Moor, *Subspace Identification for Linear Systems*. Springer US, 1996.

- [59] S. R. Ibrahim and E. C. Milkulcik, "A Method for Direct Identification of Vibration Parameters From the Free Response," *Shock Vib. Bull.*, vol. 47, pp. 183–196, 1977.
- [60] H. Vold, J. Kundrat, G. T. Rocklin, and R. Russell, "A Multi-Input Modal Estimation Algorithm for Mini-Computers."
- [61] J. N. Juang and R. S. Pappa, "An eigensystem realization algorithm for modal parameter identification and model reduction," *J. Guid. Control. Dyn.*, vol. 8, no. 5, pp. 620–627, 1985.
- [62] F. Bin Zahid, Z. C. Ong, and S. Y. Khoo, "A review of operational modal analysis techniques for in-service modal identification," *J. Brazilian Soc. Mech. Sci. Eng.*, vol. 42, no. 8, pp. 1–18, 2020.
- [63] M. Ghalishooyan and A. Shooshtari, "Operational modal analysis techniques and their theoretical and practical aspects: A comprehensive review and introduction," *6th Int. Oper. Modal Anal. Conf. IOMAC 2015*, no. January, 2015.
- [64] L. Zhang, T. Wang, and Y. Tamura, "A frequency-spatial domain decomposition (FSDD) method for operational modal analysis," 2009.
- [65] B. H. Kim, N. Stubbs, and T. Park, "A new method to extract modal parameters using output-only responses," *J. Sound Vib.*, vol. 282, no. 1–2, pp. 215–230, 2005.
- [66] D. J. Ewins, *Modal Testing*. Research Studies Press Ltd, 2000.
- [67] A. J. Felber, "Development of a Hybrid Bridge Evaluation System," The University of British Columbia, 1994.
- [68] E. M. Cárdenas and L. U. Medina, "Non-Parametric Operational Modal Analysis Methods in Frequency Domain: A Systematic Review," *Int. J. Eng. Technol. Innov.*, vol. 11, no. 1, pp. 34–44, 2021.

- [69] R. Brincker, L. Zhang, and P. Andersen, “Modal Identification from Ambient Responses using Frequency Domain Decomposition,” *IMAC 18 Proc. Int. Modal Anal. Conf.*, pp. 625–630, 2000.
- [70] M. Batel, “Operational modal analysis - Another way of doing modal testing,” *S V Sound Vib.*, vol. 36, no. 8, pp. 22–27, 2002.
- [71] C. Devriendt and P. Guillaume, “Identification of modal parameters from transmissibility measurements,” *J. Sound Vib.*, vol. 314, no. 1–2, pp. 343–356, 2008.
- [72] C. Rainieri and G. Fabbrocino, “Operational Modal Analysis: overview and applications,” *Strateg. Reduct. Seism. risk*, pp. 29–44, 2008.
- [73] R. Brincker, C. E. Ventura, and P. Andersen, “Damping Estimation by Frequency Domain Decomposition,” in *Proceedings of the 19th international modal analysis conferecne (IMAC)*, 2001, pp. 5–8.
- [74] M. D. A. Hasan, Z. A. B. Ahmad, M. S. Leong, and L. M. Hee, “Enhanced frequency domain decomposition algorithm: A review of a recent development for unbiased damping ratio estimates,” *J. Vibroengineering*, vol. 20, no. 5, pp. 1919–1936, 2018.
- [75] B. H. Kim, N. Stubbs, and T. Park, “A new method to extract modal parameters using output-only responses,” *J. Sound Vib.*, vol. 282, no. 1–2, pp. 215–230, Apr. 2005.
- [76] D. J. Ewins, *Modal Testing: Theory, Practice, and Application*. Research Studies Press Ltd, 2000.
- [77] G. H. James III, T. G. Carne, Lauffer, J. P., and J. P. Lauffer, “The Natural Excitation Technique (NExT) for Modal Parameter Extraction From Operating Wind Turbines,” *Int. J. Anal. Exp. Modal Anal.*, vol. 10, no. 4, pp. 260–277, 1993.
- [78] K. Fukuzono, *Investigation of Multiple-reference Ibrahim Time Domain Modal*

- Parameter Estimation Technique*. Cincinnati: University of Cincinnati, 1986.
- [79] D. L. Brown, R. J. Allemang, R. Zimmerman, and M. Mergeay, "Parameter Estimation Techniques for Modal Analysis," *SAE Trans.*, vol. 88, pp. 828–846, Aug. 1979.
- [80] L. Zhang, "From Traditional Experimental Modal Analysis (EMA) to Operational Modal Analysis (OMA), an Overview," in *IOMAC*, 2013, pp. 1–14.
- [81] L. Ljung, *System Identification: Theory for the User*. Upper Saddle River, NJ: Prentice Hall PTR, 1999.
- [82] J.-N. Juang, *Applied System Identification*. Upper Saddle River, NJ: Prentice-Hall, Inc, 1994.
- [83] P. Andersen and P. H. Kirkegaard, "Statistical Damage Detection of Civil Engineering Structures using ARMAV Models," 1997.
- [84] P. Andersen, R. Brincker, and P. H. Kirkegaard, "Theory of Covariance Equivalent ARMAV Models of Civil Engineering Structures," 1995.
- [85] K. A. Petsounis and S. D. Fassois, "Parametric time-domain methods for the identification of vibrating structures-a critical comparison and assessment," *Mech. Syst. Signal Process.*, vol. 15, no. 6, pp. 1031–1060, 2001.
- [86] J. B. Bodeux and J. C. Golinval, "Application of ARMAV models to the identification and damage detection of mechanical and civil engineering structures," *Smart Mater. Struct.*, vol. 10, no. 3, pp. 479–489, 2001.
- [87] M. Bertha and J. C. Golinval, "Modal identification of time-varying systems using Hilbert transform and signal decomposition," *Proc. ISMA 2014 - Int. Conf. Noise Vib. Eng. USD 2014 - Int. Conf. Uncertain. Struct. Dyn.*, pp. 2409–2420, 2014.
- [88] S.-Y. Kung, "A New Identification and Model Reduction Algorithm via Singular

- Value Decomposition,” in *Proceedings of the 12th Asilomar Conference of Circuits, Systems, and Computers*, 1978.
- [89] B. De Moor, P. Van Overschee, and J. Suykens, “Subspace algorithms for system identification and stochastic realization,” *Electr. Eng.*, no. 3280, pp. 1–12, 1990.
- [90] P. Van Overschee and B. De Moor, “Continuous-time frequency domain subspace system identification,” *Signal Processing*, vol. 52, no. 2, pp. 179–194, 1996.
- [91] R. Zhang, L., Brincker, “An Overview of Operational Modal Analysis: Major Development and Issues,” in *Proceedings of the 1st International Operational Modal Analysis Conference, IOMAC 2005*, 2005.
- [92] K. S. Arun and S. Y. Kung, “Balanced approximation of Stochastic Systems,” *SIAM J. Matrix Anal. Appl.*, vol. 11, no. 1, pp. 42–68, 1990.
- [93] B. Peeters and G. De Roeck, “Stochastic system identification for operational modal analysis: A Review,” *J. Dyn. Syst. Meas. Control. Trans. ASME*, vol. 123, no. 4, pp. 659–667, 2001.
- [94] S. Qin, J. Kang, and Q. Wang, “Operational Modal Analysis Based on Subspace Algorithm with an Improved Stabilization Diagram Method,” *Shock Vib.*, vol. 2016, no. January, 2016.
- [95] B. Peeters and G. De Roeck, “Reference-based stochastic subspace identification for output-only modal analysis,” *Mech. Syst. Signal Process.*, vol. 13, no. 6, pp. 855–878, 1999.
- [96] C. Rainieri and G. Fabbrocino, *Operational Modal Analysis of Civil Engineering Structures*. 2014.
- [97] E. Reynders, “System Identification Methods for (Operational) Modal Analysis:

- Review and Comparison,” *Arch. Comput. Methods Eng.*, 2012.
- [98] E. Reynders, K. Maes, G. Lombaert, and G. De Roeck, “Uncertainty quantification in operational modal analysis with stochastic subspace identification: Validation and applications,” *Mech. Syst. Signal Process.*, vol. 66–67, pp. 13–30, 2016.
- [99] F. Magalhães and Á. Cunha, “Explaining operational modal analysis with data from an arch bridge,” *Mechanical Systems and Signal Processing*. 2011.
- [100] M. M. Farrokhifard, M. Hatami, and V. M. Venkatasubramanian, “Performance of stochastic subspace identification methods in presence of forced oscillations,” *2019 Int. Conf. Smart Grid Synchronized Meas. Anal. SGSMA 2019*, pp. 3–5, 2019.
- [101] W. Li, V. H. Vu, Z. Liu, M. Thomas, and B. Hazel, “Extraction of modal parameters for identification of time-varying systems using data-driven stochastic subspace identification,” *JVC/Journal Vib. Control*, vol. 24, no. 20, pp. 4781–4796, 2018.
- [102] F. Liu, J. Wu, F. Gu, and A. D. Ball, “An Introduction of a Robust OMA Method: CoS-SSI and Its Performance Evaluation through the Simulation and a Case Study,” *Shock Vib.*, vol. 2019, 2019.
- [103] P. Van Overschee and B. De Moor, “Subspace algorithms for the stochastic identification problem,” *Automatica*, vol. 29, no. 3, pp. 649–660, 1993.
- [104] C. Palerm, C. Prada, B. Gerardin, A. Talon, and J. de Rosny, “Modal analysis of structures from the singular value decomposition of their acousto-elastic transmission matrix,” “*Advances Acoust. Noise Vib. - 2021*” *Proc. 27th Int. Congr. Sound Vib. ICSV 2021*, pp. 1–9, 2021.
- [105] C. Palerm, C. Prada, B. Gerardin, A. Talon, and J. De Rosny, “Singular value decomposition of acousto-elastic matrix for modal analysis of mechanical structures,” *J. Acoust. Soc. Am.*, vol. 150, no. 4_Supplement, pp. A41–A41, Oct. 2021.

- [106] C. Y. Shih, Y. G. Tsuei, R. J. Allemang, and D. L. Brown, “Complex mode indication function and its applications to spatial domain parameter estimation,” *Mech. Syst. Signal Process.*, vol. 2, no. 4, pp. 367–377, 1988.
- [107] M. H. Masjedian and M. Keshmiri, “A review on operational modal analysis researches: Classification of methods and applications,” *IOMAC 2009 - 3rd Int. Oper. Modal Anal. Conf.*, pp. 707–716, 2009.
- [108] L. Beranek, *Acoustics*. New York, 1960.
- [109] H. Kuttruff and T. J. Schultz, *Room Acoustics*, vol. 27, no. 10. 1974.
- [110] A. Schuhmacher, “Investigation of volume velocity source based on two-microphone method for measuring vibro-acoustic transfer functions.”
- [111] H. F. van Tol and J. W. Verheij, “Brite EuRam II: Loudspeaker for reciprocal measurement of near field sound transfer functions on heavy road vehicle engines,” Delft, The Netherlands, 1993.
- [112] T. Rossing and N. Fletcher, *Principles of vibration and sound*. Springer Science & Business Media, 2004.
- [113] “ISO. (2018). Acoustics - Reference zero for the calibration of audiometric equipment - Part 1: Reference equivalent threshold sound pressure levels for pure tones and supra-aural earphones. ISO 389-1:2017.” .
- [114] “KI-396 | Klipsch,” 2021. [Online]. Available: <https://www.klipsch.com/products/ki-396>. [Accessed: 23-Apr-2023].
- [115] “HBK 4250 Wideband Volume Velocity Sources.”
- [116] “Low frequency Volume Velocity Source - Microflown.” [Online]. Available: <https://www.microflown.com/products/volume-velocity-sources/low-frequency->

- volume-velocity-source. [Accessed: 24-Apr-2023].
- [117] “Mid-High Frequency Volume Velocity Source - Microflown.” [Online]. Available: <https://www.microflown.com/products/volume-velocity-sources/mid-high-frequency-volume-velocity-source>. [Accessed: 24-Apr-2023].
- [118] B. and Kjaer, “Omnipower type 4292-L loudspeaker source.” [Online]. Available: <https://www.bksv.com/en/transducers/acoustic/sound-sources/omni-power-light-4292>.
- [119] Bruel and Kjaer, “Omnisource omnidirectional sound source.”
- [120] “GRAS 42AA Pistonphone, Class 1.” [Online]. Available: <https://www.grasacoustics.com/products/calibration-equipment/reference-calibrator/product/255-42aa>. [Accessed: 23-Apr-2023].
- [121] “Calibration; Sound Level Calibrator Type 4230; Pistonphone Type 4220 - BRUEL & KJAER 4117 Instructions And Applications [Page 19] | ManualsLib.” [Online]. Available: <https://www.manualslib.com/manual/1662613/Bruel-And-Kjaer-4117.html?page=19>. [Accessed: 23-Apr-2023].
- [122] S. Müller and P. Massarani, “Transfer-function measurement with sweeps,” *AES J. Audio Eng. Soc.*, vol. 49, no. 6, pp. 443–471, 2001.
- [123] A. S. Elliott, A. T. Moorhouse, T. Huntley, and S. Tate, “In-situ source path contribution analysis of structure borne road noise,” *J. Sound Vib.*, 2013.
- [124] L. Barton, A. Elliott, A. Moorhouse, and J. Smith, “In-situ transfer path analysis of multiple vibration sources in a complex source- receiver assembly,” *Proc. Int. Congr. Acoust.*, vol. 2019-Sept, no. September, pp. 435–442, 2019.
- [125] L. E. Kinsler, A. R. Frey, A. B. Coppens, and J. V. Sanders, “Fundamentals of Acoustics (4th Edition),” *John Wiley Sons Inc.*, p. 560, 1999.

- [126] T. ten Wolde, J. W. Verheij, and H. F. Steenhoek, “Reciprocity method for the measurement of mechano-acoustical transfer functions,” *J. Sound Vib.*, vol. 42, no. 1, pp. 49–55, 1975.
- [127] T. Ten Wolde, “Reciprocity measurements in acoustical and mechano-acoustical systems. Review of theory and applications,” *Acta Acust. united with Acust.*, vol. 96, no. 1, pp. 1–13, 2010.
- [128] H. Helmholtz, “Theorie des Luftschalls in Röhren mit offenen Ende.” 1860.
- [129] J. W. Rayleigh, “Some general theorems relating to vibration,” in *Proc. Of London Math. Soc.*, 1873, vol. 4, p. 357.
- [130] J. W. S. B. Rayleigh and R. B. Lindsay, *The Theory of Sound, Volume 1*. 1945.
- [131] S. Ballantine, “Reciprocity in electromagnetic, mechanical, acoustical and interconnected systems,” in *Proceedings of the Institute of Radio Engineers*, 1929, vol. 17, no. 6, pp. 929–951.
- [132] C. Chang and Q. Du, “Interference and Noise-Adjusted,” vol. 37, no. 5, pp. 2387–2396, 1999.
- [133] G. H. Golub and C. Reinsch, *Numerical Mathematics*, vol. 14. 1970.
- [134] D. J. Ewins, *Modal testing : theory, practice, and application*, 2nd ed. Philadelphia, PA: Research Studies Press, Baldock, Hertfordshire, England, 2000.
- [135] S. Marburg and B. Nolte, “Computational acoustics of noise propagation in fluids - Finite and boundary element methods,” *Comput. Acoust. Noise Propag. Fluids -Finite Bound. Elem. Methods*, no. January 2008, pp. 1–578, 2008.
- [136] P. Langer, M. Maeder, C. Guist, M. Krause, and S. Marburg, “More Than Six Elements per Wavelength: The Practical Use of Structural Finite Element Models and

- Their Accuracy in Comparison with Experimental Results,” *J. Comput. Acoust.*, vol. 25, no. 4, pp. 1–23, 2017.
- [137] G. Lerman, “The Shannon Sampling Theorem and Its Implications,” vol. 1. pp. 1–10.
- [138] A. I. Zayed, *Advances in Shannon;s Sampling Theory*. 1993.
- [139] S. P. Timoshenko, J. M. Gere, and W. Prager, “Theory of Elastic Stability, Second Edition,” *Journal of Applied Mechanics*, vol. 29, no. 1. pp. 220–221, 1962.
- [140] R. C. Hibbeler, *Structural Analysis*, 4th ed. Upper Saddle River, N.J: Prentice Hall, 1999.
- [141] K. Leet, *Fundamentals of Structural Analysis*. Collier McMillan, 1988.
- [142] F. P. Beer, E. Russel Johnston, and J. T. DeWolf, *Mechanics of Materials*, 3rd ed. Boston: McGraw-Hill, 2002.
- [143] R. Blevins, *Formulas for Dynamics, Acoustics and Vibration*. John Wiley & Sons, Incorporated, 2015.
- [144] A. Sinha, *Vibration of Mechanical Systems*. Cambridge: Cambridge University Press, 2010.
- [145] W. Soedel, *Vibrations of Shells and Plates*, 3rd ed. .
- [146] R. D. Blevins, “Natural Frequency of Plates and Shells,” in *Formulas for Dynamics, Acoustics and Vibration*, Chichester, UK: John Wiley & Sons, Ltd, 2016, pp. 203–259.
- [147] M. Ducceschi, “Nonlinear vibrations of rectangular plates: A numerical investigation with application to wave turbulence and sound synthesis,” 2014.
- [148] A. Leissa, *Vibration of plates*. Columbus, Ohio: Ohio State University, 2008.
- [149] R. Cherif, J. D. Chazot, and N. Atalla, “Damping loss factor estimation of two-

- dimensional orthotropic structures from a displacement field measurement,” *J. Sound Vib.*, vol. 356, pp. 61–71, 2015.
- [150] G. A. Papagiannopoulos and G. D. Hatzigeorgiou, “On the use of the half-power bandwidth method to estimate damping in building structures,” *Soil Dyn. Earthq. Eng.*, vol. 31, no. 7, pp. 1075–1079, 2011.
- [151] PCB Piezoelectronics, “Dynamic pressure sensors for high frequency measurements,” *Datasheet*. .
- [152] E. N. Glish, “ICP ® PCB Piezoelectronics Pressure Sensor Datasheet,” no. 113, p. 14043, 2022.
- [153] “Briel & Kjaer 1/2" Prepolarised free-field microphone type 4966 datasheet.”
- [154] “Briel & Kjaer High-temperature CCLD Microphone Preamplifier Type 1706 Datasheet.”
- [155] Bruel and Kjaer, “Briel & Kjaer Impact Hammer Product Data,” *www.bksv.com*, vol. 6, no. 4. p. 31.
- [156] Bruel and Kjaer, “Impact Hammer Types 8206, 8206-001 8206-002, 8206-003 Product datasheet.”
- [157] K. G. Dally, J. W., Riley, W. F., & McConnell, *Instrumentation for engineering measurements*. 1984.
- [158] “BS ISO 5348-1998 Mechanical vibration and shock - Mechanical mounting of accelerometers.” International Organisation for Standardisation, 1998.
- [159] C. Scheffer and P. Girdhar, “Practical machinery vibration analysis and predictive maintenance,” *Elsevier*, 2004.
- [160] E. Guanabara, K. Ltda, E. Guanabara, and K. Ltda, “Sino Ceramics force transducer

- datasheet.”
- [161] “Sinocera remote charge amplifier.” [Online]. Available:
<https://www.sinocera.com/products/vibration-instrumentation/conditioners/remote-charge-amplifier/>.
- [162] “LDS V101 Permanent Magnet Shaker - Durham Instruments.” [Online]. Available:
<https://disensors.com/product/lds-v101-permanent-magnet-shaker/>.
- [163] “50mm 4 Ohm 25w Resonance Vibration Shaker Loudspeaker Woofer Strong Drive Plane Speaker | Fruugo UK.” [Online]. Available: https://www.fruugo.co.uk/50mm-4-ohm-25w-resonance-vibration-shaker-loudspeaker-woofer-strong-drive-plane-speaker/p-151873018-321121862?language=en&ac=croud&gclid=EAIaIQobChMI66XmyO7J_gIVTJ7tCh3ucAd8EAQYCyABEgJkMPD_BwE. [Accessed: 27-Apr-2023].
- [164] Timoshenko S P and J. M. Gere, *Mechanics of Materials*. PWS Publishing Company, 1997.
- [165] O. Şahin, B. Erbaş, J. Kaplunov, and T. Savšek, “The lowest vibration modes of an elastic beam composed of alternating stiff and soft components,” *Arch. Appl. Mech.*, vol. 90, no. 2, pp. 339–352, 2020.
- [166] G. Cheng, D. W. Herrin, and J. Stencel, “Acoustic radiation prediction using panel contribution analysis combined with scale modeling,” *Appl. Acoust.*, vol. 186, p. 108458, 2022.
- [167] T. Shin, Y. S. Kim, K. An, and S. K. Lee, “Transfer path analysis of rumbling noise in a passenger car based on in-situ blocked force measurement,” *Appl. Acoust.*, vol. 149, pp. 1–14, 2019.

